IN SITU REAL-TIME STUDIES OF ORGANIC SEMICONDUCTOR THIN FILM GROWTH

A Dissertation

Presented to the Faculty of the Graduate School

of Cornell University

In Partial Fulfillment of the Requirements for the Degree of

Doctor of Philosophy

by

Tushar Vrushank Desai

January 2012

IN SITU REAL-TIME STUDIES OF ORGANIC SEMICONDUCTOR THIN FILM GROWTH

Tushar Vrushank Desai, Ph. D.

Cornell University 2012

This thesis discusses the thin film deposition of small molecule organic semiconductors. Small molecule organics are attracting significant interest primarily due to their ability to form well ordered thin films at low temperatures with reasonable electronic properties. Potential applications of organic based electronics include thin film transistors, display technologies, flexible integrated circuits and photovoltaics. The growth and morphology of these organic thin films is very sensitive to the nature (chemical and physical) of the underlying substrate. A significant challenge in fabricating organic thin film devices with superior electrical characteristics is that of controlling and more importantly understanding the properties at the interface between the organic semiconducting layer and the underlying substrate. In this thesis, the use of supersonic molecular beams as a means to deposit organic semiconductor thin films is discussed in conjunction with *in situ* real-time synchrotron scattering and *ex situ* atomic force microscopy as thin film characterization techniques. This thesis discusses the effects of the incident kinetic energy of the small molecule organic and the nature of dielectric (clean silicon dioxide, SiO_2; or SiO_2 modified with self-assembled monolayers, SAMs, of varying thickness and chemical functionality; or SiO_2 modified with polymers of varying surface energy) on the fundamental thin film processes

occurring at the organic semiconductor/substrate interface. These thin film processes include adsorption, nucleation and diffusion, and the filling up of individual monolayers during thin film growth. Experiments have provided significant insight into these fundamental thin film processes. The results indicate that the probability of adsorption is a strong function of the incident kinetic energy of the organic molecule and thickness of the underlying SAM. The submonolayer island shape and island density is also a strong function of the underlying substrate with the later implying a change in the diffusivity of the organic with the identity of the substrate. Finally, the results suggest that multilayer thin film morphology such as feature/grain size and the thin film roughness is also a function of the underlying substrate.

BIOGRAPHICAL SKETCH

Tushar was born in Kigoma, Tanzania. Kigoma is a small town in the western most part of Tanzania near Lake Tanganyika and Gombe National Park. Shortly after his birth, his family moved to Dar es Salaam (capital city of Tanzania) where he lived for 18 years before moving to the United States. Tushar conducted his schooling years all the way from kindergarten to 12^{th} grade at the International School of Tanganyika located in Dar es Salaam, Tanzania. In May 2002, Tushar graduated from high school after completing the International Baccalaureate (IB) program. Tushar finished in the top 5 of his class. In August 2002, Tushar moved to the United States where he started his undergraduate degree at Bucknell University in Lewisburg, Pennsylvania. Tushar completed his Bachelor of Science degree in Chemical Engineering with a minor in Economics at Bucknell University in May 2006. He graduated with Magna Cum Laude honor and Tau Beta Pi Engineering honor. In August 2006, Tushar started his Ph.D. in Chemical Engineering at Cornell University. Tushar completed his Ph.D. in Chemical Engineering from Cornell University in July 2011. Tushar is going to start on a new adventure at Intel in September 2011 as a Quality and Reliability engineer.

To my mom, dad, sister, brother-in-law, niece and family

Believe

Jai Shree Krishna

ACKNOWLEDGMENTS

First and foremost, I would like to express my utmost gratitude to my advisor, Prof. James R. Engstrom. He has been an excellent mentor and teacher – his strive for excellence in all aspects of scientific research has inspired me to work hard and strive for perfection. I want to also express my gratitude towards my committee member, Dr. Arthur R. Woll. Arthur, I want to thank you for taking your time in helping me design synchrotron x-ray experiments. More importantly, I want to thank you for being a friend and for your encouragement through all the hard times during the long synchrotron runs and more. I am also grateful for my minor committee member, Prof. Paulette Clancy who helped provide excellent insights from MD simulations. I would also like to thank my minor committee member, Prof. Tobias Hanrath for his for help, support and insightful discussions into organic photovoltaics. I would also like to thank my minor committee member Prof. Emmanuel Giannelis for his help and support.

I would like to thank Prof. Stefan Kowarik (University of Berlin) and Prof. Frank Schreiber (University of Tübingen) for their collaboration and in providing the diindenoperylene and perfluoropentacene organic materials. I would also like to express my gratitude to Glenn Swan for his prompt help regarding various machining issues in the lab. I would also like to thank Bob Seeley (CHESS staff) for his help with vacuum systems. I would also like to thank Ananth Kaushik (PhD student in Prof. Clancy's group) who helped provide excellent insights (see section 3) from MD simulations. I would also like to thank Dr. Joe Goose (Clancy group, PhD 2009) for his helpful insights in organic thin film growth from MD simulations. I would also like to thank Hitesh Arora (Wiesner group, PhD 2010) for his help in spin-coating polymeric substrates. I would also like to thank Dr. John Ferguson (Brock group, PhD

2010) for his help during the synchrotron runs. I would also like to thank Prof. Aram Amassian and Dr. Vladimir Pozdin (Malliaras group members) for the fun times in the projects we worked on together.

Within the Engstrom research group (ERG), I would firstly like to thank former group members (Dr. Todd Schroeder and Dr. Aravind Killampalli) for laying the foundations for the G-line project. I would like to thank Dr. Sukwon Hong for teaching me the ins and outs of vacuum systems and his immense help during the synchrotron runs early on in my PhD career. I would also like to thank the recently graduated Dr. Kevin Hughes, for the insightful research-related discussions that we had together and for his help in the synchrotron runs during the early days of my PhD career. I would also like to thank Ed Kish, for his help during the synchrotron runs in the latter part of my PhD career. I would also like to thank the younger members in the ERG group, Wenyu Zhang and Rambert Nahm for their help and support.

I would also like to thank Manchester United Football Club (MUFC) for providing years and years of football entertainment – you have played an immense part in my life, especially in keeping me sane during my PhD career and other hard times. Glory glory Manchester United! In the end and most importantly, I would like to express my utmost eternal gratitude towards my family, especially my mom, dad, sister, brother-in-law and my baby niece, for their love, support, encouragement and inspiration.

I would like to acknowledge the Cornell Center for Materials Research (CCMR) for their financial support. I would also like to acknowledge the experimental facilities that I used during my PhD and all their staff: CNF, CCMR, NBTC and CHESS.

TABLE OF CONTENTS

LIST OF FIGURES

LIST OF TABLES

1. Introduction

In this thesis, I present studies of the thin film deposition of small molecule organic semiconductors for applications in organic based electronics. Organic based transistors cannot rival the performance of transistors based on their inorganic counterparts (e.g. Si, Ge and GaAs), which have carrier mobilities larger by three to four orders of magnitude. Consequently, organic electronics are not useful in applications involving very high switching speeds and carrier mobilities. However, the future generations of electronic products that may eventually enter the mainstream market based on organic active materials will have potential applications in novel devices such as flexible electronic circuits and existing devices such as display technologies, sensors (e.g. radio frequency identification tags) and photovoltaics. The motivation of using organic active materials over their inorganic counterparts in such devices is because organic electronics offer the potential for cheaper low-cost products due to their low temperature processing and possible reel-to-reel printing methods, compatibility with large-area flexible substrates, and their ease in tuning electronic and processing conditions by chemical synthesis. **[1, 2]** A key difference in deposition of organic materials, compared to more conventional inorganic materials like metals, semiconductors and oxides, involves the presence of strong covalent and ionic bonding in the latter class of materials, whereas organic materials are often bound by rather weak dispersion (van der Waals) forces and are often known to crystallize in different phases. As a consequence, considerable promise exists in tuning organic thin film growth by varying deposition techniques, process parameters, dielectric substrates and the chemical design of the organic molecules themselves.

Like their traditional inorganic counterparts, organic semiconductors can function either as p-type or n-type. In p-type semiconductors, the majority carriers are holes, whereas in n-type semiconductors the majority carriers are electrons. Two classes of organic semiconductors exist – conjugated semiconducting polymers **[3]** (e.g. poly(3-hexylthiophene)) and conjugated small molecule organic semiconductors (e.g. pentacene and C_{60}). Conjugated polymers are normally deposited via solution phase, whereas small molecule organics are deposited either by vapor phase or solution phase (if they can be dissolved in solvent). In both cases, to achieve superior electronic properties, it is desirable for the semiconducting molecule to self-assemble into a well packed defect free and highly crystalline thin film upon deposition. In this thesis, the deposition of small molecule conjugated organics is investigated from the vapor phase.

The basic building block of organic electronics is an organic thin film transistor (OTFT). The main features of an OTFT are highlighted in the schematic shown in Figure 1-1. During the operation of an OTFT, a bias voltage applied at the gate electrode is used to control the current flow between the source and the drain via the organic semiconducting material. The application of organic materials to electronic devices will vary based on required performance standards. For example, in liquid crystal displays, the active backplane currently consists of TFTs made from hydrogenated amorphous silicon (a–Si:H) with well-established technology for large area applications. OTFTs can enable applications that are not achievable with this inorganic technology involving flexible plastic substrates. However, for OTFTs to compete directly with a–Si:H thin film transistors, they will need to exhibit device

performance similar to the latter, i.e. field effect mobility μ = 1 $cm^2–V^{-1}–s^{-1}$, current modulation (on/off ratio, $I_{on/off}$) of 10^6 or higher and a reasonable operating threshold voltage of 15 V or less. Additionally, these transistors should be stable after prolonged exposure to ambient conditions and should not exhibit large threshold voltage shifts.

Several studies have shown that the interface between the organic semiconducting layer and the dielectric (see Figure 1-1) is critical to charge transport in OTFTs and that the majority of charge carriers are generated in the first few monolayers (MLs) of the organic layer **[4-7]** adjacent to the semiconductor/dielectric interface. Thus the chemical and physical characteristics of the dielectric interface can have a significant impact on organic semiconductor thin film growth and therefore their electrical properties. Several studies have also shown that the deposition of organic semiconductors on low energy surfaces such as self-assembled monolayers (SAMs) **[8-12]** and polymers **[12, 13]** significantly improves the electrical properties of the OTFT. The exact reasons as to why these improvements are observed are still a matter of debate, however. Clearly, the development of a better understanding of the effect of the nature (chemical and physical) of the dielectric on the initial stages of organic semiconductor thin film growth will greatly aid in resolving these issues – understanding these effects will allow for greater control over organic semiconductor thin film growth and therefore enable the fabrication of more reproducible, reliable and superior devices.

Organic thin film deposition from the vapor phase is conventionally done using thermal evaporation, in which molecules are incident on the substrate at thermal energies (i.e. 0.05 - 0.1 eV). Among other parameters that can be exploited to modify

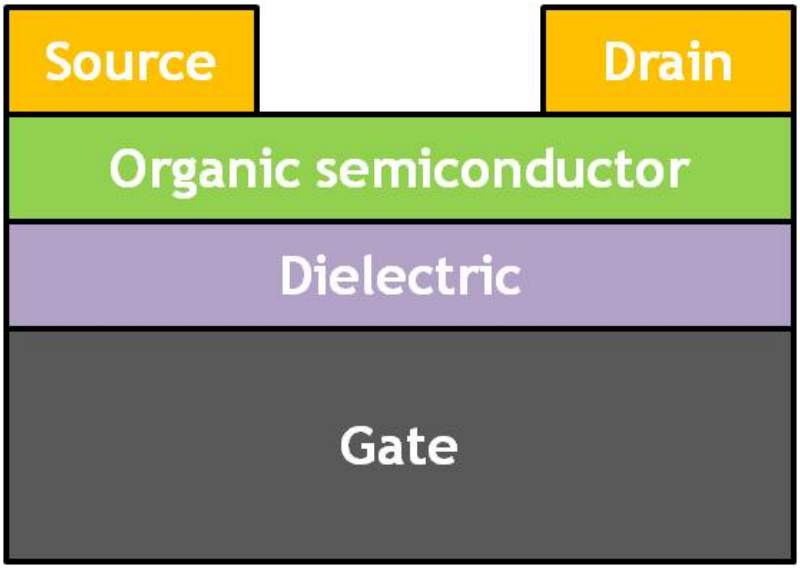

Figure 1-1 Schematic showing a top contact organic thin film transistor (OTFT)

organic thin film growth conducted in vacuum are the two most commonly used – the growth rate and the substrate temperature. One potential molecular variable that might be exploited is the kinetic energy of the depositing species. In this thesis, I have investigated the deposition of small molecule organic semiconductors of interest using supersonic molecular beams. Unlike thermal evaporation, in supersonic molecular beams, the molecules are incident on the substrate at hyperthermal kinetic energies on the order of several electron volts. Details on supersonic molecular beams can be found in chapters 1.4 and 2.1.

This thesis discusses the effects of the incident kinetic energy of the small molecule organic and the nature of dielectric (clean silicon dioxide, SiO_2; or SiO_2 modified with SAMs of varying thickness and chemical functionality; or SiO_2 modified with polymers of varying surface energy) on the fundamental thin film processes occurring at the organic semiconductor/dielectric interface. These thin film processes include adsorption, nucleation and diffusion, and the filling up of individual monolayers during thin film growth. Four different small molecule organic semiconductors have been investigated in this thesis (see Figure 1-2): diindenoperylene (DIP), pentacene, perfluoropentacene (PFP), and *N,N'*-ditridecylperlyene-3,4,9,10-tetracarboxylic diimide (PTCDI-C_{13}). Chapter 3 focuses on the effects of SAMs and incident kinetic energy on the adsorption dynamics of DIP organic thin film growth. The effects of SAMs and incident kinetic energy on the thin film morphology and roughness of DIP organic thin film growth is discussed in chapter 4. Chapter 4 also discusses on the effect of substrate temperature on the morphology of DIP organic thin film growth. Chapter 5 discusses the effect of

polymer surface energy and incident kinetic energy on pentacene thin film growth. The effect of SAMs on the submonolayer nucleation of PFP organic thin film growth is discussed in chapter 6. Finally, chapter 7 discusses the effect of SAMs and incident kinetic energy on the adsorption dynamics and submonolayer nucleation of PTCDI-C_{13} organic thin film growth.

1.1 Organic semiconductors investigated

The four organic semiconductors investigated in this thesis (see Figure 1-2) are similar in that their cores are composed of fused benzene rings. They differ in that DIP and pentacene are p-type molecules where as PFP and PTCDI-C_{13} are n-type.

1.1.1 Diindenoperylene (DIP)

The space-filling model of diindenoperylene (DIP) is shown in Figure 1-2. DIP, a red dye, is a planar molecule with a perlyene core and two side indeno groups. The chemical formula of DIP is $C_{32}H_{16}$ with molecular weight of 400 g/mol. As shown in Figure 1-2, DIP contains only carbon (gray filled spheres) and hydrogen (white filled spheres). DIP exhibits p-type semiconducting behavior in combination with gold contacts with a reported hole mobility as high as 0.12 cm^2-V^{-1}-s^{-1} **[14]**. Additional information about DIP can be found in sections 3 and 4. In the thin film phase, DIP stands upright with its long molecular axis almost perpendicular to the substrate. Both the DIP single crystal structure (at 403 K) and thin film crystal structure on SiO_2 are summarized in Table 1-1. The thin film crystal structure of DIP

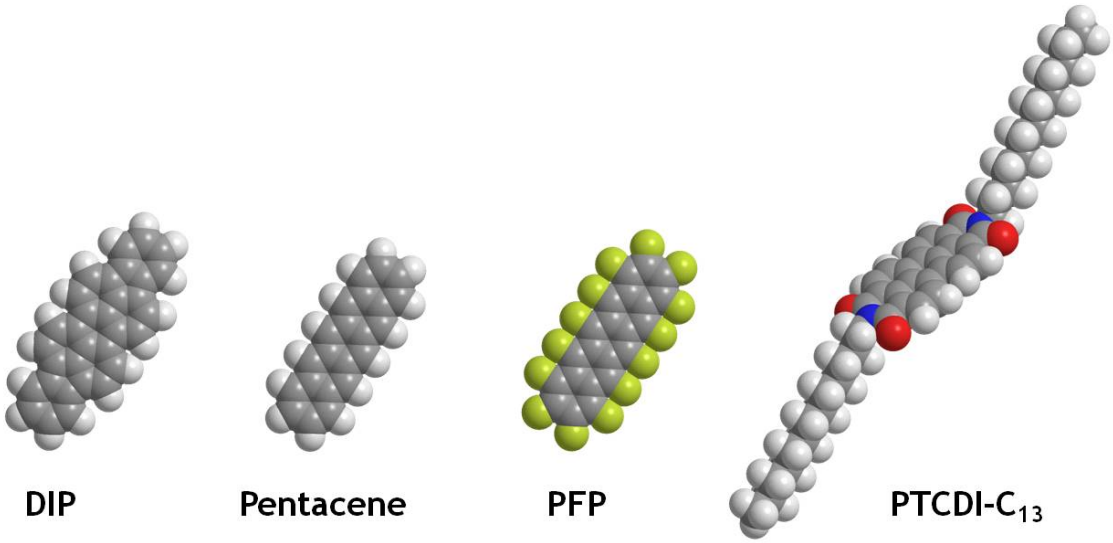

Figure 1-2 Space filling models of the organic semiconductors investigated in this thesis. From right to left: diindenoperylene (DIP), pentacene, perfluoropentacene (PFP), and *N,N'*-ditridecylperlyene-3,4,9,10-tetracarboxylic diimide (PTCDI-C_{13}).

Table 1-1 Crystal structures of DIP, pentacene, PFP and PTCDI-C_{13}

	a (Å)	*b* (Å)	*c* (Å)	*α* (°)	*β* (°)	*γ* (°)	# Molecules
DIP (single crystal) **[15]**	11.66	13.01	14.97	98.44	98.02	114.54	2
DIP/SiO_2 **[16]**	8.55	7.09	16.6 (layer height)			90	2
Pentacene (Single crystal) **[17]**	6.266	7.775	14.530	76.475	87.682	84.684	2
Pentacene/ SiO_2 **[18]**	7.58	5.91	15.43 (layer height)			90±0.2	2
Pentacene/ SiO_2 (first layer)**[18]**	7.62	5.90	15.43 (layer height)			90±0.2	2
PFP (single structure) **[19]**	15.51	4.490	11.449	90	91.567	90	2
PFP/SiO_2 **[20]**	15.76 ±0.02	4.51± 0.02	11.48± 0.02			90.4 ±0.1	2
PTCDI-C_{13} (single structure) **[21]**	4.661	8.592	25.31	86.380	85.786	82.473	2

Note: The direction of vectors *a*, *b* and *c* in the above table have been taken directly from their respective reference. These directions may not be consistent when comparing each reference. Refer to the specific reference for details.

has also been investigated as a function of substrate temperature (on SiO_2 and aluminum oxide) – in addition to the standing-up phase, at low substrate temperatures DIP also forms lying-down structures, with its long molecular axis parallel to the substrate **[22-24]**.

1.1.2 Pentacene

The space-filling model of pentacene is shown in Figure 1-2. Pentacene, the most widely studied organic semiconductor, is a planar molecule made of five fused benzene rings. The chemical formula of pentacene is $C_{22}H_{14}$ with a molecular weight of 278 g/mol. As shown in Figure 1-2, pentacene contains only carbon (gray filled spheres) and hydrogen (white filled spheres). Pentacene exhibits p-type semiconducting behavior with a hole mobility as high as 3.3 cm^2-V^{-1}-s^{-1} reported **[25]**. Detailed pentacene literature background can be found in section 5. Pentacene forms two phases in thin films: the 'thin film phase' and the 'bulk phase'. In the 'thin film' phase, pentacene is standing upright with its long molecular axis perpendicular to the substrate and a monolayer height of ~ 15.4 Å. In the 'bulk film' phase, pentacene is also standing upright with its long molecular axis perpendicular to the substrate but with a monolayer height of ~ 14.4 Å – the bulk phases forms above a critical thickness and this critical thickness is inversely proportional to the substrate temperature. The pentacene single crystal and 'thin film' phase structures are summarized in Table 1-1.

1.1.3 Perfluoropentacene (PFP)

The space-filling model of perfluoropentacene (PFP) is shown in Figure 1-2. PFP, like pentacene, is a planar molecule made of five fused benzene rings but the hydrogen atoms are replaced with fluorine atoms. The chemical formula of PFP is $C_{22}F_{14}$ with a molecular weight of 530 g/mol. As shown in Figure 1-2, PFP contains only carbon (gray filled spheres) and fluorine (green filled spheres). PFP exhibits n-type semiconducting behavior with an electron mobility as high as 0.22 cm^2-V^{-1}-s^{-1} reported **[26]**. Detailed PFP literature background can be found in section 6. Like DIP and pentacene, PFP also stands upright in the thin film phase with its long molecular axis perpendicular to the substrate. The PFP single crystal structure and thin film structure are summarized in Table 1-1.

1.1.4 *N,N'*-ditridecylperlyene-3,4,9,10-tetracarboxylic diimide (PTCDI-C_{13})

The space-filling model of *N,N'*-ditridecylperlyene-3,4,9,10-tetracarboxylic diimide (PTCDI-C_{13}) is shown in Figure 1-2. PTCDI-C_{13} is a planar molecule with a perlyene core and two side 13 carbon chains groups. The chemical formula of PTCDI-C_{13} is $C_{50}H_{62}N_2O_4$ with a molecular weight of 754 g/mol. As shown in Figure 1-2, PTCDI-C_{13} contains carbon (gray filled spheres), hydrogen (white filled spheres), oxygen (red filled spheres) and nitrogen (blue filled spheres). PTCDI-C_{13} exhibits n-type semiconducting behavior with an electron mobility as high as 2.1 cm^2-V^{-1}-s^{-1} reported **[21]**. Detailed PTCDI-C_{13} literature background can be found in section 7. Like DIP, pentacene, and PFP, PTCDI-C_{13} also stands upright in the thin film phase

with its long molecular axis perpendicular to the substrate. The PTCDI-C_{13} single crystal structure is summarized in Table 1-1. The thin film structure of PTCDI-C_{13} has not been determined yet. However, the crystal structure of a close relative (PTCDI-C_8) has been determined **[27]**.

1.2 Dielectric materials: self-assembled monolayers and polymers

Dielectric materials play an important role in the performance of organic thin film transistors, as the chemical and physical nature of these materials can dictate the nucleation and morphology of organic thin films. Studies have shown that most of the charge carriers in organic thin film devices are confined to the first few monolayers adjacent to the organic semiconductor/dielectric interface **[4-7]**. Therefore the nature (chemical and physical) can have a significant impact on organic thin film growth and thus their electrical properties. In this thesis, I have investigated the effect of the nature (chemical and physical) of the dielectric on the fundamental thin processes occurring at the organic semiconductor/substrate interface. These thin film processes include adsorption, nucleation and diffusion, and the filling up of individual monolayers during thin film growth. To this end, I have studied three different groups of dielectric materials: (1) clean SiO_2, (2) SiO_2 modified with self-assembled monolayers (SAMs) and (3) SiO_2 modified with thin polymer films.

SAMs are an organized layer of molecules formed spontaneously by the adsorption of a surfactant on a solid surface. Each molecule in a SAM film consists of three components: an active headgroup which chemically binds to a suitable substrate

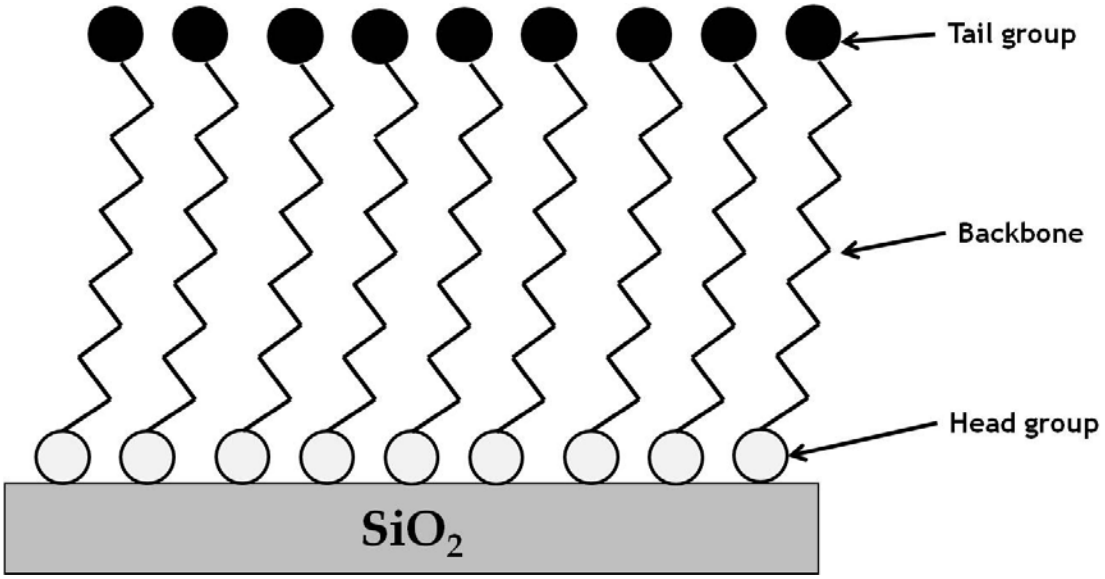

Figure 1-3 Cartoon representation of a self-assembled monolayer (SAM) showing the three individual components of each molecule namely: headgroup, backbone and tailgroup.

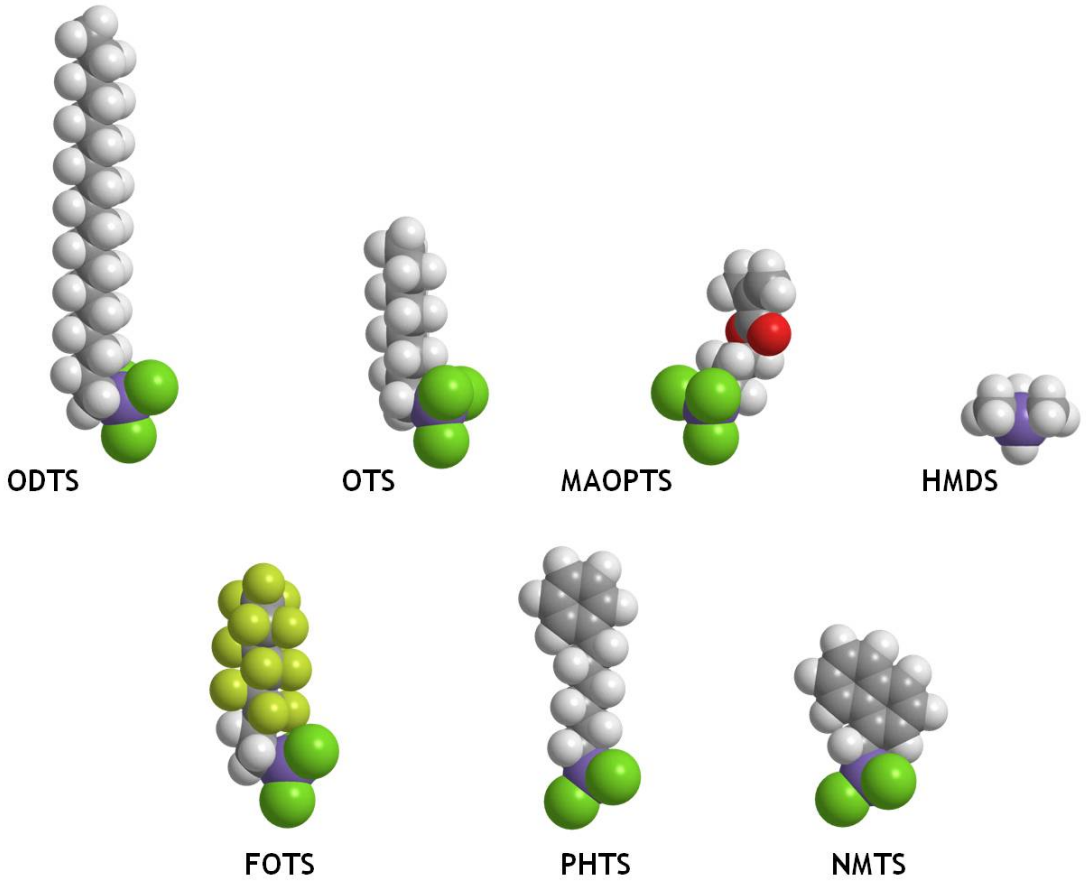

Figure 1-4 Space-filling models of self-assembled monolayers: Top row (from right to left): octadecyltrichlorosilane (ODTS), octyltrichlorosilane (OTS), 3-methacryloxypropyltrichlorosilane (MAOPTS), and hexamethyldisilazane, (HMDS). Bottom row (from right to left): perfluorooctyltrichlorosilane (FOTS), 6-phenylhexyltrichlorosilane (PHTS), 1-napthylmethyltrichlorosilane, (NMTS).

(in this case SiO_2), a functional tailgroup which provides for a wide variety of surface terminations and the backbone which permits the ordering of a layer by van der Waals interactions with neighboring molecules. By changing the functionality of the tailgroup and the backbone and the length of the backbone, the chemical and physical nature of the SAM can easily be tuned. Figure 1-3 shows the structure of a typical SAM film. A good review on SAMs can be found in reference **[28]**. Figure 1-4 shows space-filling models of the SAMs studied in this thesis. In all the SAMs studied in this thesis, the tailgroup is a trichlorosilane group (*R*-$SiCl_3$) as shown by the purple (silicon) and green (chlorine) atoms in Figure 1-4. The trichlorosilane group reacts with the hydroxyl groups on the SiO_2 surface to form –Si-O-Si– linkages.

An alternative class of dielectrics studied in this thesis is polymer thin films. Due to their ease in processing, 'flexible' in nature, and easily tunable surface properties, polymeric dielectrics are attractive and offer another means of tailoring the chemical and physical nature of the surface **[3]**. Space-filling models of the polymers (monomer units) studied are shown in Figure 1-5. The polymers studied include polystyrene (PS), polymethylmethacrylate (PMMA) and polyethylenimine (PEI). PS and PMMA are bound to the SiO_2 substrate via Van der Waals forces whereas PEI is bound to the SiO_2 substrate via electrostatic interactions.

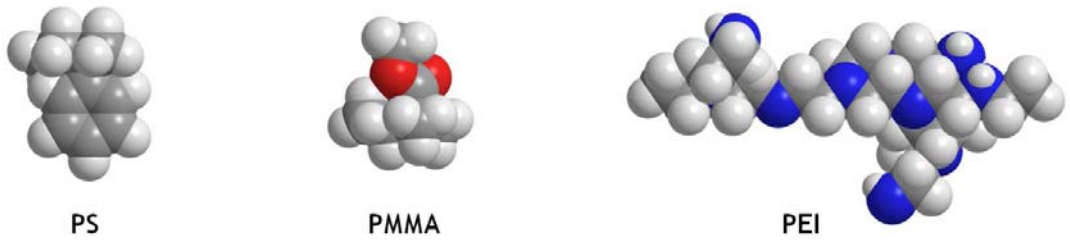

Figure 1-5 Space-filling models of polymer monomer units: From right to left: polystyrene (PS), polymethylmethacrylate (PMMA), polyethylenimine (PEI).

1.4 Thin Film Growth

In this thesis, the thin film growth of organic semiconductors (pentacene, DIP, PFP and PTCDI-C_{13}) has been investigated on various surfaces including SiO_2 and SiO_2 modified with SAMs and polymers. One of the goals of my thesis was to be able to understand how the chemical and physical nature of a substrate affects thin film growth processes that occur at the organic semiconductor/substrate interface. The theoretical and experimental background of thin film growth phenomena is broad and widespread, especially for metal on metal growth systems **[29-31]**. This section will provide a brief summary of thin film growth phenomena including pertinent thin film processes that occur in organic thin film systems, common thin film growth modes and submonolayer nucleation theory.

It is generally accepted that there are three common growth modes **[30]** that describe thin film morphology and these are described in Figure 1-6, where example thin film morphologies at coverages of <1, 1 and >2 monolayers (MLs) are shown. In one extreme, you have Frank-van der Merwe mode, where the film grows in a perfect layer-by-layer (LbL) manner – that is that each growing monolayer completely fills up before the subsequent monolayer nucleates. In the other extreme, you have Volmer-Weber mode, where the film grows in a perfect island or 3-dimensional (3D) mode. In between, one can have the Stranski-Krastanov mode, where initially, LbL growth takes place but later transforms into 3D mode after a critical film thickness. Stranski-Krastanov mode is also known as layer-plus-island growth mode.

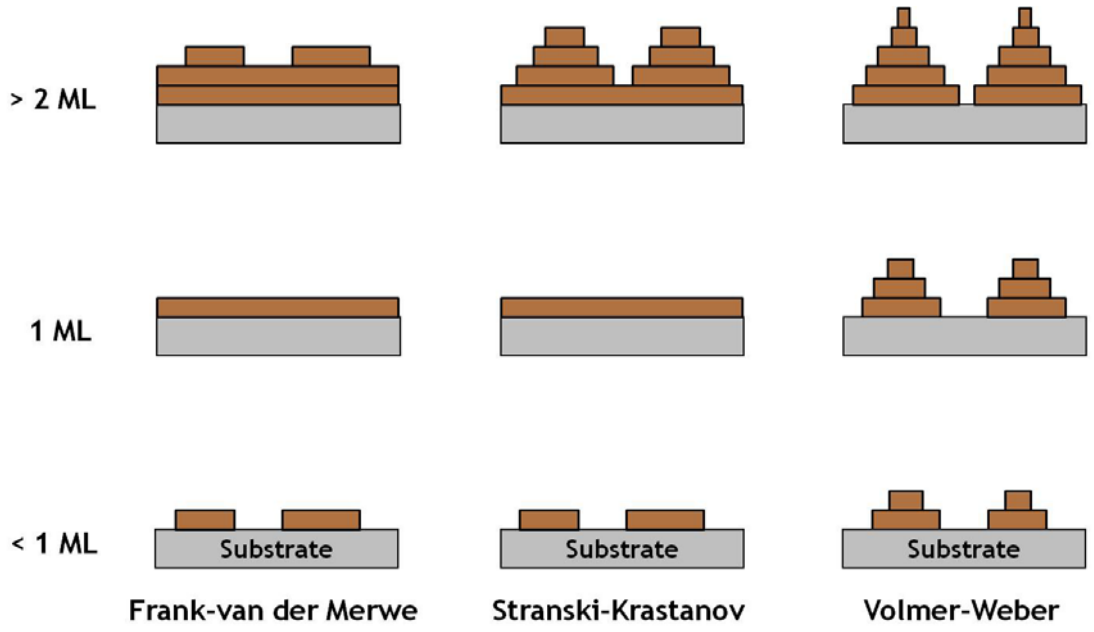

Figure 1-6 Schematic showing three different thin film growth modes.

It is important to note that the above mentioned growth modes were initially predicted using arguments based on surface energies (thermodynamic equilibrium) described by capillarity theory **[32]**:

$$\gamma_{film} + \gamma_{\text{int}erface} \leq \gamma_{substrate} \tag{1-1}$$

where γ_{film} is the surface energy of the film/vacuum interface, $\gamma_{substrate}$ is the surface energy of the substrate/vacuum interface and $\gamma_{interface}$ is the surface energy of the substrate/film interface. From capillarity theory, if the above relationship holds for a growth system, then the system is more energetically favorable towards Frank-van der Merwe or LbL growth. If the above relationship does not hold, then the system is more energetically favorable towards Volmer-Weber or island growth. In Stranski-Krastanov growth, the above relationship holds for an initially strained monolayer after which the film switches to island growth mode because the increase in the film strain contributes to the increasing interface energy of the system.

As stated earlier, the arguments above are based on surface energies and therefore represent purely thermodynamic equilibrium phenomenon. However, organic thin film growth is not an equilibrium process and is determined kinetically. The final outcome of organic thin film morphology is determined by kinetic processes such as those shown in Figure 1-7. The first process of organic thin film growth is adsorption as shown in Figure 1-7(a), where the kinetic energy of the incident molecule must dissipate in order for it to become trapped (adsorbed) onto the surface.

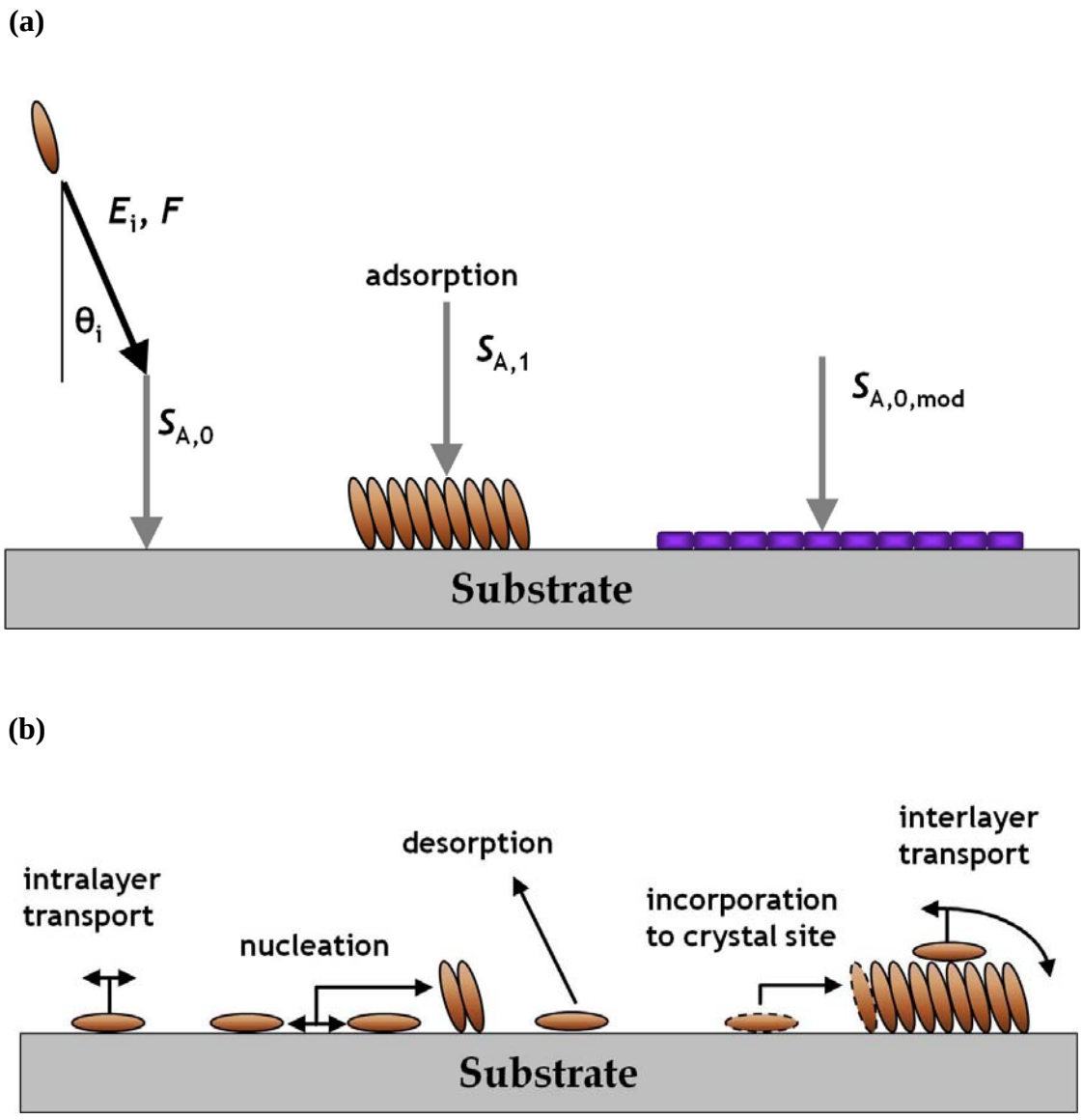

Figure 1-7 (a) Schematic showing the process of adsorption of a hyperthermal molecule from the gas phase onto a solid surface. The sticking coefficient may vary depending on where the molecule lands. (b) Schematic showing the different kinetic processes that may happen on a solid surface during organic thin film growth.

Organic thin film deposition is this thesis was done using supersonic molecular beams where the molecules in the gas phase have incident energies on the order of several electron volts (eV). In order to trap onto the surface, the molecules are going to have to dissipate this incident energy. This process of adsorption will have an associated sticking coefficient (S_A) and the sticking coefficient may vary depending on whether the molecule is landing on the bare SiO_2 ($S_{A,0}$), SiO_2 that has been modified by a SAM ($S_{A,0,mod}$) or whether the molecule is landing on the existing film ($S_{A,1}$).

Once the organic molecules are adsorbed on the surface they may undergo several thin film kinetic processes such as those shown in Figure 1-7(b), where each of these processes will have different activation barriers. Briefly, adsorbed admolecules will diffuse around the surface, a process called *intralayer transport.* When a sufficient number of these molecules meet up, they will *nucleate* islands. If these islands are stable in size, they will continue to grow bigger or else they will decay. Once the mean island-island separation is less than the diffusion length of the organic admolecule, admolecules are more likely to *incorporate* into existing island as opposed to nucleating new islands. Other processes also include admolecule diffusion around the edges of islands which may have different characteristics as compared to diffusion of isolated admolecules on the bare substrate. As the islands continue to grow, they will coalesce with other islands, the subsequent monolayer will begin to grow and so forth. The above mentioned kinetic processes will continue to proceed and dictate thin film morphology as new islands nucleate on existing islands as opposed to on the bare substrate. An important kinetic process that will determine the rate at which the film will roughen as a function of time is *interlayer transport*.

Interlayer transport is the ability of an admolecule to transfer itself from initially on top of an island to the layer below. A mechanism of interlayer transport is to diffuse to a step edge of the island and to 'hop over' onto the layer below. In order for this to happen, the organic molecule may have to overcome an additional energy barrier known as the Ehrlich-Schwoebel, *ES*, barrier **[33-37]**.

We can now relate the above kinetic processes shown in Figure 1-7 to the different thin film growth modes shown in Figure 1-6: an organic growth system will exhibit perfect LbL growth, if there exists infinite *interlayer transport*; if no *interlayer transport* is allowed such as if the *ES* barrier is too high for the molecules to overcome, then the system will exhibit perfect 3D growth; finally, if the ability of *interlayer transport* decreases with increasing film coverage, then the system will exhibit layer-plus-island growth.

The following will briefly discuss submonolayer thin film nucleation theory. In this thesis, several studies were performed quantifying how the submonolayer island density of organic thin films changed as a function of thin film growth rate and the nature (chemical) of the substrate. As shown here, such measurements allow the determination of the kinetic parameters of molecular motion on the surface. The submonolayer thin film island density (N_x) for 2D islands, complete condensation and homogenous nucleation and at film coverages where island coalescence has not taken place can be described using Venables nucleation theory **[29, 30, 38]**:

$$N_x = \eta(\theta, i^*)\left(\frac{GR}{D}\right)^{\frac{i^*}{i^*+2}} \exp\left(\frac{E_{i^*}}{(i^*+2)k_B T_S}\right) \qquad (1\text{-}2)$$

where GR is the film growth rate, D is the tracer diffusivity of the molecule, i^* is the critical cluster size, E_{i^*} is the binding energy of the critical cluster, T_s is the substrate temperature and k_B is the Boltzmann constant. The critical cluster size is defined as the largest unstable cluster, such that a cluster with $i^* + 1$ molecules is more likely to grow than to decay. The dimensionless prefactor $\eta(\theta, i^*)$ is nearly a constant—only weakly dependent on i^* and film coverage, θ **[30]**. The assumption of complete condensation implies irreversible adsorption or that desorption is negligible. This assumption is fair if the experiments were carried out at low substrate temperatures. The assumption of homogenous nucleation implies that the island density is not governed by defects on the surfaces.

Equation (1-2) shows that the critical cluster size may be determined by measuring how the maximum island density, N_x, varies with GR **[29-31, 38].** It is important to note that the above relationship shown in Equation (1-2) was derived from rate equations describing the rate of change of monomer and cluster densities on a surface **[38]**. One can refer to literature **[30]** regarding predicted island density relationships for other thin film growth regimes such as: 2D islands at incomplete condensation and 3D islands at complete and incomplete condensation. Incomplete condensation implies that desorption events cannot be neglected, such as thin film growth at elevated substrate temperatures.

1.4 Molecular Beam Techniques

In this thesis, molecular beams have been employed as a means to deposit the organic semiconductors of interest. This section will discuss two types of molecular beams: effusive molecular beams and supersonic molecular beams. Supersonic molecular beam techniques are perhaps the most powerful probe of molecule-surface interactions and provide an ideal method to tune the kinetic energy of organic molecules over a useful range that is on the order of, or greater than, the strength of the intermolecular and molecule-surface interactions. In this thesis several studies were also conducted regarding the adsorption dynamics of organic semiconductors both as a function of the incident energy of the molecular beam and the nature (chemical and physical) of the substrate. This section will also briefly discuss the different types of non-reactive adsorption and scattering events that can occur on a surface. The following sections on molecular beam techniques have been adapted from references **[39, 40]**.

1.4.1 Characterization of molecular beams

A molecular beam is a stream of electrically neutral molecules produced by expanding a gas through an orifice into a region of low pressure and collimating the flow by several apertures along the beam line. Based on the type of source, molecular beams can be classified into two broad categories: effusive and supersonic beams. The primary difference between these two types of beams is denoted by the Knudsen

number *Kn*, defined as the ratio of the molecular mean free path (λ) of the gas to a characteristic length scale of the source; in this case, the diameter of the source orifice (*d*):

$$Kn = \frac{\lambda}{d} \tag{1-3}$$

Kn determines the extent of inter–molecular interactions in a gas expanding through a given orifice. There are two limiting cases for the Knudsen number. If Kn >> 1, molecules travel long distances without undergoing collisions with each other, molecule–wall collisions are much more frequent and transport is ballistic or molecular. This is typical for an effusive beam. If Kn << 1, the molecules undergo several collisions with each other and transport is continuum as in the case of a supersonic expansion. These two types of beams are described in further detail in the next two sections.

1.4.1.1 Effusive beams

An effusive beam has low source pressure which ensures free molecular flow through the source orifice. Owing to the small number of interactions between molecules expanding in an effusive beam, they are characterized by a Maxwell–Boltzmann velocity distribution which is a function of the source temperature (T_n). The flux–weighted velocity distribution, *I(v)*, is given by:

$$I(v) = \left(\frac{2}{\alpha^4} \right) v^3 \exp\left(-\frac{v^2}{\alpha^2} \right) \tag{1-4}$$

where $\alpha^2 = 2k_BT_n/m$, k_B is the Boltzmann constant, and m is the molecular weight. From this expression the average translational energy, $\langle E_i \rangle$, can be calculated by the integration of the individual molecular kinetic energies over the flux–weighted velocity distribution. This results in $\langle E_i \rangle = 2k_BT_n$, which demonstrates the low energy nature of effusive beams. For example, for a nozzle temperature of 500 °C, $\langle E_i \rangle$ is 0.133 eV.

The flux, F_i, distribution of the effusive beam can be expressed using Boltzmann statistics, or the cosine angular distribution:

$$F_i = \frac{P_n}{\sqrt{2\pi m k_B T_n}} \frac{\pi d_n^2 / 4}{\pi x^2} \cos\theta \tag{1-5}$$

where P_n and d_n are the source pressure and nozzle diameter respectively and x is the distance between the source and substrate

The major advantages of effusive beams over supersonic beams are the ease of production and characterization. However, with the low and limited range of incident kinetic energies achievable, wide beam energy distributions, difficulties in producing high flux intensities and difficulties in producing a high beam to background intensity,

the use of effusive beams are somewhat limited to large-area dosing of surfaces. Many of these limitations are overcome with the use of supersonic molecular beams.

1.4.1.2 Supersonic molecular beams

Supersonic beams are formed via an adiabatic (isentropic) expansion of a gas from a nozzle at high pressure (stagnation pressure) into a vacuum of low pressure. The difference between the high stagnation pressure at the nozzle and low pressure in the vacuum accelerates these molecules to supersonic speeds. The *Kn* in supersonic beams is <<1 which means many more intermolecular collisions occur compared to collisions with the wall - this results in random thermal molecular motion being converted into directed translational motion. Owing to the continuum nature of the source, supersonic beams produce nearly monoenergetic beams. A schematic view comparing the generation of effusive and supersonic beams is provided in Figure 1-8.

In comparison to the effusive beam, the supersonic beam produced is more focused and intense and has a peaked flux distribution. The energy of the molecules in the supersonic beam can be further enhanced using seeding techniques, where an inert, fast moving light gas such as hydrogen or helium accelerates slow moving heavier gas molecules. The energy of the molecules in a supersonic beam can thus be tuned to a much wider range compared to the effusive beams. The flux-weighted velocity distribution, $I(v)$, of a supersonic molecular beam is given by:

a) Effusive beam

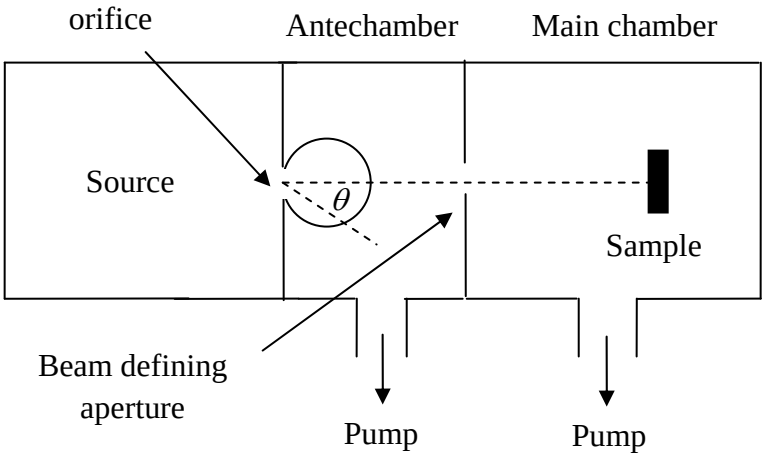

b) Supersonic beam

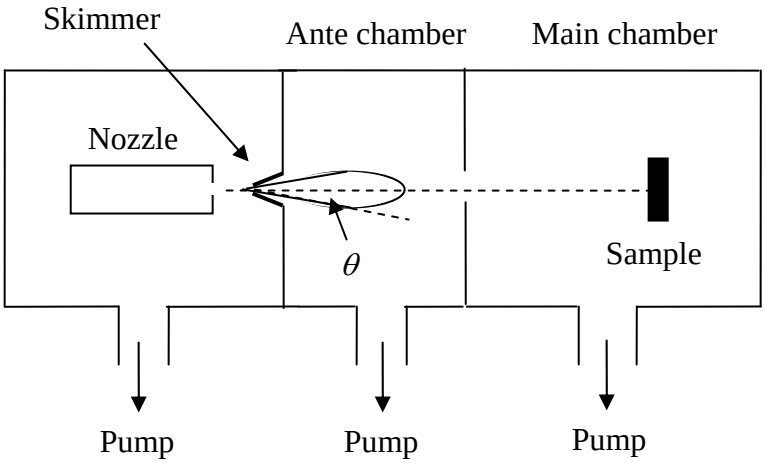

Figure 1–8 Schematic representation of: a) effusive and b) supersonic molecular beam systems. The closed curves downstream of the orifice and the skimmer represent the relative intensity distribution (reproduced from **[41]**).

$$I(v) = N(c,\alpha)v^3 \exp\left(-\frac{(v-c)^2}{\alpha^2}\right) \tag{1-6}$$

where $N(c,\alpha)$ is a normalization constant, and c is the most probable velocity, defined as:

$$c = \left[\frac{2\gamma k_B T_n}{(\gamma - 1)m}\right]^{0.5} \tag{1-7}$$

where $\gamma = C_p/C_v$ is the ratio of heat capacities, T_n is the nozzle temperature and α^2 is a measure of spread in the velocities of the gas parallel to the flow direction defined as $2k_BT_{ax}/m$, where T_{ax} is the axial translational temperature, and m is the mass of the reactant gas. Equation 1-6 reduces to an effusive beam Maxwell distribution when c = 0 and $\alpha^2 = 2k_BT_n/m$. The resultant beam has a centerline flux 2-3 times higher than the effusive beam and the angular distribution is peaked with a $\cos^4\theta$ distribution for a pure gas under ideal conditions.

Molecules start with thermal velocities in the high pressure region upstream of the nozzle called the stagnation state (pressure P_0, temperature T_0). The pressure difference imposed by vacuum downstream of the nozzle (background pressure P_b) accelerates these molecules to sonic speeds, given by $s = (\gamma k_B T_n/m)^{0.5}$ provided P_0 / P_b exceeds a critical value:

$$\frac{P_0}{P_b} \geq \left[\frac{(\gamma+1)}{2}\right]^{\gamma/(\gamma-1)} \tag{1–8}$$

which is less than 2.1 for all gases. A figure of merit for the expansion is the Mach number *M*, defined as the ratio of the gas velocity to the speed of sound. Therefore, in order for the expansion to be supersonic, the pressure ratio must be higher than the critical value to make M > 1. If the pressure ratio is less than the critical value, molecules will exit the nozzle subsonically with exit pressure P_b and without further expansion. In that case the terminal velocity, v_∞, may be derived to be:

$$v_\infty = \sqrt{\frac{2k_B}{m}\left(\frac{\gamma}{\gamma-1}\right)T_n} \tag{1-9}$$

In a seeded supersonic beam, all molecules in the mixture are accelerated to the same velocity rather than energy. This is the basis for the ability to enhance the kinetic energy of a heavy molecule in a dilute mixture with light molecules. In such a mixture, assuming ideal molar heat capacities, the maximum possible translational energy of a reactant is given by:

$$< E_i >= \frac{m_i}{< m >} < C_p > T_n \tag{1-10}$$

where m_i is the mass of the reactant gas, $<m>$ is the mole fraction mean mass of the gas mixture, $<C_p>$ is the mole fraction mean heat capacity of the mixture, and T_n is the nozzle temperature. In most cases, the expansion is not ideal and both velocity and temperature of the precursor molecule deviate from ideal values. The non-ideality from these cases is termed velocity and temperature slip respectively. For both cases, it results in a lower than expected energy from Equation 1-10. Thus Equation 1-10 should only be used as an upper limit for the average beam energy.

As illustrated in Figure 1-8, in practice, the extraction of a supersonic beam requires a skimmer placed a short distance downstream of the nozzle. An illustration of the expansion region right after the nozzle is given in Figure 1-9. The molecules traveling beyond the expansion in a supersonic beam are traveling in excess of the speed of sound. The molecules are not able to adjust to the boundary conditions downstream of the expansion since information in fluids travels at the speed of sound. As a result, very thin nonisentropic regions of large density, pressure, temperature and velocity gradients develop called shock waves. These shock waves are to be avoided in a supersonic beam and in practice, the skimmer is typically used to “extract” the supersonic expansion in the so-called zone of silence.

The skimmer is conical or trumpet–like in shape with a small aperture at the apex used to extract molecules from the zone of silence. Its shape minimizes the backscattering of molecules into the free jet stream out of the nozzle. The advantage of extracting the beam within the isentropic zone of silence is the smaller scale of the apparatus. Disadvantages include problems with skimmer interference, requirement of

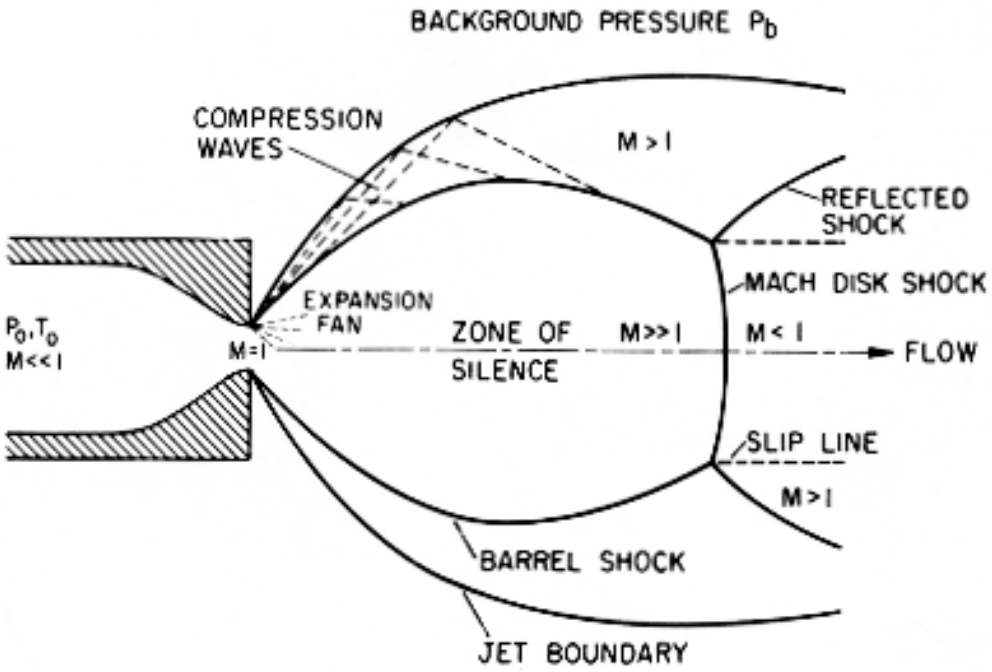

Figure 1-9 Illustration of the structures formed during a supersonic expansion. The figure shows what is commonly known as a "Free Jet" expansion which is produced without any downstream structures affecting the boundary conditions of the expansion (reproduced from **[39]**).

an additional stage to pump on the beam and potential spreading of the beam downstream of the skimmer. After extraction from the skimmer, the molecules in the beam travel into a separate chamber, usually called the ante-chamber, where further pumping minimizes the beam to background ratio. In addition, further modulation of the beam can be carried out in the ante-chamber using either a fast rotating blade chopper or a slow linear beam flag. Finally the beam passes into the main chamber through an aperture which defines the size of the beam spot on the substrate.

Besides the velocity and temperature slip problems mentioned previously, other factors such as mass focusing in a seeded beam can affect the flux distribution of the supersonic beam. Even for expansions of pure gases, a theoretical estimate of the flux is complicated by the number of variables that can affect the expansion: T_n, P_n, d_n, experimental configuration and pumping conditions in each separate chamber. Although empirical models have been developed to estimate the effects of velocity and temperature slip **[39]** and mass focusing **[39]**, it is difficult to extend these models to more complex molecules studied in this thesis. Currently, the only exact method of measuring the energy of molecules in a supersonic molecular beam is to use time of flight techniques, and this is discussed in section 2.1.2.

1.4.2 Supersonic molecular beam scattering

This section on supersonic molecular beam scattering has been adapted from references **[40, 42]**. Supersonic molecular beams have been used extensively to study the dynamics of adsorption between a gaseous molecule and the surface. The

interaction of a gaseous molecule with the surface can be broadly classified into two categories: non–reactive or reactive scattering. This classification is dependent on whether or not a reaction takes place on the surface. The outcome of the interaction between the gas molecule and substrate is dependent on the incident kinetic energy and state of the molecule and the chemical nature and temperature of the substrate. The nature of the substrate determines the intermolecular potential energy between the incident molecule and the surface. This section will briefly discuss the different types of non-reactive scattering events that occur during molecular beam impingement on a surface: 1) elastic scattering; 2) inelastic scattering; and 3) trapping and desorption.

1.4.2.1 Elastic scattering

During an elastic scattering event, the incident molecules reflect from the surface with an extremely narrow angular distribution peaked at the specular angle (incident angle = reflected angle), with no energy transfer taking place. This mechanism is characteristic of beams with light atoms such as hydrogen and helium. The simple physical nature of the process permits direct correlation of the angular distribution of the scattered beam to the surface topology. Since this is a single collision process in most situations, surface residence times are typically less than 10^{-12} sec **[43]**.

1.4.2.2 Inelastic scattering

In inelastic scattering, molecules lose translational energy after single (direct inelastic scattering) or multiple (indirect inelastic scattering) collisions with the surface of the substrate. Incident translational energy is either converted to internal energy or dissipated by the generation of surface phonons. Scattered molecules still retain memory of their incident trajectories. As a result, they have a wider energy and angular distribution compared to elastic scattering. Surface residence times are determined by the number of collisions undergone by incident molecules with the surface. As opposed to elastic scattering, this mechanism is typical for cases where the incident molecule has a similar mass compared to the surface atoms.

1.4.2.3 Adsorption (trapping) and desorption

The presence of an attractive interaction between a molecule and the solid surface can lead to the trapping or adsorption of a molecule incident from gas phase. The attractive interaction may be due to the Van der Waals interaction and in this case, we are dealing with physical adsorption or 'physiosorption'. It is important to note that adsorption is the first step in thin film growth. On a side note, if the incident molecule forms a chemical bond with the surface, then the interaction with the surface is a lot stronger and the molecule has 'chemisorbed' to the surface. It is also important to note that regarding thin film deposition of the organic semiconductors studied in this thesis, the molecules are 'physiosorbed' on the surface and there is no chemical bond to the surface.

When an incident hyperthermal molecule falls into the potential energy well, the kinetic energy in the direction normal to the surface increases. If this energy is not transferred to some other degree of freedom, the molecule will simply bounce off and there will be no adsorption. In the case of adsorption (physiosorption), the energy transfer from the incident molecule to the surface normally occurs via surface phonons. In the classical approach, a molecule with incident energy E_i will have an energy of $E_i + H_d$ inside the attractive well, where H_d is the well depth. Upon collision with the surface, the molecule will lose some fraction f, of this total energy. If the remaining energy: $(1 - f)(E_i + H_d)$ is less than H_d, then the molecule will trap (adsorb) on the surface or else it will scatter off. Using this classical argument, one would then expect that the adsorption probability of a molecule to decrease as the incident energy of the molecule increases, a process called trapping-mediated adsorption.

The molecules that are unable to adsorb on the surface will undergo desorption. Since the molecules equilibrate with the surface, the desorbing molecules will exhibit Maxwell–Boltzmann velocity distributions characterized by the temperature of the substrate. In addition, their angular distribution is symmetric and peaked about the surface normal and usually displays a sine or near cosine distribution.

1.5 References

1. Bao, Z.; Locklin, J., Eds, *Organic Field Effect Transistors*, Taylor and Francis Group, LLC, **2007.**
2. Ling, M. M.; Bao, Z. N. *Chem. Mater.* **2004**, *16*, 4824-4840.
3. Yoon, M.-H.; Kim, C.; Facchetti, A.; Marks, T. J. *J. Amer. Chem. Soc.* **2006**, *128*, 12851-12869.
4. Ruiz, R.; Papadimitratos, A.; Mayer, A. C.; Malliaras, G. G. *Adv. Mater***. 2005**, *17*, 1795-1798.
5. Dinelli, F.; Murgia, M.; Levy, P.; Cavallini, M.; Biscarini, F.; de Leeuw Dago M. *Phys. Rev. Lett.* **2004**, *92*, 116802-116804.
6. Muck, T.; Wagner, V.; Bass, U.; Leufgen, M.; Geurts, J.; Molenkamp, L. W. *Synthetic Metals* **2004**, *146*, 317-320.
7. Dodabalapur, A.; Torsi, L.; Katz, H. E. *Science* **1995**, *268*, 270-271.
8. Kelley, T. W.; Boardman, L. D.; Dunbar, T. D.; Muyres, D. V.; Pellerite, M. J.; Smith, T. P. *J. Phys. Chem. B* **2003**, *107*, 5877-5881.
9. Yang, H.; Shin, T. J.; Ling, M. M.; Cho, K.; Ryu, C. Y.; Bao, Z. *J. Am. Chem. Soc.* **2005**, *127*, 11542-11543.
10. Virkar, A.; Mannsfield, S.; Oh, J. H.; Toney, M. F.; Tan, Y. H.; Liu, G.; Scott, J. C.; Miller, R.; Bao, Z. *Adv. Funct. Mater.* **2009**, *19*, 1962-1970.
11. Shtein, M.; Mapel, J.; Benziger, J. B.; Forrest, S. R. *Appl. Phys. Lett.* **2002**, *81*, 268-270.
12. Klauk, H.; Halik, M.; Zschieschang, U.; Schmid, G.; Radlik, W.; Weber, W. *J. Appl. Phys.* **2002**, *92*, 5259-5263.

13. Jang, J.; Nam, S.; Chung, D. S.; Kim, S. H.; Yun, W. M.; Park, C. E. *Adv. Func. Mat.* **2010**, *20*, 2611-2618.

14. Amassian et al. *in preparation*

15. Heinrich, M. A.; Pflaum, J.; Tripathi, A. K.; Frey, W.; Steigerwald, M. L.; Siegrist, T. *J. Phys. Chem. C* **2007**, *111*, 18878.

16. Dürr, A. C.; Koch, N.; Kelsch, M.; Rühm, A.; Ghijsen, J.; Johnson, R. L.; Pireaux, J. -J.; Schwartz, J.; Schreiber, F.; Dosch, H.; Kahn, A. *Phys. Rev. B* **2003**, *68*, 115428/1-115428/12.

17. Mattheus, C. C.; Dros, A. B.; Baas, J.; Oostergetel, G. T.; Meetsma, A.; de Boer, J. L.; Palstra, T. M. *Synth. Met.* **2003**, *138*, 475.

18. Ruiz, R.; Mayer, A. C.; Malliaras, G.G.; Nickel, B.; Scholes, G; Kazimirov, A.; Kim, H.; Headrick, R. L.; Islam, Z. *Appl. Phys. Lett.* **2004**, *85*, 4926-4928

19. Sakamoto, Y.; Suzuki, T.; Kobayashi, M.; Gao, Y.; Fukai, Y.; Inoue, Y.; Sato, F.; Tokito, S. *J. Amer. Chem. Soc.* **2004**, *126*, 8138-8140.

20. Salzmann, I.; Duhm, S.; Heimel, G.; Rabe, J. P.; Koch, N.; Oehzelt, M.; Sakamoto, Y.; Suzuki T. *Langmuir* **2008**, *24*, 7294-7298.

21. Tatemichi, S.; Ichikawa, M.; Koyama, T.; Taniguchi, Y. *Appl. Phys. Lett.* **2006**, *89*, 112108/1-112108/3.

22. Dürr, A. C.; Nickel, B.; Sharma, V.; Taffner, U.; Dosch, H. *Thin Solid Films* **2006**, *503*, 127-132.

23. Kowarik, S.; Gerlach, A.; Sellner, S.; Schreiber, F.; Cavalcanti, L.; Konovalov, O. *Phys. Rev. Lett.* **2006**, *96*, 125504/1-125504/4.

24. Kowarik, S.; Gerlach, A.; Sellner, S.; Cavalcanti, L.; Konovalov, O.; Schreiber, F. *Appl. Phys. A: Mater. Sci. Proces.* **2009**, *95*, 233-239.

25. Kelly, T. W.; Boardman, L.D.; Dunbar, T. D.; Muyres, D. V.; Pellerite, M. J.; Smith, T. P. *J. Phys. Chem. B* **2003**, *107*, 5877-5881.

26. Sakamoto, Y.; Suzuki, T.; Kobayashi, M.; Gao, Y.; Inoue, Y.; Tokito, S. *Mol. Cryst. Liq. Cryst.* **2006**, *444*, 225.

27. Krauss, T. N.; Barrena, E.; Zhang, X. N.; de Oteyza, D. G.; Major, J.; Dehm, V.; Wurthner, F.; Cavalcanti, L. P.; Dosch, H. *Langmuir* **2008**, *24*, 12742-12744.

28. F. Schreiber, *Prog. Surf. Sci.* **65**, 151 (2000).

29. Zhang, Z.; Lagally, M. G. *Science* **1997**, *276*, 377-383.

30. Venables, J. A.; Spiller, G. D. T.; Hanbücken, M. *Rep. Prog. Phys.* **1984**, *47*, 399-459.

31. Brune, H. *Surf. Sci. Rep.* **1998**, *31*, 121-229.

32. Ohring, M. *The Materials Science of Thin Films* (Academic Press, London, UK, **1992**).

33. Ehrlich, G.; Hudda, F. G. *J. Chem. Phys.* **1966**, *44*, 1039-1049.

34. Schwoebel, R. L.; Shipsey, E. J. *J. Appl. Phys.* **1966**, *37*, 3682-3686.

35. Fendrich, M.; Krug *J. Phys. Rev. B* **2007**, *76*, 121302/1-121302/3.

36. Hlawacek, G.; Puschnig P.; Frank, P.; Winkler, A.; Ambrosch-Draxl, C.; Teichert, C. *Science* **2008**, *321*, 108-111.

37. Goose, J. E.; First, E. L.; Clancy, P. *Phys. Rev. B* **2010**, *81*, 205310/1-205310/20.

38. Venables, J. A. *Phys. Rev. B* **1987**, *36*, 4153-4162.

39. Scoles, G. *Atomic and Molecular Beam Methods* (Oxford University Press, Oxford, UK, **1998**).

40. Arumainayagam, C. R.; Madix, R. J. *Prog. Surf. Sci.* **1991**, *38*, 1-102.

41. Anderson, J. B. *Molecular Beams and Low Density Gas Dynamics*, edited by P. P. Wegener (Marcel Dekker, New York, USA, **1974**).

42. Barker, J. A.; Auerbach, D. J. *Surf. Sci. Rep.* **1984**, *4*, 1-100.

43. Rettner, C. T.; Ashfold, R. *Dynamics of Gas-Surface Interactions* (The Royal Society of Chemistry, Cambridge, UK, **1991**).

2. Experiment Procedures

In this section, we first describe the G-line ultra-high vacuum (UHV) system which was used to study the *in situ* real-time growth of organic thin films using synchrotron x-ray scattering. A description of the supersonic molecular beam delivery source will also be given. Second, the general thin film deposition procedure employed in this thesis will be described. Third, a description of time-of-flight (TOF) mass spectrometry will be given – this technique was used to measure the incident energy of the supersonic molecular beam. Fourth, we describe the effusive beam source. An effusive beam source was installed in the G-line system so as to allow one the capability of studying the growth of two organic semiconductors at the same time. Fourth, the general procedures for sample preparation will be discussed including the materials used, thermal oxide (SiO_2) formation procedure, substrate cleaning procedures, SAM synthesis procedures and polymer spin-coating procedures. Finally, the techniques that were used to characterize organic thin films will be discussed including atomic force microscopy (AFM), contact angle goniometery and x-ray scattering.

2.1 Description of G-Line UHV deposition chamber

Experiments were performed in a custom-designed multiple-stage, stainless steel ultra high vacuum (UHV) chamber that is illustrated schematically in Figures 2-1 and 2-2. The deposition chamber (volume ≈ 18 L) is pumped by a 500 L-s^{-1} compound turbomolecular pump (Pfeiffer TMU 521P) and routinely achieves base pressures of ~ 9 × 10^{-10} Torr after a ~24-48 hour bakeout at 140 °C. Note that the bakeout is carried out using heating tapes which are wrapped mainly around the main chamber and covered with aluminum foil. A bakeout oven does exist for this system and can be used with some modification – in its current form, it does not fit around the chamber at G-3 hutch (at CHESS) due to the geometry of the diffractometer table, upstream and downstream x-ray flight path and slits. A sample manipulator accommodates samples up to approximately 1 in. × 1 in. in dimension positioned vertically (from the bottom of the chamber) such that the surface of the sample is precisely at the focal point of the chamber. Typical substrate sizes that are used for depositing organic thin films are ~ 1 cm × 2 cm. Opposed to the sample are two rectangular Be windows. The first is positioned horizontally to allow synchrotron x-rays to enter the chamber from varying angles with respect to the sample surface normal. After scattering from the sample, the x-rays pass through a vertically positioned Be window before traversing a series of slits and finally being detected by a silicon avalanche photodiode detector (APD, Oxford Danfysik, Oxford, UK). The chamber is mounted on a diffractometer table allowing for the precise manipulation

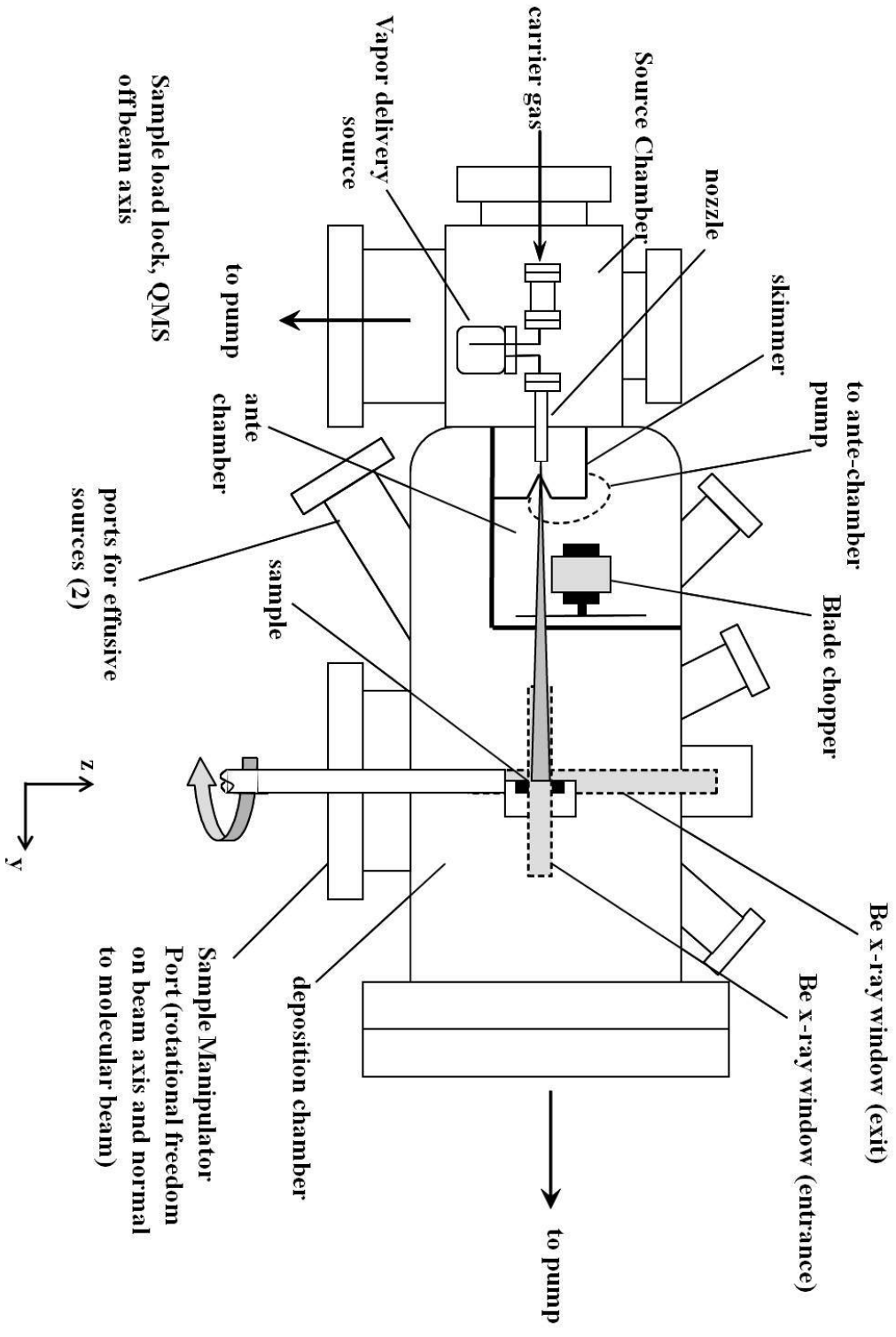

Figure 2-1 Side view schematic drawing of the G-Line deposition chamber.

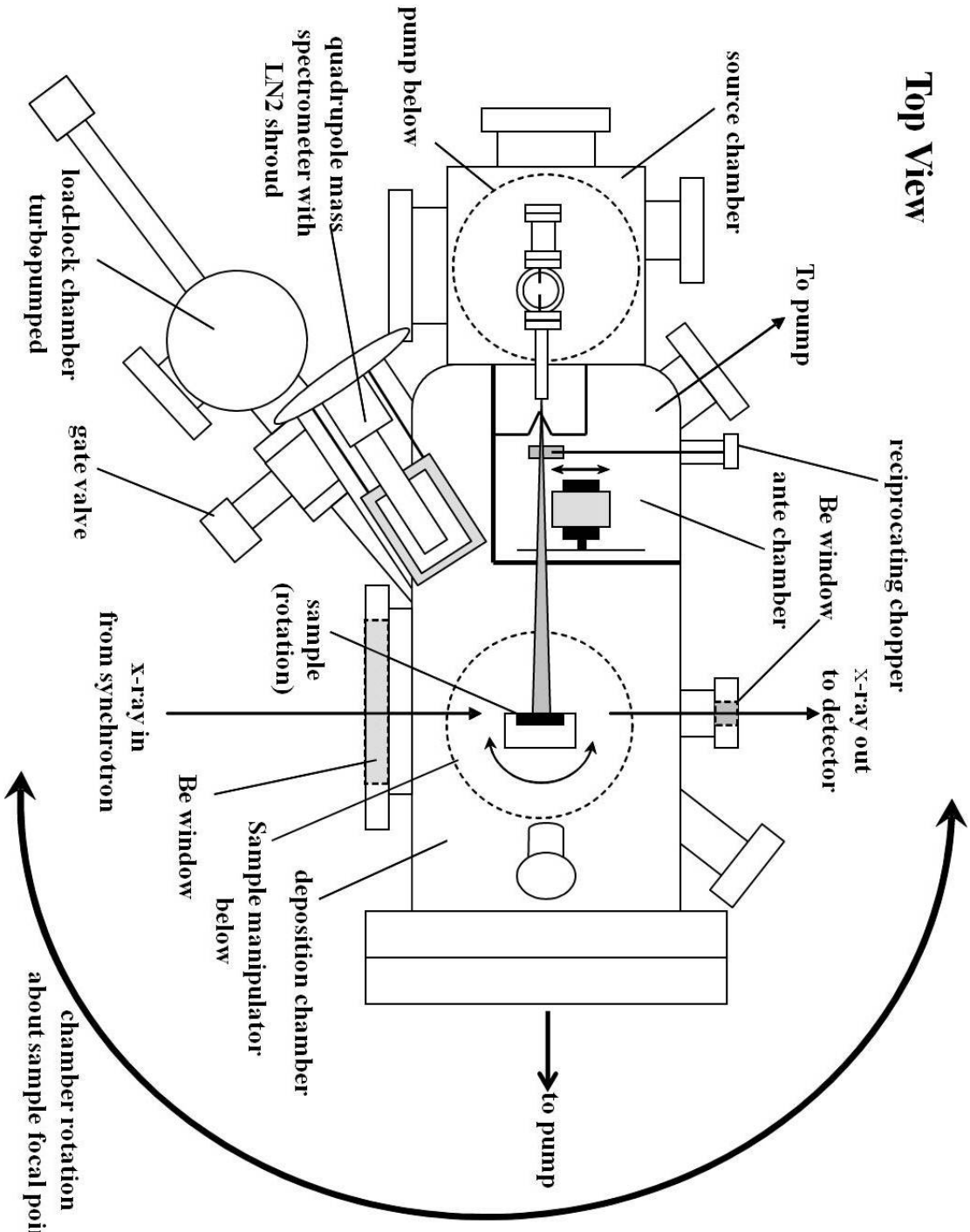

Figure 2-2 Top view schematic drawing of the G-Line deposition chamber.

(Y, Z, and rotation) of the UHV chamber with respect to the entering synchrotron x-rays. Further rotational manipulation of the sample in the plane defined by the entering x-rays as well as about the surface normal allows for a number of x-ray scans and real-time experiments to be performed (e.g. specular reflectivity and grazing incidence diffraction, GID). Monitoring the intensity of scattered x-rays during thin film growth at the so-called anti-Bragg position allows for the determination of the nature of thin film morpholgy. Following the deposition of organic thin films, specular reflectivity and GID allows for determination of the crystal lattice parameters perpendicular and parallel to the substrate respectively.

A quadrupole mass spectrometer (QMS, model: Extrel 5221) may be mounted within the deposition chamber in a number of positions. During experiments where the molecular beam is scattered from the sample surface and a direct measurements is desired, the QMS is mounted facing the sample at an angle of 55° from the supersonic molecular beam axis which is described below. During the characterization of molecular beams using time of flight (TOF) methods the QMS is mounted on a linear translator in a direct beam position such that the molecular beam is in-line with the axis of the QMS. The QMS may also be mounted on a third flange which allows the ionizer to be placed in a cross-molecular beam position (manipulator removed) or in a non line of site position to allow for indirect scattering experiments such as sticking measurement.

A liquid nitrogen shroud can be used to surround the ionizing region of the QMS. This shroud has been designed to accept several of our instruments including

the Extrel 5221, Extrel C 50, a Hiden 3F Epic and a VG SX 200. The surface of the shroud within the deposition chamber is cooled to LN2 temperatures and therefore aids in reducing the background component of condensable species, especially the background water within the chamber. The shroud is also capable of accepting a stainless steel tube or "skirt" which connects the shroud to its base flange thereby allowing non-condensable gases to be differentially pumped via a 2 ¾" CF flange teed off of the main housing.

The sample manipulator (custom, Thermionics NW Inc.) is capable of 2 rotational degrees of freedom (one horizontal and one vertical referred to as 'theta' and 'zeta' respectively) as outlined above and employs an ion pumped (2 $L\text{-}s^{-1}$) differentially sealed rotation platform. The sample dock is fitted with a radiant graphite heater which is encapsulated in pyrolytic BN and is capable of continuously heating Si samples to temperatures of ~ 400 °C. Samples are mounted on Mo platens and are transferred to and from a load-lock chamber using an STLC (Thermionics) transfer system. The load-lock chamber is pumped by a 60 $L\text{-}s^{-1}$ turbomolecular-drag pump (Pfeiffer TMU 071 P) and achieves pressures below 5×10^{-8} Torr after several hours of pumping. Typically, the load-lock chamber is pumped to ~ 10^{-7} Torr before sample transfer into the main chamber. See Appendix (section 9-1) regarding calibration data for control of temperature of the sample surface and reference heater.

Owing to the very low vapor pressure of most organic species, an *in vacuo* container (the 'bubbler', see Figure 2-3) has been designed and employed to generate

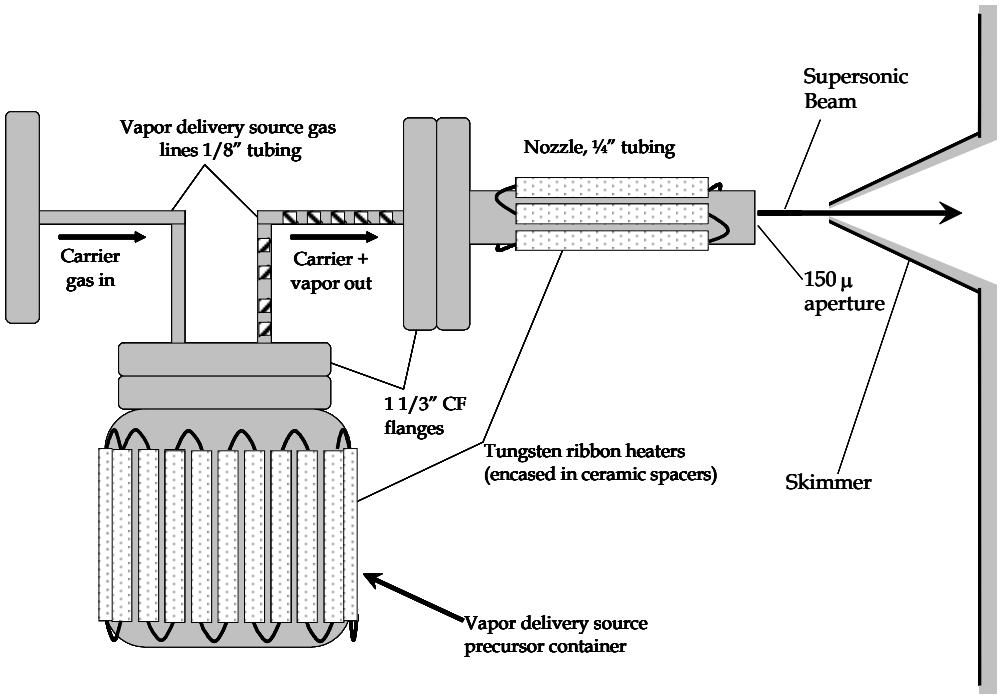

Figure 2-3 Schematic representation of supersonic beam source for low vapor pressure materials.

supersonic molecular beams in the source chamber. This bubbler is directly connected to the gas delivery line and a heatable nozzle using 1/8" tubing and 1–1/3" CF flanges. Carrier gas of helium (He) is used to produce the supersonic expansions of the organic molecules studied in this thesis. Helium is fed in to the system using general service mass flow controllers (MKS) and stagnation pressures are measured using capacitance manometers upstream of the chamber. Stagnation pressures are generally between 28 and 350 Torr depending on the He flow rate and nozzle temperature. The nozzle consists of a 150 μm aperture in a 125 μm stainless steel plate that is welded to the end of an electropolished 1/4" stainless steel tube. Both the nozzle and the bubbler can be heated using tungsten ribbon heaters, which are encased in 1/8" (ID) ceramic tubing and affixed using tantalum wire. Helium is fed into to the bubbler and is mixed with vapors of the organic species using a baffle within the bubbler, before the He–organic vapor mixture exits through a 1/8" tube and enter the nozzle. Coating of this 1/8" tubing with the organic molecule resulted in non–uniform intensities of supersonic molecular beams. To fix this problem, tungsten ribbon encased in flexible ceramic sleeves has been used to heat this section of 1/8" tubing between the stainless steel nozzle and the bubbler. The entire nozzle/bubbler assembly is mounted on a precision x–y–z manipulator and the temperatures of the nozzle (T_N), bubbler (T_B) and 1/8" tube section (T_T) can be monitored independently using chromel–alumel type (K–type) thermocouples spot welded to their surfaces. The gas mixtures are expanded into a source chamber which is pumped using a 520 $L–s^{-1}$ corrosion resistant turbomolecular pump (Pfeiffer TMU 520C). The expanded gas passes through a trumpet–shaped Ni skimmer (1.5 mm in diameter) mounted on a stainless steel plate and into the

antechamber. The vapor delivery source, nozzle and skimmer assembly are shown schematically in Figure 2-3. The skimmer can be mounted in two positions along the beamline, placing the nozzle at approximately 14 and 21 cm from the sample surface when in the so called "forward" and "rear" positions respectively. This flexibility in design provides control over reactant flux to the sample surface or quadrupole mass spectrometer (QMS) as dictated by the requirements of a specific experiment. All experiments in this thesis were carried out with the skimmer in the 'rear' position. Refer to reference **[1]** regarding optimization of supersonic molecular beams when changing the following variables: diameter of nozzle, nozzle skimmer distance, diameter of the aperture at the apex of the skimmer, location of skimmer and geometry of skimmer.

The expanded gas mixture passes through a Ni skimmer into an ante-chamber where the beam is differentially pumped before passing through a final beam defining aperture (see Figure 2-4) and entering the deposition chamber. The aperture is mounted on ¼ plate which separates the ante-chamber from the main chamber. The ante chamber is pumped by a 70 L-s^{-1} turbomolecular pump (Pfeiffer TMU 071 P) and condensable materials can be further pumped by a liquid nitrogen reservoir within the ante-chamber. A reciprocating beam flag is used, for instance, in defining molecular beam exposures to a sample in order to begin and end thin film depositions precisely. A rotating blade chopper is employed to produce fast molecular beam waveforms (timescales < 1 ms), which are used for example, in coordination with a quadrupole mass spectrometer (QMS) and a multi-channel scalar data acquisition card (ORTEC MCS-pci) during the characterization of molecular beams by time of flight (TOF)

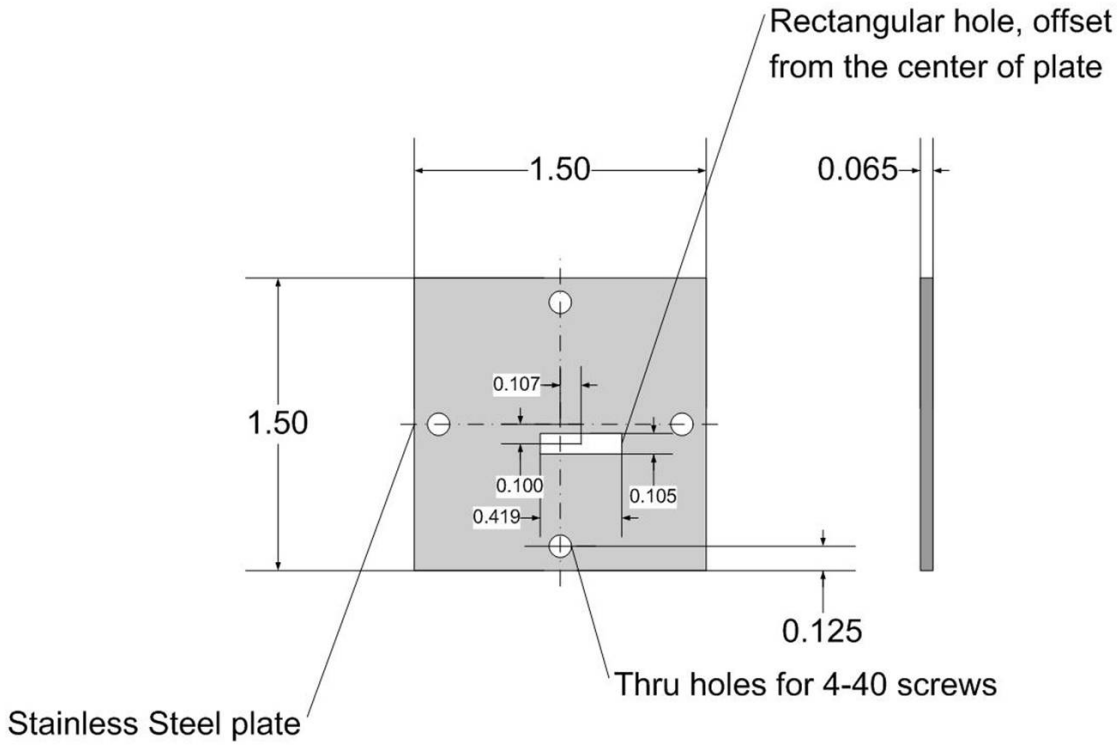

Figure 2-4 Aperture plate used for organic thin film deposition from supersonic source. Note that the aperture plate is mounted on ¼ plate covering the ante-chamber.

measurements or in modulated molecular beam reactive scattering experiments (MMBRS). Data acquisitions using the MCS card are triggered by a photo-interrupter mounted on the blade chopper. The blade chopper is mounted on a linear translation stage such that it can be translated out of the beam flight path in order to allow for both slow and fast experiments to be performed without altering the apparatus. The total distance from the nozzle to the substrate is approximately 20.5 cm with a distance traveled within the ante chamber of 8.9 cm. The blade of the fast chopper is 9.3 cm from the sample surface.

Refer to reference **[2]** for additional details regarding the G-Line deposition chamber, especially for detailed system drawings.

2.1.1 Organic thin film deposition procedure

This section will discuss the procedures for depositing organic thin films using supersonic molecular beams and procedures for characterizing the films using *in situ* real-time x-ray scattering. Pentacene (product # P1802) and PTCDI-C_{13} (product # 383783) were purchased for Sigma-Aldrich. DIP was purchased from Instiut für PAH-Forschung (Contact: Dr. W. Schmidt, pah-schmidt@web.de) and PFP was obtained from our collaborator in Germany (Dr. Frank Schreiber).

Important supersonic molecular beam experimental conditions such as T_N (nozzle temperature), T_B (bubbler temperature), He flow rate (and therefore typical

Table 2-1 Experimental conditions of supersonic beam during thin film deposition

Organic semiconductor	**T_N, °C (±3) [a]**	**T_B, °C**	**[He flow rate, sccm / P_N, Torr (±2)[a]]**
DIP	490	320	[10/47.3], [25/92.2], [70/213.5], [120/339.5]
PFP	450	235	[10/46.3], [25/90.0], [70/208.8], [100/284]
PTCDI-C_{13}	430	343	[10/47], [25/92], [70/208], [90/255]
Pentacene	470	250	[10/48], [25/92], [70/210]

[a] This is an approximate variation from experiment to experiment and not in the measurement.

nozzle pressure, P_N, values) are summarized in Table 2-1. The 1/8" tube (T_T) between the evaporator and nozzle was typically heated to temperatures within halfway of T_N and T_B. The purpose of heating the 1/8" tube section was to avoid condensation of the organic molecule in this section and therefore avoid clogging and fluctuating beam intensities.

Flow of He carrier gas was controlled using an MKS mss flowmeter upstream of the inlet to the in–vacuum bubbler. The nozzle, downstream of the bubbler, consisted of 0.25" diameter stainless steel tubing, and a 125 μm thick end plate with a 150 μm orifice. The bubbler was heated and controlled using a Eurotherm (power supply model 7100A, controller model 2416) whereas the nozzle and the tube were heated using variacs. Supersonic molecular beams were skimmed using a trumpet shaped skimmer in the rear position (1.5 mm aperture), could be shuttered and then passed through a beam defining aperture (see Figure 2-4) producing a well collimated rectangular beam spot on the substrate (typically substrate size was ~ 1 cm × 2 cm – the beam spot covered the entire width of the substrate, i.e. 1 cm, and the height of the beam spot was 4 mm). Multiple experiments (up to 4 beam spots and each adjacent beam spot was separated from the other by ~1 – 1.5 mm) could be carried out on the same substrate, which is made possible by translating the substrate perpendicular to the supersonic molecular beam, and due to the high beam-to-background flux ratio. The background contribution to the deposited films was negligible (evidenced from atomic force microscopy (AFM) images of unexposed regions of the substrate).

The following will discuss in a step-by-step manner the procedure of depositing organic thin films and characterizing them using *in situ* real-time x-ray scattering. This procedure is meant to be an overview. Please refer to logbooks for details.

1. The first step is to a define a narrow x-ray beam – typical values for horizontal (h) and vertical (v) slits are: s1v = s1h = s2v = s2h = 0.5 mm, s3v = open, s3h = 1.0 mm, s4v = 1.0 mm and s4h = 2.00 mm. See Figure 2-5.

2. Create a supersonic molecular beam of the organic semiconductor of interest using the experimental conditions shown in Table 2-1.

3. Maximize the main chamber pressure by iterating the x-y micrometer positions of the nozzle assembly. The z-position of the micrometer is fixed at ~2.3.

4. Cut and clip a piece of x-ray burn paper (similar to size of the substrate: ~ 1 cm × 2 cm) on the sample holder as if loading a new substrate. Put sample holder with the burn paper into load-lock chamber and pump down. Typically place a piece of aluminum foil behind the burn paper so that a stronger grip can be applied on to the surface of the burn paper by the sample holder clips.

5. Using the transfer arm, transfer the sample holder (with the burn paper on) from the load-lock chamber to the sample manipulator in the main chamber, like one would normally transfer a substrate. The burn paper outgases in the region of ~10^{-6} Torr so one should avoid dropping it into the vacuum chamber. If the burn paper is dropped

into the vacuum chamber, then vent, remove the burn paper, pump down and re-bakeout the chamber before continuing with experiments.

6. Deposit a supersonic molecular beam spot on the burn paper – the painted spot should be rectangular in shape as defined by the aperture plate on the ante chamber (see Figure 2-4). Check to see visually if the spot is well defined and rectangular in shape. If the painted sport is not well defined, adjust the nozzle x-y micrometers accordingly.

7. Shine the x-rays onto the burn paper – this will change the color of the burn paper and therefore indicate the position of the x-rays with respect to the supersonic molecular beam spot. The x-rays in principle should be going right through the center of the rectangular supersonic molecular beam spot. If they are not, adjust the z-position of the diffractometer table accordingly (do this by using motors *zne*, *znw* and *zs* - move them all in a relative manner).

8. After successful completion of steps 1 to 7, your supersonic molecular beam is now aligned with the x-rays from the synchrotron and you can now deposit organic thin films and monitor the growth using x-rays. Repeat steps 2-7 if the nozzle assembly is rebuilt such as to replace the organic precursor.

9. Insert a cleaned substrate into the main chamber. Make sure the beam flag is blocking the supersonic beam at this point.

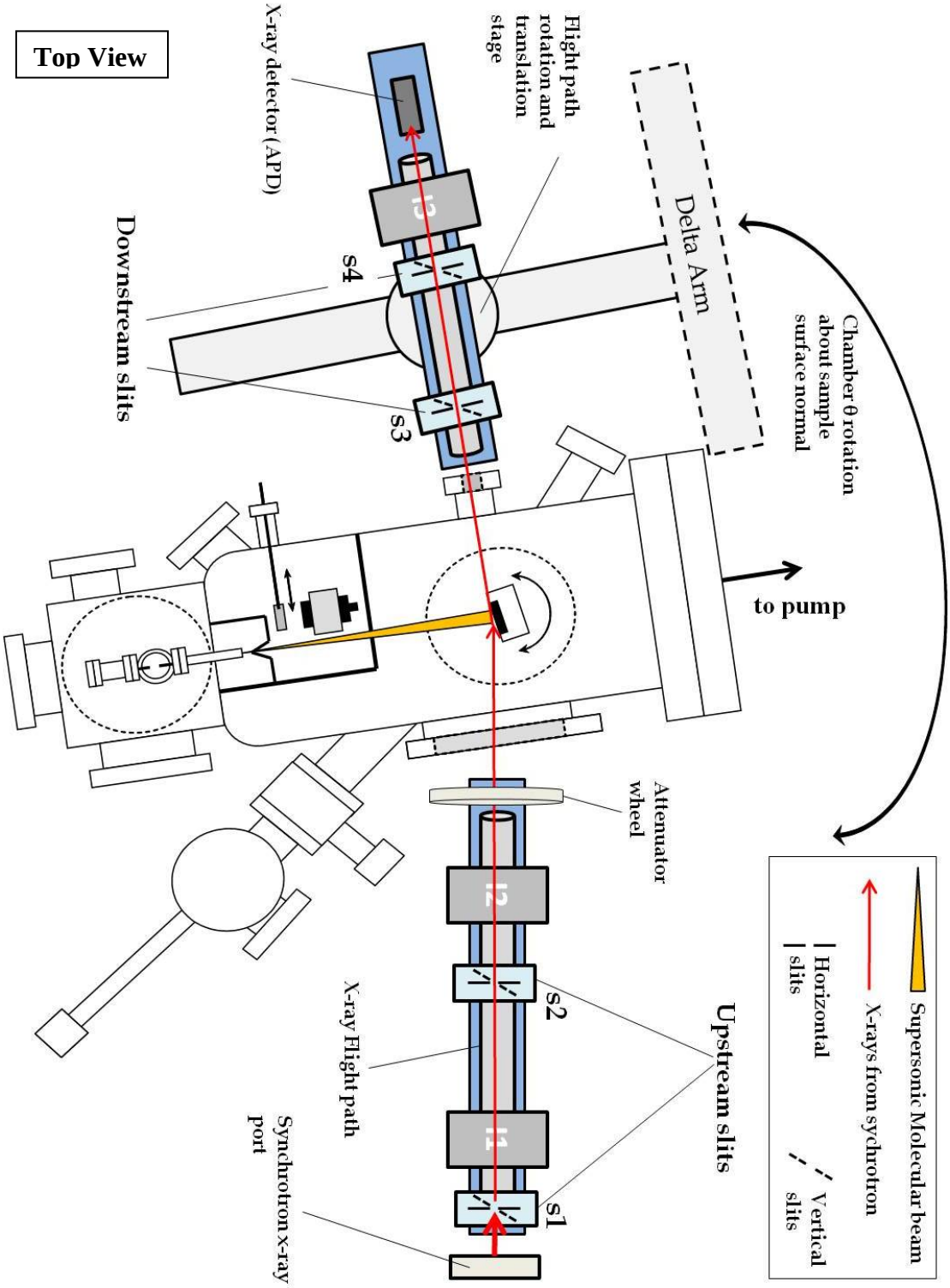

Figure 2-5 Schematic showing upstream and downstream x-ray slits.

10. Carry out preliminary x-ray scans to move the sample in the center of rotation of the x-rays. That is do a *chamy* scan to split the x-ray beam in half followed by a rocking scan (*zeta*) to move the sample in the center of rotation. Iterate these two scans until changes in the *chamy* and *zeta* positions are not observed. Do these scans using the full x-ray beam without any attenuation and with the APD (x-ray detector) blocked with a piece of lead. Use the I3 ion counter as a measure of counts when doing these scans (see Figure 2-5).

11. Once the sample is in the center of rotation with the x-rays, carry out specular reflectivity of the bare substrate. If the sample has an interfacial layer deposited on SiO_2 (i.e. SAM or polymer) one can obtain its thickness, electron density and interface widths from fitting the specular reflectivity data (see Section 2.5.3). If the substrate is bare SiO_2, specular reflectivity can be used to check the presence of any unwanted interfacial layers (i.e. water or adventitious carbon).

11. After specular reflectivity of the bare substrate has been conducted, move the substrate to anti-Bragg position of the organic semiconductor that you are about to deposit (π/d_{001}, where d_{001} is the expected monolayer interplanar spacing). Do finer rocking scans and move the substrate to the peak intensity of the rocking curve (using the *zeta* motor). Do these scans using the APD detector and with attenuating the synchrotron x-ray beam. Choose an attenuation setting so that you are getting no more than 200,000 counts/second at the anti-Bragg position – this is to prevent radiation damage of the organic thin film. Use the attenuator wheel (see Figure 2-5) to attenuate the full x-ray beam. Typical attenuation setting at the anti-Bragg

position is 4 or 5 (corresponds to an approximate attenuation of 10-1000x depending on the x-ray energy). Avoid shining the full x-ray beam to the APD as this will damage the detector.

12. Start the *tseries* scan – typically wait for 10-20 seconds to get a nice flat baseline and then open the beam flag to allow deposition of the organic film – if one has successfully completed steps 1-11, one should see growth oscillations for all organic semiconductors studied in this thesis.

Figure 2-6, shows a picture of the G-Line chamber setup at the G3 hutch (at CHESS) all ready for using x-rays from the synchrotron to monitor organic thin film growth *in situ* and real-time.

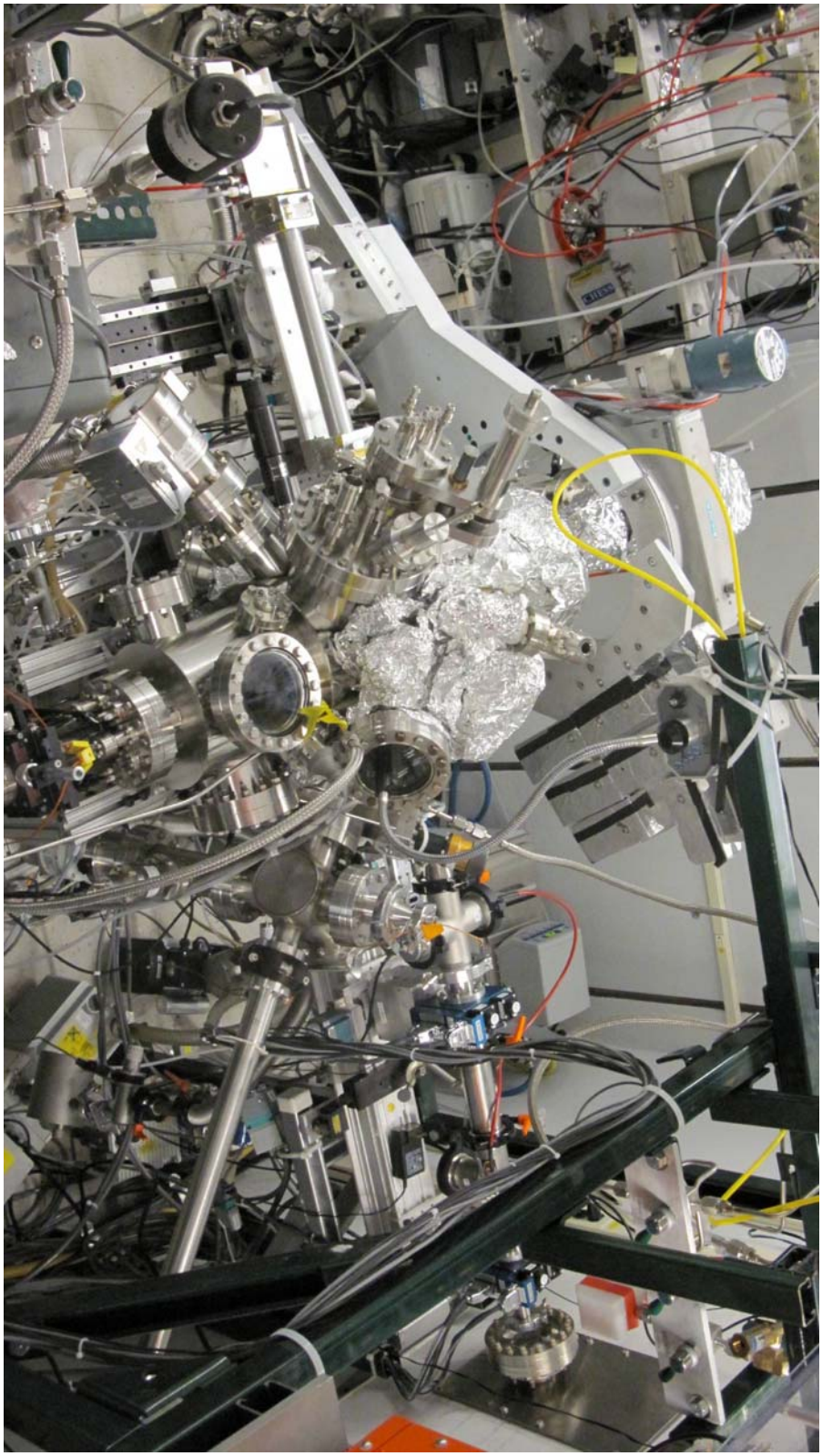

Figure 2-6 Picture showing G-Line chamber setup at the G3-Hutch at CHESS

2.1.2 Time-of-flight mass spectrometry

Time-of-flight (TOF) mass spectrometry was used in order to measure the incident energy of the supersonic molecular beams (pentacene, DIP, PFP and PTCDI-C_{13}). Using TOF technique, the translational energy of the molecules in the supersonic molecular beam can be determined – the basic principle for measuring the translational energy of molecules using the TOF technique is that of measuring the amount of time, *t*, required for said molecules to traverse a give distance *L*.

In order to do this, the quadrupole mass spectrometer (QMS: Extrel 5221) was placed on a linear translation stage and mounted on a 4-way 6 in. cross-flange which was then mounted at the center of the 12 in. vertical flange located on the molecular beam axis of the deposition chamber. As shown schematically in Figure 2-7, this configuration placed the QMS perpendicular with respect to the molecular beam axis. The distance between the rotating blade chopper (mounted within the ante-chamber – refer to reference **[2]** for details on the chopper assembly specifications) and the QMS ionizer can easily be varied in a precise manner using the linear translation stage. The top flange on the 4-way 6 in. cross-flange was blanked off and the main chamber turbomolecular pump (500 L-s^{-1}) was mounted on the bottom flange of the 4-way 6 in. cross-flange. The sample manipulator was rotated such that it was facing the horizontal Be window so that the molecular beam would not be blocked. The QMS settings used were: emission current = 3 mA, electron energy = 70 eV, multiplier voltage = 2400-2500 V.

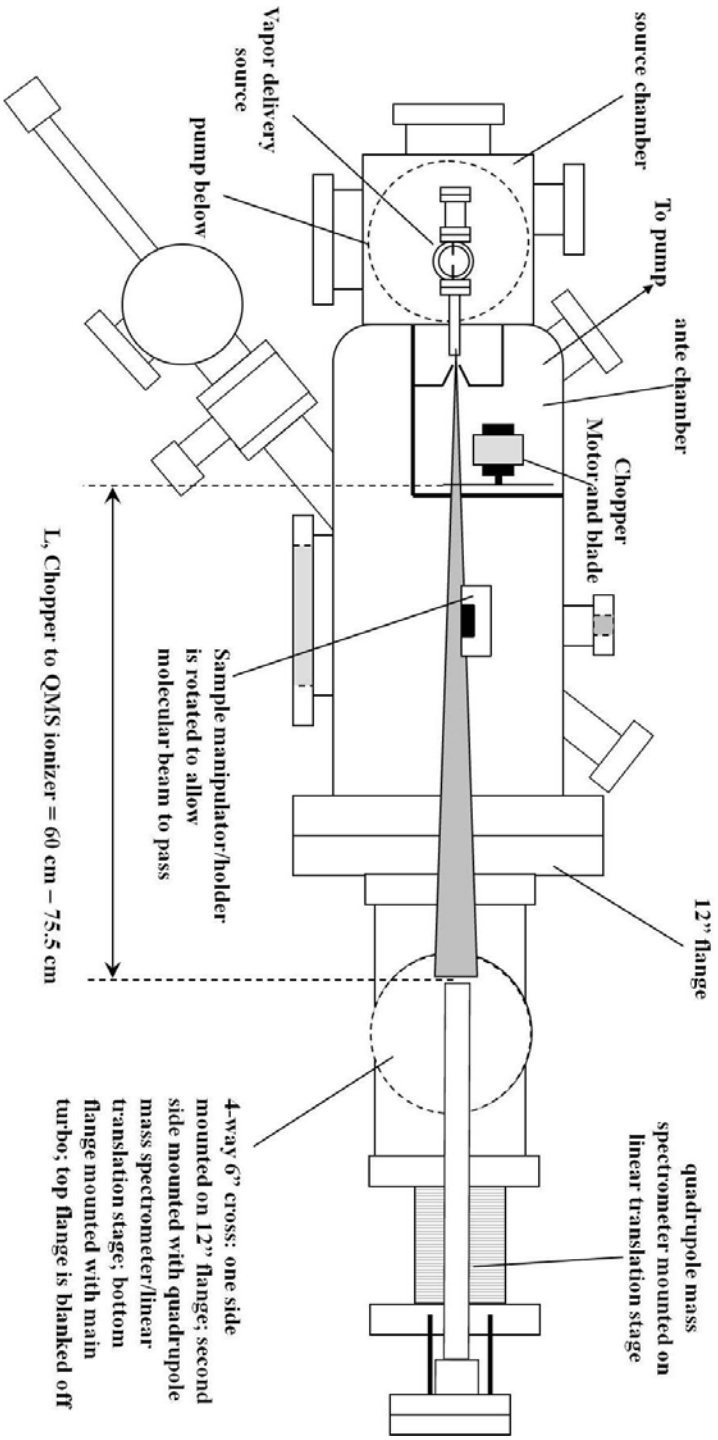

Figure 2-7 Schematic illustrating the G-Line deposition chamber configuration during time-of-flight measurements.

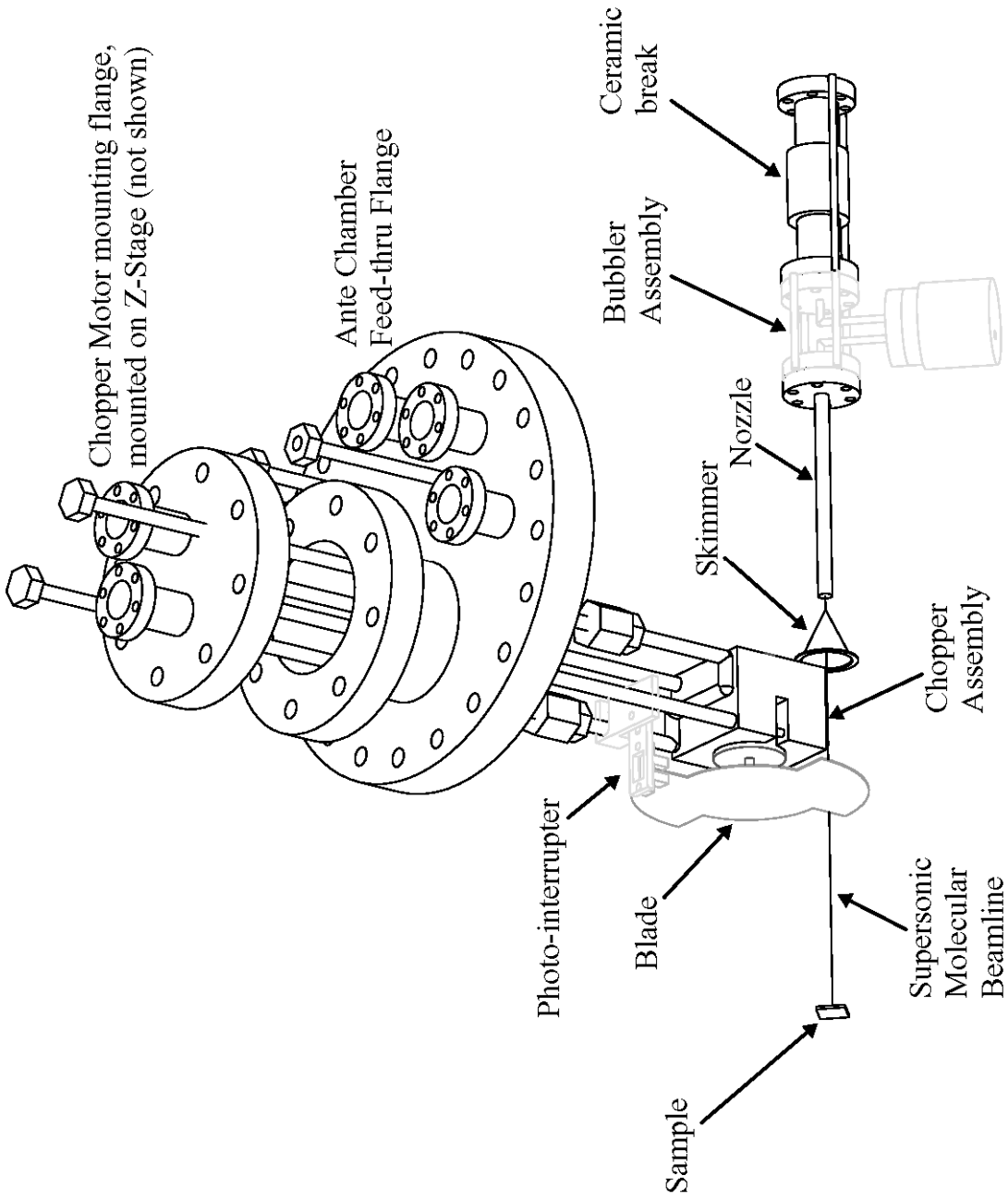

Figure 2-8 3D representation of the supersonic molecular beamline and the chopper-assembly for the G-Line deposition chamber. Internal and external chamber walls are not shown for clarity.

A 3D schematic showing the supersonic molecular beamline, the ante-chamber housing the blade chopper/motor assembly and the source chamber housing the nozzle is shown in Figure 2-8. The chopper motor was purchased from Globe Motors (part # 18A1004-2). The chopper assembly is mounted on a Z-stage so that the motor/blade can be moved in-and-out of the molecular beam. During TOF experiments, the Z-stage micrometer was set to 4.3 cm (do not go < 4.3 cm or the photo-interruptor will crash into the wall of the ante-chamber). To increase the beam-to-background signal of the organic molecule during TOF experiments, a LN2 shroud within the ante-chamber was used. The chopper motor which is housed around a copper cooling block (see Figure 2-8) was cooled with chilled water (~ 12°C) during TOF experiments to act as a heat sink for the chopper motor. During TOF experiments, it was observed that no aperture plate was required on the ante-chamber (during organic thin film deposition, a rectangular aperture is placed on the ante-chamber: see Figure 2-4) – the beam-to-background signal even without the aperture plate was > 100. The rotating blade chopper was fitted with a 25/25 4 in. blade. The blade was rotated at 50 Hz (since the blade used was a 25/25 in design, the molecular beam was effectively being chopped at 100 Hz), and the data was acquired using a multi-channel scalar card (ORTEC MCS-pci) with a sampling dwell time of 1 μs and pass length of 17000.

Acquisition of data with the MCS was triggered using a photo-interruptor that is mounted on the chopper assembly housing (see Figure 2-8) and detects the passing of the blade. The photo-interruptor consists of a GaAs LED and a silicon sensor packaged in an injection molded housing and facing each other across a ~ 3.3 mm gap (DigiKey, part # H21LOB-ND). When the photo-interruptor is ‘chopped’, that is the

when the blade passes through the ~ 3.3 mm gap and blocks the GaAs led, a TTL pulse generated from the chopper-controller triggers the MCS (MCS is set at 'External Trigger' mode via the 'Start-In' pin during TOF measurements) to start/stop accepting counts from the pre-amp of the QMS. The MCS receives counts from the pre-amp via the 'In' BNC on the MCS board.

The chopper-controller mentioned above, controls the speed of the motor and also houses the photo-interruptor interface circuitry. The chopper-controller was custom designed by Dr. John Carter (please refer to him regarding issues involving the malfunction of the controller). Important pictures of the chopper-controller assembly are shown in Appendix 9.2 (Figures 9-3 – 9-5). In addition, important specifications of the photo-interruptor are also shown in Appendix 9.2 (Figure 9-6). A 10-ft highly insulated cable (with a 10-pin male connector) was developed that connects the front panel (see Appendix 9.2, Figure 9-3) of the chopper-controller to the 10-pin female connector on the actual chopper-assembly flange (Figure 2-8). The pin assignments that the 10-pin connectors (for both male and female sides) make with the front panel of the chopper-controller assembly are shown in Appendix 9.2 (Figure 9-7).

To turn the motor on and off or to change the speed (Hz) of the motor, a software program (RDK-ACIM) was used – this program was provided along with the motor hardware board that is housed in the copper-controller (see Appendix 9.2, Figure 9-4). The motor hardware board and associated software were purchased from DigiKey (part # 726-1047-ND). The software program (RDK-ACIM) is interfaced to the chopper-controller via a doubled-side USB wire that connects the front panel of

the chopper-controller (see Appendix 9.2, Figure 9-3) to a computer (where the software program, RDK-ACIM, is installed). During initial TOF experiments, it was noticed that the TTL pulse generated by the chopper-controller (when the photo-interruptor is chopped) was very noisy – to fix this a low-pass filter was designed. In the improved setup, the TTL pulse generated from the chopper-controller now passes through a low-pass filter before connecting to the 'Start-In' pin on the MCS board (as mentioned above, the TTL pulse is used to trigger the MCS to start/stop accepting counts from the QMS).

The final TOF experimental set-up that was used to measure the mean velocity of the molecules in the incident molecular beam is described in Figure 2-9. Briefly, a supersonic molecular beam is created in the source chamber. The molecular beam passes through the ante-chamber where a blade (rotating at 50 Hz) chops the molecular beam into pulses before they arrive to the QMS. As the blade chops the molecular beam, it simultaneously chops the photo-interruptor which triggers the MCS (via a TTL generated pulse from the chopper-controller) to start/stop counting the signal it receives from the pre-amp of the QMS. Is this way, each pulse (or TOF spectra) is counted by the MCS. Note, that the MCS is also put in the 'sum mode' so that the counts from each pulse are continuously added together. In Figure 2-9, PC-1 controls all settings related to the QMS (emission current, electron energy, multiplier voltage, m/z, lens voltages, etc.) via the Merlin software provided with the Extrel QMS. PC-1 is also interfaced to the QMS controller electronics (provided by Extrel). PC-2 controls the MCS program which accepts counts from the pre-amp of the QMS when triggered by the chopper controller. A separate laptop was used to turn the

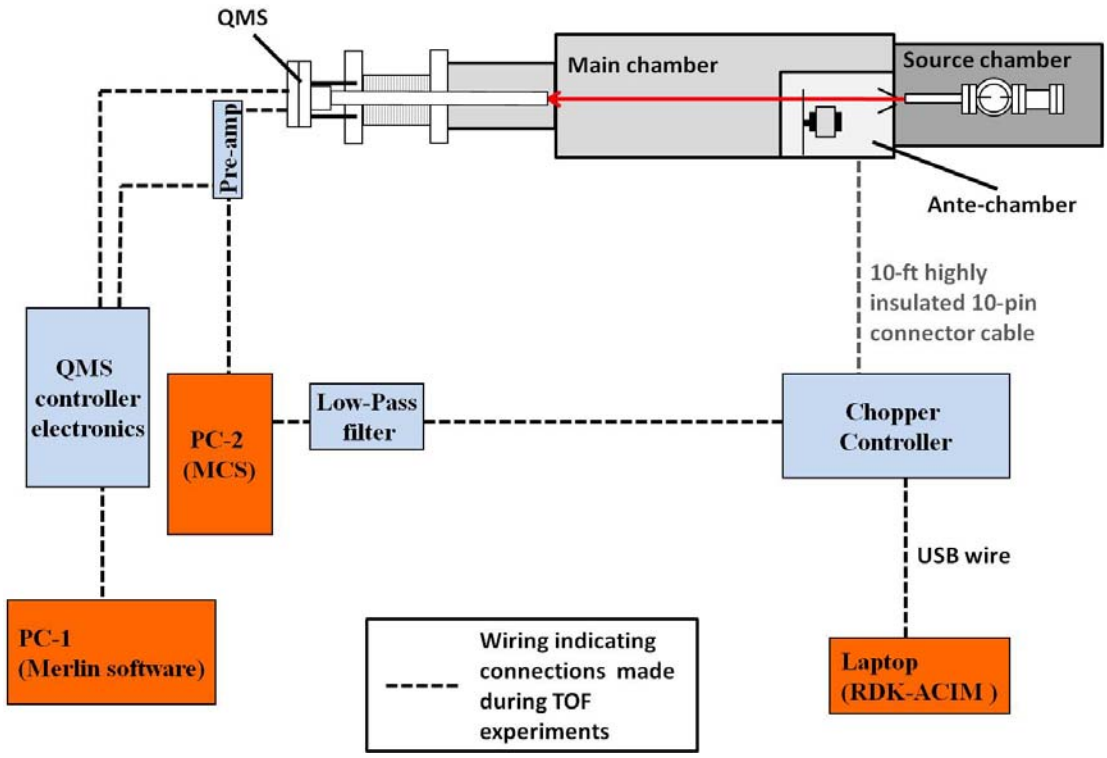

Figure 2-9 Schematic showing wiring connections between various electronic instruments during TOF experiments.

chopper motor on/off and to control its speed (Hz) via the RDK-ACIM software. The laptop was interfaced to the front panel of the chopper-controller via a USB wire.

The experimental conditions during TOF experiments (nozzle temperature (T_N), bubbler temperature (T_B) and He (helium carrier gas) flow rates) are shown in Table 2-2. The nozzle pressure (P_N) at each He flow rate is also shown in Table 2-2. At each helium flow rate, TOF experiments were repeated for at least 5 different distances between the blade and the QMS ionizer. The distance between the blade and the QMS ionizer can easily be varied using the linear translation stage – while knowing the absolute distance between the blade and the QMS ionizer very precisely is not important (~ 60 cm when the translation stage is fully compressed), knowing the relative distance between each experiment precisely is very important. Note that TOF experiments for pentacene have been done previously **[2]**. In Figure 2-10, an example TOF spectrum of intensity (at m/z of DIP) versus time is shown for the case of a DIP supersonic molecular beam at a He flow rate of 10 sccm. As observed we see a repeating square-wave form reminiscent of the shape of the 25/25 blade. If a blade with a single small slit was used, one would expect a Gaussian-like spectrum **[2]**.

In Figure 2-11, TOF spectra are shown for a DIP supersonic molecular beam at a He flow rate of 10 sccm but at 5 different blade-QMS ionizer distances. In this case, a zoomed in version of a single rising edge is shown so that the difference in the rising times can be seen. In Figure 2-11, X ~ 60 cm which is the distance when the linear translation stage is fully compressed. As expected for a relationship between velocity,

Table 2-2 Experimental conditions of supersonic beam during TOF experiments

Organic semiconductor	**T_N, °C (±3) [a]**	**T_B, °C**	**Molecular mass (g/mol)**	**[He flow rate, sccm/P_N, Torr (±2) [a]]**
DIP	490	320	400	[10/47.3], [25/92.2], [70/213.5], [120/339.5]
PFP	450	235	530	[10/46.3], [25/90.0], [70/208.8], [100/284]
PTCDI-C_{13}	430	343	754	[10/47], [25/92], [70/208], [90/255]

[a] This is an approximate variation from experiment to experiment and not in the measurement.

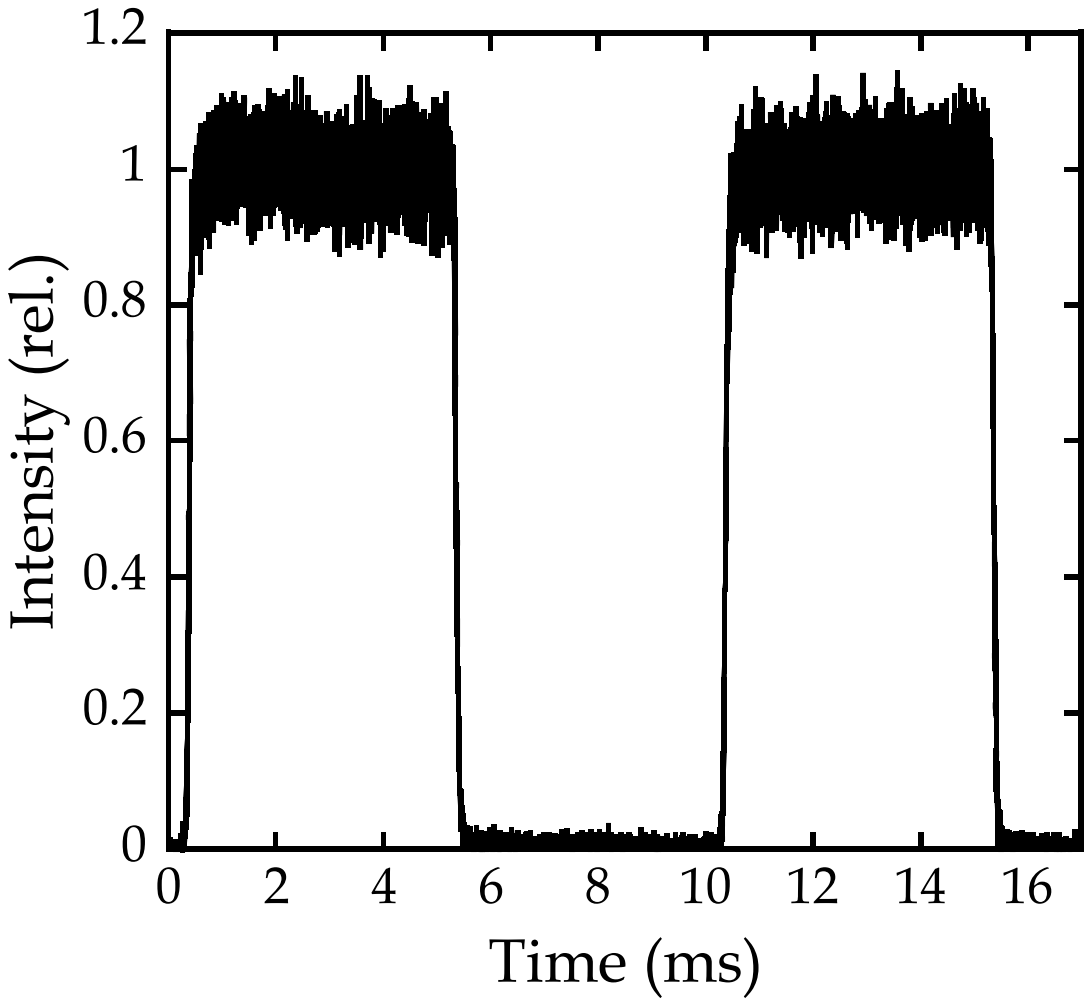

Figure 2-10 TOF spectrum of a DIP supersonic molecular beam at a He flow rate of 10 sccm.

distance and time, when the distance between the blade and the QMS ionizer increases, the time it takes for the DIP molecules to reach the QMS ionizer also increases. The rising edges (as shown in Figure 2-11) and falling edges of the TOF spectra can be fit easily using an error function to extract the rising and falling times. In Figure 2-12, as an example, the flight path (blade to QMS ionizer distance) versus rising time is plotted for the TOF spectra shown in Figure 2-11. As expected, the time taken for the DIP molecules to reach a certain flight path distance, L (between the blade and the QMS ionizer) increases with increasing L in a linear fashion. The data in Figure 2-12 can be fit to the following relationship between mean velocity (v_m), flight path distance (L) and time (t):

$$v_m = \frac{L}{t} \tag{2-1}$$

In Figure 2-12, we show a fit (black solid line) to the data using Equation (2-1), and extract a mean velocity of v_m = 142.1 ± 4.4 cm/ms (or 1421 m/s). The incident kinetic energy (E_i) of the beam can then be determined using Equation (2-2):

$$E_i = \frac{1}{2} m v_m^2 \tag{2-2}$$

where m is the mass of the organic semiconductor. Using the data shown in Figure 2-12 and Equation (2-2), an incident energy of E_i = 4.19 ± 0.26 eV can be extracted. In Figure 2-13, the incident energy, E_i, as a function of He flow rate for all organic semiconductors studied in this thesis is summarized. The values reported in Figure 2-13, are averages from two rising edges and two falling edges.

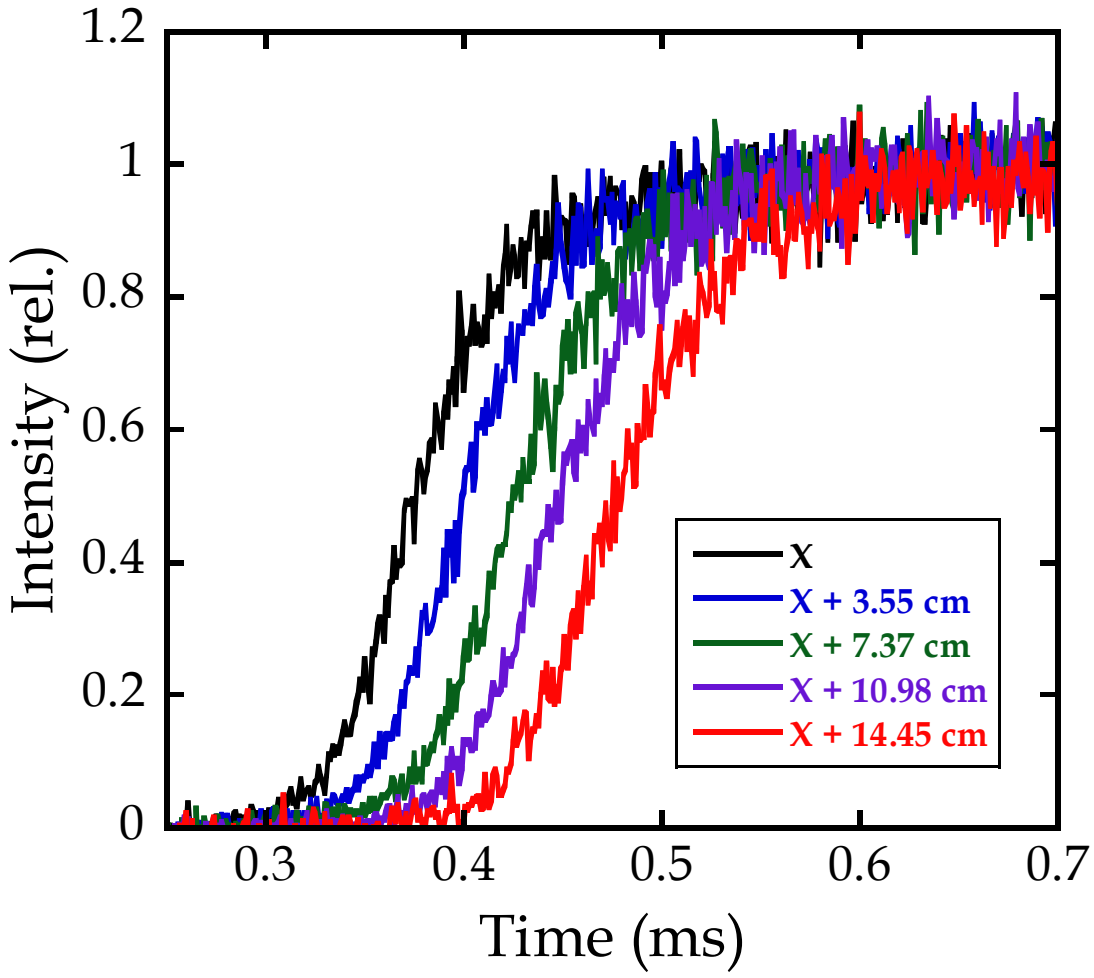

Figure 2-11 TOF spectra of a DIP supersonic molecular beam at a He flow rate of 10 sccm and at varying blade-QMS ionizer distances. Figure is showing zoomed in version of a rising edge.

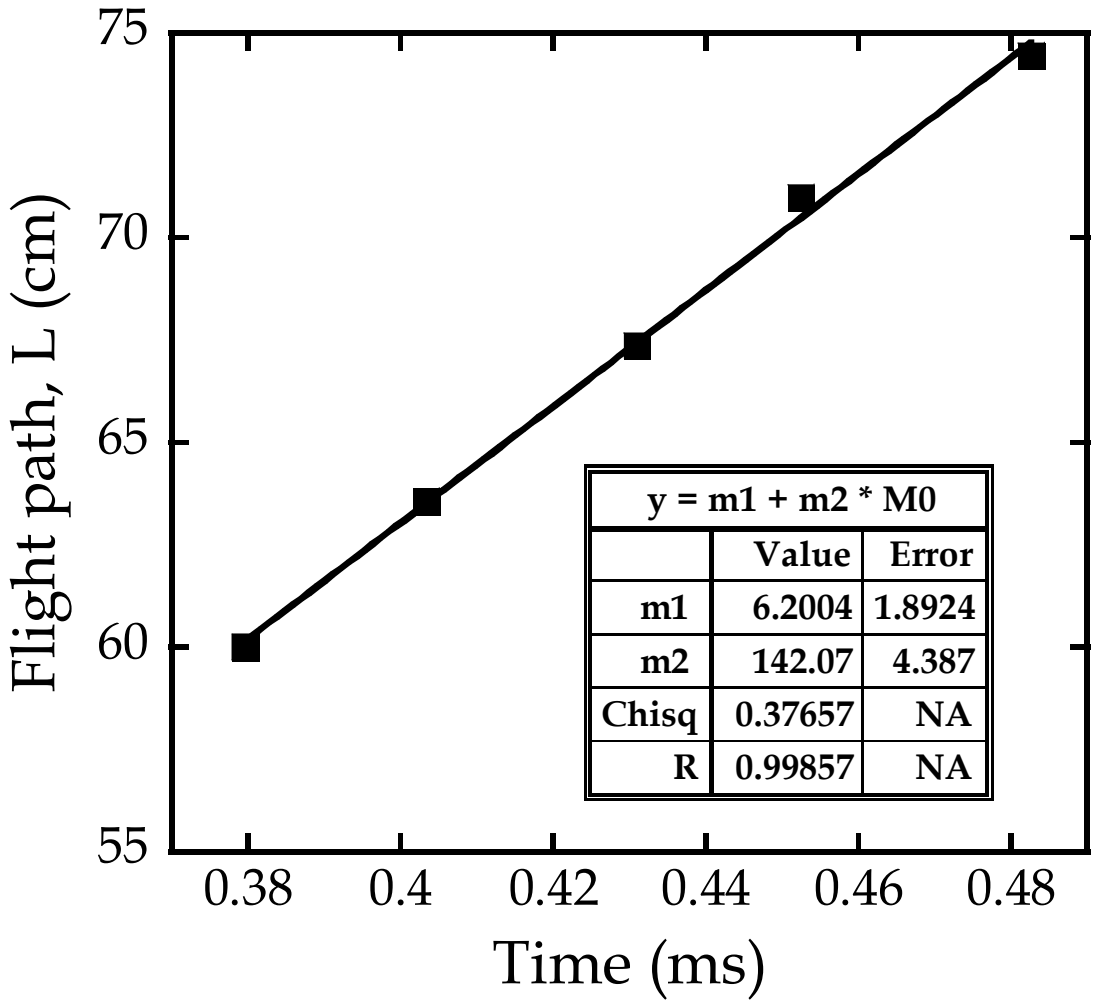

Figure 2-12 Flight path (distance between blade and QMS ionizer in cm) versus time taken for DIP molecules to reach QMS ionizer. Linear fit to data is shown by solid black line.

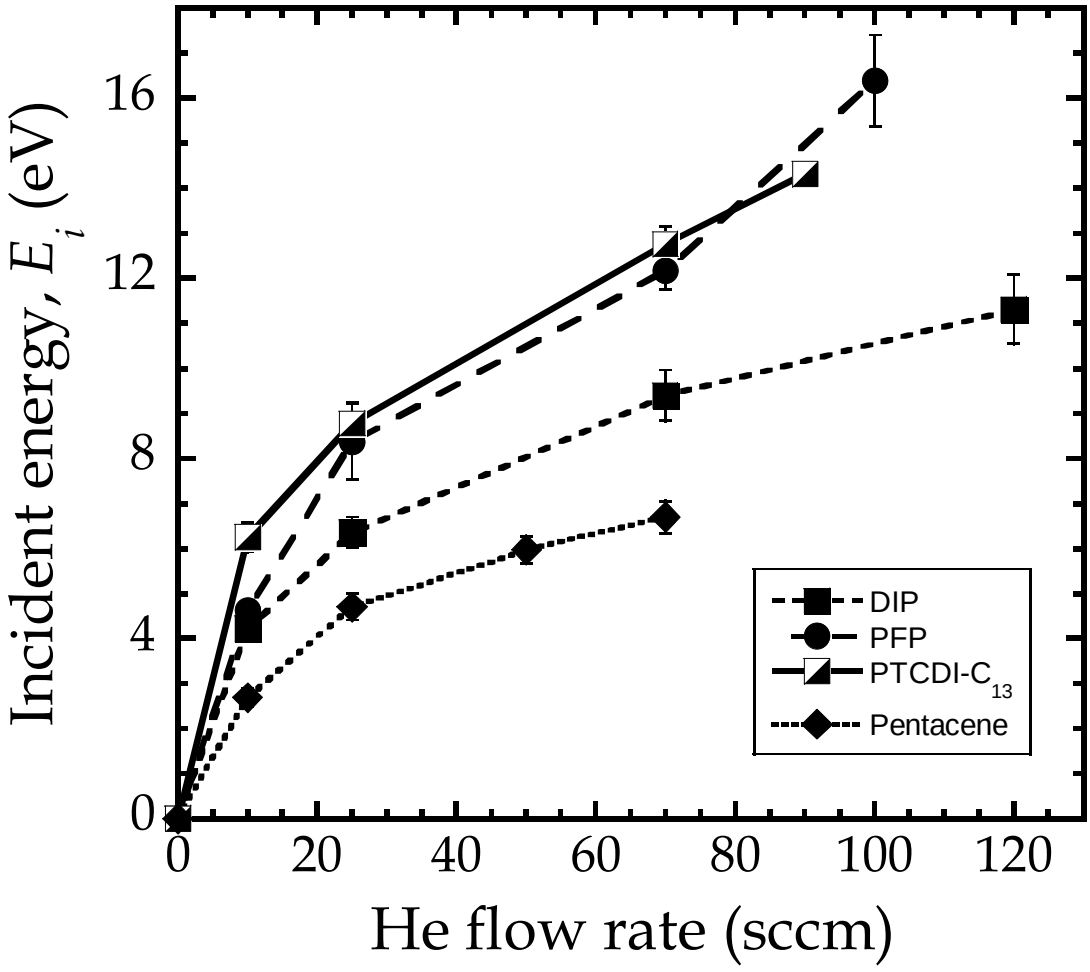

Figure 2-13 Incident energy, E_i, versus He flow rate (sccm) for all organic semiconductors studied in this thesis. Pentacene E_i data was obtained from reference **[2]**.

2.1.3 Description of effusive beam source

An effusion cell (or thermal evaporator) was first installed into the G-line deposition chamber on September 15th 2010. The purpose of installing a second deposition source (effusive source) in addition to the existing supersonic source was to be able to conduct the following types of studies:

1. Growth of organic heterostructures *in situ* and in real-time for applications in organic photovoltaics: deposition of organic semiconductor 'A' on top of organic semiconductor 'B' and *vice versa* or simultaneous deposition of 'A' and 'B'.
2. Study the effect of incident energy (thermal versus hyperthermal) on organic semiconductor thin film growth phenomena.

This chapter of the thesis will briefly describe the design, installation and operating instructions for the effusion cell. The effusion cell was manufactured by CreaTec Fischer & Co. GmbH (Germany based company), but was purchased from Sentys (USA distributors of CreaTec). Local (USA) contact person in Sentys is Ricker Kose (sales@sentys.com, Phone: 415-397-7327, Fax: 415-397-7328). The quote # of the purchased items is 2150/2.

The specifications of the effusion cell and its accessories are as follows:

1. Part description: *Low temperature effusion cell (part #: LTC-40-10-HL-SHP)*

- Mounted on a 2.75 in OD CF flange
- Length in-vacuum: 8 in (203.2 mm)
- Maximum diameter in vacuum: 1.3 in (33.0 mm)
- Maximum temperature: 800 °C
- Type K thermocouple
- 10 cc crucible made from PBN (pyrolytic boron nitride)
- Includes integrated pneumatic shutter
- Out-of-vacuum length: 10.5 in (266.7 mm)
- Bakeable up to 220 °C

2. Part description: *Power control unit (part #: CU-D-3504-280-DC)*

- PID Eurotherm controller (type 3504)
- Type K thermocouple
- 280 Watt DC power supply
- Digital indicators for current and voltage integrated in the front panel

- 6 m power cable to effusion cell
- RS 232/485 or TCP/IP interface

3. Part description: *Shutter controller (part #: EPS-1-l)*

- Note: this part is integrated into the *power control unit*
- Enables the pneumatic shutter to be operated manually or automatically
- The position of the shutter is directly proved on the front panel of the power control unit by a switch with the status displayed by a LED light

The effusion cell was mounted on port #14 in the G-Line deposition chamber as referenced in **[2]**. Figure 2-14 shows a schematic of the G-line deposition chamber (side view and front view along the molecular beam axis) indicating the port/flange used for the effusion cell. Another port that can be used for the effusion cell is port #11. Both port #14 and port# 11 are at a polar angle of 45° from the substrate surface normal. Note that port #15 houses the ante-turbo, port #8 houses the chopper assembly and port #10 is connected to the load-lock chamber and transfer arm. For other chamber details, see reference **[2]** and section 2.1.

In Figure 2-15, a schematic of the effusion cell is shown along with the relevant dimensions. Figure 2-16 shows a cross-section of the G-line deposition chamber with the effusion cell installed. The in-vacuum length of the evaporator was designed to be

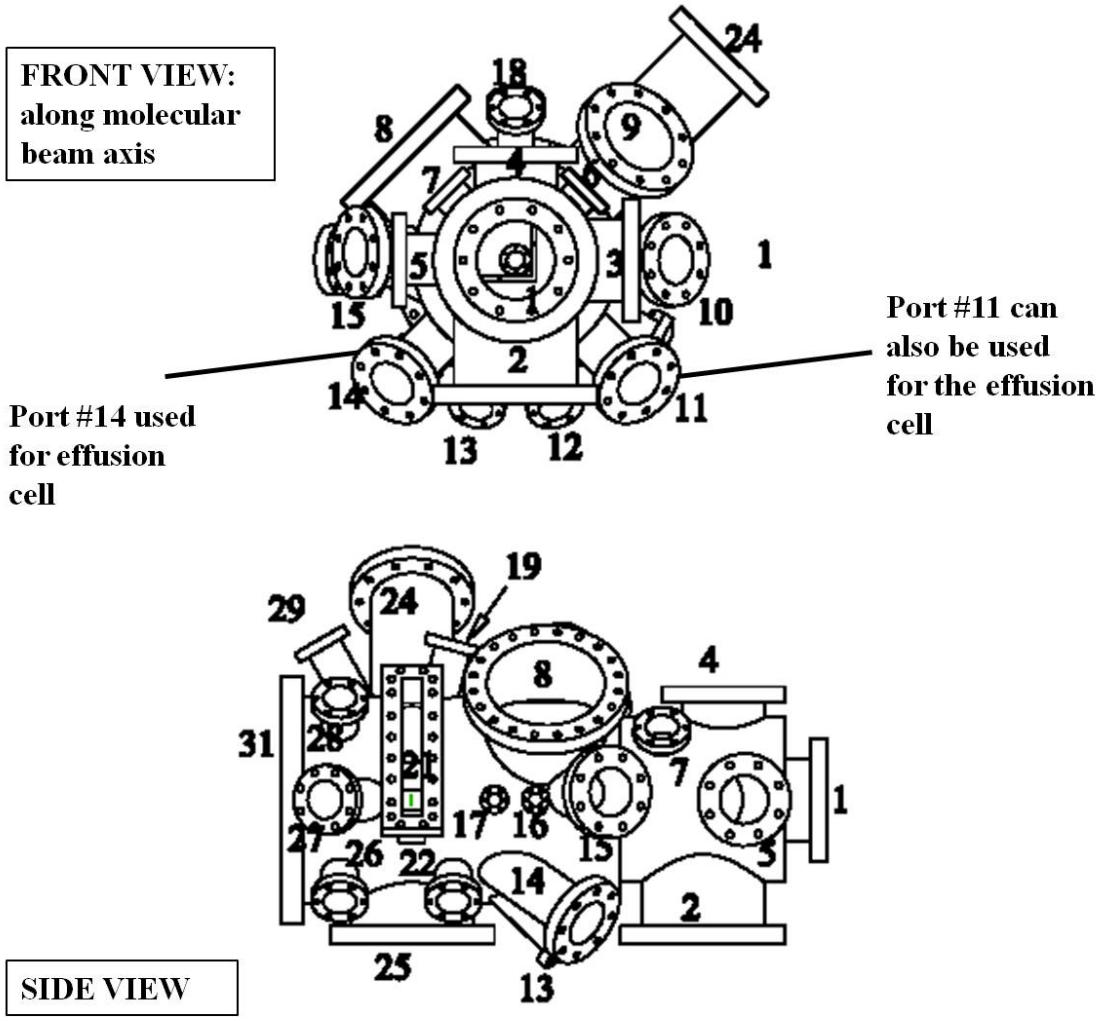

Figure 2-14 Orthographic projection of G-Line deposition chamber with ports indicated. See reference **[2]** for additional details.

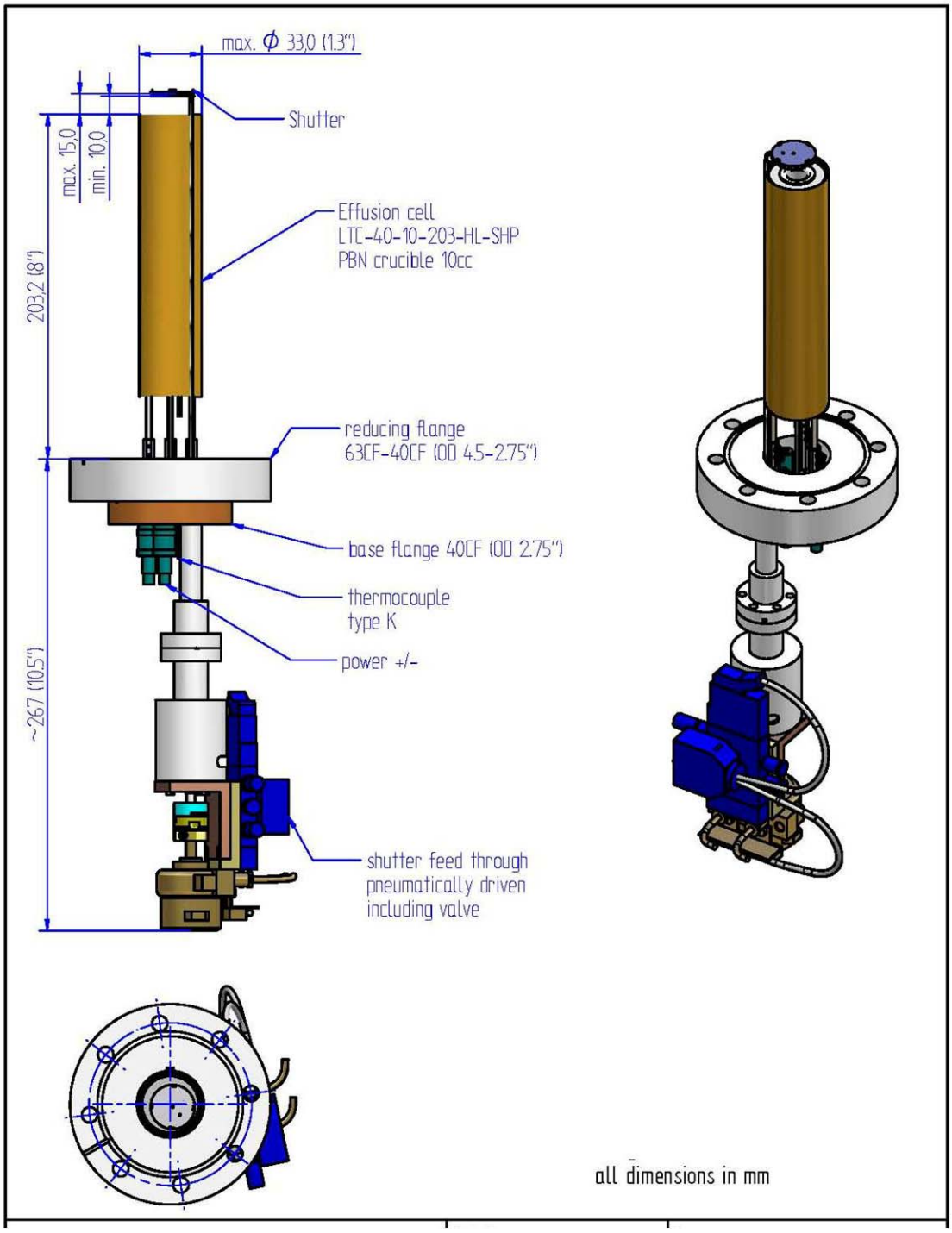

Figure 2-15 Schematic showing effusion cell with relevant dimensions. Note: this schematic was generated by CreaTec.

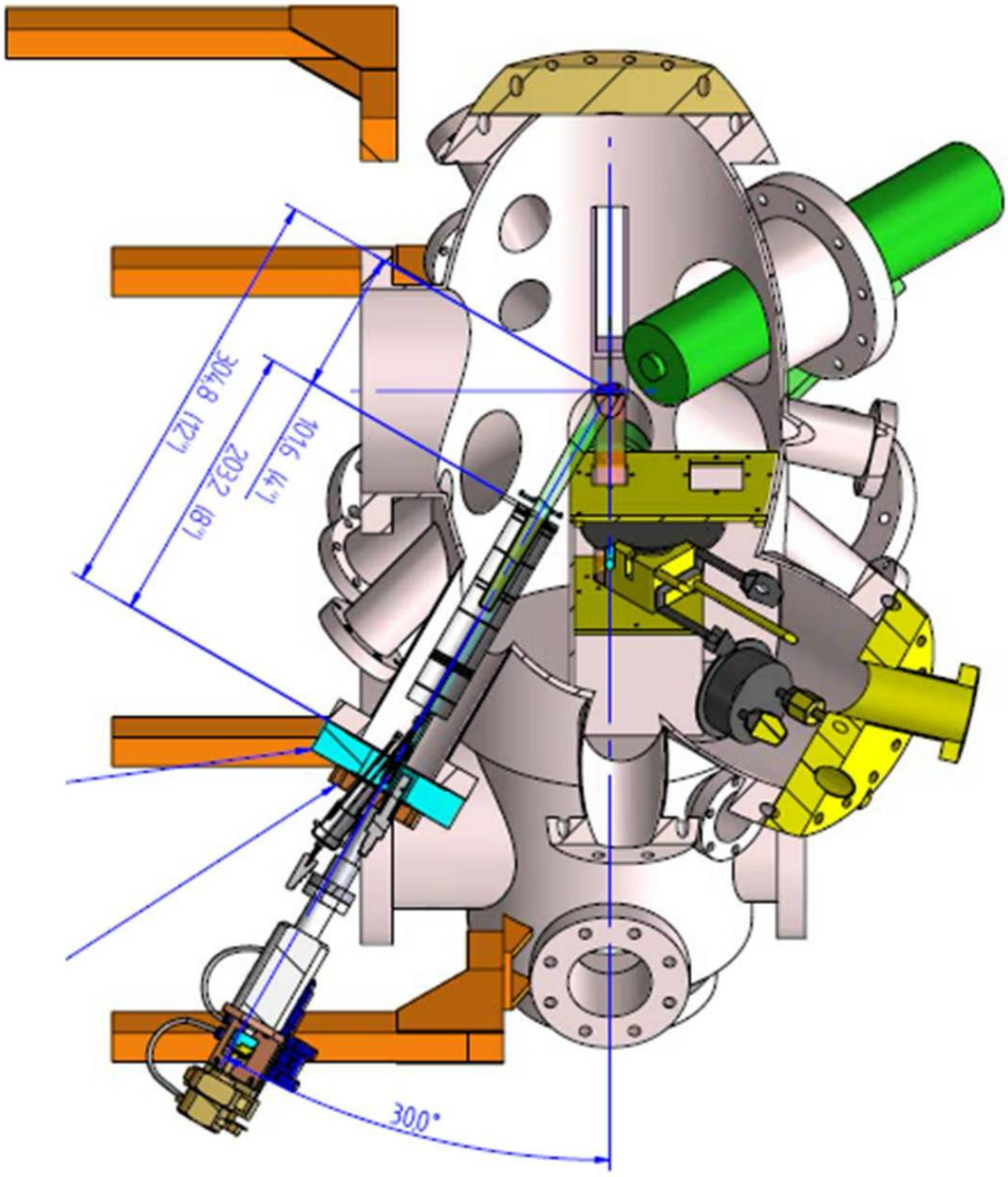

Figure 2-16 Cross section (side view) of G-Line deposition chamber showing effusion cell installed in port #14 (see Figure 2-14). Note: this schematic was generated by CreaTec.

8 in. The distance between the substrate surface and the effusion cell is 4 in. whereas the distance between the substrate surface and the base of port #14 is 12 in. (see Figure 2-16).

In Figure 2-17, another cross section (front view) of the G-line deposition chamber is shown with the effusion cell installed. The walls of the chamber are not shown for clarity purposes. As observed from Figures 2-16 and 2-17, the tip of the effusion cell is close to the bottom of the ¼ plate covering the ante-chamber. Once installed, this distance between the ¼ plate and the effusion cell is ~ 1 cm. Extreme care needs to be taken when installing and removing the effusion cell so as to avoid collision with the ante-chamber. In addition, the effusion cell needs to be installed in a position such that when the shutter is opened and closed, it rotates in the direction away from the ante-chamber. Note that the shutter rotates in a clock-wise direction (when one is facing the shutter).

In Figure 2-18, pictures of the power control unit are shown (front panel and back panel), and the important/relevant features are indicated. Refer to the power control manual for details regarding each feature. Briefly, in the front panel: the 3504 Eurotherm regulator is used to set/control the effusion cell temperature (the thermocouple is placed at the base of the PBN 10cc crucible); the Poti knob controls the amount of voltage/current that is output to the heating wires of the effusion cell and the voltage/current values are displayed digitally on the front panel; the EPS indicates the position of the shutter (open or close via a LED light) with the option of

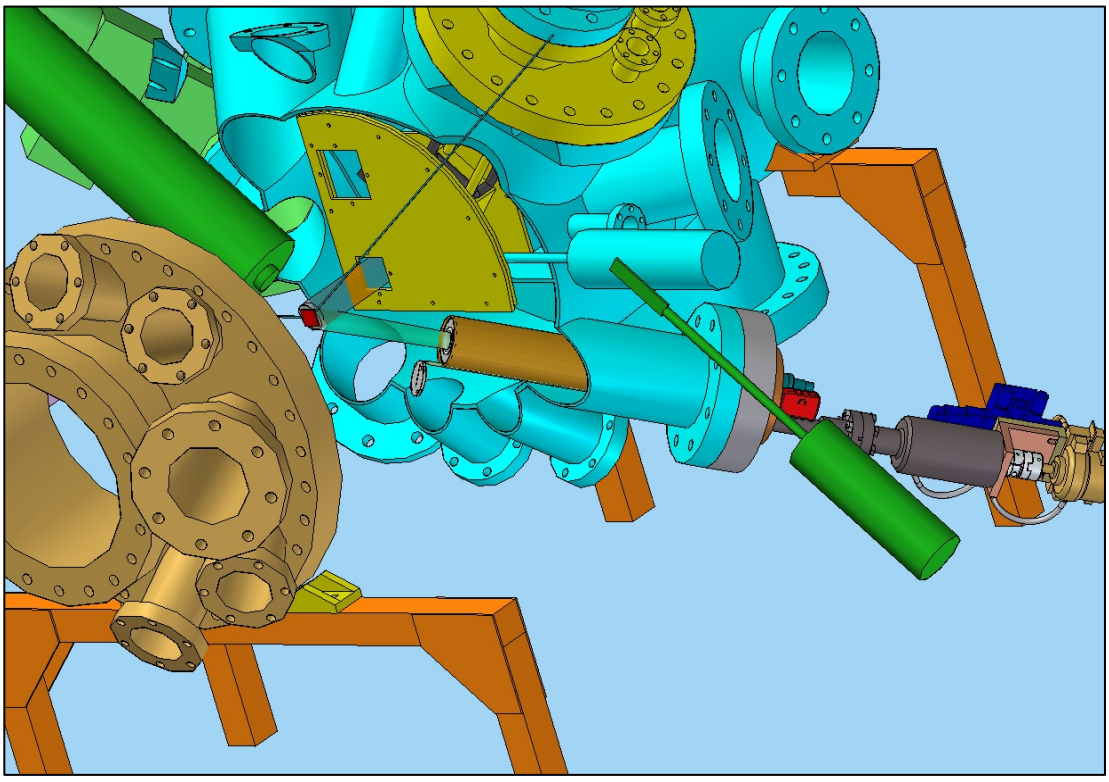

Figure 2-17 Cross section (front view) of G-Line deposition chamber showing effusion cell installed in port #14 (see Figure 2-14). Note: this schematic was generated by CreaTec.

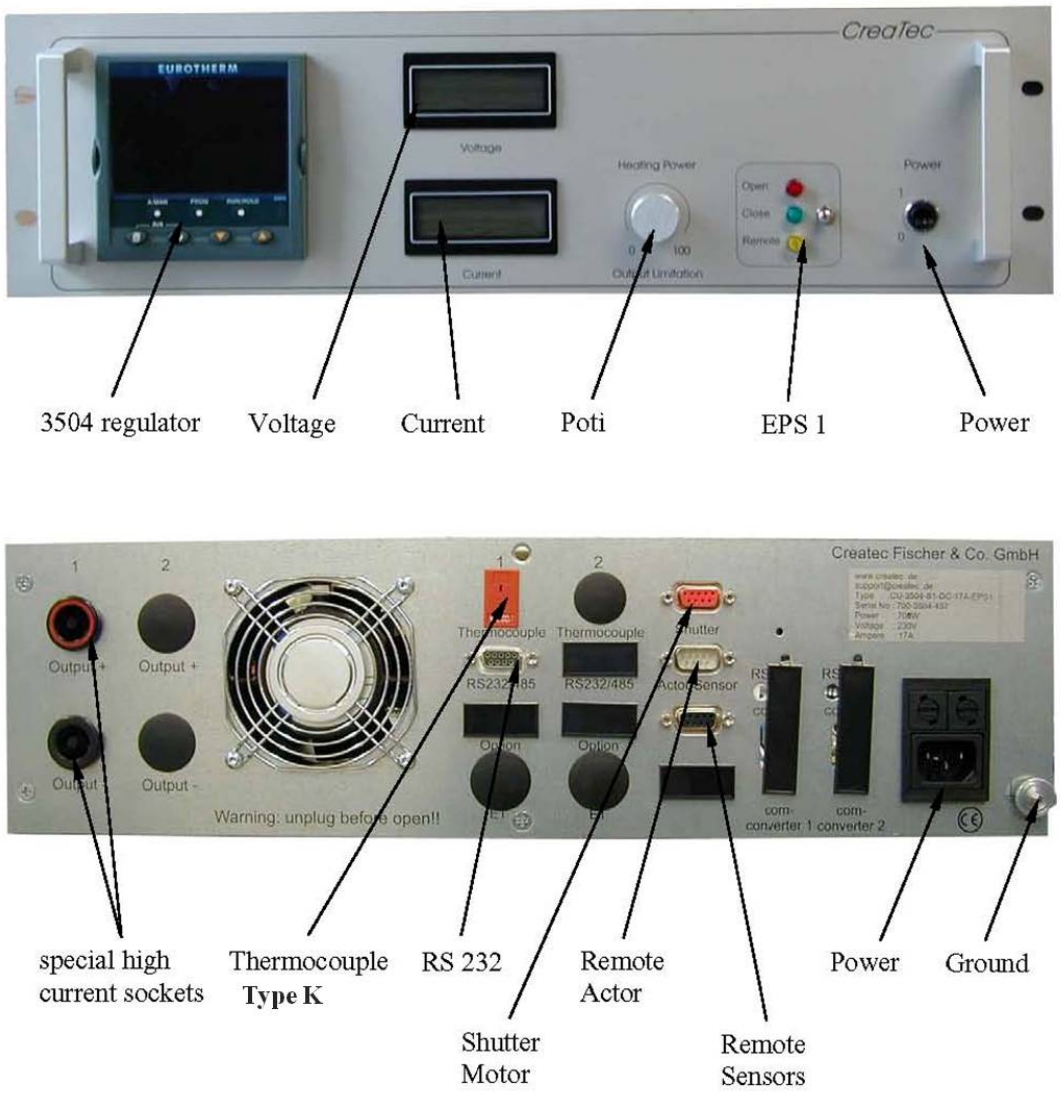

Figure 2-18 Pictures showing the front panel (top) and back panel (bottom) of the power control unit. Note: this schematic was generated by CreaTec.

controlling it automatically; the power switch is used to turn the power control unit on and off. Back panel: a power cable needs to be attached from the jack to the ‘power’ on the back panel; 6 m cables provided by CreaTec should be attached from the effusion cell to the ‘special high current sockets’ – power to heat up the effusion cell is applied through these cables; a thermocouple type K cable also should be attached from the effusion cell to the back panel; the remote actor is used to control the shutter remotely and automatically. Refer to the power control unit manual for additional details.

Unlike a supersonic molecular beam source where the flux distribution is highly directional, in an effusive source, the material emanating from the effusion cell has a cosine distribution. Due to this, and in order to paint both well defined thermal and supersonic films on the same substrate, a mask with a rectangular aperture was designed for the effusive source. This thermal mask is installed on port #19 (see Figure 2-14) and is attached to a motorized linear feedthrough which can be controlled using the SPEC software just as all the other motors in the G-3 hutch (at CHESS) are. During thermal beam deposition, the mask is lowered down to a set position so that a well defined rectangular spot can be painted on the desired position on the substrate. During supersonic beam deposition, the mask is retracted so that it will not block the supersonic molecular beam. From experimental results and under the typical growth rates operated (effusion cell) at, the beam-to-background is excellent as a result of the thermal mask effectively blocking material reaching the substrate other than through the well defined rectangular aperture.

The following lists in a step-by-step manner, an overview of the typical operating instructions for depositing organic thin films using the effusion cell:

1. Clean 10cc PBN crucible – if replacing existing material with another organic, clean by sonicating in the following: DIP, pentacene and PFP (acetone and/or isopropanol), PTCDI-C_{13} (chloroform). Take extreme care in handling crucible as it is very delicate. Always use gloves when handling the crucible.

2. Fill up the 10cc PBN crucible with ~0.1-0.2 grams of desired organic material– this amount of material should last a length of a typical CHESS run. Use a clean spatula when delivering material into the crucible.

3. Bolt the effusion cell into port #14 – make sure to use a copper gasket.

4. Pump down chamber and bake-out for ~24-48 hours.

5. Connect the power cables from the 'special high current sockets' of the power control unit back panel to the effusion cell. Also attach the thermocouple cable.

6. Turn on power control unit using the power switch on the front panel (see Figure 2-18).

7. Set the desired target temperature on the 3504 Eurotherm regulator (see Figure 2-18). See Eurotherm manual for details.

8. Turn the Poti knob (see Figure 2-18) to increase the output voltage – refer to power control unit manual for details on typical voltage-target temperature values and

ramp settings. Typically, ~ 1.5 V should be enough to target an effusion cell temperature of 100°C.

9. When the target temperature is reached, typically wait for ~15-20 min before deposition so as to achieve uniform heating all around the crucible.

10. Lower the thermal mask to the optimized deposition position (see instructions below on how to obtain this optimized deposition position).

11. Open the shutter either manually using the switch on the front panel or open shutter remotely – for operation during a CHESS run, and typically for *in situ* real-time experiments, a remote switch has been fabricated that sends a 9V signal to the 'remote actor' of power control unit (see Figure 2-18) in order to open/close the shutter.

12. Close shutter after desired growth time.

13. When finished with experiments, change the target temperature on the 3504 Eurotherm back to 0 °C, turn the Poti knob so that 0V are being output and turn off the power control unit.

The following describes instructions on how to align the effusive beam to the supersonic beam and to the x-rays from the synchrotron:

Note: x-ray position is fixed in space.

Note: steps 1 to 6 should also be used to align the supersonic molecular beam to the x-rays.

1. Create a supersonic molecular beam of the organic semiconductor of interest.

2. Maximize the main chamber pressure by iterating the x-y micrometer positions of the nozzle assembly. The z-position of the micrometer is fixed at ~ 2.3.

3. Cut and clip a piece of x-ray burn paper (similar to size of the substrate: ~ 1 cm × 2 cm) on the sample holder as if loading a new substrate. Put sample holder with the burn paper into load-lock chamber and pump down. Typically place a piece of aluminum foil behind the burn paper so that a stronger grip can be applied on to the surface of the burn paper by the sample holder clips.

4. Using the transfer arm, transfer the sample holder (with the burn paper on) from the load-lock chamber to the sample manipulator in the main chamber, like one would normally transfer a substrate. The burn paper outgases in the region of ~10^{-6} Torr so one should avoid dropping it into the vacuum chamber. If the burn paper is dropped into the vacuum chamber, then vent, remove the burn paper, pump down and re-bakeout the chamber before continuing with experiments.

5. Deposit a supersonic molecular beam spot on the burn paper – the painted spot should be rectangular in shape since as defined by the aperture plate on the ante chamber (see Figure 2-4). Check to see visually if the spot is well defined and rectangular in shape. If the painted sport is not well defined, adjust the nozzle x-y

micrometers accordingly. One can see beam spots on the substrates easily from the window of port #9 (see Figure 2-14).

6. Shine the x-rays onto the burn paper – this will change the color of the burn paper and therefore indicate the position of the x-rays with respect to the supersonic molecular beam spot. The x-rays in principle should be going right through the center of the rectangular supersonic molecular beam spot. If they are not, adjust the z-position of the diffractometer table accordingly (do this by using motors zne, znw and zs - move them all in a relative manner).

7. After successful completion of steps 1 to 6, your supersonic molecular beam is now aligned with the x-rays from the synchrotron.

8. Create an effusive beam. Keep the effusion cell shutter closed at this time. Also make sure that the beam flag in the ante-chamber is blocking the supersonic molecular beam at this point.

9. Lower the thermal mask to an initial guess position: a good starting point is 60 mm as indicated on the micrometer of the linear feedthrough.

10. Make sure the sample manipulator position (motor: samz) is set such that you are about to expose the thermal beam onto an existing supersonic molecular beam spot.

11. Open the effusion cell shutter and expose the thermal beam onto the substrate. Expose until a thick enough film has been deposited.

12. Close the effusion cell shutter and retract the thermal mask until the substrate can been seen clearly from port #9. Check to see from port #9 if the thermal beam is painted on top of the supersonic beam spot. Depending on how far (vertically) the thermal beam spot is off from the supersonic beam spot, adjust the position of the thermal mask accordingly.

13. Iterate steps 9 to 12 until the thermal mask position is optimized so that a thermal beam spot can be painted right on top of the supersonic molecular beam spot – this is the mask position for deposition using the thermal beam.

14. After successfully completing steps 1 to 13, the thermal beam and the supersonic molecular beam are now aligned both to each other and to the x-rays from the synchrotron.

15. Follow x-ray scans outlined earlier in section 2.1.1 to monitor film growth at the anti-Bragg position.

2.2 Sample Preparation

This section will discuss all procedures involved with sample preparation. The first step involves the formation of a thermal oxide (SiO_2). The thermal oxide is then cleaned vigorously before organic semiconductor thin film deposition or before growth of self-assembled monolayers or spin coating of polymer thin films.

2.2.1 Thermal oxide formation

Substrates were Si (100) wafers (Wacker–Siltronic, p–type, 4" diameter, 500–550 μm thick, 38–63 Ω–cm) subject to a RCA–1 clean, 15 seconds HF dip and a RCA–2 clean immediately before growth of SiO_2. The approximately 300 nm thick SiO_2 films were grown by wet thermal oxidation at 1100 °C – growth time was ~ 55 min. The thermal oxide furnace was used at the Cornell Nanofabrication Facility (CNF). After growth of SiO_2, the wafers are cut into smaller pieces of ~ 1 cm × 2 cm and subsequently exposed to further cleaning procedures before any organic semiconductor thin film deposition or SAM growth or polymer spin coating.

2.2.2 Thermal oxide clean

Immediately prior to organic thin film deposition or SAM formation or spin coating of polymer thin films, the SiO_2 wafers (1 cm × 2 cm) were subjected to vigorous cleaning procedures to remove any macroscopic particles and organic matter.

First, the wafers were sonicated in chloroform ($CHCl_3$) solution (J. T. Baker - 99.8% HPLC grade) for 15 minutes followed by sonication in deionized (DI) water for another 15 minutes. Next, they were washed with copious amounts of DI water and dried with nitrogen. Finally, they were subject to an ultraviolet light–ozone clean (UV–Ozone) for 25 minutes to remove any remaining organic residues. The samples were then stored in pre-cleaned fluoroware containers. Within ~ 30-45 minutes of the UV–Ozone clean, samples were either transferred into the G-Line deposition system for organic semiconductor thin film growth or exposed to further procedures to form SAMs or spin-coating of polymer thin films.

2.2.3 Formation of self–assembled monolayers (SAMs)

The following SAMs (all from Gelest Inc.): octadecyltrichlorosilane (ODTS), octyltrichlorosilane (OTS), 1-napthylmethyltrichlorosilane (NMTS) and 6-phenylhexyltrichlorosilane (PHTS), were all grown on SiO_2 wafers (1 cm × 2 cm) in solution form. See section 1.2 regarding the chemical structure of these SAMs. Deposition was carried out in a glove box (Unilab, M. Braun Inc.) with a nitrogen atmosphere, $[O_2] < 2$ ppm and $[H_2O] < 1$ ppm. All glassware was rinsed repeatedly with acetone (Mallinckrodt Chemicals - CMOS^{TM} grade), isopropanol (J. T. Baker – HPLC grade) and DI water followed by baking at 150 °C overnight before use. All solutions were 10 mM concentration of the SAM precursor molecule in anhydrous toluene (Sigma Aldrich Corp., >99%). The SiO_2 substrates were dipped in the SAM solution for 2 days and left in the glove box undisturbed, followed by sequential

rinsing in anhydrous toluene, anhydrous acetone (Sigma Aldrich Corp., > 99%) and chloroform (Sigma Aldrich Corp., HPLC grade, >99%) and finally drying with nitrogen. Upon withdrawal from the solution, if the surface appeared cloudy, the samples were sonicated in anhydrous chloroform for 10-15 minute to remove any polymerized residue, not bonded to the substrate. Finally, the substrates were stored in pre-cleaned fluoroware containers before being transferred into the G-Line deposition system for organic semiconductor thin film growth.

Perfluorooctyltrichlorosilane (FOTS), hexamethyldisilazane (HMDS) and 3-methacryloxypropyltrichlorosilane (MAOPTS) were deposited via a vapor phase deposition. See section 1.2 regarding the chemical structure of these SAMs. HMDS was deposited from the vapor phase using a YES LP–III vapor priming oven. The substrates were held at 150 °C and went through several successive evacuation and purge cycles so as to dehydrate the substrates before being exposed to the HMDS vapor. Both FOTS and MAOPTS were deposited using an MVD-100 system. In this case, the MVD-100 deposition chamber was exposed to an oxygen plasma pre-clean prior to SAM growth. See tool instruction manuals for additional details. After SAM deposition, the samples removed from the oven and were stored in pre-cleaned fluoroware containers before being transferred into the G-Line deposition system for organic semiconductor thin film growth.

2.2.4 Formation of polymer thin films

See section 1.2 regarding the chemical structure of the polymers investigated. Polystyrene (PS) and polymethylmethacrylate (PMMA) were deposited on SiO_2 wafers (1 cm × 2 cm) using spin-coating techniques. PS was purchased from Polymer Source Inc. (product # P8577-S) in solid form. PMMA was spin-coated using the NANO^{TM} 495 PMMA Series Resist in Anisole (Micro Chemicals) solution available in the CNF cleanroom. PS (M_N: 200 Kg/mol, 1 wt% in anhydrous toluene) was deposited by spin-casting on SiO_2 wafers at 5000 rpm (acceleration rate of 5000 rpm) for 60 seconds. PMMA (M_W: 495 Kg/mol, 2 wt% in anisole) was deposited by spin-casting on SiO_2 wafers at 4000 rpm (acceleration rate of 3000 rpm) for 60 seconds. The spin-coated PMMA films were subsequently annealed for 15 minutes at 170°C on a hotplate. Polyethylenimine (PEI) was purchased from Sigma Aldrich (product # 181978). PEI (M_W: 750 Kg/mol, M_N = 60 Kg/mol, 0.1 wt% in DI water) films were deposited by dipping cleaned SiO_2 substrates in solution for 15 minutes followed by rising in pure DI water and finally drying with nitrogen. After polymer spin-coating/deposition, the samples were stored in pre-cleaned fluoroware containers before being transferred into the G-Line deposition system for organic semiconductor thin film growth.

2.2.5 Characterization of SAMs and polymer thin films

The SAMs and polymer thin films were characterized using contact angle goniometery and specular x-ray reflectivity measurements (XRR). Contact angle measurements were used as an indicator of their surface wet-ability and to estimate their surface energy. XRR measurements were fit using Parratt formalism to extract estimates to film thickness, electron density and interface widths. Details of these techniques are discussed in sections 2.4 and 2.5. Atomic force microscopy (AFM) measurements were also used in a few cases to measure the film surface roughness. See sections 9.3 and 9.4 regarding the SAM and polymer contact angle and XRR measurements.

2.3 Atomic force microscopy (AFM)

Atomic force microscopy (AFM) is a high-resolution scanning probe microscope in which a sharp tip (typical silicon or silicon nitride with a radius of curvature of ~ 10 nm) is moved over a sample and the movement of the tip is monitored as a measure of the surface topography. AFM was used in this thesis as an *ex situ* characterization tool to monitor the morphology of organic thin films (pentacene, DIP, PFP and PTCDI-C_{13}) deposited on various substrates. AFM was also used to characterize the bare substrates (SiO_2, SAMs and polymers) themselves. AFM was conducted *ex situ* using a Digital Instruments Dimension 3100 scanning probe microscope (Veeco Instruments) in tapping mode. The AFM images were analyzed using Gwyddion (freeware software available for download from http://gwyddion.net/) to measure film roughness, extract height distributions and line scans. AFM images were also analyzed using Nanscope v5.0 (Veeco software) to conduct 1D power spectral density (1D PSD) measurements. 1D PSD measurements were conducted in order to quantify the sizes of islands/features/grains **[3, 4]**.

2.4 Contact angle goniometery

The SAMs and polymers were also characterized using contact angle measurements. Contact angle measurements were carried out using the VCA Optima XE system (AST Products Inc., Billerica, MA). Static contact angle measurements were carried using solvents of known surface energy (either water or formamide or both). Advancing and receding contact angle measurements were carried out only

using water as a solvent. The advancing (receding) droplet volume of about 3 (2) μL was used. Contact angles were measured on either side of the droplet and in multiple areas of each sample, and the average of these values is reported. Surface energy measurements (mJ-m^{-2}) of the SAMs and polymers were estimated using the static contact angles (water and formamide) as inputs into the Young-Dupre equation **[5]**. For SAM and polymer surface energy estimates we used the following calibrated values for formamide (water): γ_L^d = 39.5 mJ-m^{-2} (22.1 mJ-m^{-2}) and γ_L^p = 18.7 mJ-m^{-2} (50.7 mJ-m^{-2}), where γ_L^d and γ_L^p are the dispersive and polar components of the surface energy respectively. Contact angle measurements (static, advancing and receding) and surface energy measurements of all SAMs and polymers studied in this thesis are summarized in the Appendix (section 9.3).

2.5 X-ray scattering from thin films

X-ray scattering at the anti-Bragg position was employed to monitor the *in situ* real-time growth of organic semiconductors on SiO_2 and SiO_2 modified with self-assembled monolayers (SAMs) and polymers. Specular x-ray reflectivity (XRR) was used to characterize the crystal structure of organic thin films – this provided information of the organic crystal perpendicular to the substrate. XRR was also used to characterize the bare SAMs/polymers to extract their thickness, electronic density, 2D surface density and interface widths. In the following sections, basics concepts of x-ray scattering will be discussed that will enable the reader to understand the results presented in sections 3-7. The following x-ray sections are meant to be brief and concise versions of the concepts that are of interest – for detailed explanations, the reader should refer to the publications/textbooks that are referenced in the following sections.

2.5.1 Optical constants

This section is adapted from references **[6, 7]**. X-rays are electromagnetic waves with wavelengths (λ) in the region of Ångströms (Å). For electromagnetic waves, the phenomena of refraction and reflection at interfaces of media (homogeneous with sharp boundaries) are characterized by the following:

$$n = 1 - \delta + i\beta \tag{2-3}$$

where n is the refractive index. In vacuum, $n = 1$, whereas for visible light, $n > 1$. In Equation (2-3), δ and β are the dispersive and dissipative parts of the refractive index respectively. The dispersive part, δ, is proportional to the electron density, p_{el}, of medium through which the x-rays are travelling and the dissipative part, β, to the linear absorption coefficient, μ:

$$\delta = \frac{\lambda^2}{2\pi} r_0 p_{el}$$
$$\beta = \frac{\lambda}{4\pi} \mu \qquad (2\text{-}4)$$

where λ is the x-ray wavelength and r_0 (2.82×10^{-5} Å) is the Thompson scattering length (or the classical electron radius). Physically, the linear absorption coefficient, μ, describes the extent to which the x-rays are attenuated in the material. Typical values of δ range between $10^{-5} – 10^{-6}$ whereas β is much smaller: $10^{-6} – 10^{-9}$.

According to Snell's law, at the interface of a medium with the vacuum, the incident grazing angle, α_i, can be related to refracted grazing angle, α_t, through the following (see Figure 2-19):

$$\cos\alpha_i = n\cos\alpha_t \qquad (2\text{-}5)$$

Since $n < 1$ for x-rays, below a certain incident grazing angle called the critical angle, α_c, total external reflection occurs. That is the x-rays do not penetrate far into the medium. Instead, all incoming radiation is reflected.

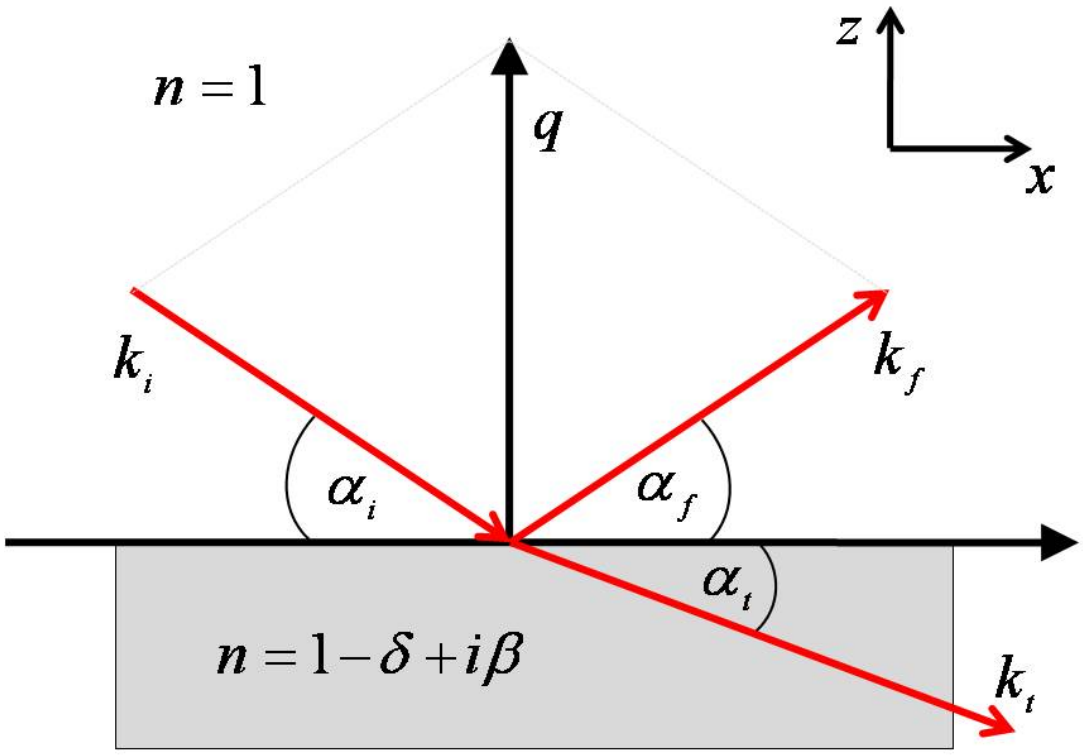

Figure 2-19 A plane electromagnetic wave with wavevector, k_i, hits a surface at grazing angle α_i. The wave splits into reflected wave, k_f, at angle α_f and transmitted wave, k_t, at angle α_t. Snell's law and the Fresnel equations can be derived by requiring continuity at the interface of the wave and its derivative. Since $n < 1$ for x-rays, it follows from Snell's law that $\alpha_i > \alpha_t$, and therefore total external reflection takes place below α_c.

Expanding the cosine (Taylor expansion using only the first two terms) in Equation (2-5) with $\alpha_i = \alpha_c$ and $\alpha_t = 0$ and using Equation (2-3), we get:

$$\cos\alpha_c \approx 1 - \frac{\alpha_c^{\,2}}{2} = (1-\delta)$$
$$\therefore \alpha_c = \sqrt{2\delta} = \lambda\sqrt{\frac{r_0 p_{el}}{\pi}} \qquad (2\text{-}6)$$

where we have assumed $\beta=0$. From Equation (2-6), it is clear that the critical angle, α_c, is proportional to both the x-ray wavelength, λ, and the electron density of the medium, p_{el}. With δ being on the order of 10^{-5}, the critical angle, α_c, is of the order of a milli-radian. In Figure 2-19, q is the wavevector transfer (or the scattering vector) and is defined as $q = \boldsymbol{k_i} - \boldsymbol{k_f}$, where $\boldsymbol{k_i}$ and $\boldsymbol{k_f}$ are the incident and diffracted wavevectors respectively. The scattering event depicted in Figure 2-19 is assumed to be elastic with $|\boldsymbol{k_i}| = |\boldsymbol{k_f}| = 2\pi/\lambda$.

2.5.2 Specular X-ray reflectivity (XRR)

Specular x-ray reflectivity measurements (XRR) were conducted to determine the crystal structure and interface structure of the organic thin films and SAMs perpendicular to the surface. In specular XRR, $\alpha_i = \alpha_f$ and $q = q_z$ with $q_x = q_y = 0$ (see Figure 2-20(a)). Since $q = q_z$ and $q_x = q_y = 0$, one can only extract information regarding the density along the surface normal. Regarding the SAMs, specular XRR

was used to extract information concerning their electron density, thickness and interface widths. For the organic thin films, specular XRR was used to determine the crystal structure in the *(001)* direction.

The measured intensity, I_m, from the detector during specular XRR experiments need to first be corrected before further analysis can be conducted. The footprint, F, of the x-ray beam on the substrate sample can be determined by the beam size, T, and the incident angle, θ, using $F = T/\sin\theta$. Since at low incident angles, F is larger than the sample dimension, S, I_m needs to be corrected using Equation (2-7), so that only the beam that is impinging on the sample is contributing to the total corrected intensity, I_{cor}:

$$I_{cor} = I_m \frac{T}{\sin\theta} \frac{1}{S} \tag{2-7}$$

In Figure 2-20(b), an example specular XRR of a thin film of PTCDI-C_{13} deposited on NMTS is shown. The purpose of this figure and following paragraph is to highlight some of the essential features/information that can be extracted from specular XRR of an organic thin film. The scattered intensity exhibits Bragg reflections (up to the 4^{th} order) with well defined Laue oscillations (smaller oscillations around the Bragg peaks) that are characteristic of a highly ordered lamellar structure. In Figure 2-20(c), a zoomed in version of Figure 2-20(b) around the *(002)* Bragg peak is shown.

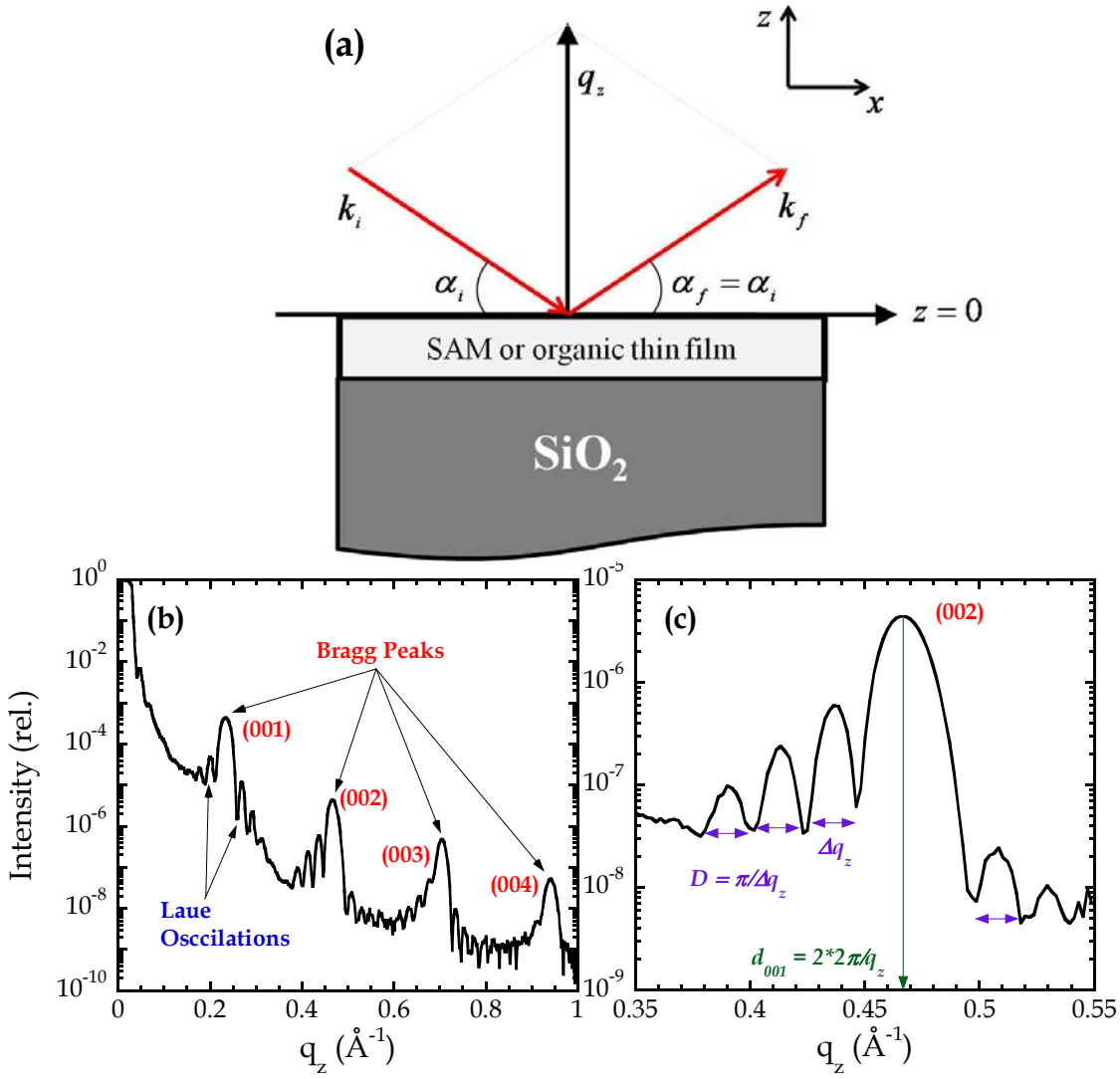

Figure 2-20 (a) Reflection of an x-ray beam on a surface at specular conditions: $\alpha_i = \alpha_f$. In specular XRR, the wavevector transfer, q, is perpendicular to the surface and hence $q = q_z$ and $q_x = q_y = 0$. (b) Specular XRR of PTCDI-C_{13} deposited on NMTS describing the main features of the plot – the Bragg peaks and Laue oscillations indicative of well ordered lamellar structure. (c) Zoomed in version of the (002) Bragg peak from Figure 2-20(b) – thickness of the thin film can be determined from the period of the Laue oscillations and the d_{001} lattice parameter from the position of the Bragg peak in q_z-space.

The following can be extracted from Figure 2-20(c):

1. From the position of the Bragg peak (in q_z-space), as determined from a Gaussian fit to the Bragg peak, the height of the unit cell, d_{001}, can be determined using $d_{001} = 2\pi/q_z$. If the *(002)* Bragg peak is used than $d_{001} = 2*2\pi/q_z$ and so forth.

2. The coherent film thickness, D, can also be determined from the period of the Laue oscillations, Δq, around the Bragg peaks via $D = \pi/\Delta q$.

The specular XRR can be fit using both Parratt formalism (which takes into account multiple scattering) and kinematic theory (only takes into account single scattering phenomena). Parratt formalism is used predominantly to fit specular XRR of SAMs and this is discussed in detail in the next section (2.5.2). Specular XRR of organic thin films is not fit in this thesis and this data is analyzed using the features described in Figure 2-20(b-c) mainly to extract film thicknesses and d_{001} lattice parameters. Kinematic theory is used to model the time resolved *in situ* real-time x-ray scattering data of organic thin film growth and this is described in detail in section 2.5.3.

2.5.3 Parratt Formalism

This section is based on references **[6, 7]**. Parratt formalism (developed by L. G. Parratt **[8]**) is used to calculate the x-ray reflectivity of multiple layers on a substrate using a recursive algorithm, where scattering from all interfaces is taken into

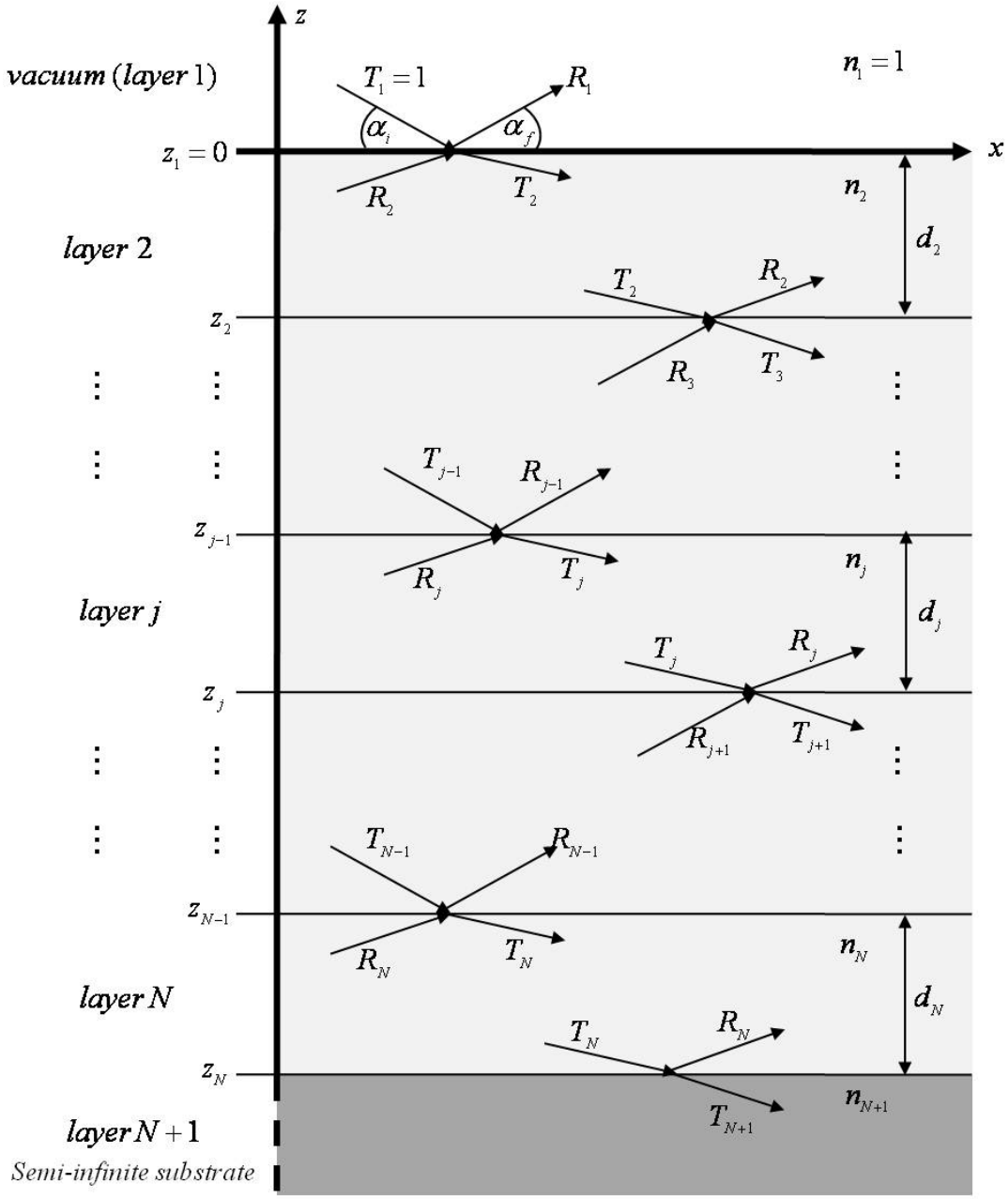

Figure 2-21 Sketch of a system consisting of *N+1* layers with *N* interfaces. In the case of specular reflectivity, the condition $\alpha_i = \alpha_f$ holds. The incident wave amplitude is normalized to unity $T_1=1$. No wave is reflected from the bottom surface of the substrate, i.e. $R_{N+1}=0$. This schematic follows the parameterization used for Parratt Formalism.

account. Figure 2-21 shows a multilayer stack consisting of N interfaces at positions $z_j \leq 0$. Each 'box' is a layer with the vacuum defined as 'layer 1' and the first interface at $z_1 = 0$. The last interface is located at z_N with the underlying semi-infinite substrate ('layer $N + 1$'). The refractive index of each layer with thickness $d_j = z_{j-1} - z_j$, is denoted by $n_j = 1 - \delta_j + i\beta_j$ and T_j is the amplitude of the transmitted wave and R_j the corresponding value for the reflected wave inside layer j. The impinging wave with an amplitude normalized to unity, $T_1=1$, hits the surface at grazing angle α_i. Using a recursive algorithm based on the Parratt formalism, the reflected amplitude, R_1 can be determined.

If X_{j+1} denotes the ratio of R_{j+1} and T_{j+1} in layer $j+1$, X_j for the layer above (layer j), can be calculated via:

$$X_j = \frac{R_j}{T_j} = \exp(-2ik_{z,j}z_j)\frac{r_{j,j+1} + X_{j+1}\exp(2ik_{z,j+1}z_j)}{1 + r_{j,j+1}X_{j+1}\exp(2ik_{z,j+1}z_j)} \tag{2-8}$$

where $r_{j,j+1}$ is the Fresnel coefficient (see Figure 2-19) of interface j:

$$r_{j,j+1} = \frac{k_{z,j} - k_{z,j+1}}{k_{z,j} + k_{z,j+1}}\exp(-2k_{z,j}k_{z,j+1}\sigma_{j,j+1}^2) \tag{2-9}$$

with $k_{z,j}$ being the z-component of the wavevector in layer j:

$$k_{z,j} = k\sqrt{(n_j^2 - \cos^2\alpha_i)} \tag{2-10}$$

In Equation (2-10), $k = 2\pi/\lambda$, λ is the x-ray wavelength and $\sigma_{j,j+1}$ is the interface width (roughness) of the $j,j+1^{th}$ interface. Since the substrate (SiO_2) is semi-infinite, one can set $R_{N+1} = X_{N+1} = 0$. The specularly reflected intensity R is obtained using $T_1 = 1$ and from Equation (2-8) after N iterations by:

$$R = \left|X_1\right|^2 = \left|R_1\right|^2 \tag{2-11}$$

The above explained Parratt formalism is used to fit the specular reflectivity of SAMs and polymers deposited on SiO_2 as shown in this thesis. A software program (Parratt32 **[9]**) based on the Parratt formalism is used to fit these systems. In what follows, the reflectivity for a system of a single layer (SAM or polymer, see Figure 2-22) deposited on a semi-infinite substrate (e.g. SiO_2) will be solved theoretically using the above equations. As an example, we will compare the final output to the case of the specular XRR of a self-assembled monolayer (NMTS, see Figure 2-23(a)) deposited on SiO_2. The input parameters (electron density, thickness and interface widths) will be used as determined from the Parratt32 software fit to the NMTS XRR data and the output determined theoretically (using the above equations) will be compared to that from the Parratt32 software. The purpose of this exercise is to convince ourselves that we understand how the software Parratt32 fits specular XRR

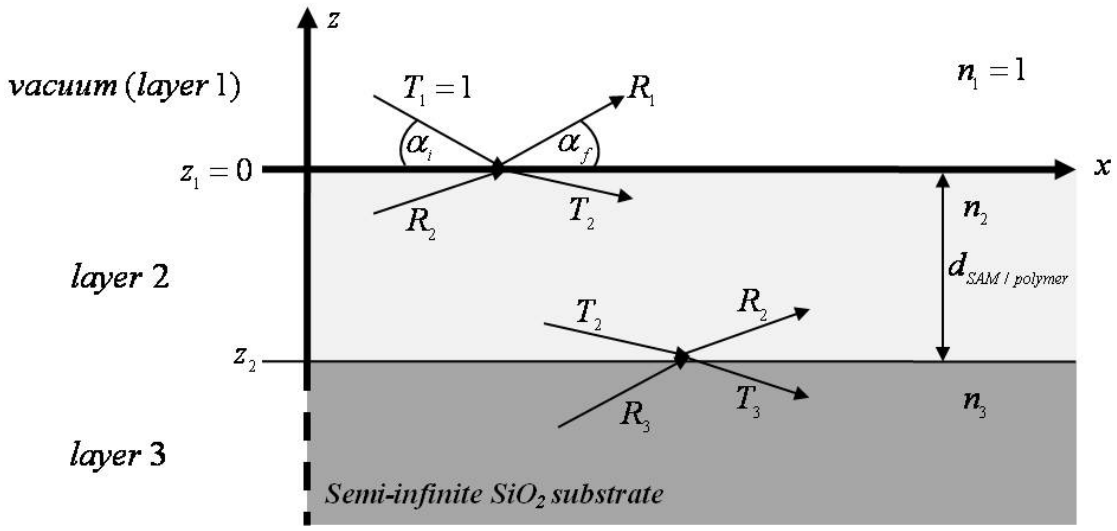

Figure 2-22 Sketch of a system consisting representing a SAM or polymer deposited on a SiO_2 substrate. This system would consist of *3* layers (vacuum, SAM or polymer and substrate) with *2* interfaces (SAM or polymer/vacuum and SiO_2/SAM or polymer). In the case of specular reflectivity, the condition $\alpha_i = \alpha_f$ holds. The incident wave amplitude is normalized to unity $T_1=1$. No wave is reflected from the substrate, i.e. $R_3=0$. This schematic follows the parameterization used for Parratt Formalism.

data. Looking at the sketch of the system shown in Figure 2-22, and using Equation (2-8), we have:

$$X_1 = \frac{R_1}{T_1} = \exp(-2ik_{z,1}z_1)\frac{r_{1,2} + X_2\exp(2ik_{z,2}z_1)}{1 + r_{1,2}X_2\exp(2ik_{z,2}z_1)}$$

$$X_2 = \frac{R_2}{T_2} = \exp(-2ik_{z,2}z_2)\frac{r_{2,3} + X_3\exp(2ik_{z,3}z_2)}{1 + r_{1,2}X_3\exp(2ik_{z,3}z_2)} \qquad (2\text{-}12)$$

Since $X_3 = 0$ because $R_3 = 0$, we have:

$$X_2 = \frac{R_2}{T_2} = \exp(-2ik_{z,2}z_2)r_{2,3} \quad \textit{and therefore}:$$

$$X_1 = \frac{R_1}{T_1} = \exp(-2ik_{z,1}z_1)\frac{r_{1,2} + r_{2,3}\exp(-2ik_{z,2}z_2)\exp(2ik_{z,2}z_1)}{1 + r_{1,2}r_{2,3}\exp(-2ik_{z,2}z_2)\exp(2ik_{z,2}z_1)}$$

$$X_1 = \frac{R_1}{T_1} = \exp(-2ik_{z,1}z_1)\frac{r_{1,2} + r_{2,3}\exp(2ik_{z,2}(z_1 - z_2))}{1 + r_{1,2}r_{2,3}\exp(2ik_{z,2}(z_1 - z_2))} \qquad (2\text{-}13)$$

$\textit{Since} \quad z_1 = 0, \textit{ and } d_{SAM/polymer} = z_1 - z_2, \textit{ we have}:$

$$X_1 = \frac{R_1}{T_1} = \frac{r_{1,2} + r_{2,3}\exp(2ik_{z,2}d_{SAM/polymer})}{1 + r_{1,2}r_{2,3}\exp(2ik_{z,2}d_{SAM/polymer})}$$

In the above, and using Equations (2-9) and (2-10), we have:

$$r_{1,2} = \frac{k_{z,1} - k_{z,2}}{k_{z,1} + k_{z,2}} \exp(-2k_{z,1}k_{z,2}\sigma_{1,2}^2)$$ Fresnel coefficient of SAM /vacuum interface

$$r_{2,3} = \frac{k_{z,2} - k_{z,3}}{k_{z,2} + k_{z,3}} \exp(-2k_{z,2}k_{z,3}\sigma_{2,3}^2)$$ Fresnel coefficient of SiO_2/SAM interface

$$k_{z,1} = k\sqrt{(n_1^2 - \cos^2\alpha_i)} = k\sqrt{(1 - \cos^2\alpha_i)}$$ z-component of wavevector in layer 1 (vacuum)

$$k_{z,2} = k\sqrt{(n_2^2 - \cos^2\alpha_i)}$$ z-component of wavevector in layer 2 (SAM or polymer)

$$k_{z,3} = k\sqrt{(n_3^2 - \cos^2\alpha_i)}$$ z-component of wavevector in layer 3 (SiO_2)

where

(2-14)

$$n_1 = n_{vacuum} = 1$$

$$n_2 = n_{SAM\ /\ polymer} = 1 - \delta_{SAM\ /\ polymer} + i\beta_{SAM\ /\ polymer}$$

$$n_3 = n_{SiO_2} = 1 - \delta_{SiO_2} + i\beta_{SiO_2}$$

$$k = \frac{2\pi}{\lambda}$$

$\sigma_{1,2} =$ Interface width (roughness) of SAM or polymer/vacuum interface

$\sigma_{2,3} =$ Interface width (roughness) of SiO_2/SAM or polymer interface

$\alpha_i =$ Incident angle

In the above, n, δ, and β are defined by Equations (2-3) and (2-4).

Finally, since $T_1=1$,

$$R = |X_1|^2 = |R_1|^2 = \left| \frac{r_{1,2} + r_{2,3} \exp(2ik_{z,2} d_{SAM\,/\,polymer})}{1 + r_{1,2} r_{2,3} \exp(2ik_{z,2} d_{SAM\,/\,polymer})} \right|^2 \tag{2-15}$$

We will now compare the theoretically predicted specular reflectivity, R, based on Equation (2-15), to that with the Parratt32 software. In Figure 2-23, we show raw XRR data for NMTS deposited on SiO_2 (open black circles) and the fit to the NMTS XRR data (solid blue line) based on the Parratt32 software. To see the quality of the fit we are only plotting 25% of the raw NMTS XRR data (1 of every 4 points). The fit to the data is excellent and the fit parameters as determined from Parratt32 software are: $p_{SiO2} = 0.671\ Å^{-3}$, $p_{NMTS} = 0.3893\ Å^{-3}$, $\sigma_{NMTS/vacuum} = 2.356\ Å$, $\sigma_{SiO2/NMTS} = 2.37\ Å$ and $d_{NMTS} = 8.13\ Å$. For the case of NMTS, fitting the imaginary part of the refractive index (β), was not necessary to get a good fit. Using these fit parameters from Parratt32 software as inputs into Equations (2-12) to (2-15), we used the above Parratt theory to predict the specular reflectivity and this is shown in Figure 2-24. As observed, the fit based on theory and Parratt32 software is identical. The properties (as determined from fitting XRR data using Parratt32 software) of the SAMs and polymers studied in this thesis are summarized in the Appendix (Table 9-2). The MATLAB code which calculates the specular reflectivity based on Parratt formalism theory can be found in the Appendix section 9.5.

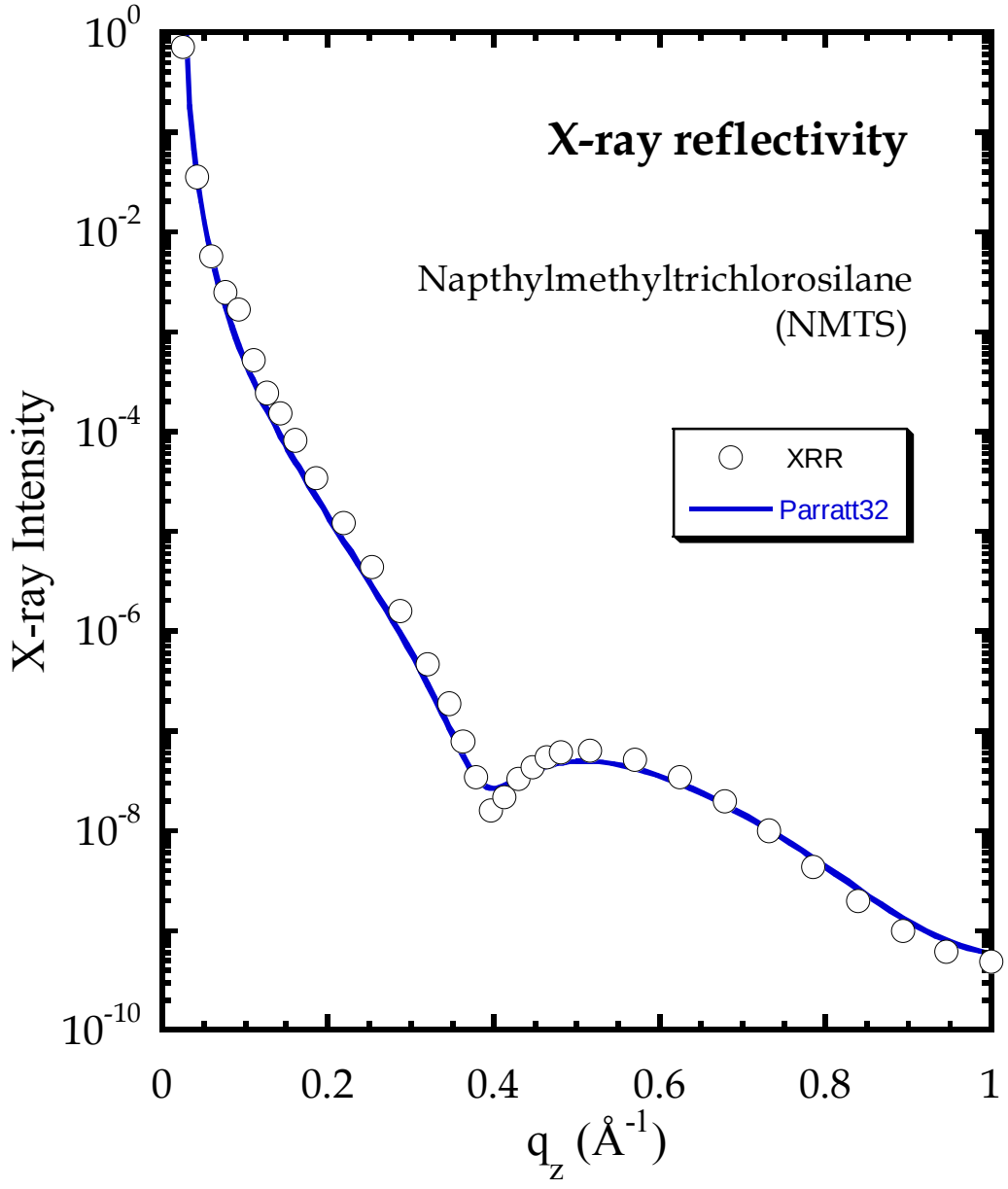

Figure 2-23 Scattered x-ray intensity (XRR) as a function of the out-of-plane scattering vector, q_z, for a monolayer of 1-napthylmethyltrichlorosilane (NMTS) on SiO_2. For clarity, only 1 of every 4 data points is plotted. The solid curve (blue) represents a fit of the data to a model based on the Parratt32 software.

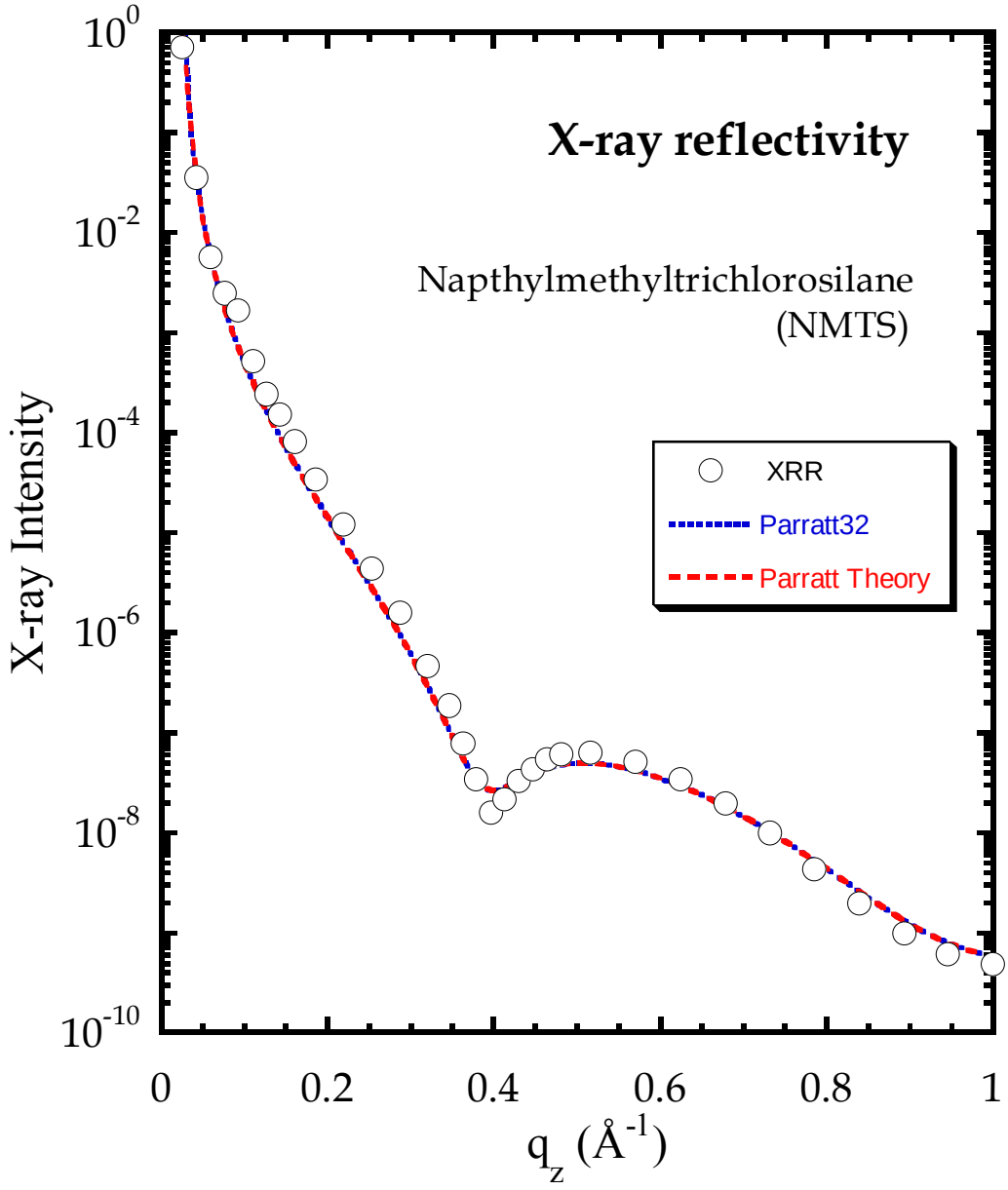

Figure 2-24 Scattered x-ray intensity (XRR) as a function of the out-of-plane scattering vector, q_z, for a monolayer of 1-napthylmethyltrichlorosilane (NMTS) on SiO_2. For clarity, only 1 of every 4 data points is plotted. The dotted curve (blue) represents a fit of the data to a model based on the Parrat32 software and dashed curve (red) represents prediction from Parratt formalism theory.

As observed from the above theory, the specular reflectivity is very sensitive to both the thickness and roughness (interface widths) of the different layers and interfaces respectively. To illustrate this, in Figure 2-25(a), we show the simulated specular reflectivity for the case of an arbitrary organic (e.g. polymer) deposited on SiO_2 at two different cases of varying film thicknesses ($d_{organic}$) – in one case, $d_{organic}$ = 25 Å whereas in the other $d_{organic}$ = 100 Å. For both cases, $p_{SiO2} = 0.671\ Å^{-3}$, $p_{organic}$ = 0.341 $Å^{-3}$, $\sigma_{organic/vacuum} = 2\ Å$, and $\sigma_{SiO2/organic} = 2\ Å$. As observed, with increasing thickness of the organic layer, the fringes ('thickness fringes') become significantly narrower. In Figure 2-25(b), we consider the effect of interface roughness, where the simulated specular reflectivity for the case of an arbitrary organic (e.g. polymer) deposited on SiO_2 at two different interface roughness's ($\sigma_{organic/vacuum}$) is shown – in one case, $\sigma_{organic/vacuum}$ = 2 Å whereas in the other $\sigma_{organic/vacuum}$ = 4 Å. For both cases, $p_{SiO2} = 0.671\ Å^{-3}$, $p_{organic}$ = 0.341 $Å^{-3}$, and $d_{organic}$ = 100 Å. As observed, with increasing roughness of the organic/vacuum interface, the thickness fringes are significantly damped. This is because, as shown in Equation (2-8), the specular intensity decreases with $exp(-\sigma^2)$. In conclusion, specular XRR is an effective technique to characterize amorphous layers of SAMs and polymers where accurate information on film thickness, electron density and interface widths can be obtained. In addition, Parratt formalism is a powerful and simple technique to fit specular XRR data. Although not studied in this thesis, the technique of Parratt formalism can also be applied to fit specular XRR data of crystalline organic thin films, e.g. pentacene, DIP, PFP and PTCDI-C_{13} (see e.g. Figure 2-20(b-c)).

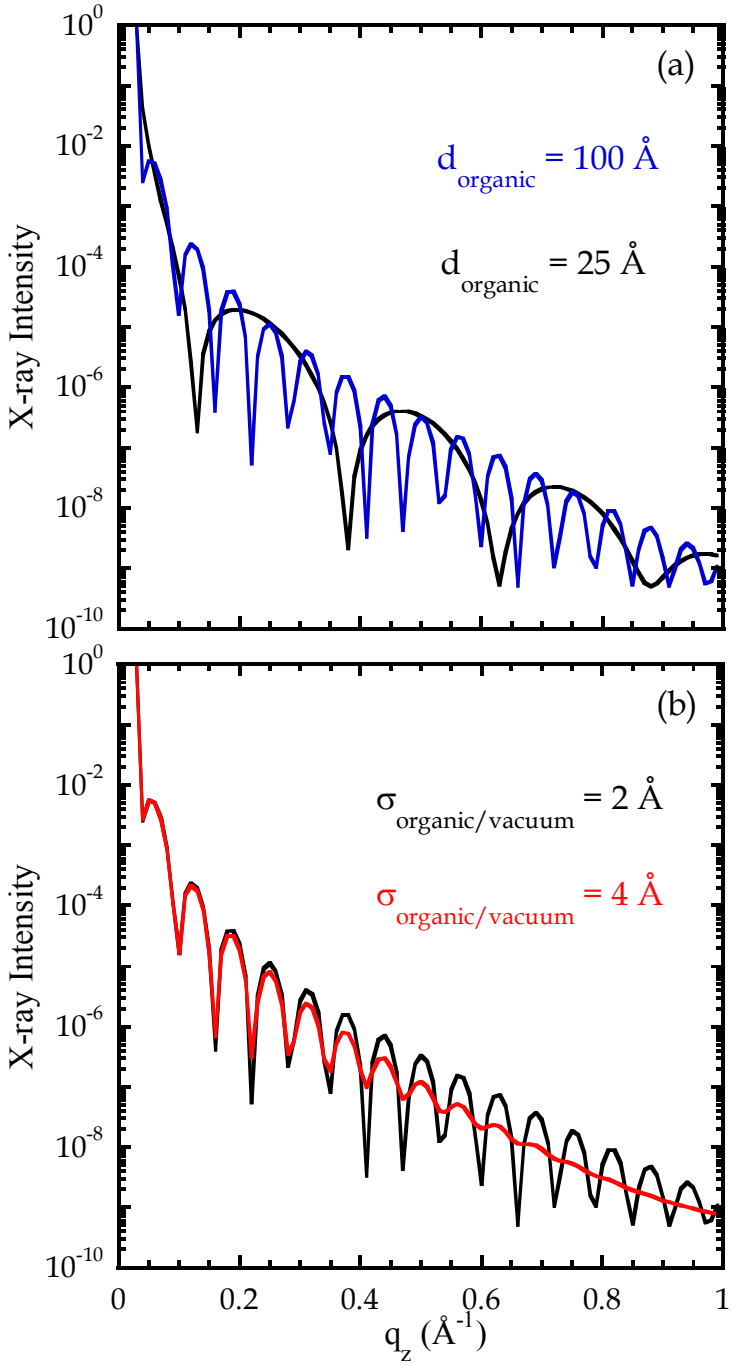

Figure 2-25 (a) Specular XRR of an arbitrary organic layer ($p_{organic}$ = 0.341 $Å^{-3}$) on SiO_2 at two different thicknesses and at (b) at two different organic/vacuum interface widths.

2.5.4 *In situ* real-time x-ray scattering at the anti-Bragg

To monitor the time resolved growth of organic semiconductors (pentacene, DIP, PFP and PTCDI-C_{13}) on different substrates (SiO_2, SAMs and polymers), *in situ* real-time x-ray scattering at the anti-Bragg position was used. *In situ* real-time x-ray scattering at the anti-Bragg position is an effective monitor of the nature of growth, *i.e.*, layer-by-layer (LbL) vs. 3D islanded growth **[10]**. Using this technique, one can extract precise information regarding film growth rate, evolution of individual monolayers, and film roughness. The general procedure that was followed in this thesis: first, x-ray scattering data is measured at CHESS which describes time resolved organic thin film growth and second, the x-ray data is fit using a model to extract the film growth rate, evolution of individual monolayers, and film roughness. In this section, the theory behind x-ray scattering at the anti-Bragg position and its modeling is discussed briefly. Unlike Parratt formalism which takes into account multiple scattering, the x-ray theory described here assumes kinematic approximation (single scattering). This is fair assumption as the time resolved growth experiments are conducted far from both the critical angle for total external reflection and the organic crystal Bragg peak. This section is meant to be a brief and concise description to enable the reader to better understand results presented in sections 3-7. For details, please refer to the following references: **[10-12]**, and in particular reference **[11]**.

In the kinematic approximation, the scattered intensity as a function of time, *I(t)*, that is measured during *in situ* real-time thin film growth at a fixed position q_z

(where q_z is the out-of-plane wavevector transfer, see Figure 2-20(a)) in reciprocal space is given by:

$$I(t) = \left| r_{subs} e^{-i\phi} + r_{film} \sum_{n=1}^{\infty} \theta_n(t) e^{-iq_z dn} \right|^2 \tag{2-16}$$

where r_{subs} and r_{film} are the scattering amplitudes of the substrate and the film, ϕ is the phase change upon reflection, d is the out-of-plane interplanar spacing (same as d_{001} described above in section 2.5.2) and $\theta_n(t)$ is the coverages of individual growing monolayers as a function of time. At the anti-Bragg position, $q_z d = \pi$, which results in a change in the sign of the thin film terms in the summation with the filling of each successive growing monolayer layer or:

$$I(t) = \left| r_{subs} e^{-i\phi} + r_{film} \sum_{n=1}^{\infty} \theta_n(t)(-1)^n \right|^2 \tag{2-17}$$

Parameters r_{subs} and r_{film} and ϕ are x-ray scattering parameters and are proportional to the electron density of the starting substrate (e.g. SiO_2), electron density of the growing film (e.g. pentacene), electron density of any interfacial layer (e.g. SAM or polymer) and thickness of any interfacial layer (e.g SAM or polymer) **[11]**. As will be seen in sections 3–7, the shape of the anti-Bragg oscillations is sensitive to the nature of the starting surface. Depending on the starting surface, there will be differences in the relative intensities at $t = 0$, at the peak of the first oscillation (~ 1 ML coverage) and for the "saturation" intensity, $t \rightarrow \infty$. These are readily understood as

manifestations of differences in the phase (ϕ) and scattering amplitudes (r_{subs} and r_{film}) **[11]**.

The coverages of individual growing monolayers as a function of time, $\theta_n(t)$, are modeled using a modified version **[11]** of a mean field model first described by Cohen et al. **[12]**:

$$\frac{d\theta_n}{dt} = S_{n-1}F\left[\left(\theta_{n-1} - \theta_n\right) - \alpha_{n-1}\left(\theta_{n-1} - \theta_n\right)\right] + S_n F \alpha_n \left(\theta_n - \theta_{n+1}\right) \qquad (2\text{-}18)$$

where n = 0 represents the substrate, n = 1 the first molecular layer, etc., S_n is the probability of adsorption for molecules incident on the n^{th} layer, F is the incident molecular flux (ML-s^{-1}), and α_n is the probability of downward interlayer transport. The terms in Equation (2-18) are described pictorially in Figure 2-26(a). The first term in Equation (2-18), describes the rate at which molecules adsorb on the nth layer – this will be proportional to product of S_nF (or the film growth rate in MLs^{-1}) and the exposed area of the n^{th} layer: $\theta_{n-1} - \theta_n$. The second term describes the fraction of those molecules from the first term that initially land on the n^{th} layer but rather than staying on that layer, drop down to layer *n-1* via some mechanism, where α_{n-1} is the probability of downward interlayer transport into layer *n-1*. Similarly, the final term describe the fraction of molecules that initially land on top of the n^{th} layer (or on layer *n+1*) but rather than staying on layer *n+1*, dropped down to layer *n* via some mechanism, where α_n is the probability of interlayer transport into the n^{th} layer.

(a)

$$\frac{d\theta_n}{dt} = S_{n-1}F\left[(\theta_{n-1} - \theta_n) - \alpha_{n-1}(\theta_{n-1} - \theta_n)\right] + S_nF\alpha_n(\theta_n - \theta_{n+1})$$

(3) $S_nF\alpha_n(\theta_n - \theta_{n+1})$

(1) $S_{n-1}F\left[(\theta_{n-1} - \theta_n)\right]$

(2) $S_{n-1}F\left[\alpha_{n-1}(\theta_{n-1} - \theta_n)\right]$

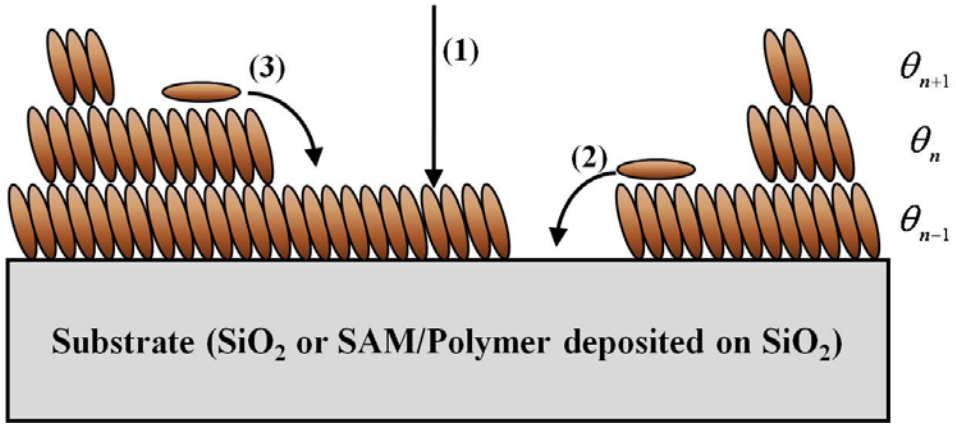

(b)

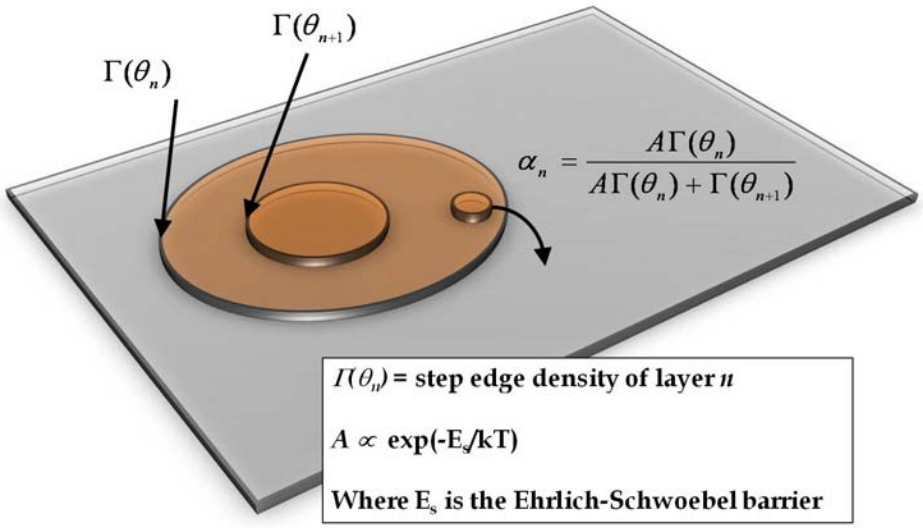

Figure 2-26 (a) Cartoon describing the terms of the growth model showing in Equation (2-18). (b) Cartoon describing the probability of downward interlayer transport parameter α being a function of step edge density $\Gamma(\theta)$.

The probability of interlayer transport, α, is proportional to the step edge density, $\Gamma(\theta)$, as shown in Figure 2-26(b) **[11]**. Details regarding the mathematical forms of $\Gamma(\theta)$ can be found in reference **[11]**. The parameters S_nF and α implicitly represent all of the kinetic processes involving molecular attachment and transport respectively. In this model we also assume that there are two values for the probability of adsorption: one for adsorption on the substrate (S_0), and one for that on previously existing molecular layers, independent of their thickness ($S_1 = S_2 = S_3\ldots$). Concerning interlayer transport, we will assume that three values are possible (note, as the substrate cannot be penetrated, $\alpha_0 = 0$), namely α_1, α_2 and $\alpha_{n \geq 3}$. "Upward" interlayer transport (movement from the n^{th} to the $n + 1$ layer) is not included in the model.

Once the layers coverages, $\theta_n(t)$, are calculated using Equation (2-18), they can then be inputted into Equation (2-17), to determine the specular reflected intensity, $I(t)$, at the anti-Bragg position. In general, $I(t)$ is measured experimentally at CHESS (at the anti-Bragg position) and is then fit using Equations (2-18) and (2-17) to extract the desirable growth parameters: film growth rate and converges of individual monolayers. The root-mean-squared (RMS) roughness (r) evolution of the film as a function of time can then be easily predicted using the coverages of individual monolayers through Equation (2-19):

$$r(t)^2 = \sum_n n^2 \theta_E(n) - \left[\sum_n n\,\theta_E(n) \right]^2$$

$$where\ \theta_E(n)\ is: \qquad (2\text{-}19)$$

$$\theta_E(n) = \theta_n(t) - \theta_{n+1}(t)$$

As a case example, let's consider the growth of an organic semiconductor with a density of 1.3 g/cm^3 deposited on SiO_2 (density of 2.2 g/cm^3). For this case, let's also assume that there is no interfacial layer (SAM or polymer) present. In Figure 2-27, simulations of the expected scattered intensity, *I(t)*, at the anti-Bragg position is shown along with the coverages of the individual monolayers $\theta_n(t)$. In Figures 2-27(a) and 2-27(b), *I(t)* and $\theta_n(t)$ are shown respectively for the case of perfect 2D or layer-by-layer (LbL) growth – that is, there is infinite downward interlayer transport and therefore each layer fills up completely before the subsequent layer grows. In Figures 2-27(c) and 2-27(d), *I(t)* and $\theta_n(t)$ are shown respectively for the case of perfect 3D growth – that is, there is no downward interlayer transport. For the case of perfect LbL growth, we see that *I(t)* oscillates with a period of 1 ML per oscillation and the oscillations do not damp, whereas for the case of prefect 3D growth, *I(t)* decays exponentially since the film is roughening up rapidly. Clear differences are also observed in $\theta_n(t)$ for both cases – for perfect LbL growth, each monolayer completes before the subsequent layer grows, whereas for perfect 3D growth, multiple layers are growing at the same time. In Figures 2-28(a) and 2-28(b), *I(t)* and $\theta_n(t)$ are shown respectively for the case of near-2D growth – that is, there is downward interlayer transport but not infinite, and the film is roughening up slowly. In Figures 2-28(c) and 2-28(d), *I(t)* and $\theta_n(t)$ are shown respectively for the case of near-3D growth – that is, the film grows LbL for ~1-2 MLs after which it beings to roughen up significantly.

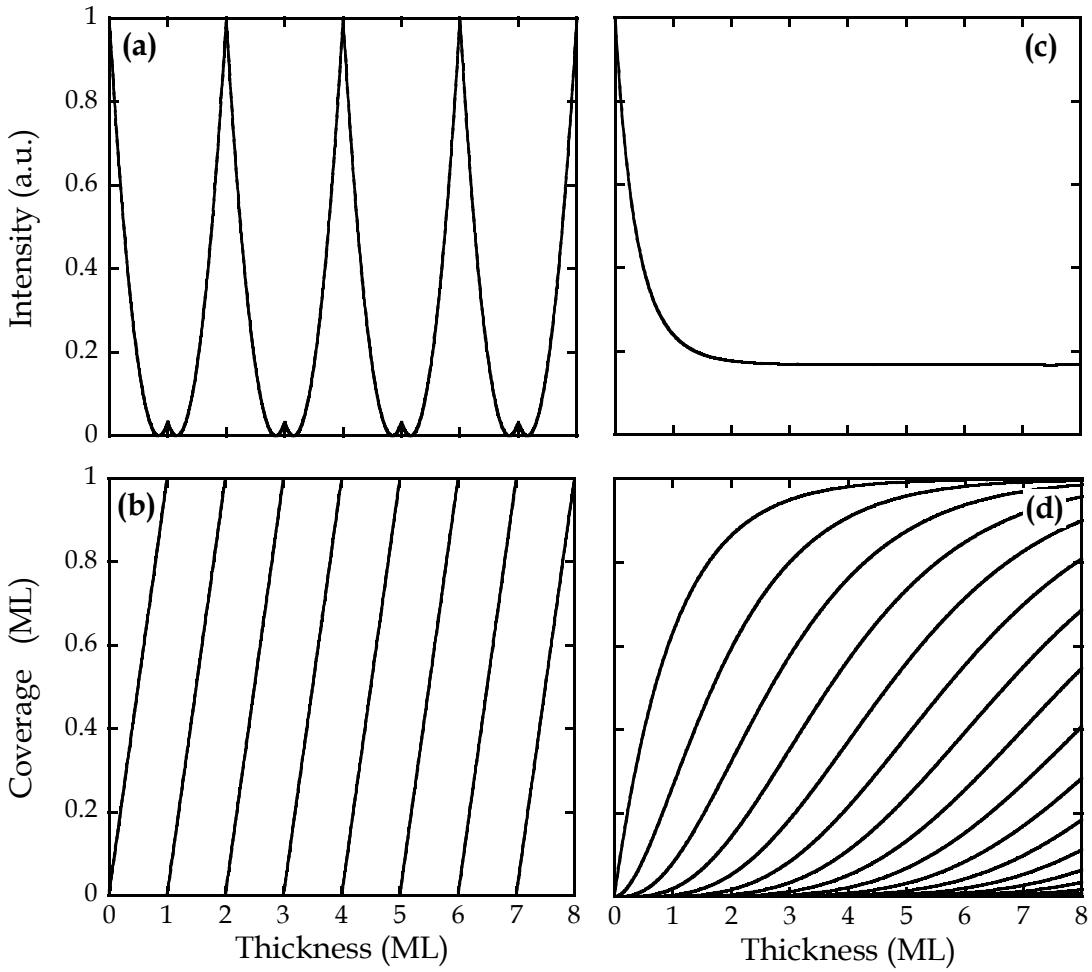

Figure 2-27 X-ray scattering at the anti-Bragg position, *I(t)*, as a function of thickness of the thin film for the case of (a) perfect 2D or LbL growth and (c) perfect 3D growth. Coverages of individual monolayers, *θ(t)*, as a function of thickness of the thin film for the case of (b) perfect 2D or LbL growth and (d) perfect 3D growth.

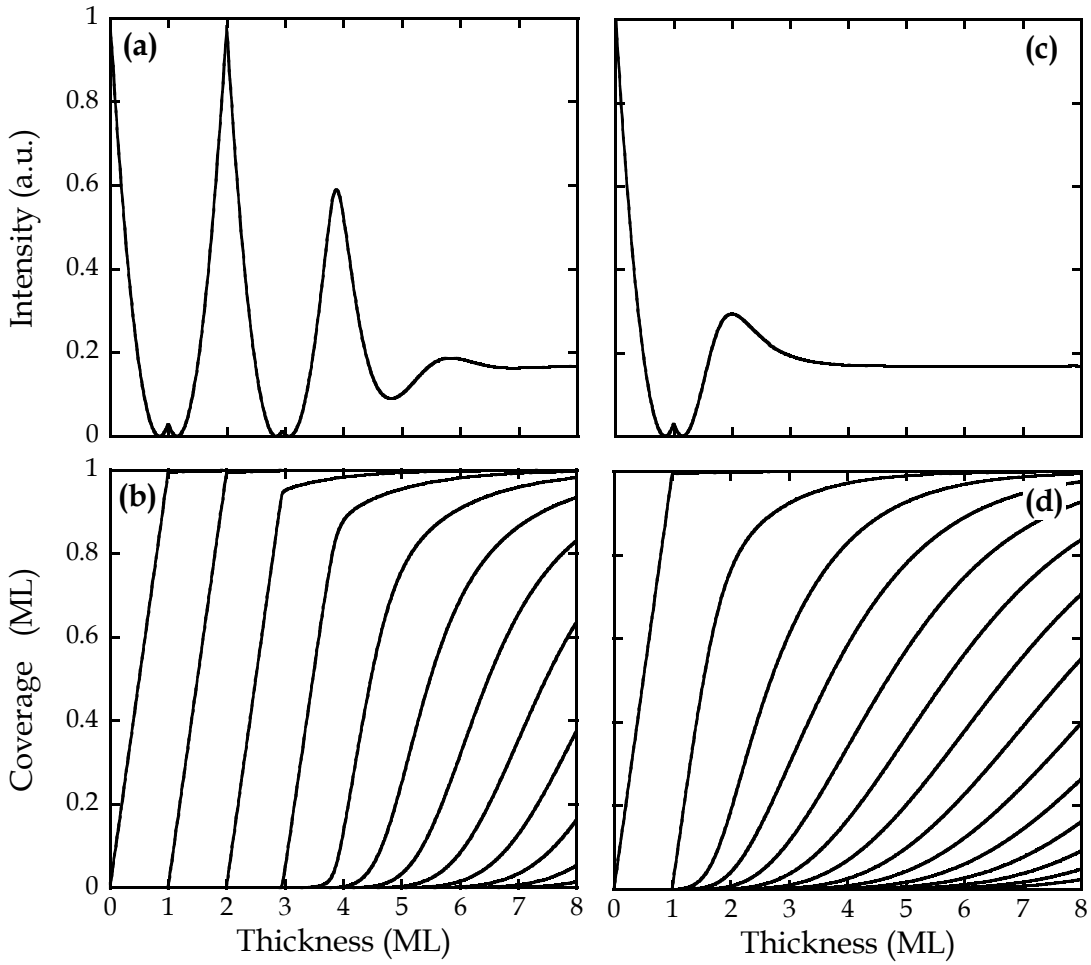

Figure 2-28 X-ray scattering at the anti-Bragg position, *I(t)*, as a function of thickness of the thin film for the case of (a) near-2D growth and (c) near-3D growth. Coverages of individual monolayers, $\theta(t)$, as a function of thickness of the thin film for the case of (b) near-2D growth and (d) near-3D growth.

The roughness evolution as a function of film thickness for all 4 growth cases discussed above (perfect LbL, perfect 3D, near-2D and near-3D) is calculated using Equation (2-19), and is shown in Figure 2-29. As expected for perfect LbL growth, we see that the roughness oscillates with a period of 1 ML and the maximum in film roughness (½ ML) occurs at coverages of n + ½ MLs. On the other extreme, as expected for prefect 3D growth, the roughness exhibits Poisson statistics where the roughness increases as $\sqrt{\theta}$. The cases of near-2D growth and near-3D growth as expected lie in between the two extremes of perfect LbL growth and perfect 3D growth.

With any model, as the one discussed above, it is important to corroborate whether the model accurately captures and predicts experimental observations. In what follows, examples will be discussed where the model was tested to experimental results of both pentacene and DIP thin film deposition on SiO_2 **[11]**. For both cases, different films were deposited on the same SiO_2 substrate at identical deposition conditions and for varying growth times (or film thicknesses) and were monitored *in situ* and in real-time at the anti-Bragg position. The x-ray data was then fit using the above growth model and the results were compared to that measured using atomic force microscopy (AFM):

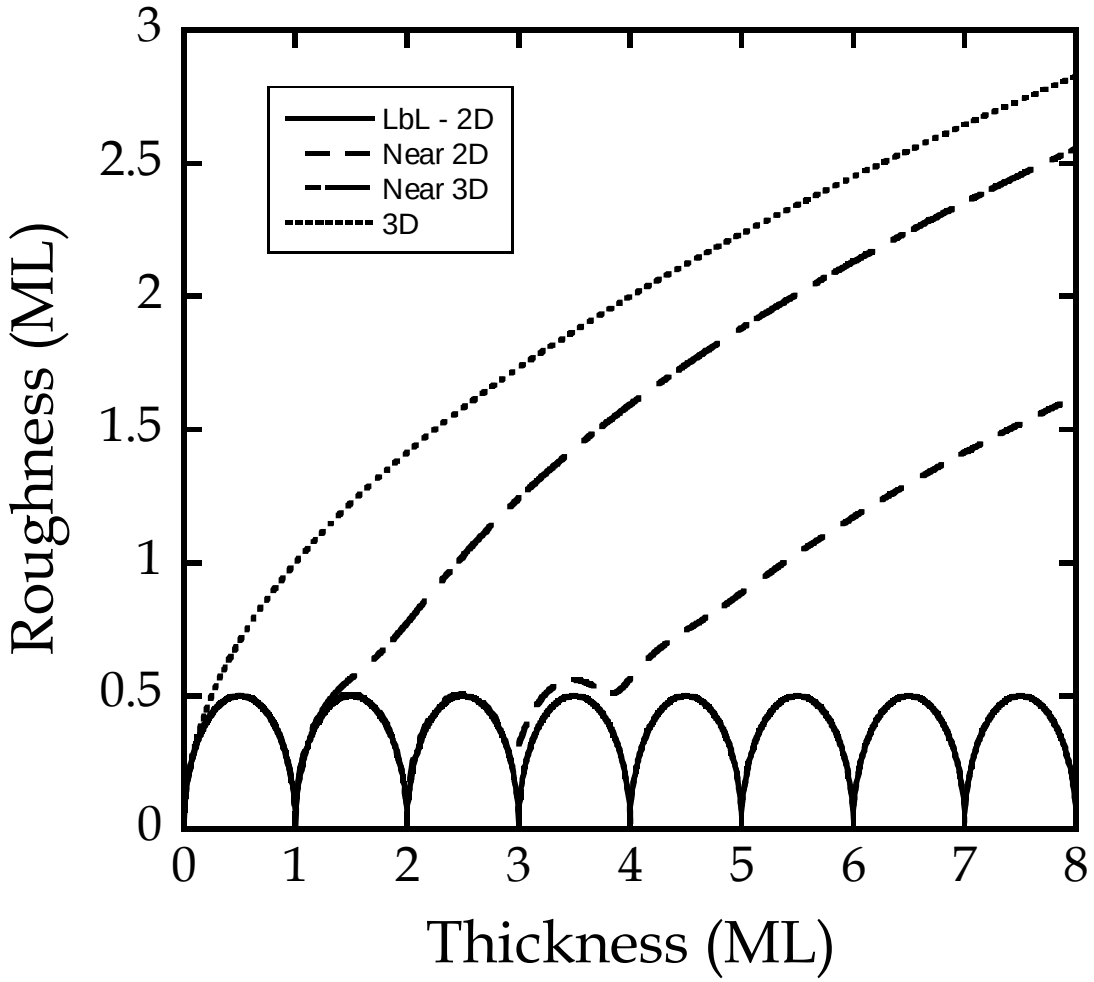

Figure 2-29 Roughness evolution of organic thin film as a function of film thickness for the case of perfect LbL growth or 2D growth (solid line), near-2D growth (dashed line), near-3D growth (small dash/big dash line) and perfect 3D growth (dotted line).

Pentacene/SiO_2

In Figure 2-30, AF micrographs (20×20 μm^2) of four pentacene films are shown of varying thicknesses deposited on SiO_2 at an incident energy (E_i) of 2.5 eV and at a substrate temperature (T_s) of 60 °C. In Figure 2-31(a) the *in situ* scattered x-ray intensity, *I(t)*, acquired in real-time at the anti-Bragg position (q_z = 00½) is shown for the growth of pentacene on SiO_2 for the thickest film (~ 4.4 ML: *cf.* Figure 2-30(d)). As may be seen, we observe, in sequence, a first small maximum (~ 1 ML), a larger maximum (~ 2 ML), a totally obscured second smaller maximum, and a strongly damped second larger maximum (~ 4 ML) after which the growth was terminated. Thus, for these conditions we see that pentacene grows in a layer-by-layer (LbL) mode until at least ~ 4 MLs. The intensity oscillation is fitted using Equations (2-18) and (2-17) – the fit to the intensity is indicated by the solid blue line, and we see that the fit to the experimental data is excellent. In Figure 2-31(a) the coverage ($\theta(t)$) of each layer is also shown with solid black lines that are predicted by the fit to the x-ray intensity oscillations. To fit the data, we had to assume a constant growth rate of $SF \sim 0.0081$ MLs^{-1}. In Figure 2-31(b), the roughness evolution of the film (calculated using Equation (2-19)) is shown. Also shown as individual points in Figure 2-31(b) is the RMS roughness obtained from AFM for the 4 images shown in Figure 2-30 – we see that the corroboration of the RMS roughness as predicted from the growth model and as measured from AFM is excellent.

In Figure 2-32, height distributions obtained from the AFM images shown in Figure 2-30 as well as those predicted by the fit to the x-ray data for all 4 individual

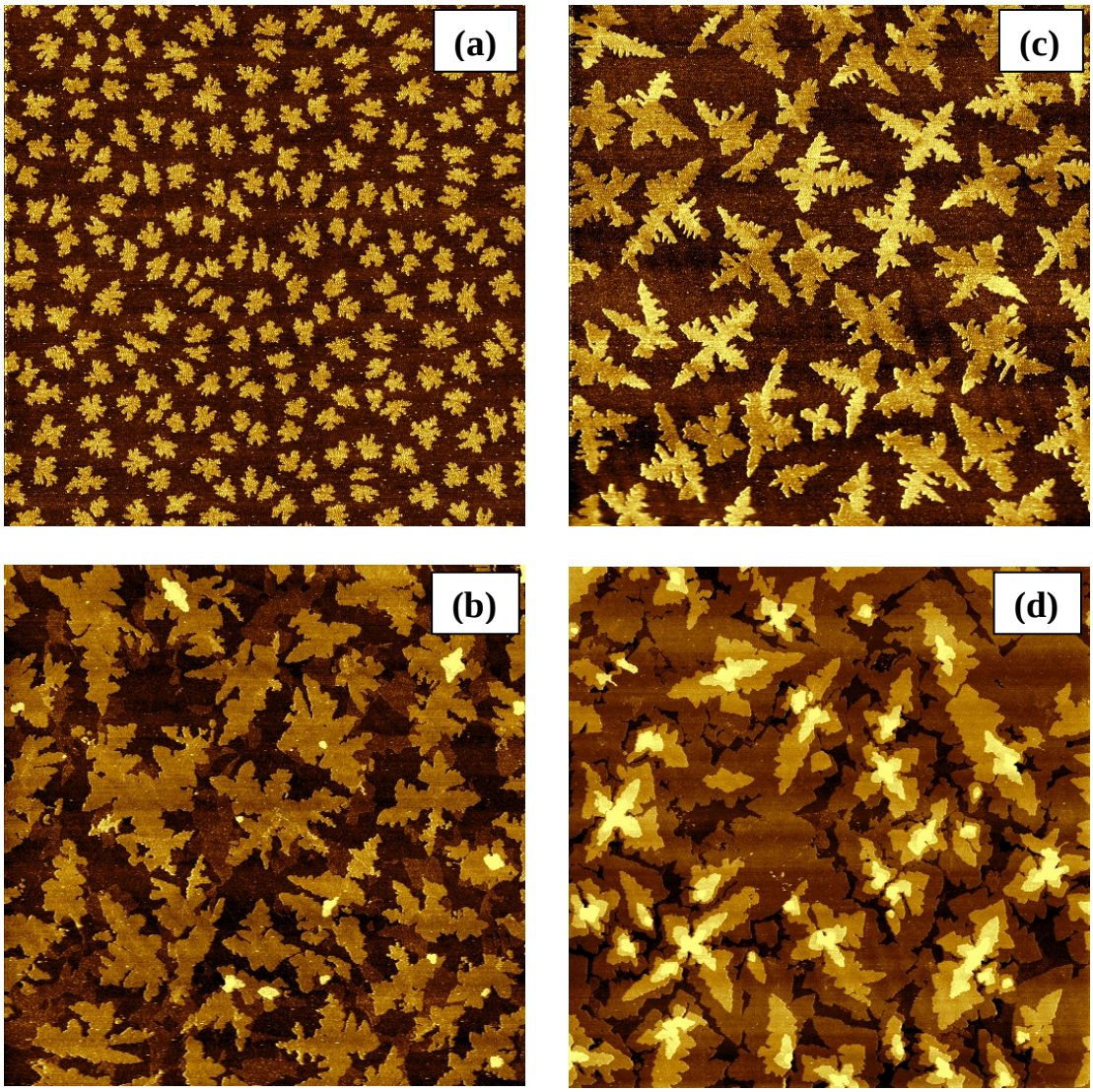

Figure 2-30 AFM images ($20 \times 20\mu m^2$) of pentacene films deposited on SiO_2 at E_i = 2.5 eV, T_s = 60 °C and at coverages of (a) 0.34 ML (b) 1.4 ML (c) 2.5 ML and (d) 4.4 ML.

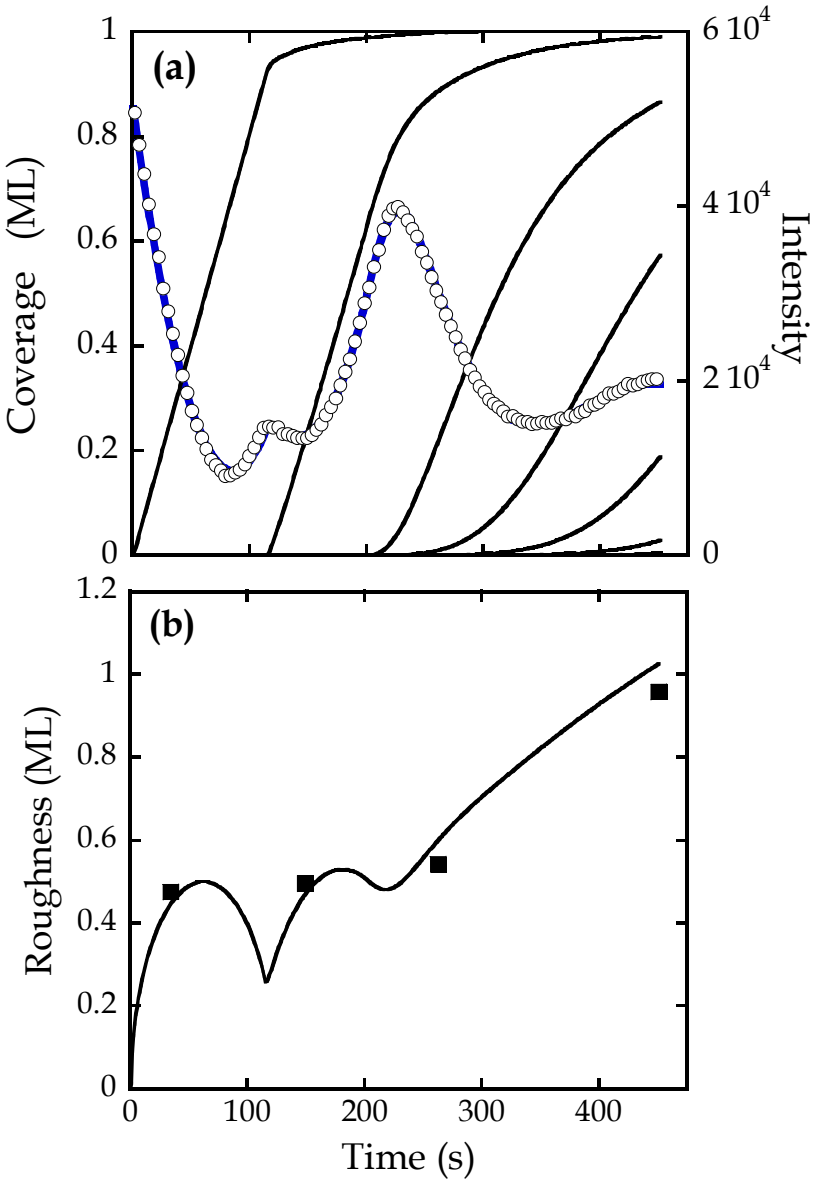

Figure 2-31 (a) X-ray intensity at the anti-Bragg condition as a function of exposure to the molecular beam (E_i = 2.5 eV) for thin film of pentacene deposited on clean SiO_2. T_s = 40 °C. Thick solid line (right ordinate) indicate a fit of the data to a model and thin solid curves (left ordinate) represent predicted coverages (θ_n) of the individual layers. (b) Thin film roughness of pentacene as a function of pentacene thickness as predicted by the fit to the x-ray data and comparing to AFM measurements (*cf.* Figure2-30).

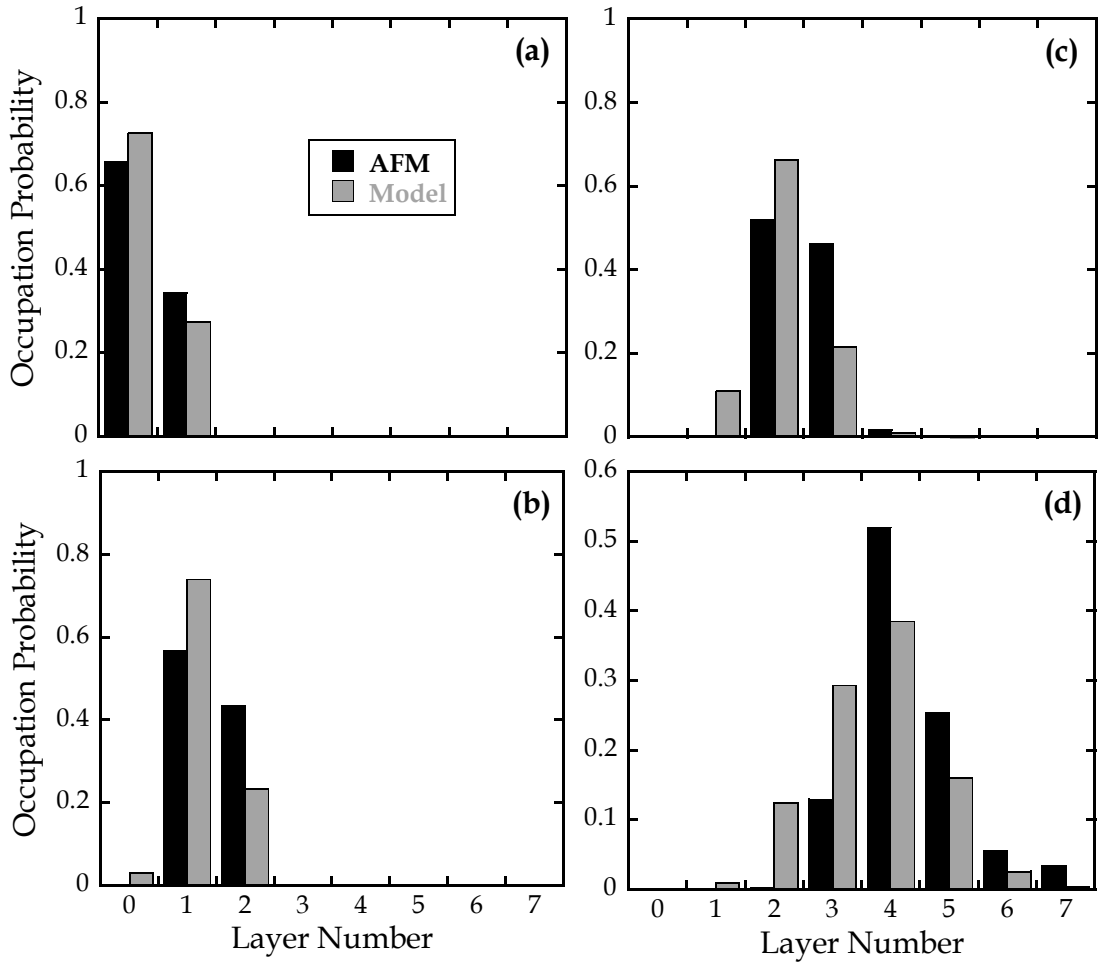

Figure 2-32 Height distribution obtained from AFM images in Figure 2-30 and from fits to x-ray scattering data for all four pentacene thin films. Pentacene thin film thicknesses of (a) 0.34 ML (b) 1.4 ML (c) 2.5 ML and (d) 4.4 ML.

films/experiments are shown. It is clear from Figures 2-31 and 2-32, that the growth model accurately captures and predicts the main features of pentacene thin film growth on SiO_2 – namely the film growth rate, coverages of individual monolayers and film roughness evolution.

DIP/SiO_2

In Figure 2-33, AF micrographs (10×10 μm^2) of four DIP thin films are shown of varying thicknesses deposited on SiO_2 at E_i = 4.2 eV and T_s = 89 °C. In Figure 2-34(a) the *in situ* scattered x-ray intensity, *I(t)*, acquired in real-time at the anti-Bragg position (q_z = 00½) is shown for the growth of DIP on SiO_2 for the thickest film (~ 11.16 ML: *cf.* Figure 2-33(d)) – the plot is only showing data until oscillations persisted. As may be seen, we observe oscillations up to ~ 5 MLs after which the intensity remains constant implying the film grew LbL for ~ 5 ML after which rapid 3D growth commenced. The intensity oscillation is fit using Equations (2-18) and (2-17) – the fit to the intensity is indicated by the solid blue line, and we see that the fit to the experimental data is excellent. In Figure 2-34(a) the coverage ($\theta(t)$) of each layer is also shown with solid black lines that are predicted by the fit to the x-ray intensity oscillations. To fit the data, we had to assume that S_0F ~ 0.0069 ML-s^{-1}, whereas $S_{n\geq 1}F$ ~ 0.0151 ML-s^{-1}. These data imply that the rate of growth has accelerated with increasing DIP coverage indicating an increase in the adsorption probability *S* with increasing coverage. In this case the adsorption probability has increased by about 112%. In fact, using the film thickness versus time data obtained from AFM

measurements, one can also calculate a similar increase in the adsorption probability of 111% **[11]**. Therefore, we have excellent agreement between two independent techniques: namely AFM and *in situ* real-time x-ray scattering. In Figure 2-34(b), the roughness evolution of the film (calculated using Equation (2-19)) is shown. Also shown as individual points in Figure 2-34(b) is the RMS roughness obtained from AFM for the 3 (excluding 11.16 MLs) images shown in Figure 2-33 – we see that the corroboration of the RMS roughness as predicted from the growth model and as measured from AFM is excellent at early growth times. At a coverage of 11.16 MLs, a ~30% difference was observed in the RMS roughness between the two different techniques, with the growth model predicting the higher film roughness.

In Figure 2-35, height distributions obtained from the AFM images shown in Figure 2-33 as well as those predicted by the fit to the x-ray data for all four individual films/experiments are shown. There is excellent agreement between the two different techniques at early growth times (≤ 4.17 ML) but not so much at 11.16 MLs. However, it is clear from Figures 2-34 and 2-35, that the growth model accurately captures and predicts the main features of DIP thin film growth on SiO_2 – namely the film growth rate, coverages of individual monolayers and film roughness, especially at early growth times. The discrepancy at late growth times is probably due to the fact that the intensity remains constant in that regime which makes it difficult to extract meaningful observations from the fit to the data.

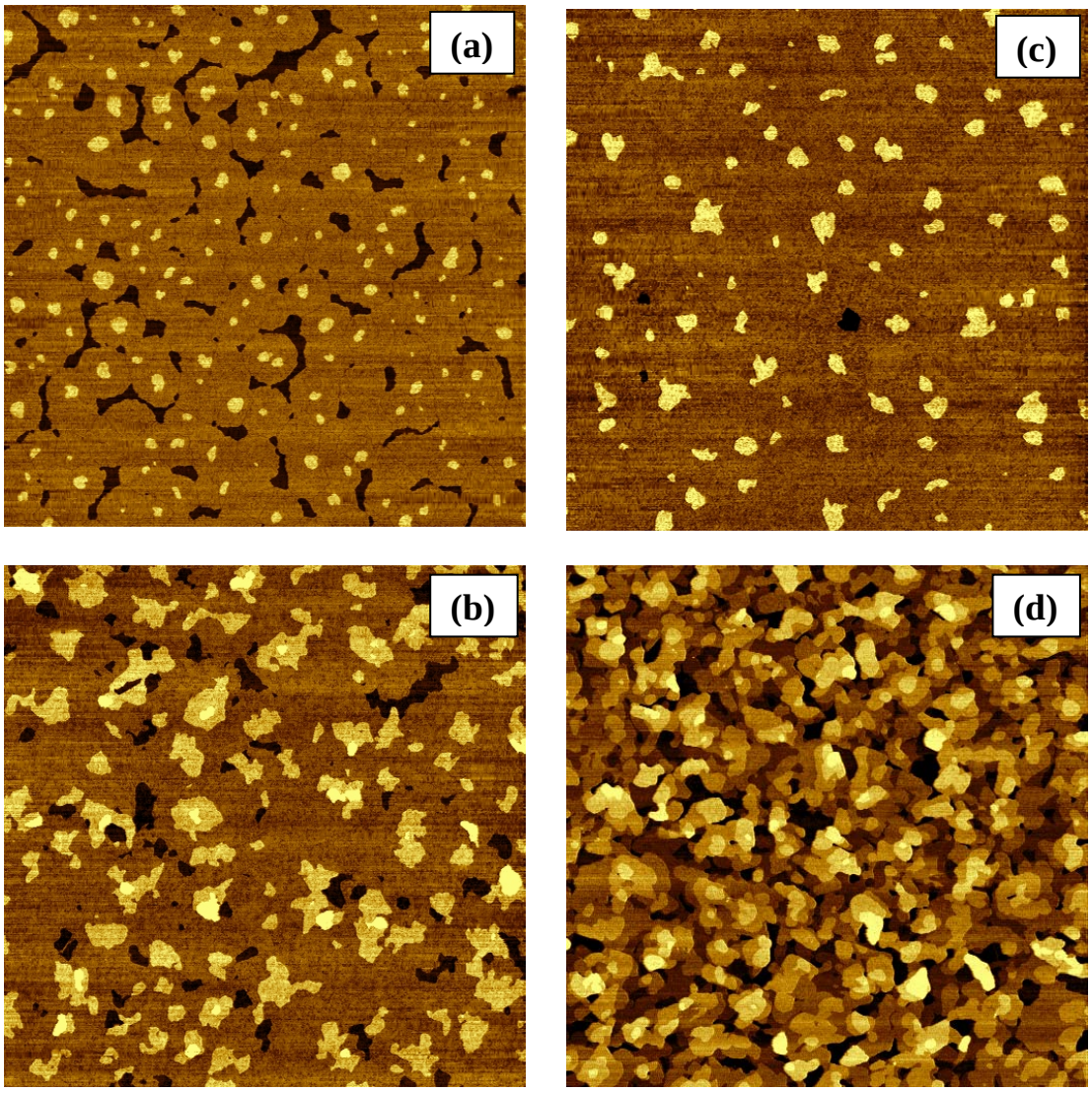

Figure 2-33 AFM images ($10 \times 10\mu m^2$) of DIP films deposited on SiO_2 at E_i = 4.2 eV, T_s = 89 °C and at coverages of (a) 0.97 ML (b) 2.06 ML (c) 4.17 ML and (d) 11.16 ML.

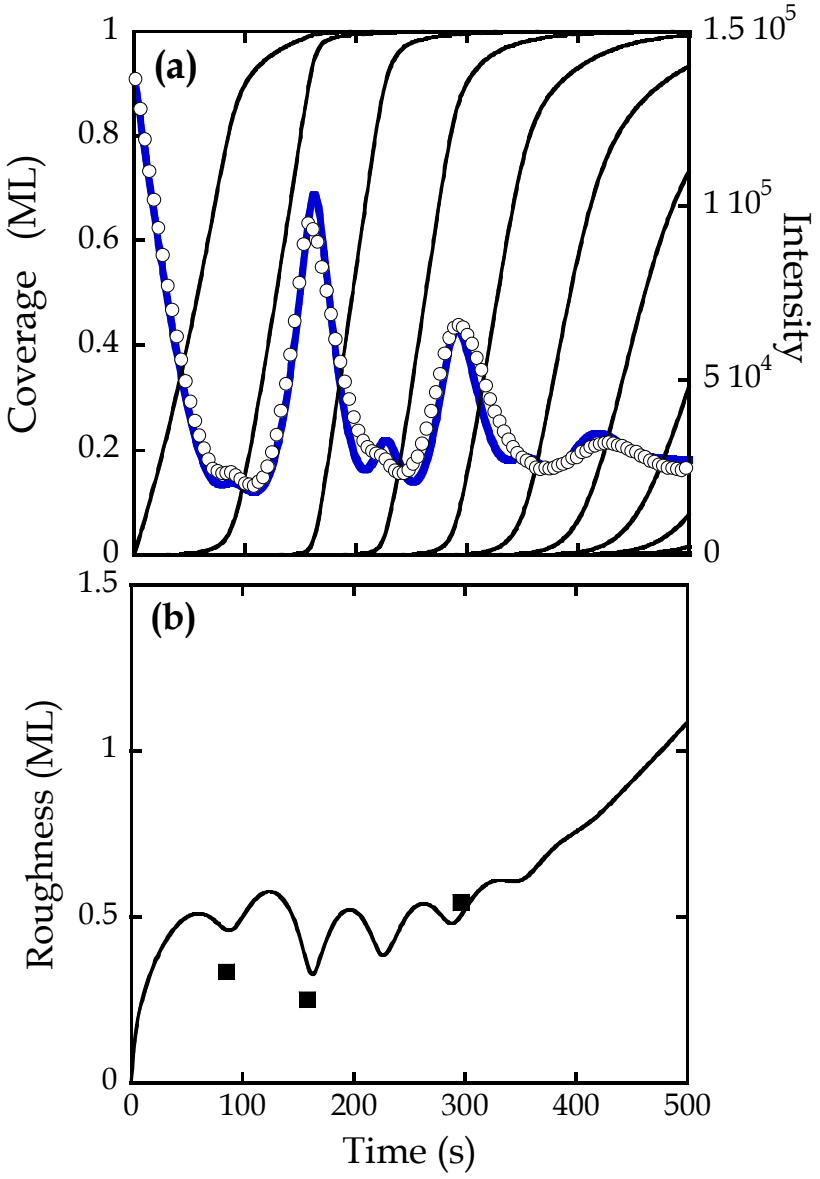

Figure 2-34 (a) X-ray intensity at the anti-Bragg condition as a function of exposure to the molecular beam (E_i = 4.2 eV) for thin film of DIP deposited on clean SiO_2. T_s = 89 °C. Thick solid line (right ordinate) indicate a fit of the data to a model and thin solid curves (left ordinate) represent predicted coverages (θ_n) of the individual layers. (b) Thin film roughness of DIP as a function of DIP thickness as predicted by the fit to the x-ray data (solid line) and compared to AFM (squares) measurements (*cf.* Figure 2-33).

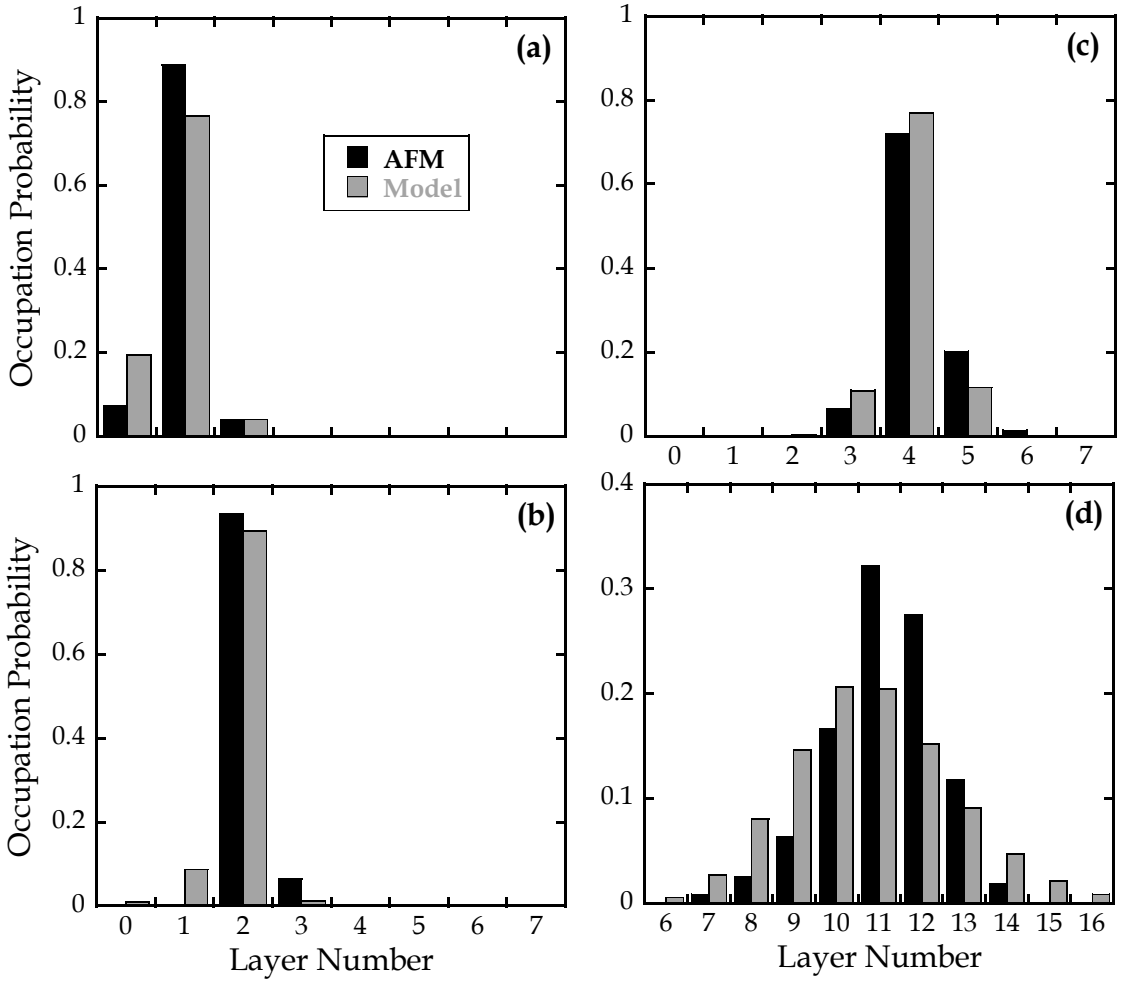

Figure 2-35 Height distribution obtained from AFM images in Figure 2-33 and from fits to x-ray scattering data for all four DIP thin films. DIP thin film thicknesses of (a) 0.97 ML (b) 2.06 ML (c) 4.17 ML and (d) 11.16 ML.

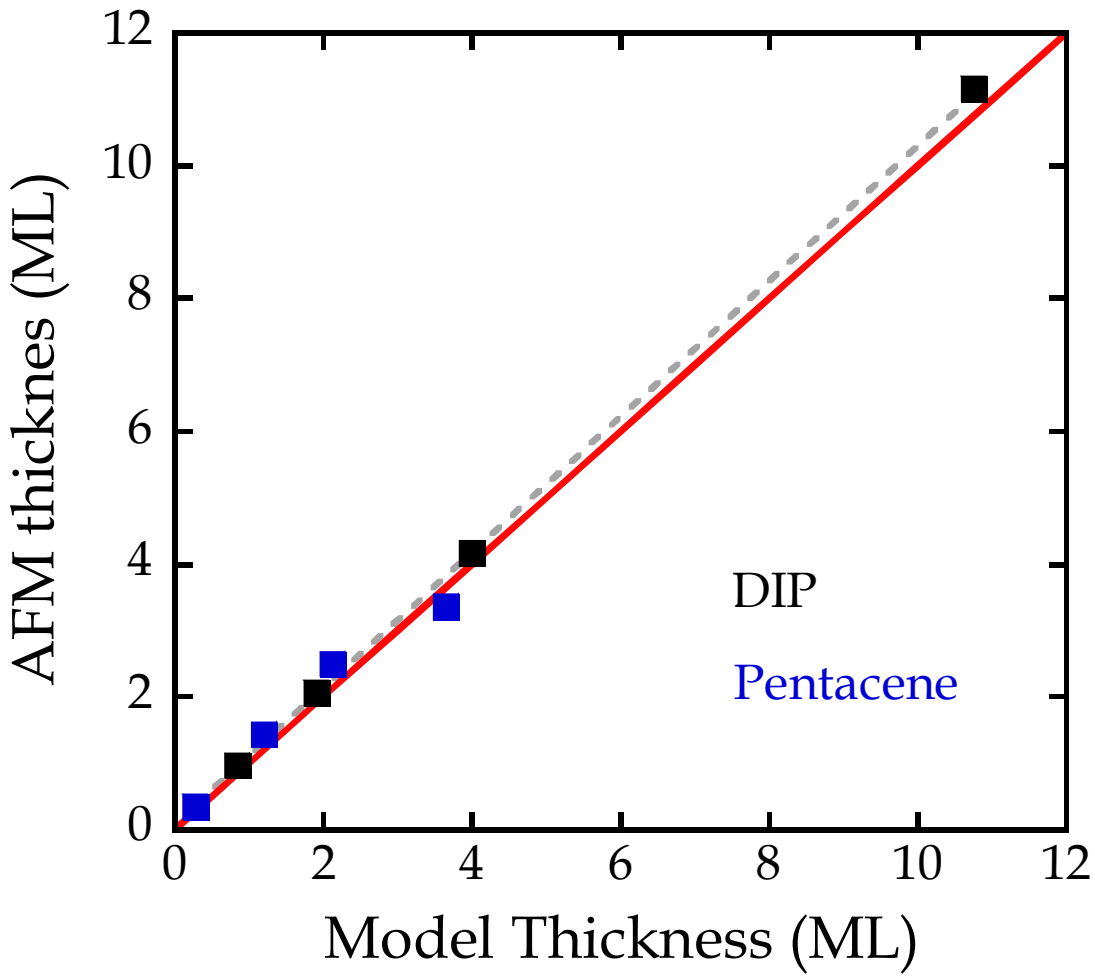

Figure 2-36 Comparison of thin film thickness as measured from AFM and to that predicted by the fits to the x-ray scattering data for both cases of pentacene/SiO_2 (blue squares) and DIP/SiO_2 (black squares). Dashed gray line is a fit to both sets of data: $y = 1.0208x + 0.09008$. The solid red line is a line of slope = 1.

In Figure 2-36, the film thickness as measured from AFM is compared to the film thickness as predicted by the fit to the x-ray scattering data for both the cases discussed above – namely pentacene/SiO_2 (blue points) and DIP/SiO_2 (black points). Also shown is a linear fit to both the data sets (dashed gray line) and a red line of *slope = 1*. Using the linear fit to the data, the thickness as predicted from AFM is ~2.1% greater than the thickness as predicted from the fit to the x-ray data. Hence, there is excellent agreement between the two independent techniques, giving confidence in the accuracy of our growth model.

In conclusion, we have shown that *in situ* real-time x-ray scattering at the anti-Bragg position is a powerful and an effective technique for studying thin film growth phenomena as it will provide direct information concerning the nature of film growth (e.g. LbL vs. 3D). In addition, using experimental cases for pentacene and DIP thin film growth on SiO_2, we have shown that we can accurately model the *in situ* real-time x-ray scattering data and extract desirable growth parameters such as the film growth rate, and coverages of individual monolayers. Using the coverages of the individual monolayers, the roughness evolution of the film can also accurately be predicted.

2.6 References

1. Killampalli, A. S. *Cornell University: Ph.D. Thesis* **2006**.
2. Schroeder, T. W. *Cornell University: Ph.D. Thesis* **2004**.
3. Barabási, A.-L.; Stanley, H. E., Eds. *Fractal Concepts in Surface Growth* (Cambridge University Press: Cambridge, U.K., **1995**)
4. Zhao, Y.; Wang, G.-C.; Lu, T.-M. *Characterization of amorphous and crystalline rough surface: principles and applications* (Academic Press, Vol. 37, **2001**).
5. Kaelble, D. H. *J. Appl. Polym. Sci.* **1974**, *18*, 1869-1889.
6. Nielsen, J. A.; McMorrow, D. *Elements of Modern X-ray Physics* (John Wiley & Sons Ltd **2001**)
7. Tolan, M. *X-ray scattering from soft-matter thin films* (Springer, Vol. 148, **1999**)
8. Parratt, L. G. *Phys. Rev. B.* **1954**, *95*, 359.
9. Braun, C. *Parratt32 program*; Berlin Neutron Scattering Center (BENSC): Hahn-Meitner Institut, **1997**.
10. Kowarik, S.; Gerlach, A.; Skoda, M.; Sellner, S.; Schreiber, F. *Eur. Phys. J. Special Topics* **2009**, *168*, 11.
11. Woll, A. R.; Desai, T. V.; Engstrom J. R. *under review at Physical Review B*. Available at: arXiv.org, e-Print Archive, Condensed Matter (2011), arXiv:1102.2676v1 [cond-mat.mtrl-sci].
12. Cohen, P. I.; Petrich, G. S.; Pukite, P. R.; Whaley, G. J.; Arrott, A. S. *Surface Sci.* **1989**, *216*, 222-248.

3. Hyperthermal organic thin film growth on surfaces terminated with self-assembled monolayers: I. The dynamics of trapping[*]

3.1 Overview

We have examined the initial stages of growth of a crystalline small molecule organic thin film, diindenoperylene (DIP), on SiO_2 surfaces terminated with a series of self-assembled monolayers. In this study we make use of supersonic molecular beam techniques to vary the incident kinetic energy of the DIP molecules, and we use *in situ*, real time synchrotron x-ray scattering to monitor the buildup of each molecular layer in the growing thin film. We find that the effects of the SAMs are most apparent concerning growth in the sub-monolayer regime, before the substrate is entirely covered by the DIP thin film. In this coverage regime on bare SiO_2, and SiO_2 terminated with either hexamethyldisilazane or perflurooctyltrichlorosilane the adsorption dynamics are consistent with trapping-mediated adsorption as observed in more simple systems, where the probability of adsorption decreases significantly with increasing kinetic energy. Once these surfaces are covered with DIP, however, the adsorption probability increases, particularly at the highest incident kinetic energy, and the probability of adsorption exhibits only a weak dependence on the incident kinetic energy. In contrast, on surfaces terminated by octyl- (OTS) and octadecyltrichlorosilane (ODTS) the trapping probability is high and exhibits little dependence on the incident kinetic energy, essentially the same as what is observed on

[*] *J. Chem. Phys. 134, 224702 (2011)*

these same surfaces covered by DIP. We postulate, which is backed by the results of molecular dynamics simulations, that direct molecular insertion into the OTS and ODTS layers is a primary explanation for efficient trapping on these surfaces.

3.2 Introduction

The study of complex conjugated molecules for applications in organic thin film electronics has received much attention owing to their ability to form highly ordered thin films with excellent electrical properties **[1,2]**. The observation that the nature of the underlying substrate can strongly affect the growth of organic thin films and, hence, potentially their electrical properties, has led to studies investigating the growth of these molecules on a variety of surfaces, including: inorganic substrates **[3-10]**, substrates patterned with surface steps **[11]**, substrates modified with interfacial organic layers (IOLs) or self-assembled monolayers (SAMs) **[12-15]**, and polymers **[15,16]**. However, in contrast to other better understood systems, such as the epitaxial growth of inorganic crystalline thin films **[17]**, there is still a significant lack of understanding of the basic growth mechanisms in organic crystal growth, especially concerning the molecular-scale interactions occurring between these molecules and the substrate surface.

Among the parameters that can be exploited to modify organic thin film growth conducted in vacuum are the two most commonly used—the growth rate and the substrate temperature. One potential molecular variable that might be exploited is the kinetic energy of the depositing species. Supersonic molecular beam techniques,

perhaps the most powerful probe of molecule-surface interactions, provide an ideal method to tune the kinetic energy of organic molecules **[18-25]** over a useful range that is on the order of, or greater than, the strength of the intermolecular and molecule-surface interactions. The kinetic energy of the incident molecule is expected to most directly affect the (non-dissociative) probability of adsorption, as this energy must be dissipated via some mechanism for the molecule to bind to the surface. The dynamics of non-dissociative adsorption has been well characterized for systems involving relatively simple molecules (e.g., diatomics) on typically inorganic substrates (e.g., low-index faces of transition metals) **[26]**. More complex systems have been studied, although less widespread, and these include adsorption on "softer" surfaces such as liquids **[27]**, ice **[28]** and surfaces modified with SAMs **[29]**.

Of the studies concerning the adsorption dynamics on SAMs, much of the focus has been on energy transfer, inelastic scattering and trapping-desorption of simple molecules (e.g., noble gases) using time-of-flight techniques. The final energy distributions of the molecules scattered from these surfaces have been shown to largely depend on the strength of the molecule-(SAM)surface interaction, the degrees of freedom associated with the terminal tail group of the SAM, the nature of intermolecular interactions within the SAM, and the rigidity of the SAM backbone **[29(a),30]**. Previous studies have also shown that the transfer of incident kinetic energy of simple molecules such as Ar is more efficient on SAMs that are less densely packed **[31]** and that the amount of energy transfer increases as the chain length of the SAM increases **[32]**. Other studies have focused on the energy distribution of rare gases scattered from surfaces modified by SAMs as a function of both the incident

kinetic energy and the angle of incidence **[33,34]**. Moreover, computational studies have shed light on scattering channels not previously appreciated, where species such as Ar **[31]** and Xe **[35]** that are sufficiently energetic are capable of *penetrating into the SAM*. Finally, in addition to these studies of relatively simple molecules, other work has focused on the scattering and reaction dynamics of high energy ionic species **[36]** and transition metal coordination complexes on surfaces modified with of a variety of SAMs possessing different lengths and terminal functional groups **[37]**.

Recently, we have examined the dynamics of the non-dissociative adsorption of diindenoperylene (DIP) on clean SiO_2, and SiO_2 substrates modified with an interfacial organic layer, hexamethyldisilazane (HMDS) **[38]**. We found that the adsorption probability of DIP on both surfaces decreased with increasing incident kinetic energy as expected for trapping-mediated adsorption. Increasing the kinetic energy has also been shown to decrease the trapping probability of pentacene on clean SiO_2, while the dependence on the angle of incidence follows behavior intermediate to normal and total energy scaling **[20]**. Moreover, experimental studies from our group and molecular dynamics simulations **[39]** have suggested the contribution of events such as direct molecular insertion, where the incident molecules (DIP **[38]** and pentacene **[40]**) can insert into pre-existing layers of these molecules at sufficiently high incident kinetic energies, and experimentally these are manifest in an increase in the trapping probability with increasing coverage.

The focus of the work presented here is to develop a better understanding of the interactions that take place between *complex* organic molecules and surfaces terminated with SAMs, where the thickness of the SAM is on the order of the size of

the incident molecule. We will achieve this by examining both the dynamics of adsorption and the kinetics of organic thin film growth of DIP on surfaces terminated with three SAMs of different lengths and chemical composition, namely : octadecyltrichlorosilane (ODTS), ≡Si-$(CH_2)_{17}$-CH_3, octyltrichlorosilane (OTS), ≡Si-$(CH_2)_7$-CH_3, and perflurooctyltrichlorosilane (FOTS), ≡Si-$(CH_2)_2(CF_2)_5$-CF_3. Ball-and-stick models of these molecules and DIP are shown in Figure 3-1, and we note the obvious difference in complexity between an Ar atom and the polyatomic molecule DIP we examine here. We will compare these results to our previous results on clean SiO_2 and SiO_2 modified with HMDS, where the latter is not a SAM as conventionally defined due to its length and branched structure. As with our previous study **[38],** we shall use *in situ* real time synchrotron x-ray scattering to monitor the dynamics of adsorption and growth from the submonolayer to the multilayer regime. In addition, in a selected set of cases we will complement our experimental results with results from molecular dynamics simulations to obtain insight into the possible molecular-scale mechanisms that occur in these systems. As we demonstrate below, termination of a SiO_2 surface with these longer chain SAMs results in important changes in the dynamics of adsorption, both when compared to bare SiO_2 and between the different SAMs themselves.

3.3 Experimental Procedures

Refer to chapter 2 for details. Only a brief summary on experimental procedures is provided in this section. All experiments using *in situ* synchrotron x-ray

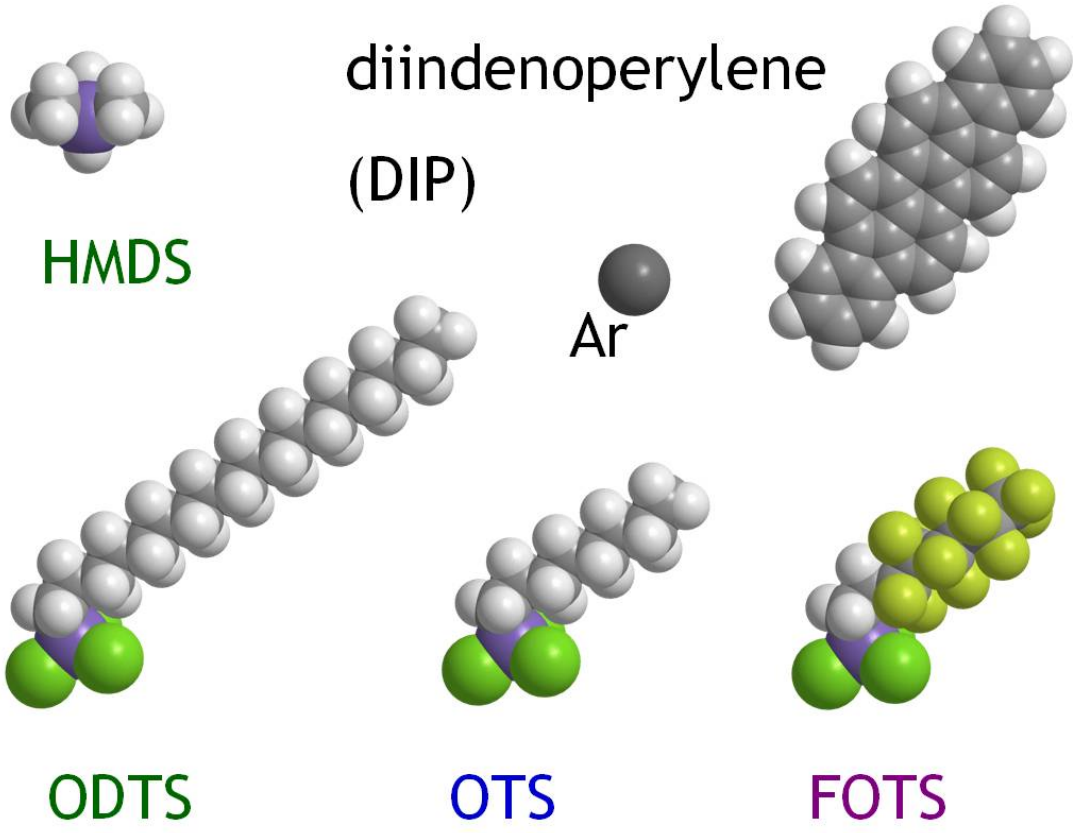

Figure 3-1 Space filling models for the molecule of interest here, diindenoperylene (DIP), and the four molecules that form the SAMs examined here: octadecyltrichlorosilane (ODTS); octyltrichlorosilane (OTS), perflurooctyltrichlorosilane (FOTS), and the chemisorbing species formed upon exposure of SiO_2 to hexamethyldisilazane (HMDS), $HSi(CH_3)_3$, where H represents the SiO_2 surface. An Ar atom is shown for comparison.

scattering were carried out in the G3 station of the Cornell High Energy Synchrotron Source (CHESS) in a custom-designed four-chamber ultrahigh vacuum (UHV) system (base pressure ~ 4×10^{-9}) fitted with Be windows that is described in detail elsewhere **[38,41]**. The starting bare substrates, consisting of (100) wafers of Si with ~ 300 nm of SiO_2, were prepared and cleaned as described in detail elsewhere **[38]**. The solution-based SAMs, OTS and ODTS, were assembled on the SiO_2|Si(100) substrates in a N_2-purged glove box ([O_2] < 10 ppm; [H_2O] < 1 ppm). All solutions were 10 mM concentration of the SAM precursor molecule in toluene. The SiO_2 substrates were dipped in the SAM solution for 2 days and left in the glove box undisturbed, followed by sequential rinsing in toluene, acetone, chloroform, DI water and finally drying with N_2 **[42]**. HMDS and FOTS were formed on the SiO_2 substrates via vapor phase deposition. HMDS was deposited using a YES LP-III Vapor Prime Oven after successive evacuation and purge cycles to dehydrate the substrate held at 150°C. FOTS was deposited using an MVD-100 system.

The SAMs were characterized using a number of techniques: contact angle measurements were carried out using the VCA Optima XE system (AST Products Inc., Billerica, MA), and the thicknesses of the SAMs were measured with a variable angle spectroscopic ellipsometer (Woolam). The thickness and density of the SAMs were also characterized using synchrotron x-ray reflectivity measurements. These measurements were conducted as indicated above in the vacuum chamber in the G3 station using 9.75 keV X-rays with a flux of ~ 10^{13} photons-mm^{-2}s^{-1} (typically attenuated), incident to the sample through a Be window. The scattered x-ray intensity was monitored using a silicon avalanche photodiode detector (APD, Oxford Danfysik,

Oxford, UK). In these experiments we obtain information concerning the electron density of the SAM along the surface normal $p_{el}(z)$ ($0 < q_z < 1.3$ Å^{-1}). The interference pattern that results from the reflection of x-rays from the two interfaces (e.g., vacuum|SAM, SAM|SiO_2) gives a series of minima and maxima which can be modeled to determine the thickness of the SAM, d_{SAM} (cm), the electron density of the SAM, $p_{el,SAM}$ (cm^{-3}), and the widths (roughness) of both interfaces **[43]**. Here, the x-ray reflectivity was modeled using a program based on Parratt formalism **[44]**. To model the surface we used both 2-layer (SAM|bulk-oxide) and 3-layer (SAM|interfacial layer|bulk-oxide) models to fit the data. For FOTS and OTS, a 2-layer model was sufficient to fit the data, whereas for ODTS, the 3-layer model provided a statistically significant better fit. Given expected changes in electron density, the reported thicknesses of the SAMs best represents the distance between the head group (Si atom) on one end and the terminal C at the tail group. To estimate the coverage or two-dimensional density of the SAMs we use n_{SAM} (cm^{-2}) = $p_{el,SAM}d_{SAM}/N_{el,SAM}$, where $N_{el,SAM}$ is the number of electrons (excluding the Si head group) in the SAM molecule **[43]**.

Supersonic molecular beams of diindenoperylene were generated by using He as a carrier gas as described in detail elsewhere **[38]**. By varying the He flow rate, the beam energy could be varied from 4.2 to 11.3 eV as determined from time of flight measurements **[41]**, while the DIP beam flux was varied by adjusting the temperature of the *in situ* temperature controlled evaporator or "bubbler" (typically, $T_b \sim 320$ °C, nozzle temperature $T_{noz} \sim 500$ °C). We estimate the seeding fraction to vary from 0.013% (4.2 eV) to 0.0019% (11.3 eV). We found no evidence for van der Waals

dimer formation using mass spectrometry. Multiple experiments could be carried out on the same substrate, by translating the substrate perpendicular to the supersonic molecular beam, and due to the high beam-to-background flux ratio. During deposition the substrate temperature was kept at T_s = 40 °C, and in all cases the beam was incident along the surface normal. The growth rate of DIP (*vide infra*) ranged between 0.0024 and 0.012 monolayers (ML)-s^{-1} for the sub-monolayer regime, and 0.0087 and 0.017 ML-s^{-1} for the multilayer regime.

Time-resolved and *in situ* measurements of the scattered x-ray synchrotron intensity (using the APD detector) occurring during DIP thin film growth were monitored at the anti-Bragg position (00½; $q_z = q_{Bragg}/2$ = 0.37/2 $Å^{-1}$), which is an effective monitor of the nature of growth, *i.e.*, layer-by-layer (LbL) vs. 3D islanded growth **[45]**. Following deposition and x-ray analysis, the samples were removed for *ex situ* analysis using atomic force microscopy (AFM), conducted in tapping mode using a DI 3100 Dimension microscope.

The anti-Bragg x-ray data was fitted**,** using a modified version **[38,46]** of the mean-field rate equation model of growth first proposed by Cohen and co-workers **[47].** Briefly, the equations for the coverage of individual layers (θ_n) are given by:

$$\frac{d\theta_n}{dt} = S_{n-1}F\left[\left(\theta_{n-1} - \theta_n\right) - \alpha_{n-1}\left(\theta_{n-1} - \theta_n\right)\right] + S_nF\alpha_n\left(\theta_n - \theta_{n+1}\right) \qquad (3\text{-}1)$$

where n = 0 represents the substrate, n = 1 the first molecular layer, etc., S_n is the probability of adsorption for molecules incident on the n^{th} layer, F is the incident molecular flux (ML-s^{-1}), and α_n is the fraction of molecules that initially impact and

land on top of the n^{th} layer, but rather than staying on the top of that layer, drop down and become part of that layer via some mechanism. In this model we will assume that there are two values for the probability of adsorption: one for adsorption on the substrate (S_0), and one for that on previously existing molecular layers, independent of their thickness ($S_1 = S_2 = S_3 \ldots$).

Once layer coverages have been calculated by integrating Equation (3-1), these can then be used to calculate the scattered x-ray intensity as a function of time **[5,24,38,45-47]**. The intensity of the scattered beam (I) depends upon the layer population, θ_n(t), according to the following relationship:

$$I(t) = \left| r_{subs} e^{-i\phi} + r_{film} \sum_{n}^{\infty} \theta_n(t) e^{-iq_z dn} \right|^2 \tag{3-2}$$

where r_{subs} and r_{film} are the scattering amplitudes of the substrate and the film, ϕ is the phase change upon reflection, q_z is the out-of-plane scattering vector and d is the out-of-plane interplanar spacing. At the anti-Bragg position, $q_z d = \pi$, which results in a change in the sign of the thin film terms in the summation with the filling of each successive layer.

3.4 Results and Discussion

A. Characterization of the self-assembled monolayers

First, we consider the results from x-ray reflectivity (XRR). In Figure 3-2 we plot the reflected intensity as a function of the out-of-plane scattering vector, q_z, for a monolayer of ODTS. We see that the quality of the fit to the data, which is shown by the smooth curve, is excellent, and we find that the thickness of this layer is d_{SAM} = 17.3 ± 1.8 Å, and the electron density of this layer is $p_{el,SAM}$ = 0.24 ± 0.02 Å^{-3}. These and other properties of the ODTS layer and the other SAMs are given in Table 3-1. Making use of the number of electrons in the ODTS backbone, we find the density of the ODTS molecules is n_{SAM} = 2.83 ± 0.29 × 10^{14} molecules-cm^{-2}. We note that both this density and this thickness for ODTS on SiO_2 are smaller than (some) values reported previously—the density of the SAM can be a function of both the reaction time and the density of reactive sites on the substrate surface. The surface preparation we use here, for example, is not as aggressive as we have used previously, which produces a higher density of –OH(a) on the surface, characteristic of the so-called chemical oxide **[48]**. Indeed, our results are closer to the low density layer reported by Tidswell et al. **[43(b)]**. We take note of the fact, however, that in both this previous work, and our work, the surface is uniformly covered by this layer, i.e., the data are not consistent with a surface partially covered by islands with a larger (~ 25 Å) thickness. Concerning other measurements as given in Table I, we see that the ellipsometric thicknesses are the same as those measured from XRR, within experimental error. The larger hysteresis in the contact angle compared to our previous work **[48]**, on the other hand, indicates that our somewhat low density ODTS layer is not as perfect as the previously examined higher density layers.

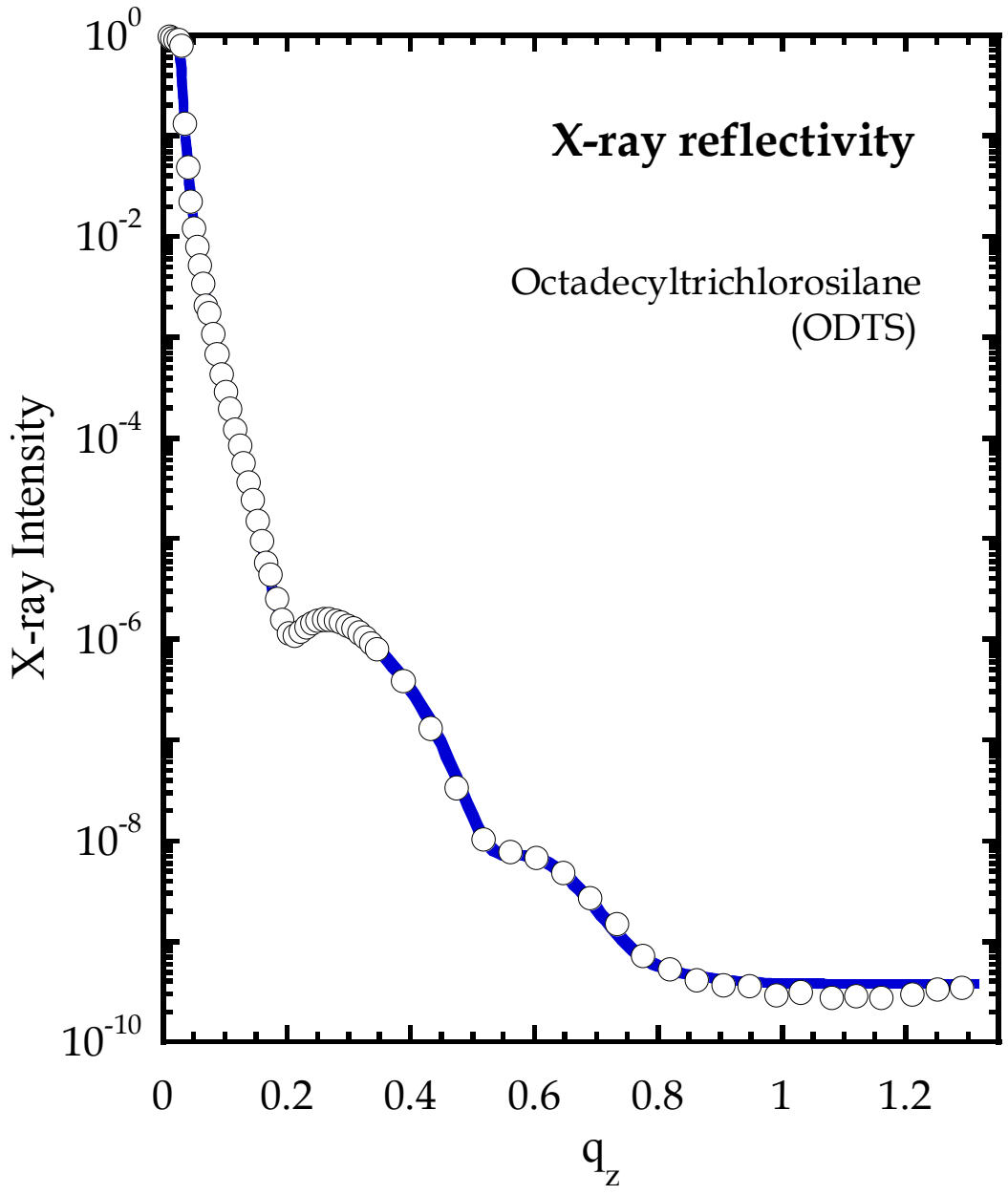

Figure 3-2 Scattered x-ray intensity as a function of the out-of-plane scattering vector, q_z, for a monolayer of octadecyltricholorosilane on SiO_2. For clarity, only 1 of every 5 data points is plotted. The solid curve represents a fit of the data to a model based on the Parratt formalism (reference **[44]**).

Table 3-1 Properties of the self-assembled monolayers*

Monolayer	Contact angle		Thickness (Å)			electron density (Å^{-3})	n_{SAM} (nm^{-2})
	adv/red	hysteresis	ellipsometry	XRR	theory (alkyl)	XRR	XRR
ODTS ≡Si-$(CH_2)_{17}$-CH_3	103 ± 1.6/ 88 ± 2.2	15	17 ± 1	17.3 ± 1.8	24.3	0.24 ± 0.02	2.83 ± 0.29
Reference **[48]**	112 ± 0.6/ 109.7 ± 4.7	2.3	27		24.3		
High coverage **[43(b)]**			25-26 ± 1	23.5 ± 0.3	24.3	0.30 ± 0.04	4.44 ± 0.49
Low coverage **[43(b)]**			14.5 ± 1	16.5 ± 1.0	24.3	0.28 ± 0.06	3.19 ± 0.71
OTS ≡Si-$(CH_2)_7$-CH_3	104 ± 1.9/ 89 ± 2.0	15	7 ± 1	6.27 ± 0.65	11.6	0.29 ± 0.03	2.74 ± 0.28
FOTS ≡Si-$(CH_2)_2$-$(CF_2)_5$-CF_3	107 ± 2.1/ 89 ± 1.2	18	7 ± 1	6.32 ± 0.5		0.53 ± 0.04	1.97 ± 0.12
≡Si-$(CH_2)_2$-$(CF_2)_7$-CF_3 **[43(b)]**				18 ± 2		0.56	3.71

*this work, unless noted otherwise

For the other two SAMs we consider here (XRR data not shown), OTS and FOTS, we find molecular densities similar to what we calculate for ODTS, $n_{SAM} \sim 2.7$ and 2.0×10^{14} molec-cm^{-2}, respectively. The thicknesses of these layers suggest also that the molecules in these layers are tilted significantly from the surface normal. Equating the XRR thickness with that due to the alkyl backbones, the tilt angle is suggested to be ~ 45° for ODTS and ~ 57° for both OTS and FOTS. Thus, due to their lower density, these SAMs either tilt or bend in order to maximize their van der Waals interactions with the surrounding molecules **[43(b)]**. Finally, we also characterized the layer formed upon exposure to HMDS. The layer formed was too thin, as would be expected, for analysis by XRR. We did analyze the layer using contact angle measurements and found advancing/receding angles of 88 ± 1°/69 ± 2°, with a hysteresis of 19°. In previous work we have estimated the coverage of the HMDS fragment, -Si$(CH_3)_3$, to be ~ $2.3 \pm 0.5 \times 10^{14}$ molec-cm^{-2}. Thus, for all 4 IOLs that we consider here, their absolute coverage falls within the range $2.0\text{-}2.8 \times 10^{14}$ molec-cm^{-2}, or ~ ± 20% of the mean. We anticipate, therefore, that our results will not speak directly to possible effects of sizeable changes in the density of the SAM on the trapping dynamics.

B. Adsorption and growth of DIP on self-assembled monolayers

In Figures 3-3 to 3-7, we present a subset of experiments we have conducted concerning the growth of DIP on clean SiO_2, and SiO_2 that has been modified with HMDS, FOTS, OTS and ODTS. The data shown represent the lowest (4.2 eV) and

highest (11.3 eV) kinetic energies examined here using a supersonic molecular beam source. All experiments were conducted at T_s = 40 ºC (*cf*. 64 ºC for our previous work on clean SiO_2 and HMDS only **[38]**) to minimize any possible effects associated with the degradation of the SAMs, or changes in surface roughness with substrate temperature. As explained in greater detail in our previous work **[38]**, the intensity oscillations at the anti-Bragg condition, observed on all 5 surfaces, are expected for layer-by-layer growth due to the alternating contributions of the odd and even layers to the magnitude of the scattered intensity [*cf*. Equation (3-2)]. As may be seen in Figures 3-3 to 3-7, the shape of the anti-Bragg oscillations is sensitive to the nature of the starting surface. For example, comparing the different starting surfaces we see that there are differences in the relative intensities at t = 0, at the peak of the first oscillation (~ 1 ML coverage) and for the "saturation" intensity, $t \rightarrow \infty$. These are readily understood as manifestations of differences in the phase (ϕ) and reflection amplitudes (r_{subs} and r_{film}) that appear in Equation (2), which are functions of the thickness and electron density of the SAM/IOL **[38,45,46]**.

We start first by examining the growth of DIP on clean SiO_2 and SiO_2 that has been modified by HMDS, as shown in Figures 3-3 and 3-4. In Figure 3-3(a) we present the scattered x-ray intensity acquired in real time at the anti-Bragg condition (q_z = 00½) for the growth of DIP on SiO_2 at E_i = 4.2 eV. As may be seen, we observe in sequence a first small maximum (~ 1ML), a larger maximum (~ 2 ML), a totally obscured second smaller maximum, a strongly damped second larger maximum (~ 4 ML), and finally a hint of a third larger maximum (~ 6ML). Thus, for these conditions we see that DIP grows in a layer-by-layer (LbL) mode until approximately 4 MLs,

Figure 3-3 (a) X-ray intensity at the anti-Bragg condition as a function of exposure to the molecular beam (E_i = 4.2 eV) for thin films of diindenoperylene deposited on clean SiO_2. T_s = 40 °C. Thick solid lines (right ordinate) indicate a fit of the data to a model and thin solid curves (left ordinate) represent predicted coverages (θ_n) of the individual layers. (b) Total coverage (θ_{tot}, left ordinate) and growth rate (right ordinate) predicted by a fit of the data displayed in (a). These figures are repeated in (c) and (d), for DIP incident at the higher incident kinetic energy (E_i = 11.3 eV) for this same surface.

(a)
(b)
(c)
(d)
Coverage (ML)
Intensity
Thickness (ML)
Growth rate (ML-s^{-1})
Time (s)
2
4
6
8
DIP on SiO$_2$
E$_i$ = 4.22 eV
E$_i$ = 11.3 eV

after which the intensity oscillations are strongly damped, indicative of 3D growth. The kinetics of growth can be modeled more precisely by making use of Equations (3-1) and (3-2) and these results are shown in Figures 3-3(a) and 3-3(b). In (a) we show the coverage of each layer (solid black curves) predicted by the fit to the intensity oscillations (solid blue line). We find that, to fit the data, we need to assume that S_0F ~ 0.0102 ML-s^{-1}, whereas $S_{n \geq 1}F$ ~ 0.0133 ML-s^{-1}. These data imply that the rate of growth has accelerated with increasing DIP coverage. Since desorption can be assumed negligible at T_s = 40 ºC, these data indicate that the acceleration in the rate is due to an increase in the adsorption probability S with increasing coverage. In this case the adsorption probability has increased by about 30%.

In Figures 3-3(c) and 3-3(d), we consider growth of DIP incident on SiO_2 at E_i = 11.3 eV. In comparison to growth of DIP on SiO_2 at 4.2 eV, we see that the maxima corresponding to ~ 4 MLs is less pronounced indicating that LbL growth is less extended for these conditions. Regarding the growth kinetics, to fit these data, we must assume that S_0F ~ 0.00455 ML-s^{-1}, whereas $S_{n \geq 1}F$ ~ 0.00938 ML-s^{-1}, an increase of ~ 106%. If we consider intermediate kinetic energies, not shown here, we find that the acceleration in the rate of growth follows a consistent trend with E_i, namely a 50% increase at E_i = 6.4 eV, and 106% at E_i = 9.4 eV.

In Figure 3-4 we display the results for the growth of DIP on SiO_2 modified with HMDS. At the lowest kinetic energy (4.2 eV) from Figure 3-4(a) we see clear intensity oscillations for the first 3 MLs, and subsequent peaks are strongly damped. From Figure 3-4(b) we see that a change in the rate of growth is also observed on HMDS, and for this energy the amount of increase is ~ 52%. At the highest kinetic

Figure 3-4 X-ray intensities, predicted layer occupancies, total coverages and growth rates for DIP incident on HMDS|SiO_2 at (a,b) E_i = 4.2 eV and (c,d) 11.3 eV. Layout details otherwise identical to Figure 3-3.

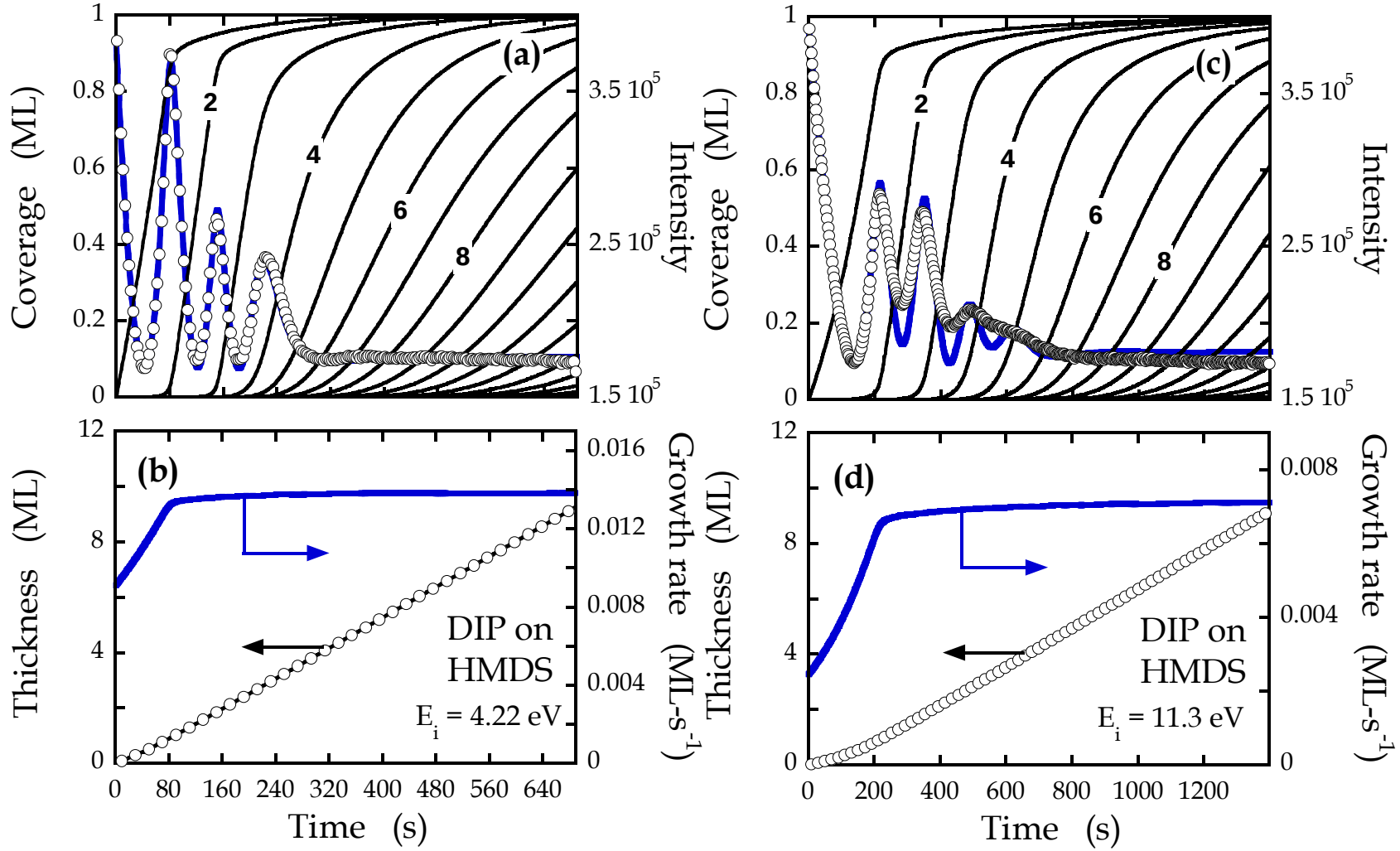
(a)
(b)
(c)
(d)
Coverage (ML)
Intensity
Thickness (ML)
Growth rate (ML-s^{-1})
Time (s)
2
4
6
8
DIP on HMDS
E_i = 4.22 eV
E_i = 11.3 eV
1
0.8
0.6
0.4
0.2
0
3.5 10^5
2.5 10^5
1.5 10^5
12
8
4
0.016
0.012
0.008
0.004
0
80
160
240
320
400
480
560
640
200
600
800
1000
1200

energy (11.3 eV) for DIP on HMDS, in Figure 3-4(c) we see three clear peaks in the intensity, and they are somewhat more damped than those at the lower kinetic energy. Concerning the kinetics of growth, acceleration in the rate of growth on the HMDS-modified surface at the highest energy is about 192%. If we consider intermediate kinetic energies, not shown here, we find that the acceleration in the rate of growth is 85% at E_i = 6.4 eV, and 170% at E_i = 9.4 eV, thus, again the amount of the increase increases with increasing kinetic energy.

We now turn our focus to the more conventional SAMs (FOTS, OTS and ODTS), where new features introduced by these layers include a variation in the length/thickness of the organic layer and the mass/chemical identity of the terminating species. In Figure 3-5(a) we present the scattered x-ray intensity acquired in real time at the anti-Bragg condition for growth of DIP on FOTS at E_i = 4.2 eV. For these conditions, the peaks corresponding to completion of ~ 1 and 3 MLs are the strongest, and a faint peak is observed corresponding to deposition of 5 MLs of DIP, indicating the growth has become very 3D by that time. Concerning the kinetics of growth, as shown in Figure 3-5(b), the acceleration in the rate of growth is ~ 41 % at E_i = 4.2 eV, an amount that is smaller compared to that on HMDS (52%), but greater than that on clean SiO_2 (30%).

In Figure 3-5(c) and 3-5(d), we display results for DIP growth on FOTS at E_i = 11.3 eV. For these conditions we see three maxima, again corresponding to the deposition of the first ~ 3 MLs of DIP. However, unlike essentially all other data we present here and have elsewhere **[38]**, as may be seen, following the last observable peak the intensity does not remain constant, but continues to decay. Due to this decay

Figure 3-5 X-ray intensities, predicted layer occupancies, total coverages and growth rates for DIP incident on FOTS| SiO_2 at (a,b) E_i = 4.2 eV and (c,d) 11.3 eV. Layout details otherwise identical to Figure 3-3.

(a)
(b)
(c)
(d)
Coverage (ML)
Intensity
Thickness (ML)
Growth rate (ML-s^{-1})
Time (s)
2
4
6
8
DIP on
FOTS
E_i = 4.2 eV
E_i = 11.3 eV

we cannot fit precisely the entire curve to our model. If we fit the entire data set, the best fit is obtained with an assumption that there is essentially no change in the rate of growth from the monolayer to the multilayer, and this rate is ~ 0.0057 ML-s^{-1}. In addition, this fit underestimates the total film thickness by 3 ML compared to the thickness determined from post-growth XRR. In comparison, the multilayer growth rate on HMDS, OTS and ODTS (*vide infra*) all lie with the range 0.0068-0.0071 ML-s^{-1}. If, on the other hand we limit the fit to the first few MLs (t < 450 s) we can obtain a good fit to the model and we obtain a more accurate estimate of the total film thickness when compared to post-growth XRR. Our fit to the data using this method is shown in 3-5(c), where for full disclosure we display also the prediction of the fit beyond t = 450 s (where the fit is obviously poor). We see that over this early stage of growth the fit to the data is good, and that the amount of acceleration is 143%. If we consider intermediate kinetic energies, not shown here, they exhibit a consistent trend with E_i, namely a 65% increase in the rate of growth at E_i = 6.4 eV, and 102% at E_i = 9.4 eV. This further adds credibility to the truncated fit of the data shown in Figure 3-5(c). Compared to growth of DIP on clean SiO_2 and HMDS, we take note of the fact that the acceleration in the rate of growth is, for all energies, less than that on HMDS but greater than that on SiO_2.

In Figures 3-6(a) and 3-6(b), we display results for DIP growth on clean SiO_2 modified by OTS at E_i = 4.2 eV. For these conditions and growth on this surface, we notice two clear maxima at ~ 1 and 3 MLs, and a nearly indistinguishable smaller maximum at ~ 2 ML. Beyond 4 MLs, there is little evidence of extended oscillations and growth has clearly transitioned to a 3D mode. Perhaps most important, as shown

Figure 3-6 X-ray intensities, predicted layer occupancies, total coverages and growth rates for DIP incident on OTS| SiO_2at (a,b) E_i = 4.2 eV and (c,d) 11.3 eV. Layout details otherwise identical to Figure 3-3.

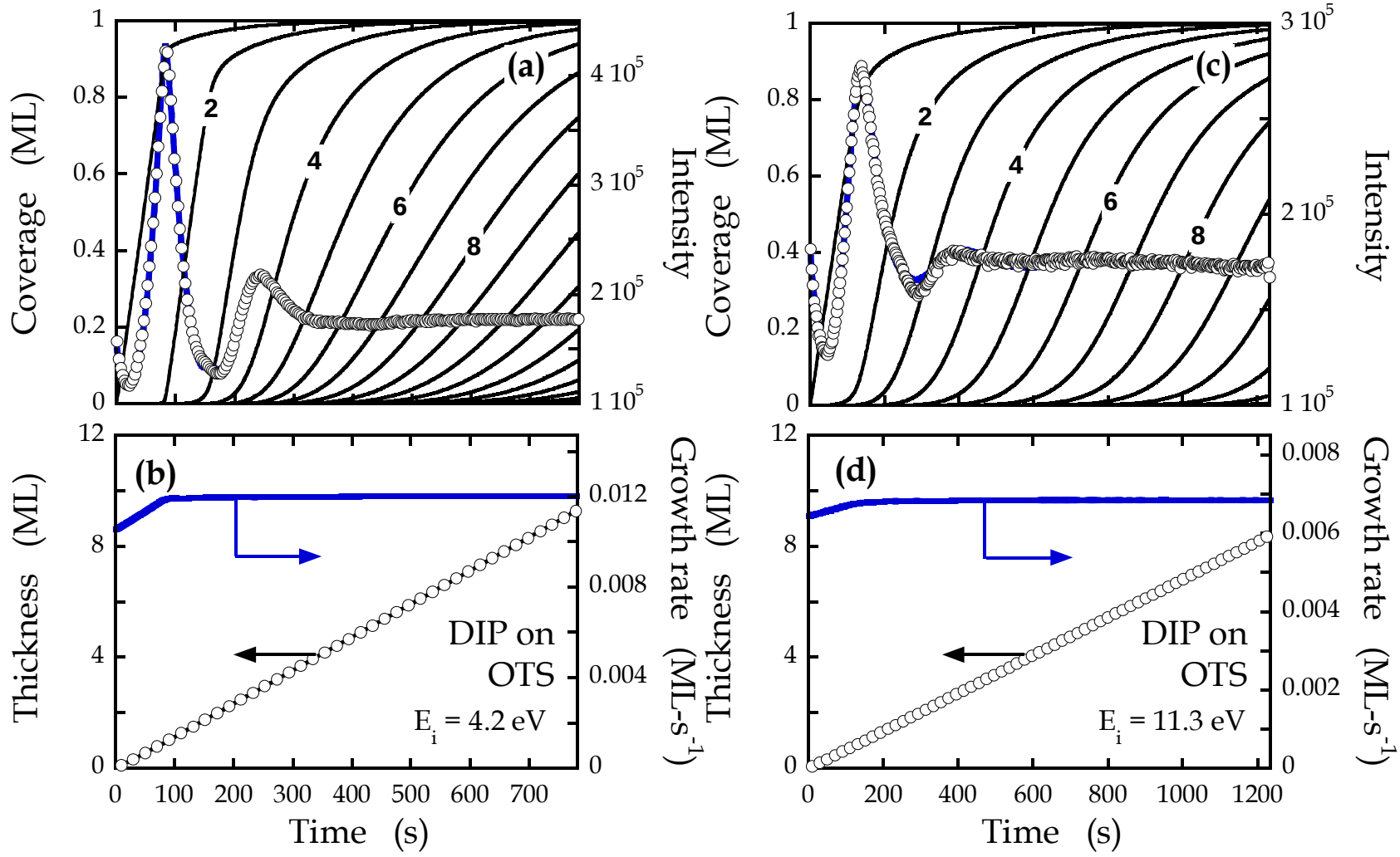
(a)
(b)
(c)
(d)
Coverage (ML)
Intensity
Thickness (ML)
Growth rate (ML-s^{-1})
Time (s)
2
4
6
8
DIP on
OTS
E_i = 4.2 eV
E_i = 11.3 eV

in Figure 3-6(b), an acceleration in the rate of growth is detected, but it is only ~ 14% , much smaller than that seen on HMDS, FOTS and bare SiO_2. This suggests that the adsorption probability of DIP on OTS and that on itself (DIP) is similar for these conditions. In Figure 3-6(c) and 3-6(d) we display results for DIP growth on OTS at the highest incident kinetic energy (11.3 eV) examined here. Similarly, for this set of growth conditions, we again see a larger maximum, followed by a minimum and a smaller maximum before significant roughening increases. The intensity at the anti-Bragg condition is quite similar to that seen at the lower energy [*cf*. Figure 3-6(a)], a noticeable difference being the weaker second large maxima observed at 3 ML. This suggests perhaps a slightly earlier transition to 3D growth at this higher energy. Concerning the kinetics of growth as shown in Figure 3-6(d), we now observe an even smaller change in the rate of growth of only about 7%. If we consider intermediate kinetic energies, not shown here, we find that the acceleration in the rate of growth to be a 9% at E_i = 6.4 eV, and 8% at E_i = 9.4 eV. Thus, on this surface, the rate of acceleration is nearly independent of the incident kinetic energy. In comparison to the other surfaces discussed above (SiO_2, HMDS and FOTS), the magnitude of the rate of change in growth on OTS is much smaller at all incident energies, implying as indicated above that the adsorption probability of DIP on OTS is close to that on DIP itself.

In Figures 3-7(a) and 3-7(b) we display results for DIP growth on SiO_2 modified with ODTS at E_i = 4.2 eV. For these growth conditions, we observe only a single clear maximum at ~ 1 ML, with hints of small modulations at larger coverage. Clearly the growth transitions to a 3D mode quickly after the formation of the first

Figure 3-7 X-ray intensities, predicted layer occupancies, total coverages and growth rates for DIP incident on ODTS| SiO_2at (a,b) E_i = 4.2 eV and (c,d) 11.3 eV. Layout details otherwise identical to Figure 3-3.

(a)
(b)
(c)
(d)
Coverage (ML)
Intensity
Thickness (ML)
Growth rate (ML-s^{-1})
Time (s)
2
4
6
8
DIP on
ODTS
E_i = 4.2 eV
E_i = 11.3 eV

monolayer, and of the systems examined here LbL growth is the least sustained on ODTS. Concerning the kinetics of growth, we see that the data is fit well by assuming that there is no acceleration in the rate of growth—to fit this data, we assumed that S_0F ~ 0.0122 ML-s^{-1}. At the highest energy (11.3 eV) examined here, shown in Figures 3-7(c) and 3-7(d), we observe growth behavior similar to that seen at the lowest energy examined here (4.2 eV), e.g., only a single maximum is observed. Concerning the kinetics of growth, these data are also fit quite well by assuming a constant growth rate, in this case, S_0F ~ 0.00680 ML-s^{-1}. At intermediate energies, not shown here, we observed similar behavior—a single maximum in the anti-Bragg intensity, and data that could be fit to a single rate of growth.

Due to the quick damping of the oscillations for growth on ODTS, it is indeed a challenge to make an accurate assessment of the change in the rate of growth from the monolayer to the multilayer. First, although there is only a single clear maximum for this surface, there is still considerable information content in the data, including the decay portion after this first maximum, and the subsequent minimum. The signal is only completely quenched after about ~ 4 ML of growth, thus, we have some confidence in our ability to fit the data in a meaningful way over this range. Second, as a check to the multilayer rate of growth we can use the final thickness, as assessed by a measurement of the coherent thickness, D ($D = 2\pi/\Delta q$, where Δq is the period of the Laue oscillations about the 00l Bragg peaks), using x-ray reflectivity. A simple calculation gives the multilayer growth rate, $(D_{tot} - 1)/(t_{tot} - t_1)$, where D_{tot} (t_{tot}) is the total thickness (time of growth) and t_1 is the time for growth of a monolayer (assessed accurately by modeling the anti-Bragg intensity). For the 4 conditions of growth

examined here we find multilayer growth rates of $S_{n\geq 1}F \sim 0.0131$ ML-s^{-1} at 4.2 eV, ~ 0.0158 ML-s^{-1} at 6.4 eV, ~ 0.0118 ML-s^{-1} at 9.4 eV and ~ 0.00692 ML-s^{-1} at 11.3 eV. Comparing these to the monolayer growth rates assessed by modeling the anti-Bragg intensity, this implicates an acceleration of the rate of growth by 7, 17, 21 and 2%, or an average of 12%. These values are sufficiently close to 0 such that they confirm that the amount of acceleration in the rate of growth on ODTS is minimal. Similar to OTS, and in contrast to FOTS, HDMS and clean SiO_2, there is no significant increase in the rate of change of growth for DIP on ODTS with increasing coverage, implying that the adsorption probability of DIP on ODTS is quite similar to that on DIP itself.

C. Dynamics of adsorption

In order to examine the effects of the incident kinetic energy on the probability of adsorption (and hence the growth rate) we need to account for changes in the incident molecular flux as we varied the kinetic energy. In order to do this we have measured the direct intensity of the molecular beam using quadrupole mass spectrometry, which measures the molecular density in the ionization region, and subsequently corrected for the effect of molecular velocity to calculate a relative incident flux. Making use of this relative molecular flux we can then calculate relative probabilities of adsorption. We note that due to the high probability of adsorption of DIP on the chamber walls, classical techniques such as beam reflectivity **[25,37,49]** are rendered useless in terms of measuring an absolute probability of adsorption.

In Figure 3-8 we present the relative probabilities of adsorption as a function of incident kinetic energy for (a) DIP on the 5 starting substrates examined here (S_0), and (b) DIP on DIP, i.e., on growing thin film ($S_{n \geq 1}$), after making an appropriate adjustment for the change in the incident flux with kinetic energy. In passing we note that we estimate that the uncertainty in the reproducibility of the flux between experiments to be about ± 5 %, not exceeding ± 10 %, whereas the change in incident flux during the experiment, which would impact any change in the growth rate, to be much less, ± 1 %. These uncertainties propagate directly to the relative probabilities of adsorption, thus their uncertainties are ± 10%. In Figure 3-8 the probabilities of adsorption have been normalized to the highest flux corrected growth rate we observe here among these three surfaces, namely multilayer growth on clean SiO_2 at E_i = 9.4 eV.

Concerning adsorption on the starting surfaces, which is shown in Figure 3-8(a), the data appear to fall into one of two groups. First, the probabilities of adsorption of DIP on both OTS and ODTS are similar to that of DIP on itself, *cf.* Figure 3-8(b), and show only a weak dependence on the incident kinetic energy. On the other three surfaces, i.e., SiO_2, FOTS and HMDS, the data exhibits the behavior expected for trapping-mediated adsorption—a smooth decrease of the probability with increasing incident kinetic energy. We have observed this behavior previously concerning the adsorption of both pentacene **[20,21]** and DIP **[38]** on clean SiO_2 and SiO_2 modified with HMDS. A major observation from these data is that trapping (adsorption) is much more efficient at high incident kinetic energies on the surfaces terminated with OTS and ODTS.

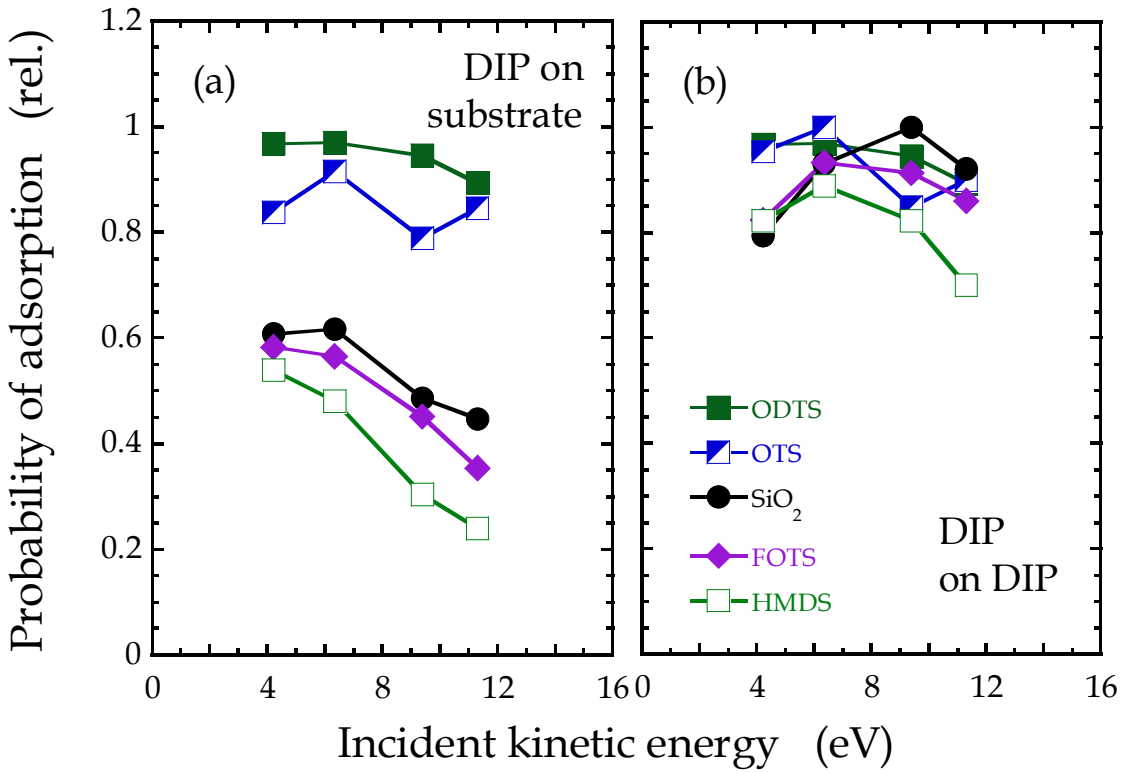

Figure 3-8 Relative probabilities of adsorption vs. the incident kinetic energy for DIP incident on (a) the 5 starting substrates and (b) the DIP-covered substrates.

Concerning multilayer growth, it is clear from Figure 3-8(b) that for all systems the probability of adsorption of DIP on DIP is nearly unity over the entire range of E_i investigated. Indeed, for DIP on DIP we see that there is little "memory" of the starting substrate, and all of the values lay within a band of about ± 10%. A slight decrease of the trapping probability with increasing incident kinetic energy is suggested if the data sets are viewed as a whole. This modest decrease in the trapping probability with increasing energy for growth in the multilayer regime has also been observed for pentacene on pentacene, both experimentally and from molecular dynamics simulations **[40]**. As we have discussed elsewhere there are two primary explanations for efficient trapping of DIP on the DIP covered surface. First, there is more efficient momentum transfer as a result of better mass-matching for DIP impinging on DIP. Second, mechanisms such as direct molecular insertion become operative at sufficiently high incident kinetic energy, and can contribute significantly to adsorption **[40]**.

To examine our results further we now consider the alternative presentation given in Figure 3-9, where we plot the ratio of the trapping probability in the monolayer regime to that in the multilayer regime (or equivalently the growth rates, as the incident flux is the same for each set of conditions). In this construction we are less susceptible to errors arising from run-to-run variations in the flux of the molecular beam, which, as stated above, may be as much as ± 10 %, whereas it is closer to ± 1 % during the course of a single experiment. We see that this representation of the results gives trends similar to that given by Figure 3-8(a), which is as expected, as the trapping probability of DIP on the growing DIP surface shows only a weak

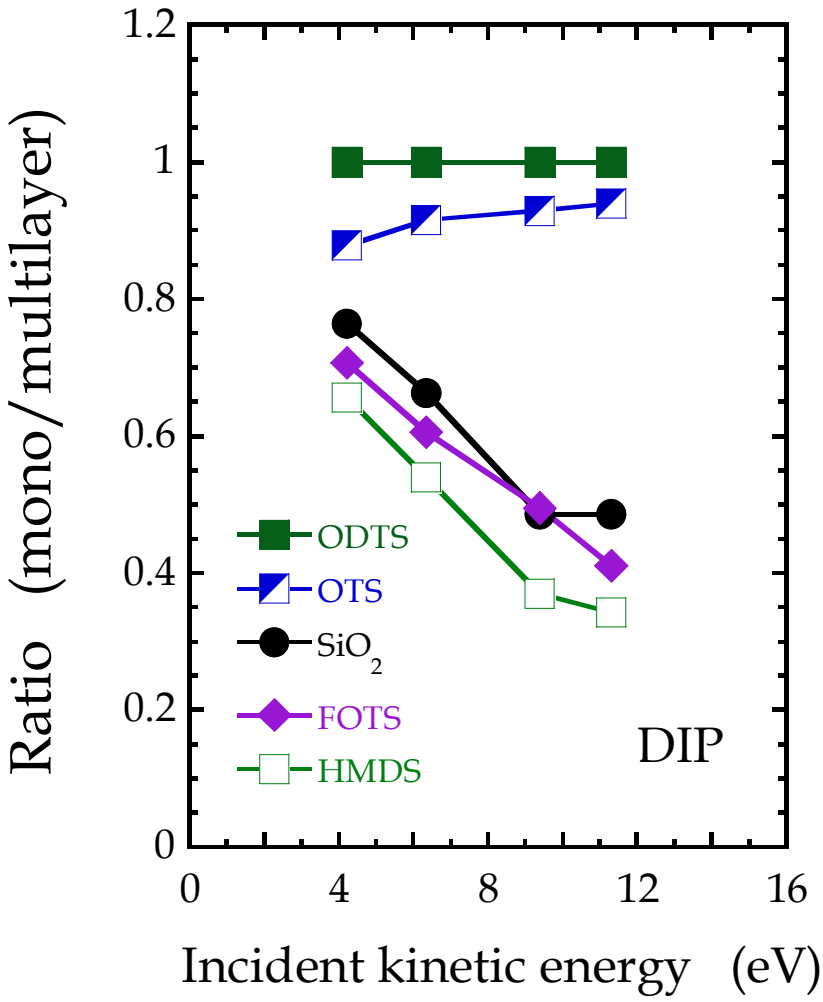

Figure 3-9 Ratio of the probabilities of adsorption (initial monolayer/multilayer) vs. the incident kinetic energy for DIP on the 5 substrates considered here.

dependence on incident kinetic energy and the identity of the starting surface. These data further reinforce the grouping of the dynamics of adsorption into two sets: (i) OTS and ODTS; and (ii) SiO_2, FOTS, and HMDS. If we consider the mechanisms indicated above that could account for the efficient trapping of DIP on DIP, namely direct molecular insertion, and apply it to these results, insertion is clearly not possible on bare SiO_2, while it is unlikely on SiO_2 modified with HMDS, due to the thickness of that layer (< 5 Å). For the other 3 SAMs, ODTS, OTS and FOTS, however, insertion may play a role.

To explore possible reasons for the differences in the trapping probabilities we can begin by discarding some explanations. First, all of the SAMs/IOLs examined here are relatively low energy surfaces and, in all cases, we observed large (H_2O) contact angles (> 88°). Yet, clean SiO_2 (contact angle ~ 0°) is grouped with HMDS- and FOTS-terminated SiO_2 in terms of the DIP trapping dynamics. Thus, contact angle measurements, often linked to the density and presence of organic functional groups, are of little help here. Thickness of the organic layer seems to play some role, as trapping seems to be the most efficient on the thickest organic layer (ODTS), and least efficient on the thinnest (HMDS). This argument loses some backing when we consider OTS and FOTS, layers that have essentially the same thickness, yet DIP exhibits different trapping dynamics on these two surfaces. It would seem *thickness* plays some role; the *density* of the layer also plays a role if insertion is active (effectively steric hindrance), and finally the *strength of interaction* (well depth) between the molecule and the layer may also play a role.

A possible interpretation of our results involves the following. First, the trapping of DIP on ODTS is likely efficient as insertion events are probably frequent, given our previous results concerning pentacene on pentacene, where, even for a crystalline surface, insertion was observed at comparable incident kinetic energies **[40]**. The ODTS layer examined here is as much as 36% less dense as what can be formed using alternative preparation methods **[43(b)]**, suggesting that penetration of the ODTS layer by DIP is certainly possible, particularly when compared to a well packed organic crystal. Molecules that do penetrate the organic layer will experience many collisions with the constituents that comprise the organic layer (head group, back bone groups), and these events will act as a drag or frictional force as the molecule penetrates the layer, possibly encounters the underlying substrate, and then rebounds. One can understand that this kind of trajectory may be a very effective mechanism to dissipate the molecule's incident kinetic energy. On a HMDS–terminated surface, in contrast, although this surface may possess a similar density of terminal $–CH_3$ functional groups, and consequently a similar gas-surface potential, penetration of the layer, if it occurs, is limited to a small portion of the DIP molecule. Most trajectories will interact with the terminal $–CH_3$ groups. Thus, the nature of rotational/vibrational modes that may be excited are much more limited with the HMDS layer, in comparison to the ODTS layer, which due to its structure will have a much higher density of states of low lying modes. Thus, it seems that convincing arguments can be made to reconcile trapping on HMDS vs. ODTS.

Why is trapping different on OTS vs. FOTS, molecules with similar structure that form layers of similar thickness? One argument that can be made is the effective

mass. Given the size of DIP, it is probably misleading to think solely in terms of total molecular weight (*vis-à-vis*, say, Ar). Particularly in terms of the excitation of relatively soft modes of vibration, the mass of constituent (local) groups on the molecule may also be an effective point of view. For example, a -CH- group on DIP striking a $–CH_3$ vs. a CF_3 group on OTS and FOTS, respectively. Momentum transfer should be more efficient with the former (OTS).

On the other hand, the strength of interaction between DIP and OTS, and DIP and FOTS might be different. To make a first order estimate for these interactions, calculations were conducted (by A. P. Kaushik and P. Clancy) using density functional theory and the hybrid M06 functional **[50]**. In this approach the surface was modeled using ~ 10-20 molecules of OTS or FOTS arranged in an array that corresponded to the density measured using XRR (*cf.* Table I). DIP was brought to this surface such that its molecular plane was parallel to the surface, thus maximizing its van der Waals interaction. From this calculation the binding energy of DIP on FOTS was ~ 0.05 eV larger than that on OTS (MM3 gave 0.1 eV for this difference). Thus, we deem it unlikely that the trapping dynamics of DIP on OTS vs. FOTS are different primarily due to a difference in the binding energy of DIP on these surfaces.

A final factor that might affect the dynamics of trapping could be the density of the two layers, as this will play some role in the relative importance of insertion into the organic layer. As discussed in the Introduction, previous studies have also shown that the transfer of incident kinetic energy of simple molecules such as Ar is more efficient on SAMs that are less densely packed **[31]**, and species such as Ar **[31]** and Xe **[35]** that are sufficiently energetic can penetrate into the SAM. As may be seen

from Table I, from XRR we estimate that the OTS layer is denser than the FOTS layer, with values of 2.74 ± 0.28 and 1.97 ± 0.12 molec-nm^{-2}, respectively. However, based on liquid phase densities for alkanes vs. fluoroalkanes, we might expect that FOTS would form a less dense layer. The molecular density for C_8H_{18} is 3.68×10^{21} cm^{-3}, whereas that for C_8F_{18} is 2.38×10^{21} cm^{-3}. Thus, using the thicknesses, also measured from XRR, we see that the OTS layer has a density that is ~ 1.19 of the corresponding liquid, whereas the FOTS layer is ~ 1.31 of the liquid. From these observations, it would seem that the OTS layer, due to its reduced density compared to expectations for condensed phases, is more likely to be penetrated by the DIP molecule.

To conclude our comparison of the trapping dynamics on OTS vs. FOTS we considered 3 possible contributing factors: effective mass, interaction potential and density of the organic layer. Concerning the first, the effective mass of the organic layer may certainly play a role, as may the specific identity of the constituents of the organic layer, e.g., -CH_2- vs. –CF_2- groups. Based on a DFT calculation we found only small differences between the binding energy for DIP on OTS, and DIP on FOTS, thus, arguing against the importance of the attractive part of the molecule-surface interaction. Finally, based on our measurements of the densities of the organic layers examined here, the OTS layer is more likely to be penetrated by the DIP. Thus the more efficient trapping observed on OTS vs. FOTS is most likely due to more efficient momentum exchange, and more penetration/insertion of DIP into the organic layers.

D. Molecular simulation*

Molecular Dynamics simulations were conducted in order to gain some insight into the molecular-scale events that lead to the adsorption of DIP on surfaces terminated by SAMs. These simulations were performed by my collaborators, A. P. Kaushik and P. Clancy, as a complement to my experimental observations **[50]**. For details on the simulation setup, please refer to reference **[50]**.

First we consider a comparison of the probability of adsorption predicted from the simulation to those measured experimentally. In Figure 3-10(a) we plot the adsorption probabilities as a function of the incident kinetic energy for the adsorption of DIP on ODTS, OTS and FOTS. In terms of the results from simulation, we found there were 4 possible outcomes given the time scale of the simulation: (*i*) molecules scatter (rebound) from the surface; (*ii*) molecules adsorb on the surface, ending up "on top" of the SAM layer; (*iii*) molecules absorb via direct insertion into the SAM layer; (*iv*) molecules penetrate and pass through the SAM layer entirely. The first three of these outcomes can be classified as contributing to adsorption in a straightforward fashion, i.e., only (*ii*) and (*iii*) contribute. The fourth outcome occurs since we do not simulate the underlying substrate explicitly. For example, as the SAMs are tethered to regular lattice points in space, but at relatively low densities, coupled with the considerable in-plane translational mobility of the chains ("wavy" motions), deep penetration of the SAM layers in a handful of cases is not entirely unexpected. Physically, such molecules could strike the underlying substrate and rebound back into

*MD simulations were done by A. P. Kaushik (Prof. Clancy group).

the gas phase contributing to (*i*); or they may lose sufficient energy to remain either trapped in the SAM layer or on top of it contributing to (*iii*) or (*ii*). In our analysis we consider both possibilities when computing the probability of adsorption.

From 3-10(a) we see that the predicted probability of adsorption on the ODTS layer is high (> 0.9), even for incident kinetic energies of ~ 12 eV. On ODTS, no DIP molecules were observed to completely pass through the SAM layer. We also see that the agreement between experiment and simulation is quite good in this case, where there are only small deviations (~ 0.1) at the highest two incident kinetic energies considered experimentally. Moving on to the results for OTS, here we found a non-negligible amount of molecules passed through the SAM layer entirely, thus we plot a square-hatched region to represent the possible range of adsorption probabilities predicted from simulation. As may be seen, all but one of the experimental values lie in the range of the values predicted from simulation, and the agreement is, again, quite good. Finally, for adsorption on FOTS, we again have to deal with a small fraction of trajectories that pass through the SAM layer entirely, and we plot a diamond-hatched region to represent the range of predicted values. Here we see that the agreement between experiment and simulation is not as quantitatively accurate as on the other SAMs; the simulation seems to overestimate adsorption on this surface by about 0.2. Nevertheless, the simulation has captured well the order we observe here experimentally in terms of adsorption probabilities: highest on ODTS, followed by OTS, and then FOTS.

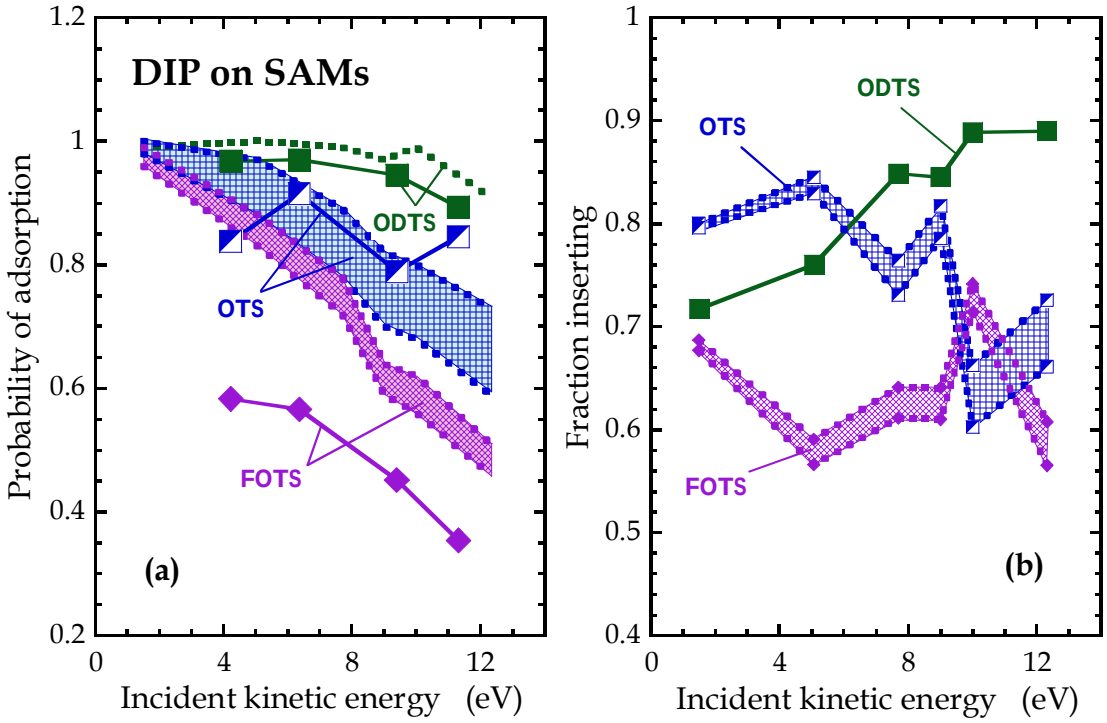

Figure 3-10 (a) Probabilities of adsorption vs. the incident kinetic energy for DIP incident on SiO_2 modified with ODTS; OTS and FOTS from experiment: solid lines and symbols [*cf.* Figure 3-8(a)], and predictions from molecular simulation: dotted lines and hatched areas. (b) Fraction that adsorb via insertion into the SAM as a function of incident kinetic energy, as predicted from molecular simulation.

What is most interesting from the molecular simulation is not the absolute values for the probabilities of adsorption but, rather, the nature of the events that lead to trapping and adsorption. As described above, we observed both conventional trapping and adsorption on the surface of the SAM, but also direct molecular insertion into the organic layer. In Figure 3-10(b) we consider the relative contributions of these two outcomes, where we plot the fraction of those molecules that adsorb that end up trapped within the SAM layer as a function of the incident kinetic energy. On ODTS, we see that the fraction is always > 0.7, and it exhibits an increase with increasing energy, where greater than ~ 90% of the DIP molecules are predicted to insert at incident kinetic energies at and above 10 eV. Such a dependence on incident kinetic energy may suggest that there is, in effect, a barrier to the insertion of DIP into the ODTS layer. If true, one might expect that this barrier may depend upon the molecular density in the SAM layer. In contrast, on the OTS surface, we observe a modest decrease in the fraction of molecules that insert into the SAM layer, perhaps indicating that insertion into this layer is not activated. We note that the jagged nature of these results with E_i (for both OTS and FOTS) is probably associated with the modest number of trajectories simulated here.

Moving on to the results for FOTS we see that the predicted fraction of DIP molecules that insert into this SAM is less than that observed for OTS, except for a single value of E_i. The dependence on incident kinetic energy is difficult to assign in this case, as there is not an obvious trend with E_i. Regardless, the fraction that insert (of those that adsorb) into the FOTS layer is still quite high, > 50% for the entire range of incident kinetic energies considered here. What factors may contribute to the

imperfect agreement between the total adsorption probability measured and that predicted by simulation? In Sec. III.C we argued, based on the densities of the SAMs measured for x-ray reflectivity, that the FOTS layer may be expected to be more difficult to penetrate by the incident DIP molecule. Indeed, the density of the SAM can play an important role in terms of the contributions of insertion to adsorption, and the total probability of adsorption. In work presented elsewhere **[50]**, increasing the SAM density by about ~ 50% can lead to a decrease in the adsorption probability by a factor of 2, particularly at high incident kinetic energies. Much of this is due to a decreased fraction that insert into the SAM layer.

3.5 Conclusions

We have examined the initial stages of growth of a small molecule crystalline organic thin film, diindenoperylene, on surfaces terminated with self-assembled monolayers. We considered explicitly the effects of the thickness of the SAM, and less so, the chemical composition of the terminating layer. For growth on bare SiO_2, and SiO_2 modified by both HMDS and FOTS, the probability of adsorption on the starting surface decreases significantly with increasing incident kinetic energy. This is consistent with conventional trapping-mediated adsorption, where a sufficient fraction of the incident kinetic energy must be transferred to the substrate surface. On these same surfaces, once the substrate is covered by the growing DIP thin film, the adsorption probability increases significantly. This increase in the adsorption probability reflects more efficient energy exchange between the incident DIP, and the DIP present in the growing thin film, due to better mass-matching, and the possible contributions of direct molecular insertion into the DIP layer. Concerning adsorption on two straight-chain alkylsilanes, OTS and ODTS, we find efficient trapping both on the starting surfaces, and on the DIP thin film in these two cases. These results suggest that there are energy dissipation channels that contribute significantly on the OTS- and ODTS- terminated surfaces, either not present on the surfaces terminated by the shorter SAM produced by HMDS, or that contribute less on the fluorinated SAM, FOTS. Experimental data suggest that molecular insertion can play a role in more efficient energy transfer on the OTS- and ODTS- terminated surfaces, while it clearly will have a much reduced role on the much thinner HMDS- terminated layer on SiO_2.

Results from molecular simulation bear out these interpretations in the case of OTS and ODTS, and back the conclusion that molecular insertion is significant on these surfaces.

3.6 References

1. Y. Y. Lin, D. J. Gundlach, S. F. Nelson, and T. N. Jackson, IEEE Electron Device Letters **18**, 606 (1997).
2. T. W. Kelley, L. D. Boardman, T. D. Dunbar, D. V. Muyres, M. J. Pellerite, and T. P. Smith, J. Phys. Chem. B **107**, 5877 (2003).
3. D. Knipp, R. A. Street, A. Volkel, and J. Ho, J. Appl. Phys. **93**, 347 (2003).
4. R. Ruiz, B. Nickel, N. Koch, L.C. Feldman, R. F. Haglund Jr., A. Kahn, F. Family, and G. Scoles, Phys. Rev. Lett. **91**, 136102 (2003).
5. A. C. Mayer, R. Ruiz, R. L. Headrick, A. Kazimirov, and G. G. Malliaras, Organic Electronics **5**, 257 (2004).
6. S. Pratontep, F. Nuesch, L. Zuppiroli, and M. Brinkmann, Phys. Rev. B **72**, 085211 (2005).
7. Y. L. Wang, W. Ji, D. X. Shi, S. X. Du, C Seidel, Y. G. Ma, H.-J. Gao, L. F. Chi, and H. Fuchs, Phys. Rev. B **69**, 075408 (2004).
8. F.-J. Meyer zu Heringdorf, M. C. Reuter, and R. M. Tromp, Nature, **412**, 517 (2001)
9. S. Kowarik, A. Gerlach, S. Sellner, F. Schreiber, L. Cavalcanti and O. Konovalov, Phys Rev. Lett. **96**, 125504 (2006).
10. A. C. Dürr, N. Kock, M. Kelsch, A. Rühm, J. Ghijsen, R. L. Johnson, J,-J. Pireaux, J. Schwartz, F. Schreiber, H. Dosch, and A. Kahn, Phys. Rev. B **68**, 115428 (2003).

11. V. Ignatescu, J.-C. M. Hsu, A. C. Mayer, J. M. Blakely, and G. G. Malliaras, Appl. Phys. Lett. **89**, 253116 (2006).

12. I. Yagi, K. Tsukagoshi, and Y Aoyagi, Appl. Phys. Lett. **86**, 103502 (2005).

13. H. Yang, T. J. Shin, M. M. Ling, K. Cho, C. Y. Ryu, and Z. Bao, J. Am. Chem. Soc. **127**, 11542 (2005).

14. M. Shtein, J. Mapel, J. B. Benziger, and S. R. Forrest, Appl. Phys. Lett. **81**, 268 (2002).

15. H. Klauk, M. Halik, U. Zschieschang, G. Schmid, W. Radlik, and W. Weber, J. Appl. Phys. **92**, 5259 (2002).

16. C. Kim, A. Facchetti, and T. J. Marks, Science, **318**, 76 (2007).

17. See, e.g., *Atomistic Aspects of Epitaxial Growth*, M. Kotrla, N. I. Papanicolaou, D. D. Vvedensky, and L. T. Wille, Eds. (Kluwer Academic, New York, 2002).

18. Casalis, M. F. Danisman, B. Nickel, G. Bracco, T. Toccoli, S. Iannotta, and G. Scoles, Phys. Rev. Lett. **90**, 206101 (2003).

19. S. Iannotta and T. Toccoli, J. Polymer Sci. B **41**, 2501 (2003).

20. A. S. Killampalli, T. W. Schroeder, and J. R. Engstrom, Appl. Phys. Lett. **87**, 033110 (2005).

21. A. S. Killampalli and J. R. Engstrom, Appl. Phys. Lett. **88**, 143125 (2006).

22. T. Toccoli, A. Pallaoro, N. Coppede, S. Iannotta, F. De Angelis, L. Mariucci, and G. Fortunato, Appl. Phys. Lett. **88**, 132106 (2006).

23. Y. Wu, T. Toccoli, N. Koch, E. Iacob, A. Pallaoro, P. Rudolf, and S. Iannotta, Phys. Rev. Lett. **98**, 076601 (2007).

24. S. Hong, A. Amassian, A. R. Woll, S. Bhargava, J. D. Ferguson, G. G. Malliaras, J. D. Brock, and J. R. Engstrom, Appl. Phys. Lett. **92**, 253304 (2008).

25. L. Q. Xia, M. E. Jones, N. Maity, and J. R. Engstrom, J. Vac. Sci. Technol. A **13**, 2651 (1995).

26. See, e.g., C. T. Rettner, D. J. Auerbach, J. C. Tully, and A. W. Kleyn, J. Phys. Chem. **100**, 13021 (1996).

27. G. M. Nathanson, Ann. Rev. Phys. Chem. **55**, 231 (2004).

28. (a) K. Bolton and J. B. C. Pettersson, Chem. Phys. Lett. **312**, 71 (1999); (b) K.Bolton, M. Svanberg, and J. B. C. Pettersson, J. Chem. Phys. **110**, 5380 (1999); (c) P. U. Andersson, M. B. Någård, K. Bolton, M. Svanberg, and J. B. C. Pettersson, J. Phys. Chem. A **104**, 2681 (2000).

29. (a) S. R. Cohen, R. Naaman, and J. Sagiv, Phys. Rev. Lett. **58**, 1208 (1987); (b) F. Schreiber, Prog. Surf. Sci. **65**, 151 (2000).

30. (a) B. S. Day, S. F. Shuler, A. Dcure, and J. R. Morris, J. Chem. Phys. **119**, 8084 (2003); (b) M. E. Bennett, W. A. Alexander, J. W. Lu, D. Troya, and J. R. Morris, J. Phys. Chem. C **112**, 17272 (2008); (c) M. K. Ferguson, J. R. Lohr, B. S. Day and J. R. Morris, Phys. Rev. Lett. **92**, 073201 (2004); (d) S. F. Shuler, G. W. Davis, and J. R. Morris, J. Phys. Chem. **116**, 9147 (2002).

31. B. S. Day, and J. R. Morris, J. Chem. Phys. **122**, 234714 (2005).

32. B. S. Day, and J. R. Morris, J. Phys. Chem. B **107**, 7120 (2003).

33. K. D. Gibson, N. Isa, and S. J. Sibener, J. Chem. Phys. **119**, 13083 (2003).

34. N. Isa, K. D. Gibson, T. Yan, W. Hase, S. J. Sibener, J. Chem. Phys. **120**, 2417 (2004).

35. K. D. Gibson, N. Isa, and S. J. Sibener, J. Phys. Chem. A **110**, 1469 (2006).

36. (a) S. A. Miller, H. Luo, S. J. Pachuta, R. G. Cooks, Science, **275**, 1447 (1997); (b) N. Wade, C. Evans, F. Pepi, and R. G. Cooks, J. Phys. Chem. B **104**, 11230 (2000); (c) D. G. Schultz, S. B. Wainhaus, L. Hanley, P. d. S. Claire, and W. L. Hase, J. Chem. Phys. **106**, 10337 (1997); (d) S. B. Wainhaus, H. Lim, D. G. Schultz, and L. Hanley, J. Chem. Phys. **106**, 10329 (1997); (e) K. V. Wolf, D. A. Cole, and S. L. Bernasek, Langmuir **17**, 8254 (2001); (f) V. J. Angelico, S. A. Mitchell, and V. H. Wysocki, Anal. Chem. 72 2603 (2000).

37. P. F. Ma, A. Dube, A. S. Killampalli, and J. R. Engstrom, J. Chem. Phys. **125**, 035706 (2006).

38. A. Amassian, T. V. Desai, S. Kowarik, S. Hong, A. R. Woll, G. G. Malliaras, F. Schreiber and J. R. Engstrom, J. Chem. Phys. **130**, 124701 (2009).

39. J. E. Goose and P. Clancy, J. Phys. Chem. C 111, 15653 (2007);

40. J. E. Goose, A. S. Killampalli, P. Clancy, and J. R. Engstrom, J. Phys. Chem C, **113**, 6068-6073 (2009).

41. T. W. Schroeder, Ph.D. Thesis (Cornell University, 2004).

42. R. Chen, H. Kim, P. C. McIntyre, and S. F. Bent, Chem. Mater. **17**, 536 (2005).

43. (a) S. R. Wasserman, G. M. Whitesides, I. M. Tidswell, B. M. Ocko, P. S. Pershan, and J. D. Axe, J. Amer. Chem. Soc. **111**, 5852 (1989); (b) I. M. Tidswell, B. M. Ocko, P. S. Pershan, S. R. Wasserman, G. M. Whitesides, and J. D. Axe, Phys. Rev. B **41**, 1111 (1990).

44. L. G. Parratt, Phys. Rev. B. **95,** 359 (1954).

45. S. Kowarik, A. Gerlach, M. Skoda, S. Sellner, F. Schreiber, Eur. Phys. J. Special Topics, **168**, 11 (2009).

46. A. R. Woll, T. V. Desai, and J. R. Engstrom, *under review at the J. Phys. Rev. B.*

47. P. I. Cohen, G. S. Petrich, P. R. Pukite, G. J. Whaley, A. S. Arrott, Surface Sci. **216**, 222 (1989).

48. A. S. Killampalli, P. F. Ma and J. R. Engstrom, J. Amer. Chem. Soc. **127**, 6300-6310 (2005).

49. D. A. King and M. G. Wells, Surface Sci. **29**, 454 (1972).

50. A. P. Kaushik and P. Clancy, Surf. Sci. **605**, 1185, (2011).

4. Hyperthermal organic thin film growth on surfaces terminated with self-assembled monolayers: II. Morphology and effect of substrate temperature

4.1 Overview

We have examined the effects of substrate temperature (T_s), incident energy (E_i), and chemical nature of self-assembled monolayers (SAMs) on the growth and morphology of diindenoperylene (DIP) thin films. The SAMs investigated were low surface energy hydrophobic surfaces: perfluorooctyltrichlorosilane, (FOTS), octadecyltrichlorosilane (ODTS), octyltrichlorosilane (OTS) and hexamethyldisilazane, (HMDS). We also compared to results on clean SiO_2. Our results indicate that increasing T_s leads to smoother DIP thin films with larger in-plane features/grains on both clean SiO_2 and HMDS-modified SiO_2. At identical deposition conditions DIP grows similar all surfaces investigated except on the thickest SAM layer, ODTS, where roughness increases very quickly after the first monolayer. The chemical nature of the surface also significantly affects the DIP in-plane feature/grain size. At identical deposition conditions, the largest features/grains are formed on FOTS and the smallest sized features/grains on ODTS and clean SiO_2. Incident energy, E_i, does not affect the in-plane feature/grain size on any of the surfaces investigated. Viewing the results as a whole, incident energy, E_i, has the least effect on DIP thin film growth and morphology whereas substrate temperature, T_s, and chemical nature of SAM have the greatest.

4.2 Introduction

The study of complex conjugated molecules, for applications in organic thin film electronics and photonics has received much attention owing to their ability to form highly ordered thin films with excellent electrical properties **[1-3]**. Studies have shown that the interface between the organic semiconducting layer and the dielectric is critical to charge transport and that the majority of charge carriers are generated in the first few monolayers (MLs) of the organic layer **[4-7]**. Several studies have also shown that the deposition of organic semiconductors on low energy surfaces such as self-assembled monolayers (SAMs) significantly improves the electrical properties of the organic thin film transistor (OTFT) **[8-12]**. The exact reasons as to why this improvement is observed are still a matter of debate, however. Clearly, the development of a better understanding of the effects of SAMs on the thin film growth and morphology will greatly aid in resolving these issues.

An organic semiconductor that has recently been of significant research interest **[13-15]** and an excellent candidate for applications in both organic thin film transistors and organic photovoltaics is diindenoperylene (DIP). Studies have shown that DIP thin films on silicon dioxide (SiO_2) transition from a layer-by-layer growth mode to rapid roughening after the first few monolayers (MLs) of DIP growth **[16-18]**. Regarding structural orientation, studies have shown that the both the DIP in-plane lattice parameter and tilt (with respect to the surface normal) increase during the first few MLs of DIP growth on SiO_2 **[16, 17, 19]**. Other studies have investigated the effect of substrate temperature on DIP growth on both SiO_2 **[20, 21]** and SiO_2 modified with a SAM (amino-terminated) **[22]** and show that the in-plane grain size

increases with T_s. Several studies have also studied the formation of organic heterostructures, where they have investigated the deposition of DIP on other organic semiconductors and vice versa **[21, 23-26]**. Finally, the combined use of DIP and C_{60} in organic photovoltaics has also been investigated, where power conversion efficiencies as high as 4.1% have been reported **[27]**. Studies investigating the thin film growth of DIP on SAMs however remain limited, especially concerning the understanding of the effect of the chemical nature of a SAM on the thin film growth and morphology of DIP.

Here we report on the effects of self-assembled monolayers (SAMs) on the thin film deposition of DIP, concentrating on the initial stages of growth and morphology using a combination of both *in situ* and *ex situ* surface sensitive techniques. The focus is to develop a better understanding of the interactions that take place between DIP and surfaces terminated with SAMs and their effects on DIP thin film growth and morphology. Concerning the SAMs, we consider four layers that differ in terms of their thickness and chemical nature, namely: octadecyltrichlorosilane, (ODTS), octyltrichlorosilane, (OTS), perflurooctyltrichlorosilane (FOTS) and hexamethyldisilazane, (HMDS). We also compare to results on clean SiO_2. We deposit thin films of DIP in ultrahigh vacuum (UHV) using a collimated supersonic molecular beam **[28-30]** and, as with our previous studies **[30-32]**, we use *in situ* real-time synchrotron x-ray scattering to monitor the growth from the submonolayer to the multilayer regime. In our previous studies **[31, 32, 33]**, we concentrated on the effects of the chemical nature of the SAM on the adsorption and trapping dynamics of DIP thin film growth, whereas, in this

study, we concentrate on the effect of the chemical nature of the SAM on the growth and morphology of DIP thin films. In addition, we also investigate the effect of substrate temperature, T_s, on DIP growth on both clean SiO_2 and SiO_2 modified with HMDS. To probe the effects of the SAMs on the morphology of DIP we use *ex situ* atomic force microscopy (AFM). We show that both T_s and the chemical nature of the substrate have a significant impact on the growth mode and morphology of DIP thin film growth.

4.3 Experimental Procedures

Refer to chapter 2 for details. Only a brief summary on experimental procedures is provided in this section. All experiments using *in situ* synchrotron x-ray scattering were carried out in the G3 station of the Cornell High Energy Synchrotron Source (CHESS) in a custom-designed four-chamber ultrahigh vacuum (UHV) system (base pressure ~ 4×10^{-9}) fitted with Be windows that is described in detail elsewhere **[29]**. The starting bare substrates, consisting of (100) wafers of Si with ~ 300 nm of SiO_2, were prepared and cleaned as described in detail elsewhere **[32]**. The solution-based SAMs, OTS and ODTS, were assembled on the SiO_2|Si(100) substrates in a N_2-purged glove box ([O_2] < 10 ppm; [H_2O] < 1 ppm). All solutions were 10 mM concentration of the SAM precursor molecule in toluene. The SiO_2 substrates were dipped in the SAM solution for 2 days and left in the glove box undisturbed, followed by sequential rinsing in toluene, acetone, chloroform, DI water and finally drying with N_2 **[32]**. HMDS and FOTS were formed on the SiO_2 substrates via vapor phase deposition. HMDS was deposited using a YES LP-III Vapor Prime Oven after

successive evacuation and purge cycles to dehydrate the substrate held at 150°C. FOTS was deposited using an MVD-100 system.

The SAMs (shown in Figure 4-1) were characterized using a number of techniques as described in detail elsewhere **[32]**. Contact angle measurements were carried out using the VCA Optima XE system (AST Products Inc., Billerica, MA), and the thicknesses of the SAMs were measured with a variable angle spectroscopic ellipsometer (Woolam). The thickness, electron density and surface coverage of the SAMs were also characterized using synchrotron x-ray reflectivity (XRR) measurements. These measurements were conducted as indicated above in the vacuum chamber in the G3 station using 9.75 keV X-rays with a flux of ~ 10^{13} photons-$mm^{-2}s^{-1}$ (typically attenuated), incident to the sample through a Be window. The scattered x-ray intensity was monitored using a silicon avalanche photodiode detector (APD, Oxford Danfysik, Oxford, UK). Details of the XRR experiments, including their fitting procedures and the properties of the SAMs can be found elsewhere **[32]**. Properties of the SAMs can also be found in Table 3-1. Briefly, as determined from XRR measurements, the thickness (density) of ODTS, OTS and FOTS is 17.3 ± 1.8 Å (2.83 ± 0.29 nm^{-2}), 6.27 ± 0.65 Å (2.74 ± 0.28 nm^{-2}) and 6.32 ± 0.50 Å (1.97 ± 0.12 nm^{-2}) respectively. The surface energy of FOTS, OTS and HMDS was measured to be 11.1, 16.7, 32.7 mJ-m^{-2}, respectively. The surface energy of ODTS is expected to be similar to OTS – static water contact angles between the two differed by ~1° **[32]**. From previous studies, the surface energy of ODTS was measured to be 23.5-25.38 mJ-m^{-2} **[34]**.

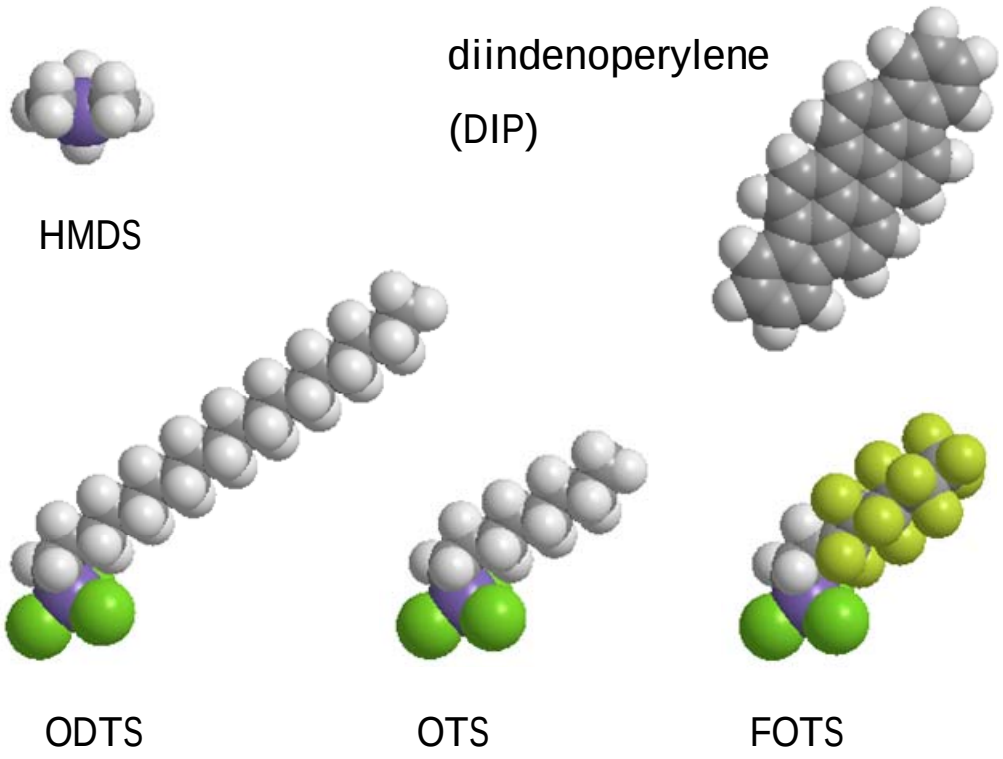

Figure 4-1 Space-filling models for the molecule of interest here, diindenoperylene (DIP), and the four molecules that form the SAMs examined here: octadecyltrichlorosilane (ODTS); octyltrichlorosilane (OTS), perflurooctyltrichlorosilane (FOTS), and the chemisorbing species formed upon exposure of SiO_2 to hexamethyldisilazane (HMDS), $HSi(CH_3)_3$, where H represents the SiO_2 surface.

Supersonic molecular beams of diindenoperylene were generated by using He as a carrier gas as described in detail elsewhere **[31, 32]**. By varying the He flow rate, the beam energy could be varied from 4.2 to 11.3 eV as determined from time of flight measurements **[29]**, while the DIP beam flux was varied by adjusting the temperature of the *in situ* temperature controlled evaporator or "bubbler" (typically, $T_b \sim 320$ °C, nozzle temperature $T_{noz} \sim 500$ °C). Multiple experiments could be carried out on the same substrate, by translating the substrate perpendicular to the supersonic molecular beam, and due to the high beam-to-background flux ratio. For growth on clean SiO_2 and HMDS, the substrate temperature was varied between $T_s = 40$ °C, 64 °C and 89 °C, whereas, for growth on ODTS, OTS and FOTS, the substrate temperature was fixed at $T_s = 40$ °C. In all cases, the beam was incident along the surface normal.

Time-resolved and *in situ* measurements of the scattered x-ray synchrotron intensity were made using a silicon avalanche photodiode detector (APD, Oxford Danfysik, Oxford, UK). During pentacene thin film growth the intensity was monitored at the anti-Bragg position (00½; $q_z = q_{Bragg}/2 = 0.41/2$ Å^{-1}), which is an effective monitor of the nature of growth, i.e., layer-by-layer (LbL) vs. 3D islanded growth **[35]**. Following deposition and x-ray analysis, the samples were removed for *ex situ* analysis using AFM, conducted in tapping mode using a DI 3100 Dimension microscope.

The x-ray data at the anti-Bragg position was fitted using a modified version **[31, 32, 36]** of the mean-field rate equation model of growth first proposed by Cohen and co-workers **[37].** Briefly, the equations for the coverage of individual layers (θ_n) are given by:

$$\frac{d\theta_n}{dt} = S_{n-1}F\left[\left(\theta_{n-1} - \theta_n\right) - \alpha_{n-1}\left(\theta_{n-1} - \theta_n\right)\right] + S_nF\alpha_n\left(\theta_n - \theta_{n+1}\right) \quad (4\text{-}1)$$

where $n = 0$ represents the substrate, $n = 1$ the first molecular layer, etc., S_n is the probability of adsorption for molecules incident on the n^{th} layer, F is the incident molecular flux (ML-s^{-1}), and α_n is the fraction of molecules that initially impact and land on top of the n^{th} layer, but rather than staying on the top of that layer, drop down and become part of that layer via some mechanism. In this model we also assume that there are two values for the probability of adsorption: one for adsorption on the substrate (S_0), and one for that on previously existing molecular layers, independent of their thickness ($S_1 = S_2 = S_3\ldots$). Concerning interlayer transport, we will assume that three values are possible (note, as the substrate cannot be penetrated, $\alpha_0 = 0$), namely α_1, α_2 and $\alpha_{n \geq 3}$. "Upward" interlayer transport (movement from the n to the $n + 1$ layer) is not included in the model.

Once layer coverages have been calculated by integrating Equation (4-1), these can then be used to calculate the scattered x-ray intensity as a function of time **[31, 32 ,35-37]**. The intensity of the scattered beam (I) depends upon the layer population, θ_n(t), according to the following relationship:

$$I(t) = \left| r_{subs}e^{-i\phi} + r_{film}\sum_{n}^{\infty}\theta_n(t)e^{-iq_z dn} \right|^2 \quad (4\text{-}2)$$

where r_{subs} and r_{film} are the scattering amplitudes of the substrate and the film, ϕ is the phase change upon reflection, q_z is the out-of-plane scattering vector and d is the out-of-plane interplanar spacing. At the anti-Bragg position, $q_z d = \pi$, which results in a change in the sign of the thin film terms in the summation. If each layer fills sequentially, such as in perfect LbL growth, an oscillation in the intensity results.

4.4 Results and Discussion

We start first by examining the growth of DIP on clean SiO_2 as a function of substrate temperature (T_s = 40 °C, 64 °C and 89 °C), as shown in Figure 4-2. In Figure 4-2(a) we present the scattered x-ray intensity acquired in real time at the anti-Bragg condition (q_z = 00½) for the growth of DIP on SiO_2 at E_i = 4.2 eV, T_s = 40 °C and growth rate, *GR*, of 0.013 MLs^{-1}. As may be seen, we observe in sequence a first small maximum (~ 1 ML), a larger maximum (~ 2 ML), a totally obscured second smaller maximum, a strongly damped second larger maximum (~ 4 ML), and finally a hint of a third larger maximum (~ 6 ML). Thus, for these conditions we see that DIP grows in a layer-by-layer (LbL) mode until approximately 4 MLs, after which the intensity oscillations are strongly damped, indicative of 3D growth. The intensity oscillation can be fit using a modified version **[36]** of the mean-field, rate equation model of growth first proposed by Cohen and co-workers **[37]**. The fit to the intensity is indicated by the solid blue line, and we see that the fit to the experimental data is excellent. In Figure 4-2(a) we also show the coverage (occupancy) of each layer with solid black lines that are predicted by the fit to the intensity oscillations. After a total growth of 2 MLs, the 2nd layer is ~ 85% full, whereas after 4 MLs the 4th layer is only

Figure 4-2 X-ray intensity at the anti-Bragg condition as a function of exposure to the molecular beam for thin films of pentacene deposited on SiO_2 at E_i = 4.2 eV and T_s = (a) 40 °C (c) 64 °C and (e) 89 °C . Thick solid lines (right ordinate) indicate a fit of the data to a model and thin solid curves (left ordinate) represent predicted coverage of individual layers. AFM images, 3×3 μm^2, of pentacene thin films deposited on SiO_2 at T_s = (b) 40 °C (d) 64 °C and (f) 89 °C.

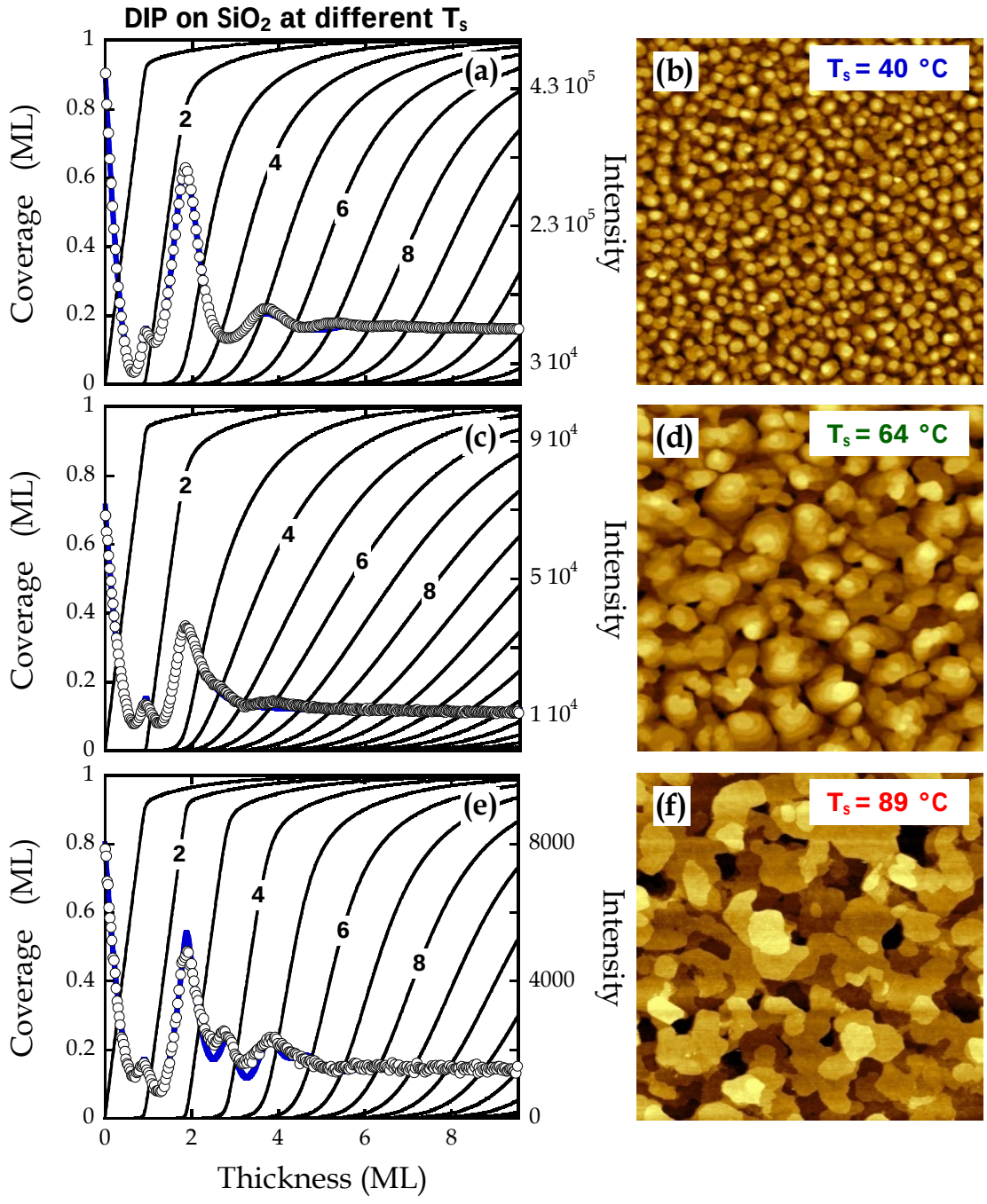
DIP on SiO2 at different Ts
Coverage (ML)
Intensity
Thickness (ML)
(a)
(b)
(c)
(d)
(e)
(f)
2
4
6
8
4.3 10^5
2.3 10^5
3 10^4
9 10^4
5 10^4
1 10^4
8000
4000
0
Ts = 40 °C
Ts = 64 °C
Ts = 89 °C

~ 69% full. These results indicate that DIP grows in a layer-by-layer (LbL) mode for approximately 4 MLs before significant roughening begins to occur. In Figure 4-2(c), we present the growth of DIP on SiO_2 at E_i = 4.2 eV, T_s = 64 °C and *GR* of 0.0090 MLs^{-1}. Regarding the growth, we observe intensity oscillations up to ~4 MLs after which the intensity remains constant indicating that rapid 3D growth has commenced. However, the oscillations appear somewhat more damped compared to growth at 40 °C (*cf.* Fig 2(a)) – for example, after a total growth of 2 MLs, the 2nd layer is ~ 85% full (similar to that at 40 °C), whereas after 4 MLs the 4th layer is only ~ 59% full (69% at 40 °C). In Figure 4-2(e), we present the growth of DIP on SiO_2 at E_i = 4.2 eV, T_s = 89 °C and *GR* of 0.010 MLs^{-1}. Regarding the growth, we observe intensity oscillations up to ~4-5 MLs after which the intensity remains constant indicating that rapid 3D growth has commenced. In comparison to DIP growth on SiO_2 at 40 °C and 64 °C, at 89 °C, we also see growth oscillations until ~4-5 MLs but they are more pronounced – for example, the intensity oscillation at ~3 MLs is more prominent. Using the fit to the data, after a total growth of 2 MLs, the 2nd layer is ~ 93% full and after 4 MLs the 4th layer is ~ 84% full (~ 69% and ~ 59% at 40 °C and 64 °C respectively) – these results imply that DIP on SiO_2 grows in a more LbL manner at higher T_s **[21]**. In Figures 4-2(b, d, and f), we present the AF micrographs (3 × 3 μm^2) of DIP on SiO_2 at 40 °C, 64 °C and 89 °C respectively. The nominal film thicknesses as determined from the fit to the x-ray scattering data is 9.5 ML, 10.9 ML and 10.0 ML at 40 °C, 64 °C and 89 °C respectively. As observed, at all three T_s, we see compact shaped features/grains and the lateral size of the feature/grains increases significantly with increasing T_s **[21]**. Increasing T_s increases the surface diffusivity of

DIP, therefore resulting in larger in-plane features/grains. A detailed analysis of the features shown in Figures 4-2(b, d, f) will be discussed later.

The films of DIP on clean SiO_2 shown in Figures 4-2(b, d, and f) were also characterized using post-growth x-ray reflectivity (XRR) – in fact, the average d_{001} spacing for the DIP thin films on all surfaces investigated in this study was determined to be 1.68 ± 0.01 nm, similar to other reported studies **[20, 38]**. Thin films of DIP deposited on SiO_2 and HMDS were also characterized using grazing incidence diffraction (GID) at all T_s investigated (40 °C, 64 °C and 89 °C). Multiple peaks were observed in the GID spectra indicating the random distribution of the domains in the plane of the surface – the peaks observed here and are in agreement with the previously reported "thin film" phase **[20, 38]**.

Experiments for the growth of DIP on SiO_2 at 64 °C and 89 °C were conducted twice (in separate CHESS runs and separate batches of SiO_2) and we show the second set of results in Figure 4-3. In Figure 4-3(a), we present the growth of DIP on SiO_2 at E_i = 4.2 eV, T_s = 64 °C and *GR* of 0.014 MLs^{-1}. Regarding the growth, we observe intensity oscillations up to ~6 MLs after which rapid 3D growth commences. Compared to Figure 4-2(c), growth in this case is more LbL – this modest difference in growth mode maybe due to subtle differences in the bare SiO_2 substrate or in *GR* (0.014 MLs^{-1} vs. 0.0090 MLs^{-1}) . Figure 4-3(c), shows the growth of DIP on SiO_2 at E_i = 4.2 eV, T_s = 89 °C and *GR* of 0.015 MLs^{-1}. Regarding the growth, we observe intensity oscillations up to ~7-8 MLs after which rapid 3D growth commences. Compared to Figure 4-2(e), growth in this case is more LbL – this modest

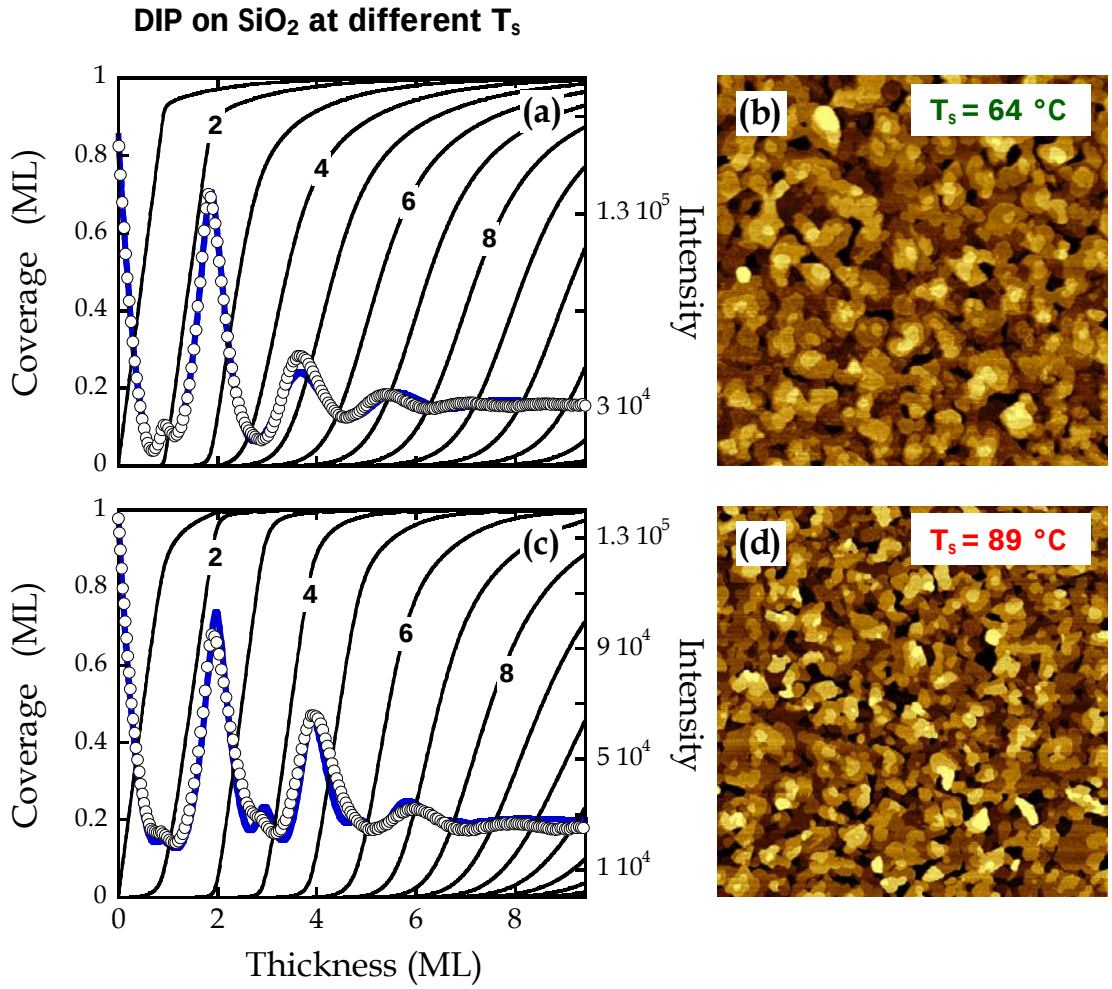

Figure 4-3 X-ray intensity at the anti-Bragg condition as a function of exposure to the molecular beam for thin films of pentacene deposited on SiO_2 at E_i = 4.2 eV and T_s = (a) 64 °C and (c) 89 °C . Thick solid lines (right ordinate) indicate a fit of the data to a model and thin solid curves (left ordinate) represent predicted coverage of individual layers. AFM images of pentacene thin films deposited on SiO_2 at T_s = (b) 64 °C, 3×3 μm^2 and (d) 89 °C, 10×10 μm^2.

difference in growth mode maybe due to subtle differences in the bare SiO_2 substrate or in *GR* (0.015 MLs^{-1} vs. 0.010 MLs^{-1}). However, in comparison to growth at the lower T_s, 40 °C (*cf.* Figure 4-2(a)) and 64 °C (*cf.* Figure 4-2(c) and Figure 4-3(a)), growth at 89 °C (*cf.* Figure 4-2(e) and Figure 4-3(c)) is more LbL. Viewing both sets of experiments, (*cf.* Figure 4-2 and Figure 4-3), the results clearly indicate that the growth mode of DIP on SiO_2 is more LbL as T_s increases **[21]**. In Figure 4-3(b and d), we present the AF micrographs of DIP on SiO_2 at 64 °C (3×3 μm^2) and 89 °C (10×10 μm^2) respectively. As in Figure 4-2, we observe compact shaped features/grains at both T_s, and the in-plane sizes of the features/grains increases with T_s. In fact, from AFM image analysis, the differences in the in-plane sizes of the features shown in Figures 4-2 and 4-3 are negligible at their respective substrate temperatures. Image analysis of the DIP morphology will be discussed in detail later.

In Figure 4-4 we plot the RMS surface roughness (as determined from the fit to the x-ray scattering data) as a function of the thickness of the thin film for DIP growth on SiO_2 and the different T_s we have examined here (*cf.* Figures 4-2 and 4-3). We consider coverages up to 6 MLs, which covers the range where we observe significant growth oscillations, and thus we have the most confidence in the occupation of the individual layers. In Figure 4-4(a), we show roughness predictions for the set of results shown in Figure 4-2 and in Figure 4-4(b), the set results shown in Figure 4-3. Also shown in Figure 4-4(b), as individual points, are the surface roughness values found from AFM analysis for DIP growth on SiO_2 at 89 °C – as observed, the corroboration between the fit to the x-ray data and AFM is excellent **[36]**. Viewed as a whole, Figure 4-4 indicates what was observed via the intensity growth oscillations

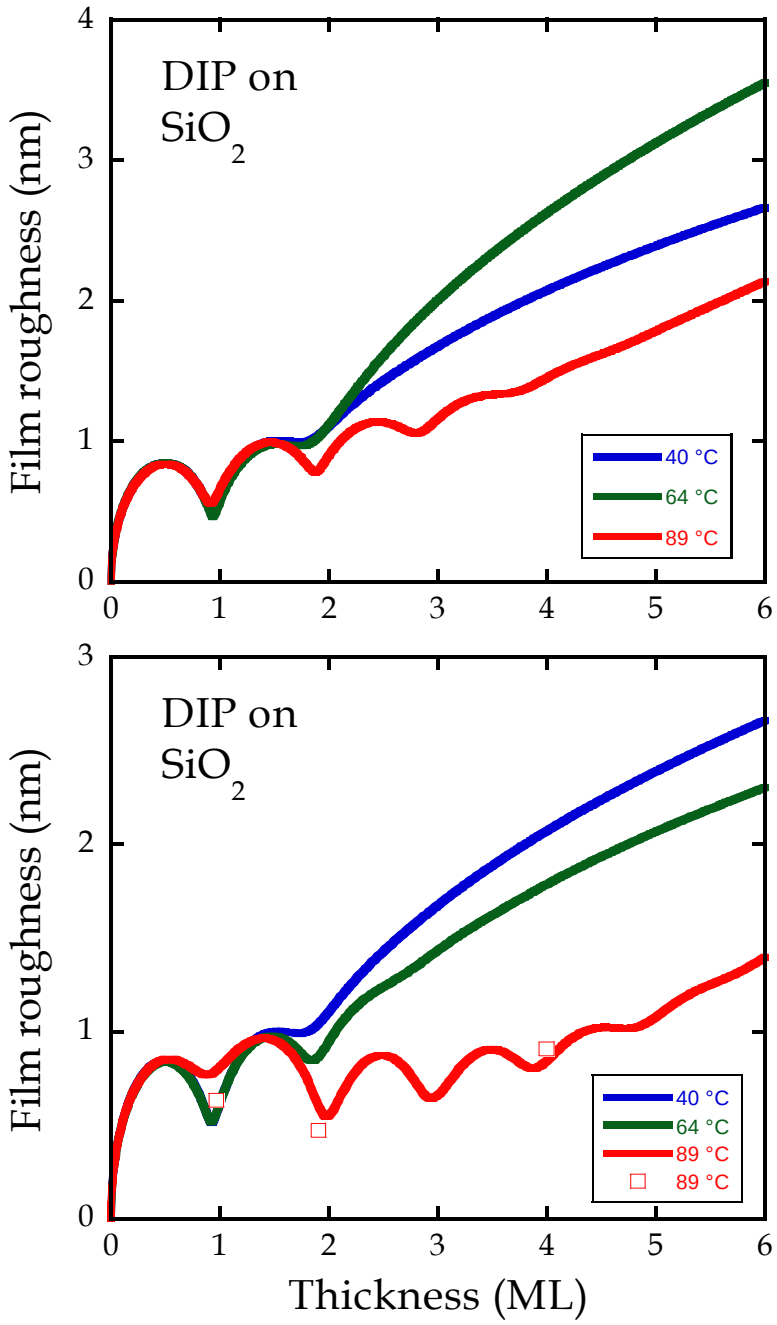

Figure 4-4 The RMS surface roughness as a function of the thickness of the DIP thin film, based on fits to the anti-Bragg intensities shown above in Figures 4-2 and 4-3 respectively. We consider the results for DIP incident at E_i = 4.2 eV and T_s = 40 °C for the 5 surfaces we have examined here.

shown in Figures 4-2 and 4-3, that DIP on clean SiO_2 grows in a more LbL manner and therefore smoother as T_s increases **[21]**. The rate of film roughening or sustained LbL growth will depend on the degree of interlayer transport – the ability of a molecule to transfer itself from on top of layer *n* initially, on to layer *n* via some mechanism. One mechanism is to diffuse to a step edge of an island and 'hop over' onto the layer below, but the DIP molecule will have to overcome a sufficient energy barrier in order for this to happen (Ehrlich-Schwoebel, *ES*, barrier **[39-43]**). By increasing T_s, the probability of overcoming the *ES* barrier will be higher and therefore facilitating interlayer transport and leading to more LbL growth. Thus, the observation of better LbL growth with increasing T_s may indicate the presence of an ES barrier.

In Figure 4-5(a), we present the growth of DIP on HMDS at E_i = 4.2 eV, T_s = 40 °C and *GR* of 0.014 MLs^{-1}. We observe intensity oscillations up to ~3 MLs after which the intensity remains constant indicating that rapid 3D growth has commenced. In Figure 4-5(c), we present growth of DIP on HMDS at E_i = 4.2 eV, T_s = 64 °C and *GR* of 0.010 MLs^{-1}. We observe intensity oscillations up to ~5 MLs after which rapid 3D growth commences. Compared to growth at 40 °C, LbL growth of DIP on HMDS is more prolonged at 64 °C – for example, after a total growth of 2 MLs, the 2^{nd} layer is ~ 89% full (~ 90% at 40 °C), whereas after 5 MLs the 5^{th} layer is ~ 71% full (only ~ 61% at 40 °C). In Figure 4-5(e), we present growth of DIP on HMDS at E_i = 4.2 eV, T_s = 89 °C and *GR* of 0.0096 MLs^{-1}. Regarding the growth, we observe intensity oscillations up to ~7 MLs after which the intensity remains constant indicating that rapid

Figure 4-5 X-ray intensity at the anti-Bragg condition as a function of exposure to the molecular beam for thin films of pentacene deposited on HMDS at E_i = 4.2 eV and T_s = (a) 40 °C (c) 64 °C and (e) 89 °C . Thick solid lines (right ordinate) indicate a fit of the data to a model and thin solid curves (left ordinate) represent predicted coverage of individual layers. AFM images, 3×3 μm^2, of pentacene thin films deposited on SiO_2 at T_s = (b) 40 °C (d) 64 °C and (f) 89 °C.

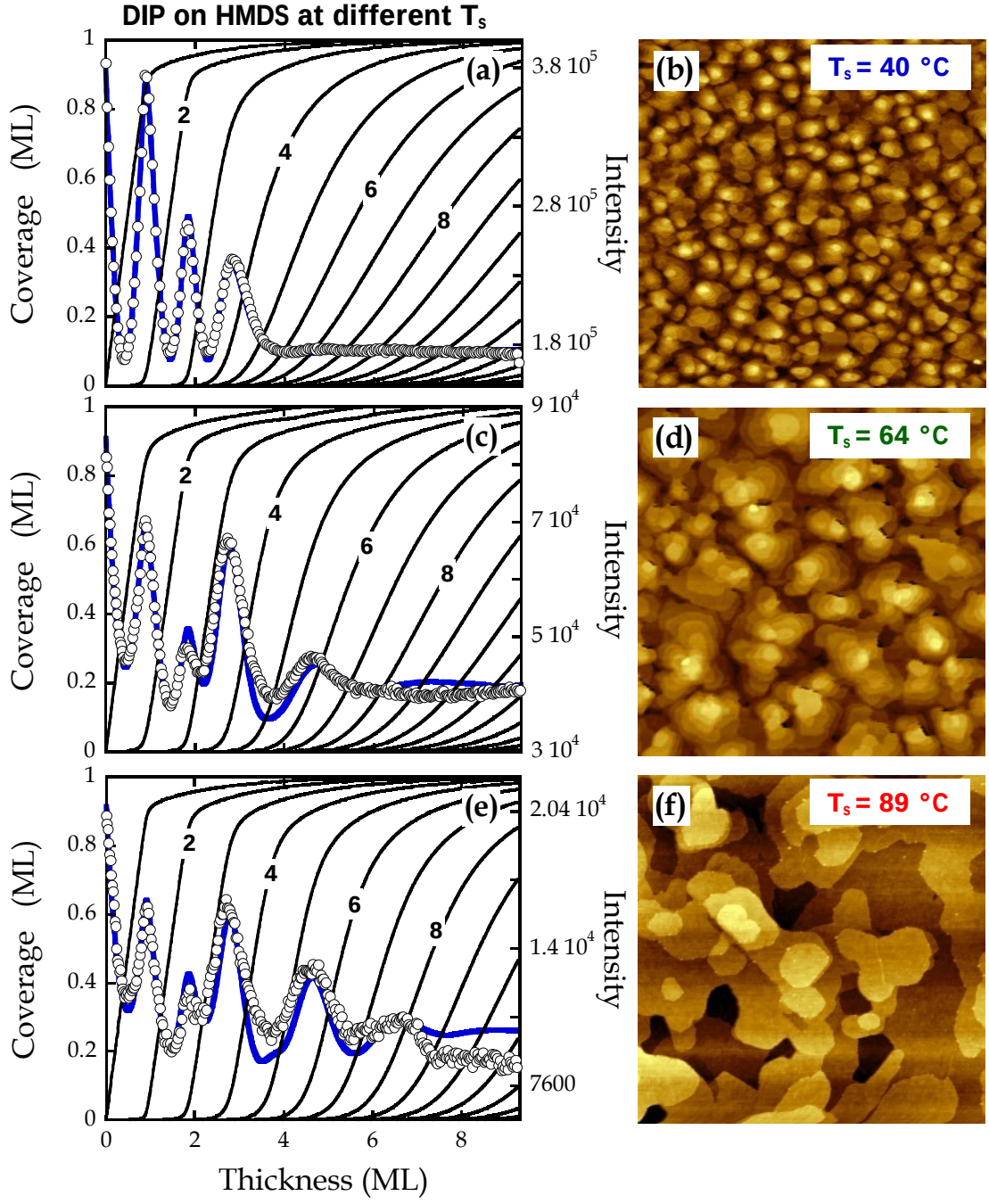
DIP on HMDS at different T_s
Coverage (ML)
Intensity
Thickness (ML)
(a)
(b)
T_s = 40 °C
(c)
(d)
T_s = 64 °C
(e)
(f)
T_s = 89 °C
2
4
6
8
3.8 10^5
2.8 10^5
1.8 10^5
9 10^4
7 10^4
5 10^4
3 10^4
2.04 10^4
1.4 10^4
7600

roughening has commenced. Looking at the results as a whole, DIP growth is most LbL at the highest temperature (89 °C) followed by 64 °C and 40 °C – for example, after a total growth of 7 MLs, the 7nd layer is ~ 71% full, ~ 61% full and ~ 57% full at 89 °C, 64 °C and 40 °C respectively – these results indicate that similar to that on clean SiO_2, increasing T_s promotes LbL growth for DIP deposited on HMDS. In Figures 4-5(b, d, and f), we present the AF micrographs (3×3 μm^2) of DIP growth on HMDS at 40 °C, 64 °C and 89 °C respectively. The nominal film thicknesses as determined from the fit to the x-ray scattering data is 9.3 ML, 10.6 ML and 9.3 ML at 40 °C, 64 °C and 89 °C respectively. As observed and similar to DIP growth on clean SiO_2, at all three T_s, we see compact shaped features/grains and the lateral size of the features/grains increases significantly with increasing T_s. Increasing T_s most likely increases the surface diffusivity of DIP, therefore resulting in larger in-plane features/grains. However, when compared to DIP growth on clean SiO_2 (*cf.* Figures 4-2 and 4-3), the in-plane sizes of the features/grains are greater on HMDS at each respective T_s. A detailed analysis the features shown in Figures 4-5(b, d, f) will be discussed later.

In Figure 4-6 we plot the RMS surface roughness (as determined from the fit to the x-ray scattering data) as a function of the thickness of the thin film for DIP growth on HMDS at the different T_s we have examined here (*cf.* Figure 4-5). We consider coverages up to 6 MLs, which covers the range where we observe significant growth oscillations, and thus we have the most confidence in the occupation of the individual layers. As observed in Figure 4-6, the roughness evolution at all T_s investigated is similar until at total coverage of ~ 3 MLs after which the film begins to

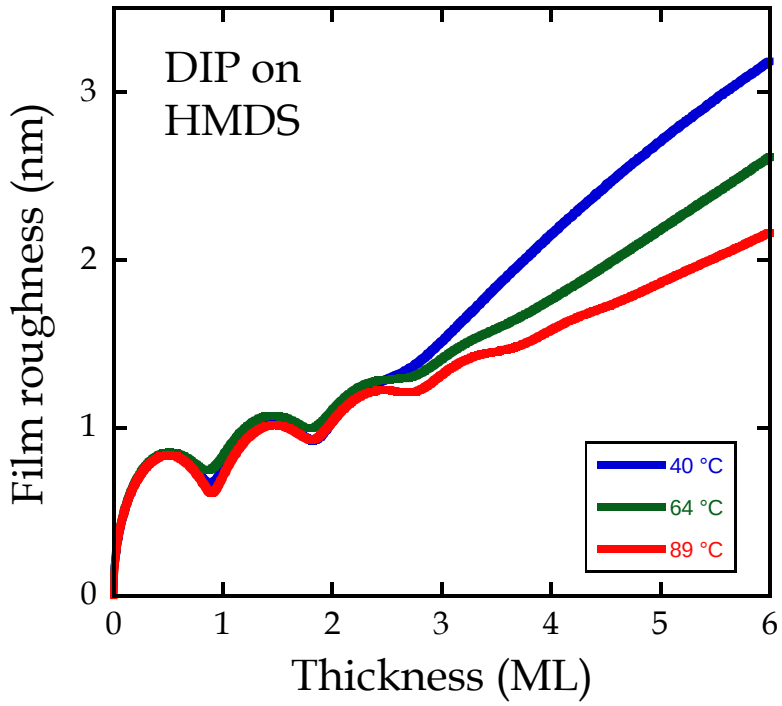

Figure 4-6 The RMS surface roughness as a function of the thickness of the DIP thin film, based on fits to the anti-Bragg intensities shown above in Figure 4-5. We consider the results for DIP incident at E_i = 4.2 eV and T_s = 40 °C, 64 °C and 89 °C for DIP deposited on HMDS.

grow rougher at the lowest T_s (40 °C) and the smoothest at the highest T_s (89 °C). As indicated in Figure 4-6 and confirming the observation via the intensity growth oscillations shown in Figure 4-5, that increasing T_s promotes LbL and hence smoother growth of DIP on HMDS – with increasing T_s, the probability of overcoming the *ES* barrier will be greater and therefore facilitating interlayer transport and leading to more prolonged LbL growth.

In order to quantify the features/grains of DIP on SiO_2 and HMDS at various T_s (*cf.* Figures 4-2, 4-3 and 4-5) we have analyzed these images by calculating their 1D power spectral density (1D PSD). For surfaces that are self-affine, the 1D PSD exhibits two linear regions on a log-log plot – a plateau region at low spatial frequencies (or inversely, lateral length scale) denoting the absence of correlations and a frequency dependent falloff region indicative of the self-affine nature of the film. Where these two regions intersect defines the lateral correlation length, ξ **[44, 45]**. In Figure 4-7(a), we plot example 1D PSD spectra of DIP deposited on HMDS (*cf.* Figure 4-5(e)) and on clean SiO_2 (*cf.* Figure 4-2(e)) at 89 °C and E_i = 4.2 eV. The spectra were taken using 10 × 10 μm^2 AF micrographs. In Figure 4-7(a), the filled circles and squares denote the points used in determining the fits to the plateau and falloff regions for DIP growth on HMDS and clean SiO_2 respectively. As can be observed, the intersection between the plateau region and falloff region appears at a lower spatial frequency for DIP deposited on HMDS indicating a larger correlation length. This is consistent with the larger features/grains observed on HMDS (*cf.* Figure 4-5(e)) versus that on SiO_2 (*cf.* Figure 4-2(e)). In Figure 4-7(b), we summarize

Figure 4-7 (a) Example 1D PSD spectra for DIP deposited HMDS and SiO_2 at E_i = 4.2 eV and T_s = 89 °C. Filled circles and squares indicate points used to determine fits for plateau and linear regions. (b) Lateral correlation length (right) and surface slope (left) for DIP deposited on HMDS and SiO_2 as a function of substrate temperature, T_s.

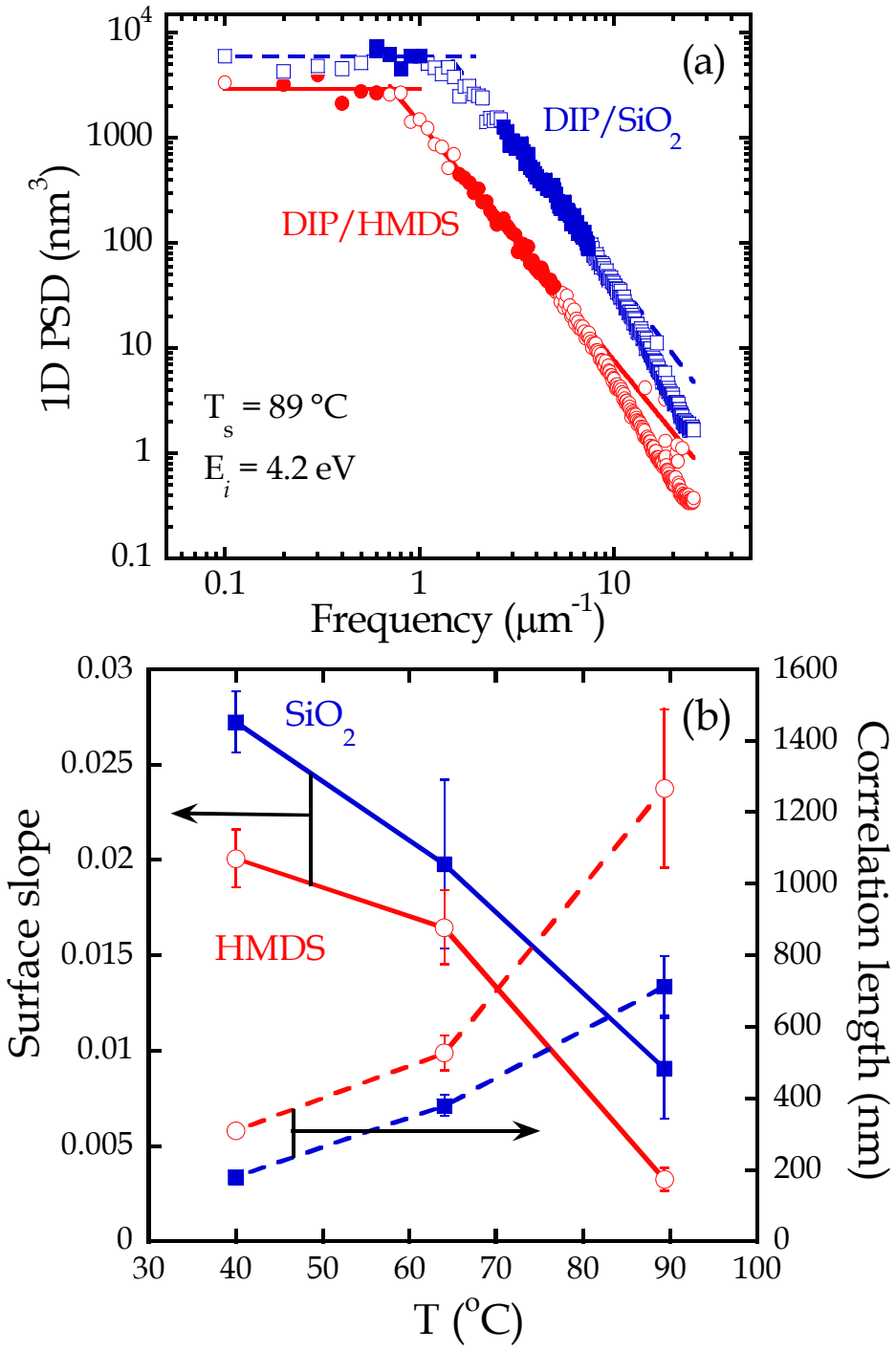
(a)
DIP/SiO2
DIP/HMDS
Ts = 89 °C
Ei = 4.2 eV
1D PSD (nm3)
Frequency (μm-1)
(b)
SiO2
HMDS
Surface slope
Correlation length (nm)
T (°C)

the DIP correlation length (as determined from ID PSD analysis of AF micrographs) as a function of T_s for DIP deposited on HMDS and on clean SiO_2. The reported values are an average and their respective error (standard deviation) associated from experiments taken at E_i = 4.2 eV (*cf.* Figures 4-2, 4-3, and 4-5), 6.4 eV, 9.4 eV and 11.3 eV. The DIP correlation length increases as a function of T_s on both HMDS and SiO_2. On SiO_2, the correlation increases from 180 ± 6 nm at 40 °C to 714 ± 84 nm at 89 °C. Similar increase in DIP correlation length with T_s is reported elsewhere for thermally deposited DIP on SiO_2 **[21]**. On HMDS, the correlation increases from 309 ± 11 nm at 40 °C to 1267 ± 221 nm at 89 °C. Increase in correlation length with T_s is most likely due to enhanced surface diffusivity at higher T_s. Interestingly, at each T_s investigated, the correlation length is greater on HDMS modified SiO_2 - we will return to why this may be occurring later in the discussion.

In Figure 4-7(b), we also plot the surface slope as a function of T_s for DIP deposited on HMDS and clean SiO_2. The reported values are an average and their respective error (standard deviation) associated from experiments taken at E_i = 4.2 eV (*cf.* Figures 4-2, 4-3, and 4-5), 6.4 eV, 9.4 eV and 11.3 eV. The surface slope is a measure of the film steepness and is defined as the ratio of the film roughness (RMS) to the film correlation length (RMS/2ξ). So a film that is dominated by pyramid shaped islands will have a higher surface slope, whereas a film dominated by smooth flat surfaces will have a lower surface slope. As can be observed, the surface slope decreases as a function of T_s for DIP on both HMDS and SiO_2 – this is as expected since DIP grows smoother with increasing T_s and the in-plane feature/grain size increases with increasing T_s (*cf.* Figures 4-2 to 4-7). This indicates that increasing T_s

promotes flatter and smoother features for DIP growth on both HMDS and clean SiO_2. In addition, our results indicate that the surface slope is slightly smaller for DIP deposited on HMDS at each T_s investigated – this is most likely dominated by the larger features/grains observed for DIP growth on HMDS.

We now turn our focus on comparing the effect of the chemical nature of the SAM on the growth and morphology of DIP thin films. In Figure 4-8, we present the growth of DIP deposited on ODTS, OTS and FOTS at E_i = 4.2 eV and T_s = 40 °C. Experiments on SAMs were conducted at T_s = 40 ºC to minimize any possible effects associated with the degradation of the SAMs, or changes in surface roughness with substrate temperature. In Figure 4-8(a), we present the growth of DIP on ODTS at *GR* of 0.012 MLs^{-1} where we observe intensity oscillations up to ~1-2 MLs after which rapid 3D growth commences. Compared to growth on SiO_2 (*cf.* Figure 4-2(a)) and HMDS (*cf.* Figure 4-5(a)) at similar growth conditions, DIP growth on ODTS roughens up very quickly. In Figure 4-8(c), we present the growth of DIP on OTS at *GR* of 0.012 MLs^{-1} where we observe intensity oscillations up to ~3 MLs after which rapid 3D growth commences. DIP growth on OTS is similar to that on SiO_2 and HMDS but smoother compared to that on ODTS. In Figure 4-8(e), we present the growth of DIP on FOTS at *GR* of 0.014 MLs^{-1}. We observe clear intensity oscillations up to ~3 MLs with hints (smaller oscillations) at ~5 MLs, after which rapid 3D growth commences. Similar to that on OTS, HMDS and SiO_2, growth on FOTS is smoother compared to that on ODTS. In Figure 4-9, we plot the RMS surface roughness as a function of the thickness of the thin film for the 5 surfaces we have examined here at identical deposition conditions. We consider coverages up to 4 MLs, which covers

Figure 4-8 X-ray intensity at the anti-Bragg condition as a function of exposure to the molecular beam for thin films of pentacene deposited at E_i = 4.2 eV, T_s = 40 °C and on (a) ODTS (c) OTS and (d) FOTS. Thick solid lines (right ordinate) indicate a fit of the data to a model and thin solid curves (left ordinate) represent predicted coverage of individual layers. AFM images, 3×3 μm^2, of pentacene thin films deposited on (b) ODTS (d) OTS and (f) FOTS.

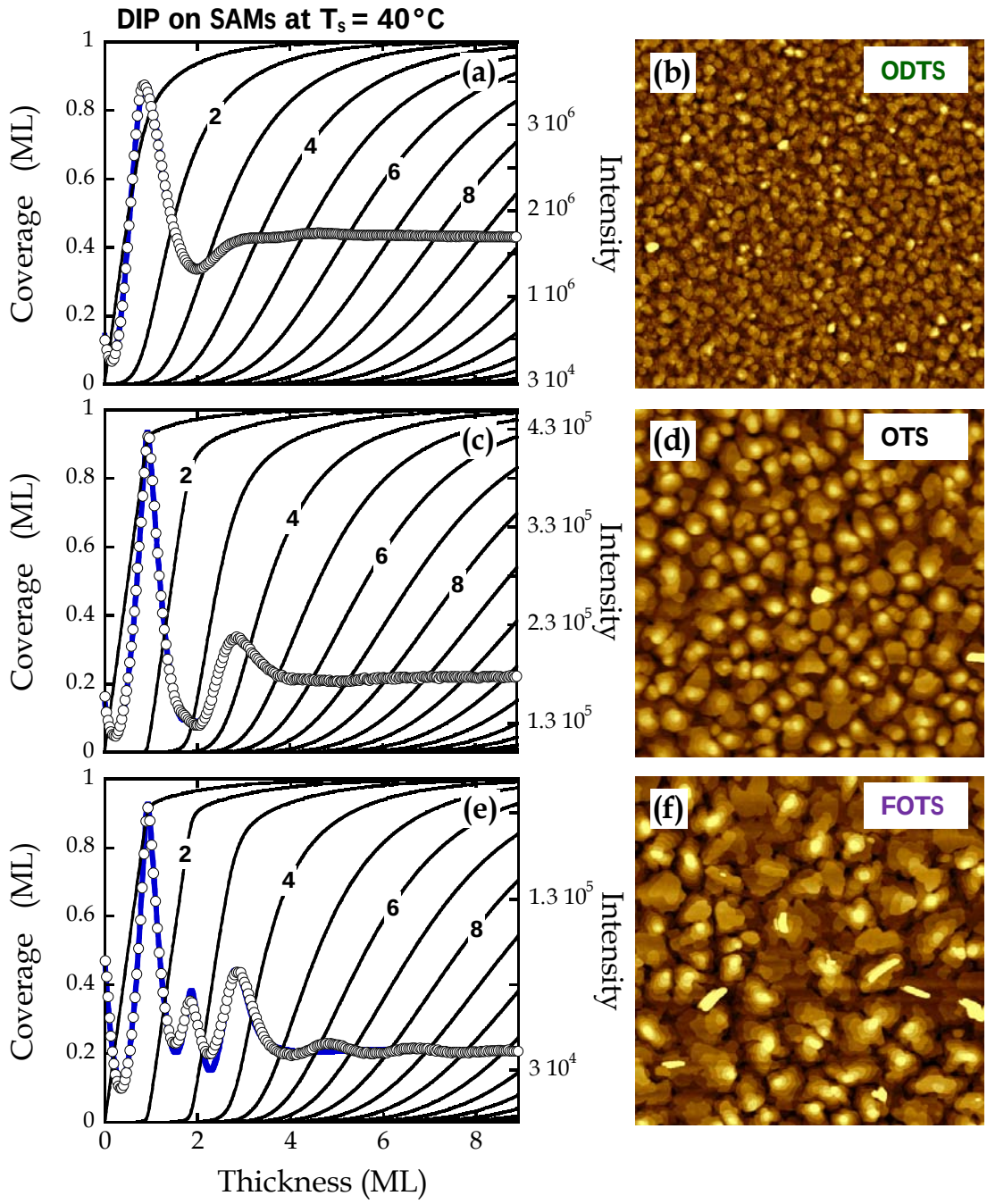
DIP on SAMs at T_s = 40°C
(a)
(b)
ODTS
(c)
(d)
OTS
(e)
(f)
FOTS
Coverage (ML)
Intensity
Thickness (ML)
2
4
6
8
3 10^6
2 10^6
1 10^6
3 10^4
4.3 10^5
3.3 10^5
2.3 10^5
1.3 10^5

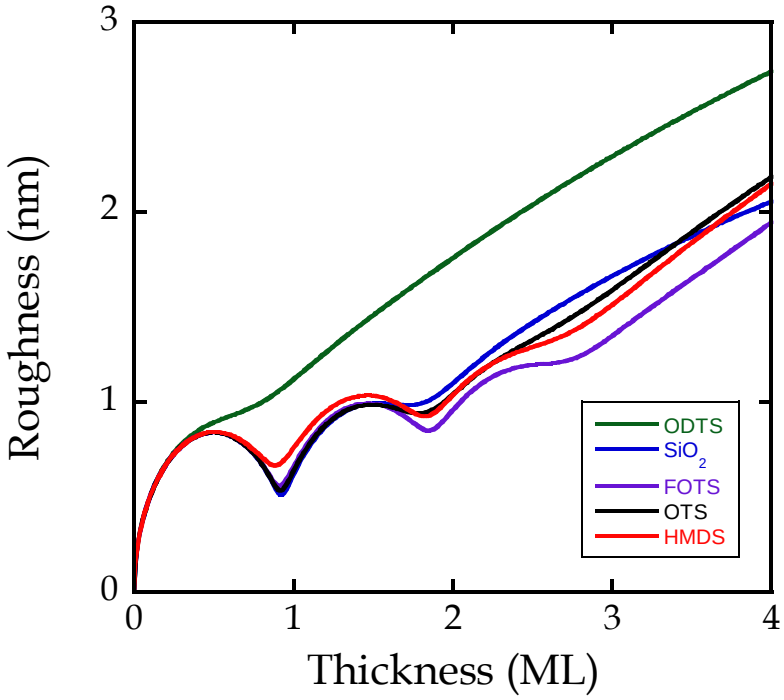

Figure 4-9 The RMS surface roughness as a function of the thickness of the DIP thin film, based on fits to the anti-Bragg intensities shown above in Figures 4-8, 4-5 and 4-2. We consider the results for DIP incident at E_i = 4.2 eV and T_s = 40 °C for the 5 surfaces we have examined here.

the range for which we observe in most cases significant oscillations, and thus we have the most confidence in the occupation of the individual layers. In Figure 4-9 we consider the results for DIP incident at E_i = 4.2 eV. As may be seen, the results seem to fall into two groups—unmodified SiO_2, HMDS, OTS, and FOTS in one group, and ODTS being its own group. Concerning the first group, for all four cases a clear minimum in the RMS is observed as the first monolayer is completed. For these cases, we also observe a pronounced second minimum, as the second monolayer is completed. Examining the layer occupancies predicted by the model, at 1 ML, on SiO_2 essentially all (99.99%) of the molecules are in the 1st (93.2%) and 2nd (6.7%), in contrast with ODTS where the first three are significantly occupied: 1st (79.7%); 2nd (18.5%); and 3rd (1.6%). At 2 ML, the differences continue with essentially only the first three layers occupied on SiO_2: 1st (97.1%); 2nd (85.3%); and 3rd (16.6%); as compared to on ODTS where 5 are significantly occupied: 1st (93.6%); 2nd (69.3%); 3rd (27.7%), 4th (7.5%), and 5th (1.5%). These results indicate that in the early stages of deposition, growth is smoothest on these surfaces, and roughest on the ODTS-terminated surface.

Taking the results in Figures 4-8 and 4-9 as a whole, clearly rougher films are formed on ODTS. Arguments based solely on the surface energies of the starting substrates would seem to be insufficient to explain differences we observe here. For example, the surface energies of ODTS, FOTS and OTS are all expected to be low and similar, while HMDS is intermediate and unmodified SiO_2 has the largest surface energy. This grouping is not reflected in the results for the evolution of surface roughness, where ODTS is the outlier. Rougher films can result if there is a difference

in interlayer transport with surface termination. How might surface termination effect interlayer transport? First, films can roughen due to step-edge barriers to "downward" interlayer transport, i.e., the Ehrlich-Schwoebel barrier. Such a barrier might depend on surface termination if the underlying layer affects island shape and/or size. For example, if a low density of large islands is formed, which possess relatively smooth boundaries, interlayer transport may be more hindered with respect to a monolayer consisting of small islands with rough edges. As DIP undergoes post-deposition reorganization **[46]** on all of the surfaces terminated by SAMs considered here, we were unable to directly determine the submonolayer island density or shape. We know from other work **[47, 48]**, however, that surface termination can greatly affect both submonolayer island shape and density at otherwise identical growth conditions. Indeed, concerning the submonolayer growth of perfluoropentacene, island shapes were the most irregular on clean SiO_2, which might facilitate interlayer transport. Thus, this effect may be in play concerning growth on ODTS vs. the other four surfaces we consider here.

Other possible factors that can influence the rates of interlayer transport involve the detailed molecular motions occurring at the edges of islands. One effect could concern the degrees of freedom of molecules bound to the edges of islands, and how the underlying substrate may contribute to the motion of these molecules and hence, interlayer transport. The ODTS layer is the thickest of the SAMs we consider here, and its density is as much as 36% less than that of a well organized monolayer of the same molecule (see experimental section). As such, the deformability of this layer should be greater than that of the other SAMs and, certainly, unmodified SiO_2.

Increased displacement/motion of molecules bound on the periphery of islands, due to partial penetration of the SAM by these molecules, could fundamentally change interlayer transport rates. If, for example, "upward" transport of molecules from the 1st layer to the 2nd layer occurred more readily on ODTS, and if it occurred on a time scale fast compared to growth of a single molecular layer, then it could explain the differences seen in Figure 4-9. Key to this interpretation is the speed of the reorganization, as our modeling of the intensities at the anti-Bragg condition does not formally account for upward transport, e.g., the occupation of all layers increase with time. If reorganization events occur with a time scale of ~ 1 s or less, these would be difficult to observe here.

We have also examined the thin film morphology at higher coverages using *ex situ* AFM. For sufficiently high coverages, significant post-deposition reorganization is unlikely, as we have demonstrated previously concerning pentacene on SiO_2, and SiO_2 terminated with HMDS and FOTS **[46]**. Thus, *ex situ* AFM should provide an accurate assessment of the thin film morphology as formed. In Figures 4-8(b, d and f) we display AF micrographs of DIP thin films grown on ODTS, OTS and FOTS respectively. AF micrographs of DIP on SiO_2 and HMDS are shown in Figure 4-2(b) and Figure 4-5(b) respectively. In each case, the incident beam energy was E_i = 4.2 eV, T_s = 40 °C and the total thickness was approximately constant, spanning the range of 8.7-9.5 ML, based on the prediction of the models. Post-deposition measurement of film thicknesses using x-ray reflectivity gave similar results, albeit consistently higher by ~ 15% than those predicted by the model. First, we see that there are significant differences in the morphology of these ~ 10 ML-thick DIP thin films. The two

substrates giving the most granular thin films of DIP are SiO_2 (*cf.* Figure 4-2(b)) and SiO_2 modified with ODTS (*cf.* Figure 4-8(b)). Intermediate in grain/feature size are the films grown on HMDS (*cf.* Figure 4-5(b)) and OTS-modified SiO_2 (*cf.* Figure 4-8(d)). The films exhibiting the largest features and the most easily identified terraces are those grown on FOTS-modified SiO_2 (*cf.* Figure 4-8(f)). Similarly, previous studies have shown that pentacene feature/grain size also depends on the chemical nature of the surface **[9, 49]**.

In order to quantify these observations we have analyzed these images both in terms of the height-height correlation function (HHCF), and the 1D PSD. The former will show a maximum (r_{max}) corresponding to the radius of the grains/mounds/features, while the latter gives the correlation length from the intersection of the plateau and fall-off regions in the 1D-PSD. In Figure 4-10(a) we plot the correlation length, ξ, vs. the incident kinetic energy, for DIP thin films grown on the five substrates. Analysis of the HHCF gave similar results (within ± 5%), i.e., $2r_{max} \sim \xi$. Using results from both the model and XRR, except for three cases, the thicknesses all lay within one standard deviation of the mean, the outliers being growth on FOTS at E_i = 9.4 and 11.3 eV and growth on OTS at 6.4 eV. We see that the behavior of the correlation length can be placed into three groups, consistent with what was seen by eye: FOTS yields the largest features, followed by HMDS and OTS, and SiO_2 and ODTS giving the smallest features. Excepting the film grown on FOTS at E_i = 4.2 eV, incident kinetic energy does not seem to influence greatly the size of the features that are formed. In Figure 4-10(b), we plot the surface slope for these same films as a function of the incident kinetic energy. On all the surfaces, the

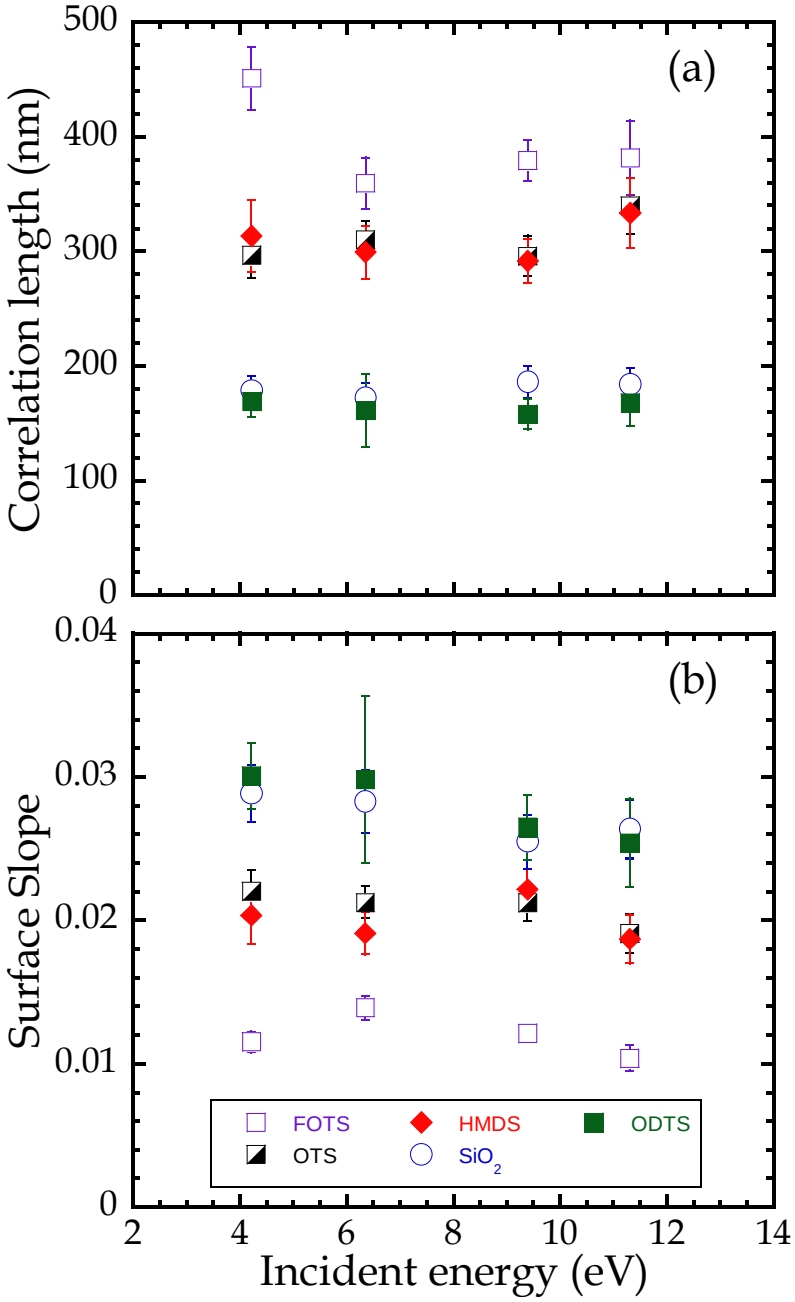

Figure 4-10 (a) Lateral correlation length of DIP deposited on the five surfaces examined here at T_s = 40 °C and as a function of incident energy. (b) Surface slope of DIP deposited on the five surfaces examined here at T_s = 40 °C and as a function of incident energy.

effect of incident kinetic energy on surface slope is not so apparent. The surface slope follows the opposite trend to the correlation length, where the surface slope is the least on FOTS, intermediate on HMDS and OTS and highest on SiO_2 and ODTS.

Summarizing the results we have just presented in Figures 4-8 to 4-10, in the very initial stages of growth, the evolution of the layer occupancies is quite similar, excepting the case for growth on ODTS-terminated SiO_2. One possible explanation for rougher films in this case might involve enhanced "upward" interlayer transport, perhaps facilitated by the flexibility of the ODTS layer. Concerning the size of the features that are formed at high coverages (~10 ML thick films), we observed little effect of the incident kinetic energy, but a strong effect of the underlying substrate. Features are largest on FOTS, intermediate on HMDS and OTS, and smallest on SiO_2 and ODTS. These results can be reconciled, with the notable exception of ODTS, if the surface energy of the substrate is important in determining the size of the features. In other work **[49]**, we have found that the density of islands formed in the sub-monolayer regime exceeds that of the features that appear in the multilayer, thick film regime, by about a factor of 3-5. One possible explanation for this is that, as the second layer and more are being formed, a few neighboring islands are able to coalesce into one larger island, which acts to control the feature sizes as step edge barriers help to prevent the formation of a smooth uniform thin film. The ability of neighboring islands to fuse and eliminate defects (e.g., grain boundaries) should depend on the surface energy of the DIP/substrate interface. A low-energy interface, characterized by weak binding of DIP to the substrate, molecules near the inter-island boundary can rearrange more easily. If the energy of the interface scales with that of

the free substrate surface, we would expect the largest features for the lowest energy surface, FOTS, and the smallest features for the highest energy surface, SiO_2. How might ODTS, a low energy surface, still fit into this explanation? If transport is limited at the DIP/ODTS interface in some way that is not expected based on its surface energy, then ODTS could also be explained. The relatively low density of the ODTS layer examined here might lead to a more diffuse and perhaps rough interface. These factors might lead to reduced rearrangements near inter-island boundaries.

4.5 Conclusions

In conclusion, we have investigated the effect substrate temperature (T_s), incident energy (E_i), and chemical nature of a self-assembled monolayer (SAM) on the growth and morphology of diindenoperylene (DIP) thin films. Concerning substrate temperature, T_s, we showed that increasing T_s leads to smoother films with larger in-plane features/grains on both clean SiO_2 and HMDS modified SiO_2. Smoother films are probably a result of enhanced interlayer transport at higher T_s, and larger in-plane feature/grain sizes are probably due to enhanced surface diffusivity of DIP at higher T_s. Varying the incident energy, E_i, does not have a significant impact on DIP morphology on both clean SiO_2 and HMDS at all T_s investigated. Concerning growth on SAMs (at constant T_s = 40 °C), we showed that DIP grows similarly on all surfaces except on ODTS-terminated SiO_2, where it grows the roughest, especially at the early stages of film growth. Rougher films on ODTS may be due to enhanced "upward" interlayer transport, perhaps facilitated by the flexibility of the ODTS layer. The

chemical nature of the surface also significantly affects the in-plane feature/grain size. At identical deposition conditions, the largest features are formed on FOTS, intermediate sized features on HMDS and OTS and smallest sized features on ODTS and SiO_2. Incident energy, E_i, does not affect the in-plane feature/grain size on any of the surfaces investigated. Viewing the results as a whole, we have investigated the effect of three process parameters, namely T_s, E_i and chemical nature of SAM, on the DIP thin film growth and morphology. Of these process parameters, our results indicate that E_i has the least effect on DIP thin film growth and morphology whereas T_s and chemical nature of SAM have the greatest.

4.6 References

1. Hamers, R. J.; *Nature* **2001**, *412*, 489-490.
2. Dimitrakopoulos, C. D. ; Malenfant, P. R. L. *Adv. Mater.* **2002**, *14*, 99-117.
3. Lin, Y. Y.; Gundlach, D. J.; Nelson, S. F.; Jackson, T. N. *IEEE Electron Device Letters* **1997**, *18*, 606-608.
4. Ruiz, R.; Papadimitratos, A.; Mayer, A. C.; Malliaras, G. G. *Adv. Mater***. 2005**, *17*, 1795-1798.
5. Dinelli, F.; Murgia, M.; Levy, P.; Cavallini, M.; Biscarini, F.; de Leeuw Dago M. *Phys. Rev. Lett.* **2004**, *92*, 116802-116804.
6. Muck, T.; Wagner, V.; Bass, U.; Leufgen, M.; Geurts, J.; Molenkamp, L. W. *Synthetic Metals* **2004**, *146*, 317-320.
7. Dodabalapur, A.; Torsi, L.; Katz, H. E. *Science* **1995**, *268*, 270-271.

8. Kelley, T. W.; Boardman, L. D.; Dunbar, T. D.; Muyres, D. V.; Pellerite, M. J.; Smith, T. P. *J. Phys. Chem. B* **2003**, *107*, 5877-5881.

9. Yang, H.; Shin, T. J.; Ling, M. M.; Cho, K.; Ryu, C. Y.; Bao, Z. *J. Am. Chem. Soc.* **2005**, *127*, 11542-11543.

10. Virkar, A.; Mannsfield, S.; Oh, J. H.; Toney, M. F.; Tan, Y. H.; Liu, G.; Scott, J. C.; Miller, R.; Bao, Z. *Adv. Funct. Mater.* **2009**, *19*, 1962-1970.

11. Shtein, M.; Mapel, J.; Benziger, J. B.; Forrest, S. R. *Appl. Phys. Lett.* **2002**, *81*, 268-270.

12. Klauk, H.; Halik, M.; Zschieschang, U.; Schmid, G.; Radlik, W.; Weber, W. *J. Appl. Phys.* **2002**, *92*, 5259-5263.

13. Gerlach, A.; Sellner, S.; Kowarik, S.; Schreiber, F. *Phys. Stat. Sol.* **2008**, *205*, 461-474.

14. Kowarik, S.; Gerlach, A.; Schreiber, F. *J. of Phys.: Cond. Mat.* **2008**, 20, 184005/1-184005/12.

15. Dürr, A. C.; Koch, N.; Kelsch, M.; Rühm, A.; Ghijsen, J.; Johnson, R. L.; Pireaux, J. -J.; Schwartz, J.; Schreiber, F.; Dosch, H.; Kahn, A. *Phys. Rev. B* **2003**, *68*, 115428/1-115428/12.

16. Zhang, X. N.; Barrena, E.; de Oteyza, D. G.; Dosch, H. *Surf. Sci.* **2007**, *601*, 2420-2425.

17. Zhang, X.; Barrena, E.; Goswami, D.; de Oteyza, D. G.; Weis, C.; Dosch, H. *Phys. Rev. Lett.* **2009**, *103*, 136101/1-136101/4.

18. Dürr, A. C.; Schreiber, F.; Ritley, K. A.; Kruppa, V.; Krug, J.; Dosch, H.; Struth, B. *Phys. Rev. Lett.* **2003**, *90*, 016104/1-016104/4.

19. Kowarik, S.; Gerlach, A.; Sellner, S.; Schreiber, F.; Cavalcanti, L.; Konovalov, O. *Phys. Rev. Lett.* **2006**, *96*, 125504/1-125504/4.

20. Dürr, A. C.; Nickel, B.; Sharma, V.; Taffner, U.; Dosch, H. *Thin Solid Films* **2006**, *503*, 127-132.

21. Zhang, Y.; Barrena, E.; Zhang, X.; Turak, A.; Maye, F.; Dosch, H. *J. Phys. Chem. C* **2010**, *114*, 13752-13758.

22. Zhang, X. N.; Barrena, E.; de Oteyza, D. G.; De Souza, E.; Dosch, H. *J. Appl. Phys.* **2008**, *104*, 104308/1-104308/4.

23. de Oteyza, D. G.; Barrena, E.; Zhang, Y.; Tobias, N. K.; Turak, A.; Vorobiev, A.; Dosch, H. *J. Phys. Chem. C.* **2009**, *113*, 4234-4239.

24. Hinderhofer, A.; Gerlach, A.; Kowarik, S.; Zontone, F.; Krug, J.; Schreiber, F. *EPL* **2010**, *91*, 56002/p1-56002/p5.

25. de Oteyza, D. G.; Krauss, T. N.; Barrena, E.; Sellner, S.; Dosch, H.; Ossó, J. O. *Appl. Phys. Lett.* **2007**, *90*, 243104/1-243104/3.

26. Barrena, E.; de Oteyza, D. G.; Sellner, S.; Dosch, H.; Ossó, J. O.; Struth, B. *Phys. Rev. Lett.* **2006**, *97*, 076102/1-076102/4.

27. Wagner, J.; Gruber, M.; Hinderhofer, A.; Wilker, A.; Bröker, B.; Frisch, J.; Amsalem, P.; Vollmer, A.; Opitz, A.; Koch, N.; Schreiber, F.; Brütting, W. *Adv. Func. Mater.* **2010**, *20*, 4295-4303.

28. Killampalli, A. S.; Schroeder, T. W.; Engstrom, J. R. *Appl. Phys. Lett.* **2005**, *87*, 033110/1-033110/3.

29. Schroeder, T. W. *Cornell University: Ph.D. Thesis* **2004**.

30. Hong, S.; Amassian, A.; Woll, A. R.; Bhargava, S.; Ferguson, J. D.; Malliaras, G. G.; Brock, J. D.; Engstrom, J. R. *Appl. Phys. Lett.* **2008**, *92*, 253304.

31. Amassian, A.; Desai, T. V.; Kowarik, S.; Hong, S.; Woll, A. R.; Malliaras, G. G.; Schreiber, F.; Engstrom, J. R. *J. Chem. Phys.* **2009**, *130*, 124701/1-124701/9.

32. Desai, T.; Hong, S.; Woll, A. R.; Hughes, K. J.; Ananth, P.; Clancy, P.; Engstrom, J. R. *Journal of Chemical Physics* **2011**, *134*, 224702.

33. Kaushik, A. P.; Clancy, P. *Surf. Sci.* **2011**, *605*, 1185-1196.

34. Janssen, D.; De Palma, R.; Verlaak, S.; Heremans, P.; Dehaen, W. *Thin Solid Films* **2006**, *515*, 1433-1438.

35. Kowarik, S.; Gerlach, A.; Skoda, M.; Sellner, S.; Schreiber, F. *Eur. Phys. J. Special Topics* **2009**, *168*, 11-18.

36. Woll, A. R.; Desai, T. V.; Engstrom J. R. *under review at the J. Phys. Rev. B*.

37. Cohen, P. I.; Petrich, G. S.; Pukite, P. R.; Whaley, G. J.; Arrott, A. S. *Surface Sci.* **1989**, *216*, 222-248.

38. Kowarik, S.; Gerlach, A.; Sellner, S.; Cavalcanti, L.; Konovalov, O.; Schreiber, F. *Appl. Phys. A: Mater. Sci. Proces.* **2009**, *95*, 233-239.

39. Ehrlich, G.; Hudda, F. G. *J. Chem. Phys.* **1966**, *44*, 1039-1049.

40. Schwoebel, R. L.; Shipsey, E. J. *J. Appl. Phys.* **1966**, *37*, 3682-3686.

41. Fendrich, M.; Krug *J. Phys. Rev. B* **2007**, *76*, 121302/1-121302/3.

42. Hlawacek, G.; Puschnig P.; Frank, P.; Winkler, A.; Ambrosch-Draxl, C.; Teichert, C. *Science* **2008**, *321*, 108-111.

43. Goose, J. E.; First, E. L.; Clancy, P. *Phys. Rev. B* **2010**, *81*, 205310/1-205310/20.

44. Barabasi, A. -L.; Stanley, H. E., Eds. *Fractal Concepts in Surface Growth*; Cambridge University Press: Cambridge, U.K., **1995**.

45. Zhao, Y.; Wang, G. -C.; Lu, T. –M. *Characterization of Amorphous and Crystalline Rough Surface: Principles and Applications*; Academic Press, San Diego, CA, **2001**, *37*.

46. Amassian, A.; Pozdin, V.; Desai, T. V.; Hong, S.; Woll, A. R.; Ferguson, J. D.; Brock, J. D.; Malliaras, G. G.; Engstrom, J. R. *J. Mater. Chem.* **2009**, *19*, 5580-5592.

47. Desai, T. V.; Woll, A. R.; Schreiber, F.; Engstrom, J. R. *J. Phys. Chem. C.* **2010**, *114*, 20120.

48. Desai, T. V.; Kish, E. R.; Woll, A. R.; Engstrom, J. R. *under review at the J. Phys. Chem. C.*

49. Papadimitratos, A.; Amassian, A.; Killampalli, A. S.; Mack, J. L.; Malliaras, G. G.; Engstrom, J. R. *Appl. Phys. A: Mater. Sci. Proces.* **2009**, *95*, 29-35.

5. *In situ* real-time growth of pentacene on polymeric dielectrics

5.1 Overview

We have examined the thin film growth of pentacene on SiO_2 and on a variety of polymeric dielectrics using *in situ* synchrotron x-ray scattering and *ex situ* atomic force microscopy (AFM). The polymeric dielectrics ranged from low surface energy hydrophobic surfaces (polystyrene, PS), to higher surface energy hydrophilic surfaces (polyethylenimine, PEI). From *in situ* real-time x-ray scattering, we find that pentacene exhibits layer-by-layer (LbL) growth on all surfaces investigated, but the extent of LbL growth is a strong function of the underlying substrate. In particular, LbL growth is significantly more prolonged on PEI, (up to ~6 MLs), and least extended on PS (up to ~ 3 MLs). The extent of LbL growth and therefore the final thin film roughness follows a trend with the surface energy of the underlying substrate – pentacene thin film growth is more LbL-like and smoother as the surface energy of the underlying substrate increases.

5.2 Introduction

The study of complex conjugated molecules, e.g. pentacene, for applications in organic thin film electronics and photonics has received much attention owing to their ability to form highly ordered thin films with excellent electrical properties **[1-4]**. Studies have shown that the interface between the organic semiconducting layer and the dielectric is critical to charge transport and that the majority of charge carriers are generated in the first few monolayers (MLs) of the organic layer **[5-8]**, emphasizing the need of investigating in detail the first few monolayers of organic thin film growth. Despite these observations, there is still a significant lack of understanding of the basic mechanisms of organic crystal growth, especially concerning the molecular-scale events that occur between these molecules and the dielectric, and how these interactions affect small molecule organic thin film growth.

Due to their ease in processing, 'flexible' in nature, and easily tunable surface properties **[9]**, polymeric dielectrics are attractive and offer another means of tailoring organic thin film growth. Previous studies have shown the nature of the polymeric dielectric greatly affects both the morphology and electrical properties of pentacene thin film growth. The charge mobility of pentacene thin film has been shown to improve on polymeric substrates as compared to on clean silicon dioxide (SiO_2) **[10]** and also shown to be easily varied depending on the chemistry of the underlying polymeric dielectric **[11]**. Studies have shown that by simply changing the surface chemistry of the polymer, the pentacene grain size can be controlled, with the thin film charge mobility increasing with increasing pentacene grain size **[12, 13]**. On the

contrary, other studies have found no correlation **[11]** or the opposite correlation **[14]** between pentacene grain size and charge mobility on polymeric substrates. Studies have also investigated the effect of polymer viscoelasticity **[12]** and degree of polymer crosslinking **[15]** on pentacene thin film growth. Studies have also shown that the chemistry of the polymer affects the pentacene thin film crystalline structure **[16]**. In addition, using *ex situ* atomic force microscopy (AFM), studies have shown that the chemistry of the polymer affects the growth mode, where the pentacene thin films transition from 2D mode to 3D mode with increasing polymer surface energy **[16, 17]**. Finally, studies have also investigated the effect of polymeric substrates on the submonolayer nucleation dynamics of pentacene thin films and have shown that the pentacene critical cluster size is independent of the underlying polymeric dielectric but the absolute submonolayer island density varies considerably indicating that the diffusivity of pentacene varies with the nature of the underlying polymeric substrate **[18, 19]**.

Here, we investigate the effects of the chemical nature of polymeric dielectrics on the growth of pentacene thin films concentrating on the first few MLs of thin film growth using a combination of both *in situ* and *ex situ* surface sensitive probes. Concerning the polymers, we consider three layers that differ in their chemical nature: polystyrene (PS), polymethylmethacrylate (PMMA), and polyethylenimine (PEI). For comparison, we also consider unmodified SiO_2. In terms of surface energies, the surfaces follow the order (high-to-low): PEI, unmodified SiO_2, PMMA and PS. We deposit thin films of pentacene in ultrahigh vacuum (UHV) using a collimated supersonic molecular beam **[20-22]**. We make use of *ex situ* AFM to probe the thin

film morphology and employ *in situ* real-time synchrotron x-ray scattering measurements at the "anti-Bragg" configuration **[22-24]** to directly probe the filling of each successive molecular layer of pentacene during thin film growth. The advantage of using *in situ* x-ray scattering techniques is that it eliminates any post-growth artifacts that can be missed using *ex situ* techniques, such as AFM **[25]**. We will find below that the nature of the polymer affects significantly both the growth mode and thin film roughness of pentacene thin films.

5.3 Experimental Procedures

Refer to chapter 2 for details. Only a brief summary on experimental procedures is provided in this section. The experiments conducted *in situ* and in real-time were carried out in the G3 station of the Cornell High Energy Synchrotron Source (CHESS) in a custom-designed UHV system fitted with Be windows that is described elsewhere **[21]**. Briefly, the system consists of four separately pumped chambers: a main scattering chamber, a source and antechamber, which act to produce the supersonic beam, and a fast entry load-lock. All chambers are pumped by high-throughput turbomolecular pumps. The base pressure of the chamber was typically ~ 4×10^{-9} Torr and samples were loaded via the load-lock chamber, which was evacuated to ~10^{-7} Torr prior to sample transfer into the main chamber. X-ray reflectivity (XRR) and grazing incidence diffraction (GID) experiments, conducted *ex situ*, were carried out in the G2 station at CHESS.

Substrates were Si(100) wafers (Wacker-Siltronic, *p*-type, 100 mm dia., 500-550 μm thick, 38-63 Ω-cm) subject to a SC-1 clean, 15 s HF dip and a SC-2 clean

followed by growth of ~ 300-nm-thick SiO_2 films by wet thermal oxidation at 1100°C. Next, these wafers were cleaned and degreased by sonication for 15 min in anhydrous $CHCl_3$ solution (99 %+), sonicated in deionized (DI) water for 15 min, washed with DI water, dried with N_2 and exposed to UV-ozone for 15 min. These processes provided a clean and reproducible hydrophilic surface. PS (200 Kg/mol, 1 wt% in toluene) and PMMA (495 Kg/mol, 2wt% in anisole) films were deposited on the cleaned SiO_2 substrates by spin coating. The spin-coated PMMA films were annealed for 15 min. at 170°C on a hotplate. PEI (750 Kg/mol, 0.1wt% in DI water) films were deposited by dipping cleaned SiO_2 substrates in solution for 15 min. followed by rinsing in pure DI water and finally drying with N_2. The chemical structure on the polymers investigated is shown in Figure 5-1.

The SiO_2 substrates modified with PS, PMMA, and PEI were characterized by contact angle, XRR and AFM. Contact angles were measured in two solvents (water and formamide) and using the Young-Dupre equation **[26]** we calculated the energy of surfaces modified with PS, PMMA and PEI, and found values of 25.0, 35.6, and ≥ 73.4 mJ-m^{-2}, respectively. In comparison, the surface energy of clean, unmodified SiO_2 has been reported to lie between 50 and 60 mJ-m^{-2} **[27, 28]** and the surface energy of the (001) crystal plane of pentacene is reported to be 50-82 mJ-m^{-2} **[29, 30]**. Fits to the XRR data were performed, as described in detail elsewhere **[24]**, with the Parratt32 software package **[31]** (based on the Parratt formalism **[32]**), from which we obtain the thickness of the organic layers, and the mean electron density. Details concerning the properties of the polymers are given in Table 5-1.

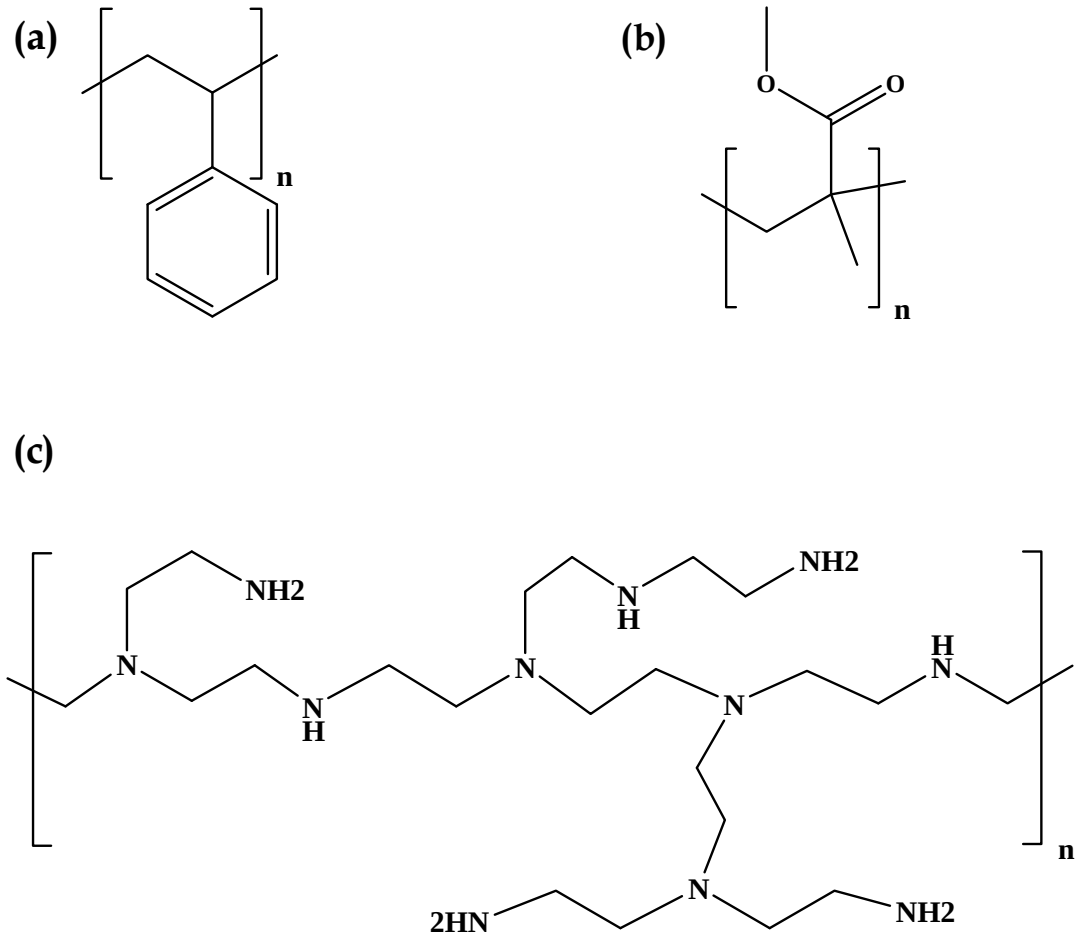

Figure 5-1 Chemical structure showing monomer units of (a) PS, (b) PMMA and (c) PEI.

Supersonic molecular beams of pentacene were generated by using He as a carrier gas and is described in detail elsewhere **[23]**. By varying the He flow rate, the beam energy could be varied from 2.5 to 7.0 eV as determined from time of flight measurements **[21]**. Multiple experiments could be carried out on the same substrate, by translating the substrate perpendicular to the supersonic molecular beam, and due to the high beam-to-background flux ratio. During deposition the substrate temperature was kept at T_s = 40 °C, and in all cases the beam was incident along the surface normal.

Time-resolved and *in situ* measurements of the scattered x-ray synchrotron intensity were made using a silicon avalanche photodiode detector (APD, Oxford Danfysik, Oxford, UK). During pentacene thin film growth the intensity was monitored at the anti-Bragg position (00½; $q_z = q_{Bragg}/2 = 0.41/2$ Å^{-1}), which is an effective monitor of the nature of growth, i.e., layer-by-layer (LbL) vs. 3D islanded growth **[33]**. Following deposition and x-ray analysis, the samples were removed for *ex situ* analysis using AFM, conducted in tapping mode using a DI 3100 Dimension microscope.

The x-ray data at the anti-Bragg position was fitted using a modified version **[23, 34]** of the mean-field rate equation model of growth first proposed by Cohen and co-workers **[35].** Briefly, the equations for the coverage of individual layers (θ_n) are given by:

$$\frac{d\theta_n}{dt} = S_{n-1}F\left[\left(\theta_{n-1} - \theta_n\right) - \alpha_{n-1}\left(\theta_{n-1} - \theta_n\right)\right] + S_nF\alpha_n\left(\theta_n - \theta_{n+1}\right) \qquad (5\text{-}1)$$

where n = 0 represents the substrate, n = 1 the first molecular layer, etc., S_n is the probability of adsorption for molecules incident on the n^{th} layer, F is the incident molecular flux (ML-s^{-1}), and α_n is the fraction of molecules that initially impact and land on top of the n^{th} layer, but rather than staying on the top of that layer, drop down and become part of that layer via some mechanism. In this model, we also assume that there are two values for the probability of adsorption: one for adsorption on the substrate (S_0), and one for that on previously existing molecular layers, independent of their thickness ($S_1 = S_2 = S_3 \ldots$). Concerning interlayer transport, we will assume that three values are possible (note, as the substrate cannot be penetrated, $\alpha_0 = 0$), namely α_1, α_2 and $\alpha_{n \geq 3}$. "Upward" interlayer transport (movement from the n to the $n + 1$ layer) is not included in the model.

Once layer coverages have been calculated by integrating Equation (5-1), these can then be used to calculate the scattered x-ray intensity as a function of time **[23,33-35]**. The intensity of the scattered beam (I) depends upon the layer population, θ_n(t), according to the following relationship:

$$I(t) = \left| r_{subs} e^{-i\phi} + r_{film} \sum_{n}^{\infty} \theta_n(t) e^{-iq_z dn} \right|^2 \tag{5-2}$$

where r_{subs} and r_{film} are the scattering amplitudes of the substrate and the film, ϕ is the phase change upon reflection, q_z is the out-of-plane scattering vector and d is the out-of-plane interplanar spacing. At the anti-Bragg position, $q_z d = \pi$, which results in a

change in the sign of the thin film terms in the summation. If each layer fills sequentially, such as in perfect LbL growth, an oscillation in the intensity results.

5.4 Results and Discussion

The polymers (shown in Figure 5-1) were characterized using the methods described above in the experimental section, namely: synchrotron x-ray reflectivity measurements, contact angle measurements, and AFM. First, we consider the results from x-ray reflectivity (XRR) of the polymers themselves. In Figure 5-2(a) and Figure 5-2(b) we plot the reflected intensity as a function of the out-of-plane scattering vector, q_z, for clean SiO_2 modified with PEI and PS respectively. In this figure, for PEI/PS we plot only 20/50% of the data (1 of every 2/5 points) to show the quality of the fit, which is shown by the smooth curve. The fit to the data is excellent, and from the fit, we extract a thickness of d_{PEI} = 0.86 nm (8.58 Å) and d_{PS} = 23.9 nm. From Figure 5-2, we notice the difference in their XRR between the two polymers, where many more thickness fringes are observed for PS which are significantly narrower (Δq_z)–this is due to the thicker nature of the PS film. For the other polymer, PMMA (XRR data not shown), we extract thicknesses of d_{PMMA} = 50.2 nm. Using *ex situ* AFM, we find that the bare polymers are smooth and the roughness is between 0.29 - 0.36 nm. The static contact angles (water) and surface energy of PMMA and PS agree well with values reported in literature **[9, 13, 17, 18]**. These and other properties of the polymers considered in this study are given in Table 5-1.

In Figure 5-3(a) we plot the scattered intensity measured *in situ* and in real-time for the growth of pentacene on PS at E_i = 2.5 eV and growth rate, *GR*, of 0.011

Table 5-1 Properties of the polymers

Monolayer	Contact angle (H_2O/formamide)	Surface energy ($mJ\text{-}m^{-2}$)	Thickness, XRR (nm)	AFM Roughness (nm)	Electron density ($Å^{-3}$)
PS	92°/74°	25.0	23.9	0.29	0.44
PMMA	70°/56°	35.6	50.2	0.36	0.49
PEI	~0°/0°	≥73.4	0.86 ± 0.03	0.34	0.35 ± 0.04

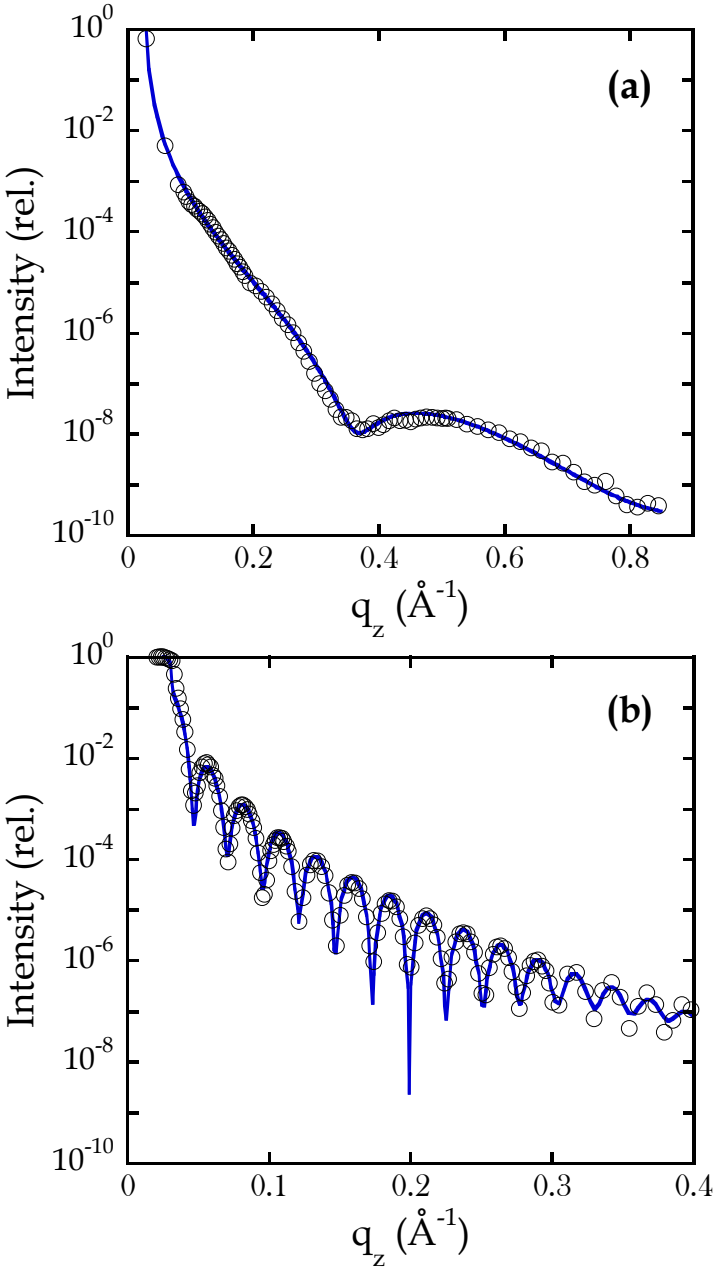

Figure 5-2 Scattered x-ray intensity as a function of the out-of-plane scattering vector, q_z, for (a) PEI and (b) PS. The solid curve represents a fit of the data to a model based on the Parratt formalism (reference **[32]**).

MLs^{-1}. As may be seen, for growth on this surface we observe a single, cusp-like peak, which coincides with completion of the first monolayer, but the anticipated second (small, similar to the zero-coverage intensity), and third (large, similar to the first peak) peaks are more damped. Beyond the deposition of ~3 monolayers (MLs) the intensity remains constant. This suggests that growth becomes 3D quickly after completion of the first ~3 MLs. The intensity oscillation can be fit using a modified version **[34]** of the mean-field, rate equation model of growth first proposed by Cohen and co-workers **[35]**. The fit to the intensity is indicated by the solid blue line, and we see that the fit to the experimental data is excellent. In Figure 5-3(a) we also show the coverage (occupancy) of each layer with solid black lines that are predicted by the fit to the intensity oscillations. After a total growth of 2 MLs, the 2^{nd} layer is ~ 76% full, whereas after 4MLs the 4^{th} layer is only ~ 63% full. These results indicate that pentacene grows in a layer-by-layer (LbL) mode for approximately 3 MLs before significant roughening begins to occur. Indeed, we observe essentially identical growth behavior concerning the intensity oscillations at the anti-Bragg condition for growth at all incident kinetic energies (E_i = 2.5, 4.7 and 7.0 eV) investigated on PS as shown in Figures 5-3(a, c, e) respectively. Growth rates for pentacene deposited on PS at 5.3 eV and 7.4 eV are similar and are 0.014 MLs^{-1} and 0.008 MLs^{-1} respectively. At all three incident energies, we see growth oscillations until ~3 MLs after which 3D growth commences, suggesting that E_i has no significant effect on the growth mode of pentacene deposited on PS. In Figures 5-3(b, d, f), we show the AF micrographs (5×5 μm^2) of the pentacene deposited on PS at E_i= 2.5, 4.7 and 7.0 eV respectively and at nominal film thicknesses of 9.1 ML, 9.7 ML and 8.9 ML respectively, as determined

Figure 5-3 X-ray intensity at the anti-Bragg condition as a function of exposure to the molecular beam for thin films of pentacene deposited on PS at E_i = (a) 2.5, (c) 4.7, and (e) 7.0 eV. Thick solid lines (right ordinate) indicate a fit of the data to a model and thin solid curves (left ordinate) represent predicted coverage of individual layers. AFM images, 5×5 μm^2, of pentacene thin films deposited on PS at E_i = (b) 2.5, (d) 4.7, and (f) 7.0 eV.

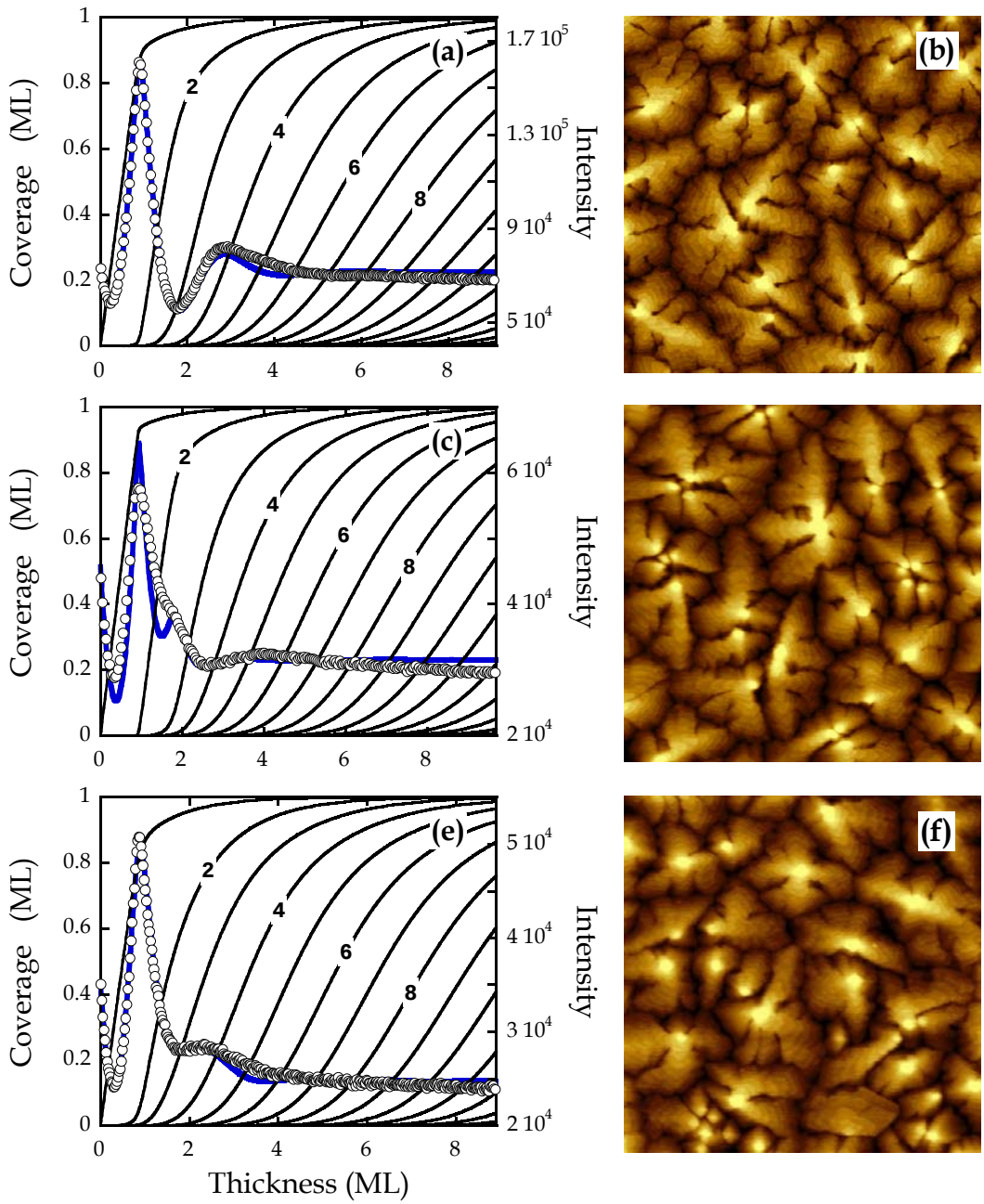
(a)
(b)
(c)
(e)
(f)
2
4
6
8
Coverage (ML)
Intensity
Thickness (ML)
1.7 10^5
1.3 10^5
9 10^4
5 10^4
6 10^4
4 10^4
2 10^4
3 10^4

from the fit to the x-ray data (*cf.* Figures 5-3(a, c, e)). At all E_i, the AF micrographs reveal the formation of tall, pyramid-shaped islands with dendritic features **[13, 16]**. No obvious changes in morphology can be observed with E_i (*cf.* Figs 3(b, d, f)).

The evolution of surface roughness can be assessed by the modeling of the anti-Bragg oscillations considered above (*cf.* Figs 3(a, c, e)), and by direct measurement using AFM. We note that both techniques are susceptible to inaccuracies: the roughness from *in situ* x-ray scattering depends on the accuracy of the model, but nevertheless does represent a real time result; whereas the results from *ex situ* AFM may be compromised by post-deposition reorganization of the thin film **[25]**. In Figure 5-4, we present the rms roughness predicted by our fits to the anti-Bragg oscillations as a function of film thickness for growth of pentacene on PS at E_i = 2.5, 4.7 and 7.0 eV. Also shown as individual points, are the surface roughness values found from AFM analysis (*cf.* Figs 3(b, d, f)). We see from Figure 5-4, there is very little difference in the evolution of surface roughness with E_i, suggesting that E_i does not affect pentacene growth mode on PS. In addition, the corroboration between AFM rms points and as predicted from x-rays is excellent (does not exceed 9%) and also confirms that E_i does not affect pentacene growth on PS.

In Figure 5-5a, we display specular XRR of pentacene deposited on PS at E_i = 2.5 eV (*cf.* Figs 3(a-c)). The scattered intensity exhibits Bragg reflections (up to the 2^{th} order) with well defined thickness fringes arising from the smooth underlying PS substrate and pentacene film. From the (00*l*) Bragg peaks, the average d_{001} spacing for the pentacene thin films on all surfaces investigated was determined to be 15.54 ± 0.02 Å, similar to other reported studies **[36, 37]**. In Figure 5-5b, we display GID data for

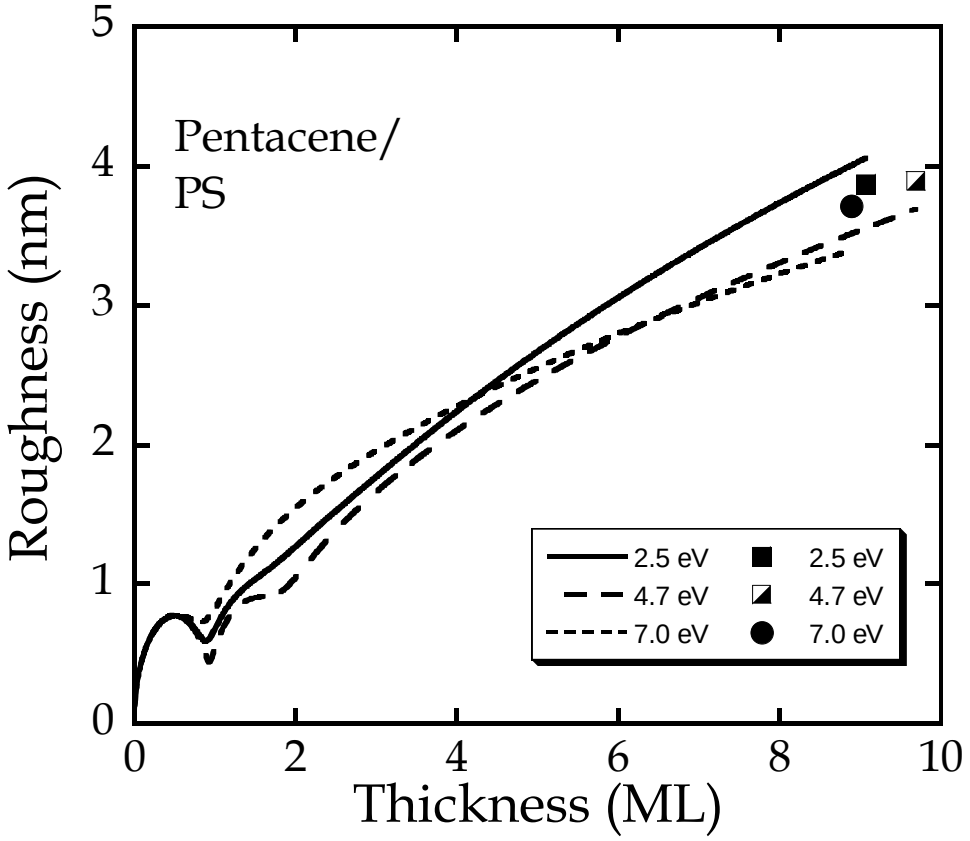

Figure 5-4 Thin film roughness as a function of pentacene thin film thickness deposited on PS at E_i = 2.5, 4.7, and 7.0 eV. The points shown represent roughness values obtained directly from 5×5 μm^2 AFM images.

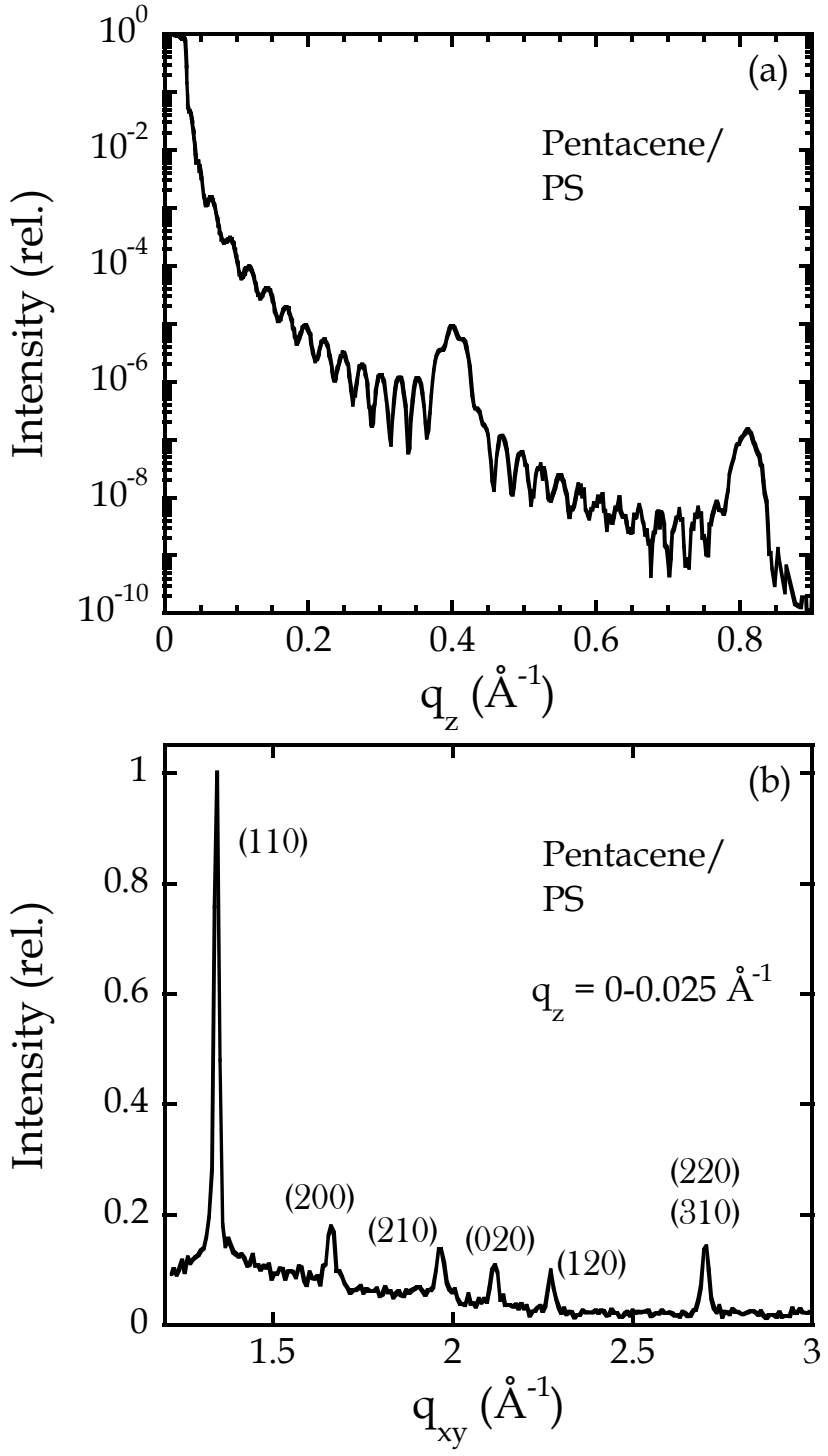

Figure 5-5 (a) X-ray reflectivity scan and (b) grazing incidence diffraction scan for pentacene deposited on PS at E_i = 2.5 eV.

pentacene deposited on PS at E_i = 2.5 eV (*cf.* Figures 5-3(a-c)). The scattered intensity showing multiple peaks (indexed using previous reports **[36, 37]**), are indicative of the random distribution of the domains in the plane of the surface. The same peaks are observed on all surfaces investigated here, and are in agreement with the previously reported "thin film" phase **[36]**. The lower limits of the coherent in-plane island sizes, $D_{\|}$, can be determined using the full width half maximum of the GID peaks. Using the [110] peak, the average $D_{\|}$ was determined to be $D_{\|}$ = 47 ± 1 nm – this value is significantly smaller than the observed feature sizes observed here for pentacene on all surfaces investigates and suggests that the pentacene features are made up of several smaller grains.

In Figures 5-6(a, c, e) we plot the scattered intensity measured *in situ* and in real-time for the growth of pentacene on PMMA at E_i = 2.5, 4.7 and 7.0 eV respectively. At each E_i, we plot the fit to the intensity as indicated by the solid blue line, and also show the coverage (occupancy) of each growing layer with solid black lines that are predicted by the fit to the intensity oscillations. The film growth rate at each E_i (2.5, 4.7 and 7.0 eV) are similar to pentacene on PS and are 0.0087 MLs^{-1}, 0.012 MLs^{-1} and 0.0070 MLs^{-1} respectively. At each E_i, we see that the film grows in an LbL mode for approximately ~4 MLs before significant roughening commences. At 7.4 eV (*cf.* Figure 5-6(e)), we see that the anti-Bragg oscillations are slightly more prolonged indicating that LbL growth is extended to higher coverages for these conditions. In comparison to growth of pentacene on PS, we see that the anti-Bragg oscillations at each E_i (*cf.* Figures 5-6(a, c, e)) are slightly more prolonged (up to ~4 MLs) indicating that pentacene grows smoother on PMMA. In Figures 5-6(b, d, f), we

Figure 5-6 X-ray intensity at the anti-Bragg condition as a function of exposure to the molecular beam for thin films of pentacene deposited on PMMA at E_i = (a) 2.5, (c) 4.7, and (e) 7.0 eV. Thick solid lines (right ordinate) indicate a fit of the data to a model and thin solid curves (left ordinate) represent predicted coverage of individual layers. AFM images, 5×5 μm^2, of pentacene thin films deposited on PS at E_i = (b) 2.5, (d) 4.7, and (f) 7.0 eV.

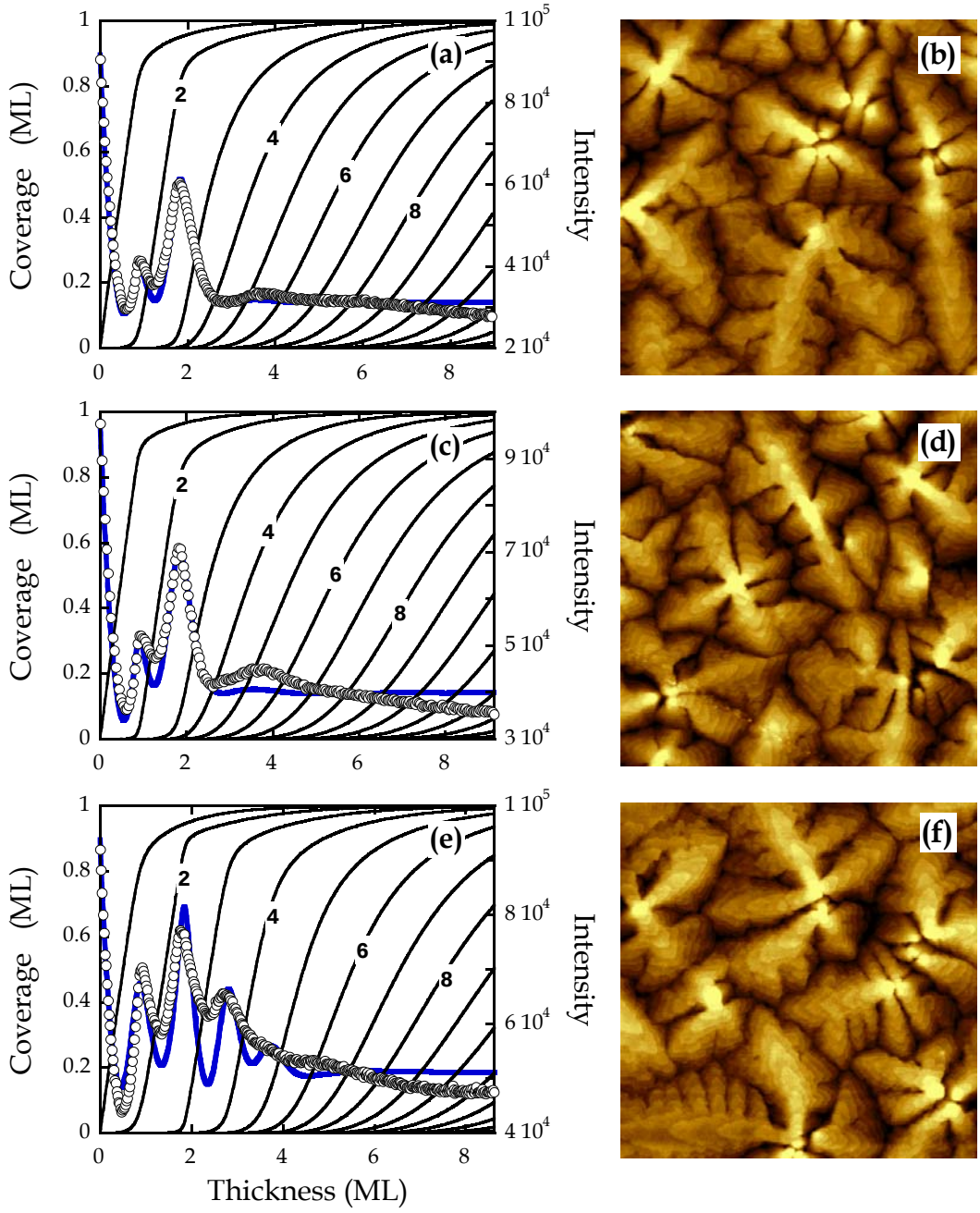
(a)
(b)
(c)
(d)
(e)
(f)
2
4
6
8
Coverage (ML)
Intensity
Thickness (ML)
0
0.2
0.4
0.6
0.8
1
2
4
6
8
2 10^4
4 10^4
6 10^4
8 10^4
1 10^5
3 10^4
5 10^4
7 10^4
9 10^4

show the AF micrographs (5×5 μm^2) of pentacene deposited on PMMA at their respective E_i of 2.5, 4.7 and 7.0 eV and nominal film thicknesses of 9.0 ML, 9.1 ML and 8.6 ML respectively. At all E_i, the AF micrographs reveal the formation of tall, pyramid-shaped islands with dendritic features. No obvious changes in morphology can be observed with E_i (*cf.* Figs 6(b, d, f)). However, in comparison to pentacene deposited on PS (*cf.* Figs 3(b, d, f)), at each E_i, the feature sizes (densities) are greater (smaller) **[12]** for pentacene deposited on PMMA. In the supporting information section (Figure 5-SI-1), a representative AF micrograph (10×10 μm^2) of pentacene deposited on PMMA at E_i = 7.0 eV is shown. It should be noted that the bright features in the AF micrograph are up to ~ 100 nm (or equivalently ~65 pentacene MLs using 1.55 nm/ML assuming pentacene is standing upright in these bright features) in height. These tall features, though low in density, could be a result of post-growth dewetting **[25]** or contamination and were observed only for pentacene deposition on PMMA and PEI. The roughness analysis presented here using 5×5 μm^2 AF micrographs ignores these all features.

In Figure 5-7, we present the rms roughness predicted by our fits to the anti-Bragg oscillations as a function of film thickness for growth of pentacene on PMMA at all E_i investigated. Also shown as individual points, are the surface roughness values found from AFM analysis (*cf.* Figs 6(b, d, f)). We see from Figure 5-7, there is very little difference in the evolution of surface roughness at E_i = 3.0 and 5.3 eV, but slightly smoother at early film thicknesses for E_i = 7.0 eV. In addition, the corroboration between AFM rms points and as predicted from x-rays is excellent (does not exceed 7%) and also confirms that E_i does not have a significant impact on

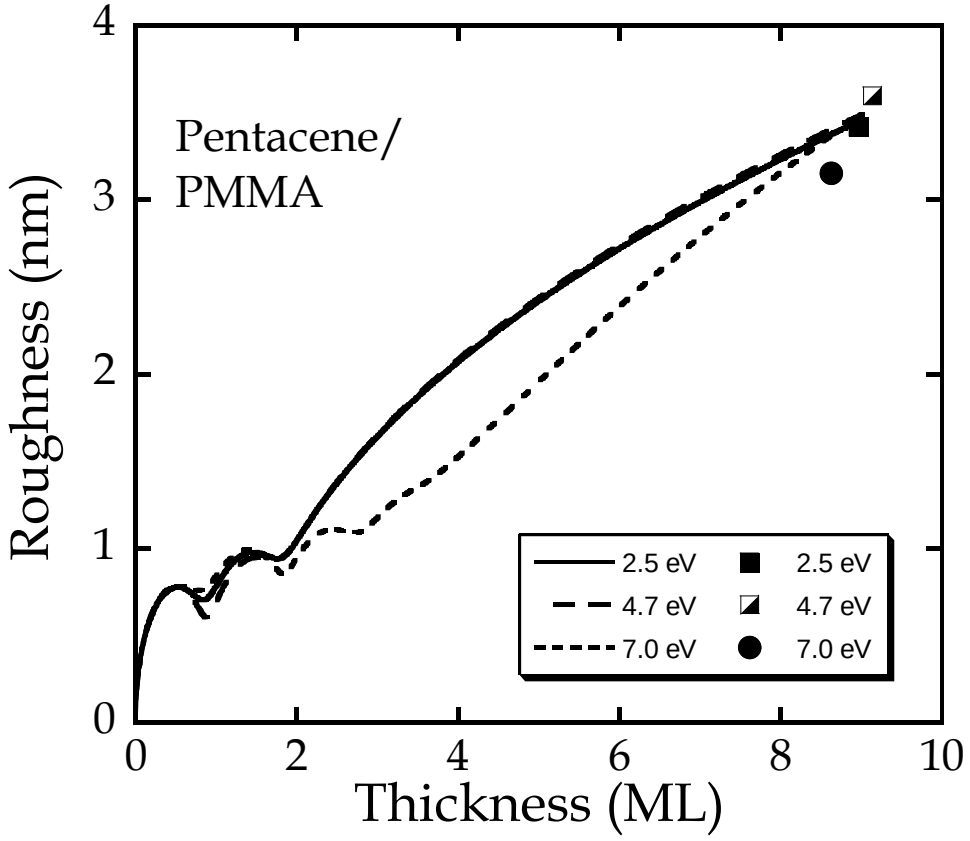

Figure 5-7 Thin film roughness as a function of pentacene thin film thickness deposited on PMMA at E_i = 2.5, 4.7, and 7.0 eV. The points shown represent roughness values obtained directly from 5×5 μm^2 AFM images.

pentacene growth on PMMA. Comparing to the roughness evolution for pentacene on PS, the evolution of pentacene growth on PMMA is slightly smoother, especially at early growth times (≤ 2 MLs). For example, at E_i = 2.5 eV, the film roughness at a total coverage of 2 ML was 1.27 nm for pentacene on PS but 1.04 nm for pentacene on PMMA, as determined from the fit to the *in situ* real-time x-ray scattering data.

In Figures 5-8(a, c, e) we plot the scattered intensity measured *in situ* and in real-time for the growth of pentacene on SiO_2 at E_i = 2.5, 4.7 and 7.0 eV respectively. At each E_i, we plot the fit to the intensity as indicated by the solid blue line, and also show the coverage (occupancy) of each growing layer with solid black lines that are predicted by the fit to the intensity oscillations. The film growth rate at each E_i (2.5, 4.7 and 7.0 eV) are similar to that of pentacene on PS and PMMA and are 0.0069 MLs^{-1}, 0.0088 MLs^{-1} and 0.0052 MLs^{-1} respectively. Incident energy does not seem to have any impact on pentacene thin film growth on clean SiO_2, as at each E_i, we see that the film grows in an LbL mode for approximately 4 MLs before significant roughening commences **[37]**. Compared to pentacene on PS, the film growth mode is smoother (LbL up to 4 MLs) but is similar to pentacene on PMMA. In Figures 5-8(b, d, f), we show the AF micrographs (5×5 μm^2) of pentacene deposited on clean SiO_2 at their respective E_i of 2.5, 4.7 and 7.0 eV and nominal film thicknesses of 8.8 ML, 8.7 ML and 9.2 ML respectively. At all E_i, the AF micrographs reveal the formation of tall, pyramid-shaped islands with dendritic features **[37]**. No obvious changes in morphology can be observed with E_i (*cf.* Figs 8(b, d, f)). In comparison to pentacene deposited on PS (*cf.* Figs 3(b, d, f)), at each Ei, the feature sizes (densities) are greater (smaller) for pentacene deposited on clean SiO_2. In comparison to pentacene deposited

Figure 5-8 X-ray intensity at the anti-Bragg condition as a function of exposure to the molecular beam for thin films of pentacene deposited on SiO_2 at E_i = (a) 2.5, (c) 4.7, and (e) 7.0 eV. Thick solid lines (right ordinate) indicate a fit of the data to a model and thin solid curves (left ordinate) represent predicted coverage of individual layers. AFM images, 5×5 μm^2, of pentacene thin films deposited on PS at E_i = (b) 2.5, (d) 4.7, and (f) 7.0 eV.

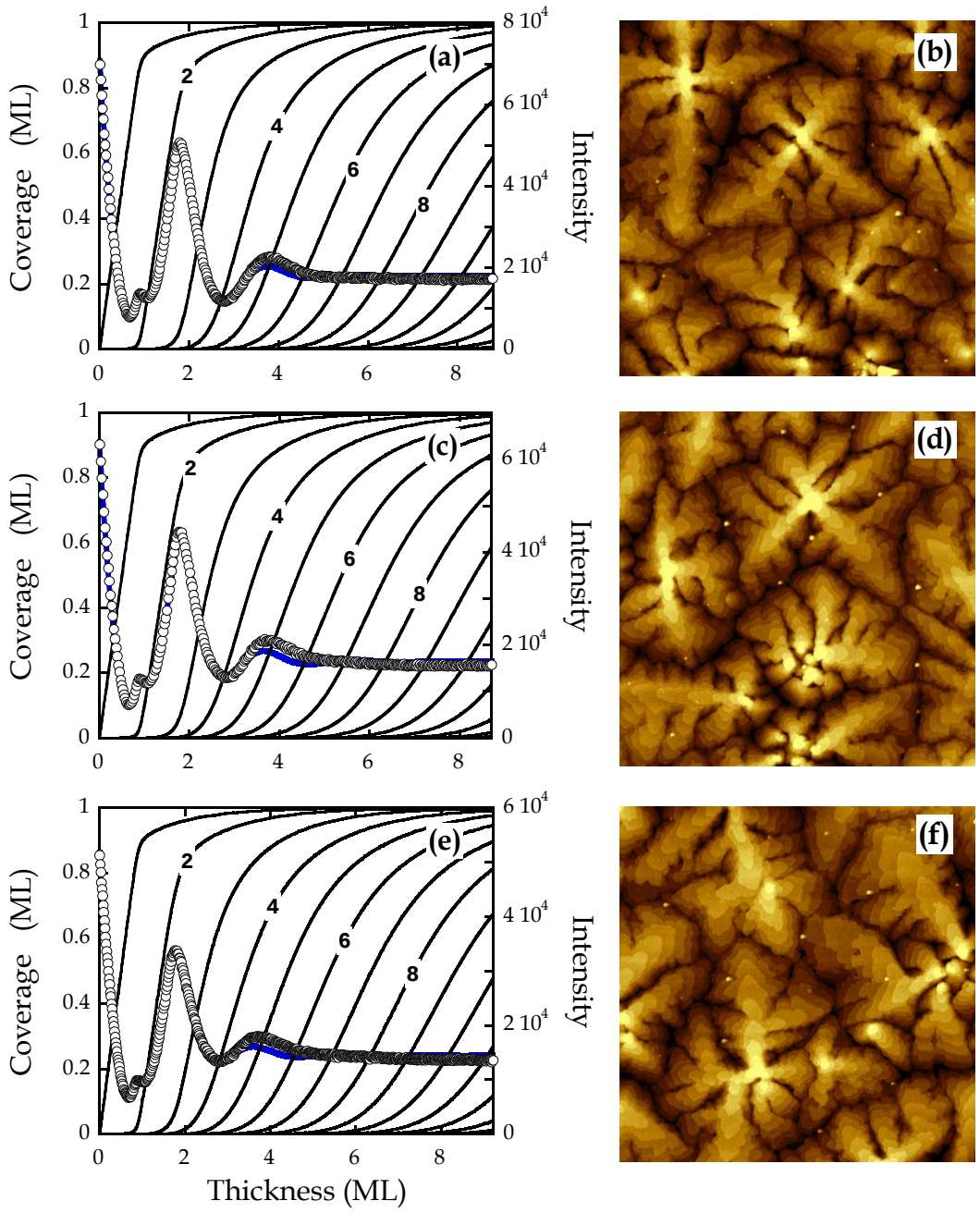
(a)
(b)
(c)
(d)
(e)
(f)
2
4
6
8
Coverage (ML)
Intensity
Thickness (ML)
0
0.2
0.4
0.6
0.8
1
2
4
6
8
2 10^4
4 10^4
6 10^4
8 10^4

on PMMA (*cf.* Figs 6(b, d, f)), the morphology and feature sizes are very similar. In Figure 5-9, we present the rms roughness predicted by our fits to the anti-Bragg oscillations as a function of film thickness for growth of pentacene on clean SiO_2 at all E_i investigated. Also shown as individual points, are the surface roughness values found from AFM analysis (*cf.* Figs 8(b, d, f)). We see from Figure 5-9, there is no difference in the evolution of surface roughness with E_i. In addition, the corroboration between AFM rms points and as predicted from x-rays is excellent (does not exceed 10%) and also confirms that E_i does not have a significant impact for pentacene growth on clean SiO_2. Comparing to the roughness evolution for pentacene on PS, the evolution of pentacene growth on clean SiO_2 is slightly smoother but similar to pentacene on PMMA. After a total coverage of 4MLs (E_i = 2.5 eV), the film roughness is 2.24 nm, 2.07 nm and 1.88 nm for pentacene on PS, PMMA and clean SiO_2 respectively.

In Figures 5-10(a, c, e) we plot the scattered intensity measured *in situ* and in real-time for the growth of pentacene on PEI at E_i = 2.5, 4.7 and 7.0 eV respectively. At each E_i, we plot the fit to the intensity as indicated by the solid blue line, and also show the coverage (occupancy) of each growing layer with solid black lines that are predicted by the fit to the intensity oscillations. The film growth rate at each E_i (2.5, 4.7 and 7.0 eV) are similar to that of pentacene on other surfaces investigated and are 0.0088 MLs^{-1}, 0.011 MLs^{-1} and 0.0066 MLs^{-1} respectively. Incident energy does not seem to have significant impact on pentacene thin film growth on PEI, as at each E_i, we see that the film grows in an LbL mode for approximately ~6 MLs before the x-ray intensity remains constant implying significant roughening has commenced.

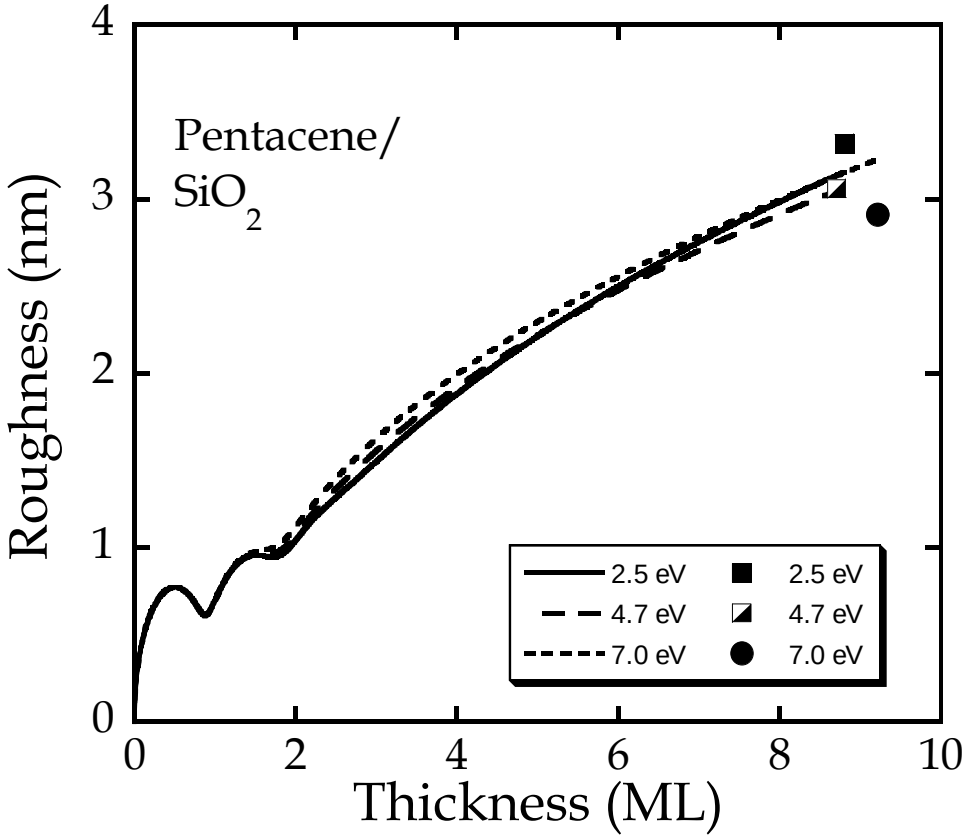

Figure 5-9 Thin film roughness as a function of pentacene thin film thickness deposited on SiO_2 at E_i = 2.5, 4.7, and 7.0 eV. The points shown represent roughness values obtained directly from 5×5 μm^2 AFM images.

Figure 5-10 X-ray intensity at the anti-Bragg condition as a function of exposure to the molecular beam for thin films of pentacene deposited on PEI at E_i = (a) 2.5, (c) 4.7, and (e) 7.0 eV. Thick solid lines (right ordinate) indicate a fit of the data to a model and thin solid curves (left ordinate) represent predicted coverage of individual layers. AFM images, 5×5 μm^2, of pentacene thin films deposited on PS at *Ei* = (b) 2.5, (d) 4.7, and (f) 7.0 eV.

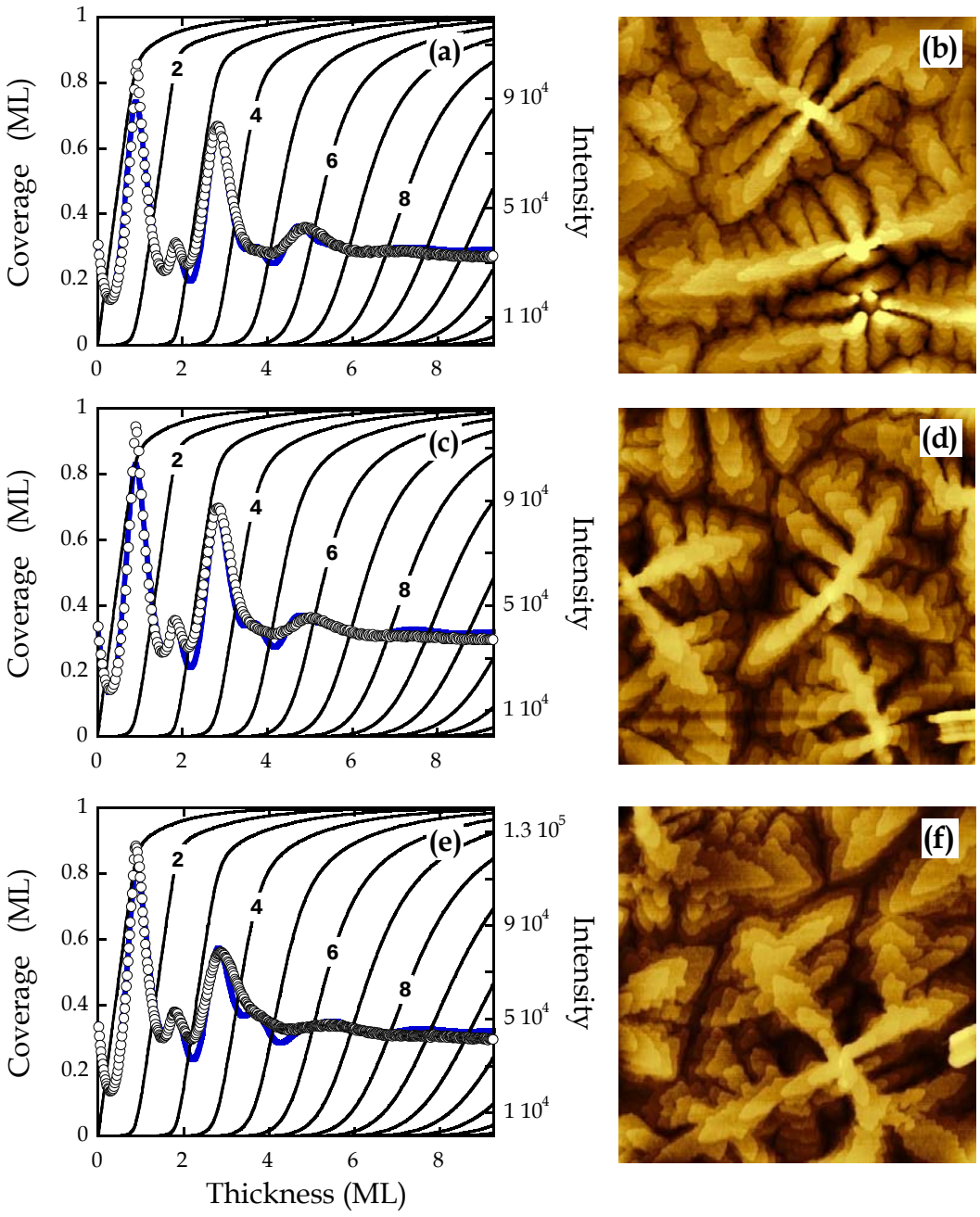
(a)
(b)
(c)
(d)
(e)
(f)
2
4
6
8
Coverage (ML)
Intensity
Thickness (ML)
0
0.2
0.4
0.6
0.8
1
2
4
6
8
1 10^4
5 10^4
9 10^4
1.3 10^5

Compared to pentacene on PS, PMMA and clean SiO_2, the film growth mode is significantly smoother, where LbL growth is extended up to 6 MLs. In Figures 5-10(b, d, f), we show the AF micrographs (5×5 μm^2) of pentacene deposited on PEI at their respective E_i of 2.5, 4.7 and 7.0 eV and nominal film thicknesses of 9.3 ML, 9.3 ML and 9.3 ML respectively. At all E_i, the AF micrographs reveal the formation of tall, pyramid-shaped islands with dendritic features. No obvious changes in morphology can be observed with E_i (*cf.* Figs 10(b, d, f)). In comparison to pentacene deposited on PS, at each E_i, the feature sizes (densities) are greater (smaller) for pentacene deposited on PEI. In comparison to pentacene deposited on PMMA and clean SiO_2, the morphology is similar.

In Figure 5-11, we present the rms roughness predicted by our fits to the anti-Bragg oscillations as a function of film thickness for growth of pentacene on PEI at all E_i investigated. Also shown as individual points, are the surface roughness values found from AFM analysis (*cf.* Figures 5-10(b, d, f)). We see from Figure 5-11, there is no difference in the evolution of surface roughness with E_i. In addition, the corroboration between AFM rms points and as predicted from x-rays is excellent (does not exceed 16%) and also confirms that E_i does not have a significant impact for pentacene growth on PEI. Comparing to the roughness evolution for pentacene on PS, PMMA and clean SiO_2, the evolution of pentacene growth on PEI is significantly smoother. For example, after a total coverage of 4MLs (E_i = 2.5 eV), the film roughness is 2.24 nm, 2.07 nm, 1.88 nm and 1.36 nm for pentacene on PS, PMMA, clean SiO_2 and PEI respectively.

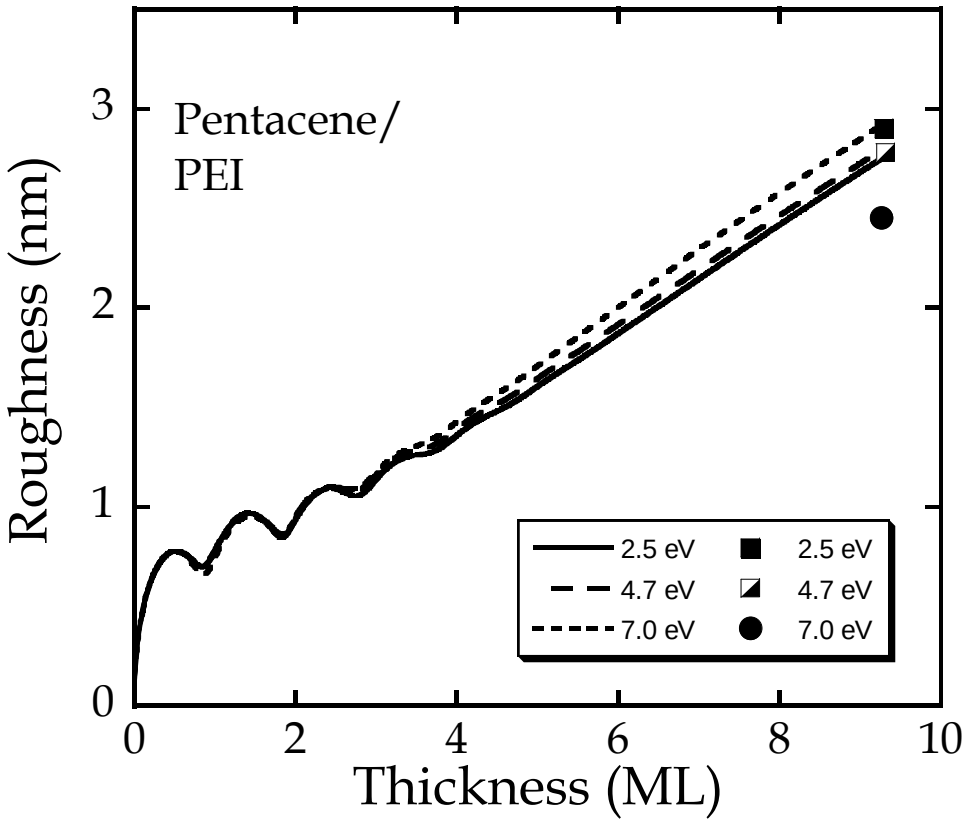

Figure 5-11 Thin film roughness as a function of pentacene thin film thickness deposited on PEI at E_i = 2.5, 4.7, and 7.0 eV. The points shown represent roughness values obtained directly from 5×5 μm^2 AFM images.

In Figure 5-12, we compare the rms roughness predicted by the fits to the anti-Bragg oscillations as a function of film thickness for growth of pentacene on all surfaces investigated at E_i = 2.5 eV. We also show as individual points, the surface roughness values found from AFM analysis at E_i = 2.5 eV for each surface investigated. From Figure 5-12, we see clearly that the roughness evolution of pentacene is a strong function of the chemical nature of the underlying substrate. In particular, as corroborated by the anti-Bragg oscillations discussed earlier, pentacene grows in a much more LbL manner and therefore significantly smoother on PEI followed by clean SiO_2, PMMA and PS. Similar trends are also observed at all E_i investigated. Why would the chemical nature of the substrate affect the growth mode of pentacene thin film growth? This is indeed an interesting question, as once the substrate is covered by a monolayer of pentacene, pentacene is then growing on itself, so why would it continue to grow more LbL on one surface as opposed to another?

From XRR and GID analysis, we found the same crystal structure, in-plane and out-of-plane, for pentacene on all surfaces investigated so a substrate dependent pentacene crystal structure cannot explain our observations. Regarding the bare polymers themselves, they are all equally smooth, so the smoothness/roughness of the polymers also cannot explain our results. Indeed, there is a correlation with the surface energy of the underlying substrate, where our results indicate that pentacene grows more LbL as the surface energy of the underlying substrate increases. In Figure 5-13, we plot the pentacene thin roughness versus surface energy of the underlying substrate at all three E_i investigated. From, Figure 5-13, we observe that there is a smooth decrease in the pentacene thin film roughness with the surface energy of the

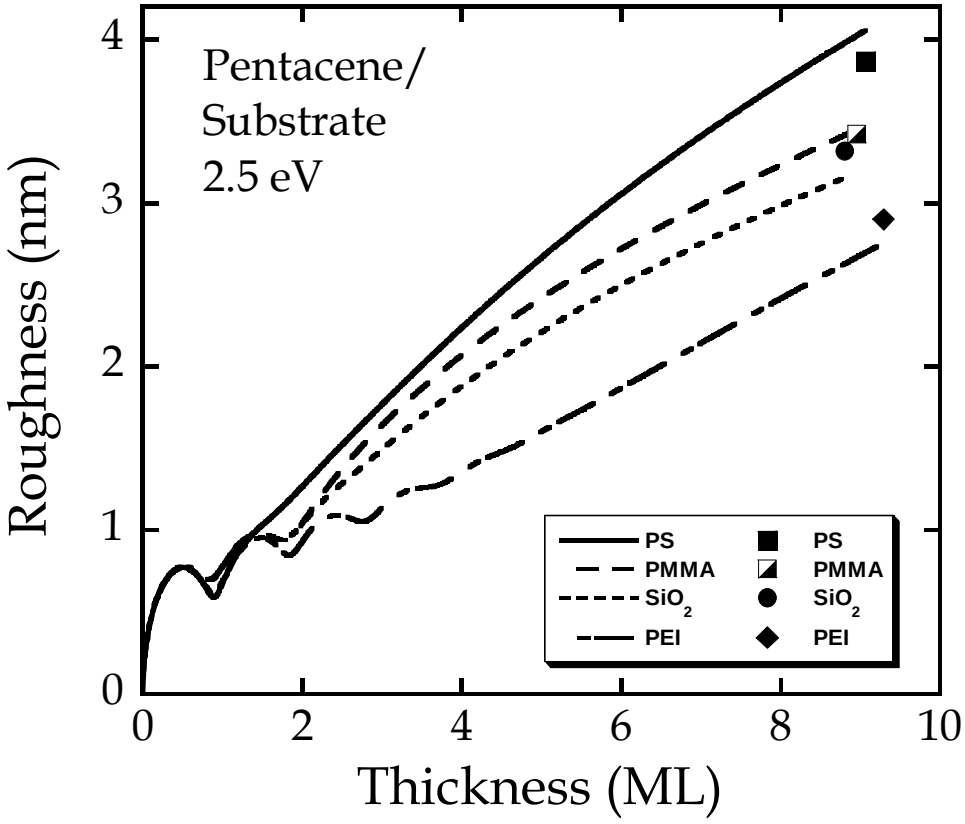

Figure 5-12 Thin film roughness as a function of pentacene thin film thickness deposited on PS, PMMA, SiO_2 and PEI at E_i = 2.5 eV. The points shown represent roughness values obtained directly from 5×5 μm^2 AFM images.

underlying substrate. With increasing surface energy of the underlying substrate, it is likely, that there will be an energetic preference for pentacene to wet the substrate surface. However, it is not clear, how this initial wetting effect of the first monolayer can propagate to the subsequent monolayers. Thermodynamic arguments can be put forth to explain these observations. From an energetic point of view, one would expect LbL growth (or Frank-van der Merwe growth) if the sum of the surface energy of the depositing species (i.e. pentacene) and the interface between the depositing species and the underlying substrate is less than the surface energy of the underlying substrate **[38]**. The surface energy of the (001) pentacene crystal face is reported to be 50-82 mJ-m^{-2} **[29, 30]**, whereas the surface energy of PS, PMMA and PEI was measured to be 25.0, 35.6, and ≥ 73.4 mJ-m^{-2} respectively. The surface energy of SiO_2 is reported to be 50-60 mJ-m^{-2} **[27, 28]**. With these values in mind, it would be energetically favorable for pentacene to grow more LbL on PEI as opposed to on PS. However, we also note, that thin film growth phenomena are most likely kinetically driven and not thermodynamically, and therefore these thermodynamic arguments are only put forth as a possible explanation and not the most likely one.

The rate of film roughening or sustained LbL growth will depend on the degree of interlayer transport – the ability of a molecule to transfer itself from on top of layer *n* initially, on to layer *n* via some mechanism. One mechanism is to diffuse to a step edge of an island and 'hop over' onto the layer below, but the pentacene molecule will have to overcome a sufficient energy barrier in order for this to happen (Ehrlich-Schwoebel, *ES*, barrier **[39-43]**). Since the growth mode of pentacene is dependent on the underlying substrate, our results indicate that the ability of interlayer transport, or

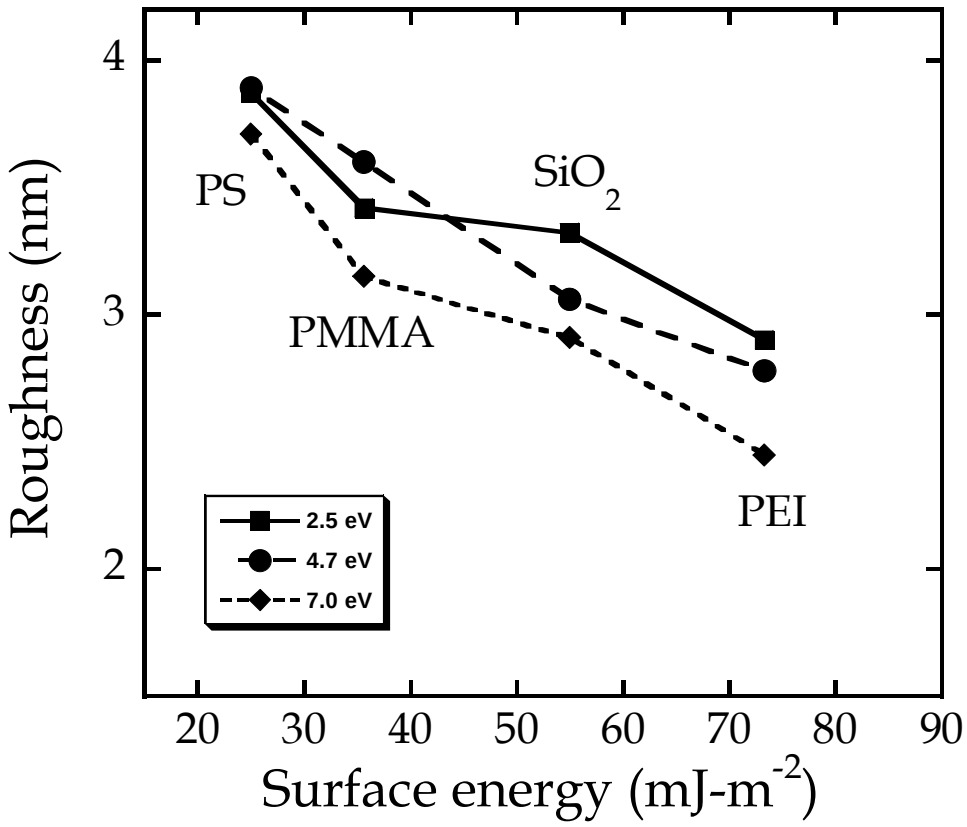

Figure 5-13 Pentacene thin film roughness (obtained directly from 5×5 μm^2 AFM images) as a function of substrate surface energy at E_i = 2.5, 4.7 and 7.0 eV.

the *ES* barrier, is a function of the chemical nature of the substrate – in particular, the *ES* barrier is the least on PEI, whereas it is the greatest on PS. However, it is not clear the exact mechanism of how the chemical nature of the substrate would affect the pentacene *ES* barrier if indeed this were happening. Previous results have suggested the presence of a film thickness dependent or molecular tilt dependent *ES* barrier for organic systems **[42, 44]**. For the case of the diindenoperylene (DIP) organic semiconductor, a previous study has shown that during DIP thin film growth, the DIP tilt angle (with respect to the substrate normal) increases and the *b* in-plane lattice parameter increases until ~ 4MLs after which both the tilt angle and *b* in-plane lattice parameter remain constant. Accompanied by the fact that since the onset of DIP rapid roughening begins after ~4 MLs of film growth, the study argues that this suggests the presence of a layer-dependent *ES* barrier **[44]**. In another previous study for the case of sexiphenyl organic semiconductor, the study concluded a gradual increase in the *ES* barrier with film thickness and attributed this to decrease (with respect to the substrate normal) in the sexiphenyl molecular tilt with increasing coverage **[42]**. It is important to note that while DIP has a rigid backbone, sexiphenyl has a flexible backbone which can bend and twist **[42, 43]**. If we use these studies **[42, 44]** as a precedent to explain our observations, it is plausible that the pentacene molecular tilt or in-plane lattice structure maybe changing during thin film growth leading to smoother or rougher films and this apparently depends on the chemical nature of the underlying substrate. Since, we observed the same crystal structure (out-of-plane and in-plane) using *ex situ* techniques, on all surfaces investigated after a total film coverage of ~ 10 ML, this suggests that any changes in crystal structure would have to be transient. If there are

any transient structure changes occurring during pentacene thin film growth that may explain these observations, then conducting i*n situ* real-time XRR and GID techniques during pentacene thin film growth will help in elucidating these changes **[45]**. This however, is beyond the scope of this study.

5.5 Conclusions

In conclusion, we have examined the effects of polymeric dielectrics on the thin film growth of pentacene, a *p*-type organic semiconductor. We have also compared the results to pentacene growth on clean SiO_2. From *in situ* real-time x-ray scattering, we find that pentacene exhibits layer-by-layer (LbL) growth on all surfaces investigated, but the extent of LbL growth is a strong function of the underlying substrate. In particular, LbL growth is significantly more prolonged on PEI, (up to ~6 MLs), followed by SiO_2 and PMMA (up to ~4 MLs) and finally PS (up to ~ 3 MLs). The extent of LbL growth and therefore the final thin film roughness follows a trend with the surface energy of the underlying substrate–pentacene thin film growth is more LbL-like and smoother as the surface energy of the underlying substrate increases.

5.6 References

1. Hamers, R. J.; *Nature* **2001**, *412*, 489-490.
2. Dimitrakopoulos, C. D. ; Malenfant, P. R. L. *Adv. Mater.* **2002**, *14*, 99-117.

3. Lin, Y. Y.; Gundlach, D. J.; Nelson, S. F.; Jackson, T. N. *IEEE Electron Device Letters* **1997**, *18*, 606-608.

4. Ling, M. M; Bao, Z, *Chem*. *Mater*. **2004**, *16*, 4824-4840.

5. Ruiz, R.; Papadimitratos, A.; Mayer, A. C.; Malliaras, G. G. *Adv. Mater*. **2005**, *17*, 1795-1798.

6. Dinelli, F.; Murgia, M.; Levy, P.; Cavallini, M.; Biscarini, F.; de Leeuw Dago M. *Phys. Rev. Lett.* **2004**, *92*, 116802-116804.

7. Muck, T.; Wagner, V.; Bass, U.; Leufgen, M.; Geurts, J.; Molenkamp, L. W. *Synthetic Metals* **2004**, *146*, 317-320.

8. Dodabalapur, A.; Torsi, L.; Katz, H. E. *Science* **1995**, *268*, 270-271.

9. Yoon, M.-H.; Kim, C.; Facchetti, A.; Marks, T. J. *J. Amer. Chem. Soc.* **2006**, *128*, 12851-12869.

10. Klauk, H; Halik, M.; Zschieschang, U.; Schmid, G.; Wolfgang, R. *J. Appl. Phys.* **2002**, *92*, 5259-5263.

11. Nunes Jr., G.; Zane, S. G.; Meth, J. S. *J. Appl. Phys.* **2005**, *98*, 104503/1-104503/6.

12. Kim, C.; Facchetti, A.; Marks, T. J. *Science* **2007**, *318*, 76-90.

13. Kim, C.; Facchetti, A.; Marks, T. J. *Adv. Mater.* **2007**, *19*, 2561-2566.

14. Yang, S. Y.; Shin, K.; Park, C. E. *Adv. Func. Mater.* **2005**, *15*, 1806-1814.

15. Kim, C.; Quinn, J. R.; Facchetti, A.; Marks, T. J. *Adv. Mater.* **2010**, *22*, 342-346.

16. Yang, H.; Kim, S. H.; Yang, L.; Yang, S. Y.; Park, C. E. *Adv. Mater.* **2007**, *19*, 2868-2872.

17. Kim, S. H.; Jang, M.; Yang, H.; Park, C. E. *J. Mater. Chem.* **2010**, *20*, 5612-5620.

18. Ribic, P. R.; Kalihari, V.; Frisbie, C. D.; Bratina, G. *Phys. Rev. B* **2009**, *80*, 115307/1-115307/8.

19. Stadlober, B.; Haas, U.; Maresch, H.; Haase, A. *Phys. Rev. B* **2006**, *74*, 165302/1-165302/9.

20. Killampalli, A. S.; Schroeder, T. W.; Engstrom, J. R. *Appl. Phys. Lett.* **2005**, *87*, 033110/1-033110/3.

21. Schroeder, T. W. *Cornell University: Ph.D. Thesis* **2004**.

22. Hong, S.; Amassian, A.; Woll, A. R.; Bhargava, S.; Ferguson, J. D.; Malliaras, G. G.; Brock, J. D.; Engstrom, J. R. *Appl. Phys. Lett.* **2008**, *92*, 253304.

23. Amassian, A.; Desai, T. V.; Kowarik, S.; Hong, S.; Woll, A. R.; Malliaras, G. G.; Schreiber, F.; Engstrom, J. R. *J. Chem. Phys.* **2009**, *130*, 124701/1-124701/9.

24. Desai, T.; Hong, S.; Woll, A. R.; Hughes, K. J.; Ananth, P.; Clancy, P.; Engstrom, J. R. *Journal of Chemical Physics* **2011**, *134*, 224702.

25. Amassian, A.; Pozdin, V.; Desai, T. V.; Hong, S.; Woll, A. R.; Ferguson, J. D.; Brock, J. D.; Malliaras, G. G.; Engstrom, J. R. *J. Mater. Chem.* **2009**, *19*, 5580-5592.

26. Kaelble, D. H. *J. Appl. Polym. Sci.* **1974**, *18*, 1869-1889.

27. Knieling, T.; Lang, W.; Bencke, W. *Sensors and Actuators B: Chemical* **2007**, *126*, 13-17.

28. Kawai, A.; Kawakami, J. *J. Photopolym. Sci. Technol.* **2003**, *16*, 665-668.

29. Northrup, J. E.; Tiago, M. L.; Louie, S. G. *Phys Rev. B* **2002**, *66*, 121404/1-121404/4.

30. Nabok, D.; Puschnig, P.; Ambrosch-Draxl, C. *Phys. Rev. B* **2008**, *77*, 245316/1-245316/4.

31. Braun, C. *Parratt32 program*; Berlin Neutron Scattering Center (BENSC): Hahn-Meitner Institut, 1997.

32. Parratt, L. G. *Phys. Rev. B.* **1954**, *95*, 359.

33. Kowarik, S.; Gerlach, A.; Skoda, M.; Sellner, S.; Schreiber, F. *Eur. Phys. J. Special Topics* **2009**, *168*, 11.

34. Woll, A. R.; Desai, T. V.; Engstrom J. R. *under review at the J. Phys. Rev. B*.

35. Cohen, P. I.; Petrich, G. S.; Pukite, P. R.; Whaley, G. J.; Arrott, A. S. *Surface Sci.* **1989**, *216*, 222-248.

36. Ruiz, R.; Mayer, A. C.; Malliaras, G.G.; Nickel, B.; Scholes, G; Kazimirov, A.; Kim, H.; Headrick, R. L.; Islam, Z. *Appl. Phys. Lett.* **2004**, *85*, 4926-4928

37. Hong, S.; Amassian, A.; Woll, A. R.; Bhargava, S.; Ferguson, J. D.; Malliaras, G. G.; Brock, J. D.; Engstrom, J. R. *Appl. Phys. Lett.* **2008**, *92*, 253304/1-253304/3.

38. Venables, J. A.; Spiller, G. D. T.; Hanbücken, M. *Rep. Prog. Phys.* **1984**, *47*, 399-459.

39. Ehrlich, G.; Hudda, F. G. *J. Chem. Phys.* **1966**, *44*, 1039-1049.

40. Schwoebel, R. L.; Shipsey, E. J. *J. Appl. Phys.* **1966**, *37*, 3682-3686.

41. Fendrich, M.; Krug *J. Phys. Rev. B* **2007**, *76*, 121302/1-121302/3.

42. Hlawacek, G.; Puschnig P.; Frank, P.; Winkler, A.; Ambrosch-Draxl, C.; Teichert, C. *Science* **2008**, *321*, 108-111.

43. Goose, J. E.; First, E. L.; Clancy, P. *Phys. Rev. B* **2010**, *81*, 205310/1-205310/20.

44. Zhang, X.; Barrena, E.; Goswami, D.; de Oteyza, D. G.; Weis, C.; Dosch, H. *Phys. Rev. Lett.* **2009**, *103*, 136101/1-136101/4.

45. Kowarik, S.; Gerlach, A.; Sellner, S.; Schreiber, F.; Cavalcanti, L.; Konovalov, O. *Phys. Rev. Lett.* **2006**, *96*, 125504/1-125504/4.

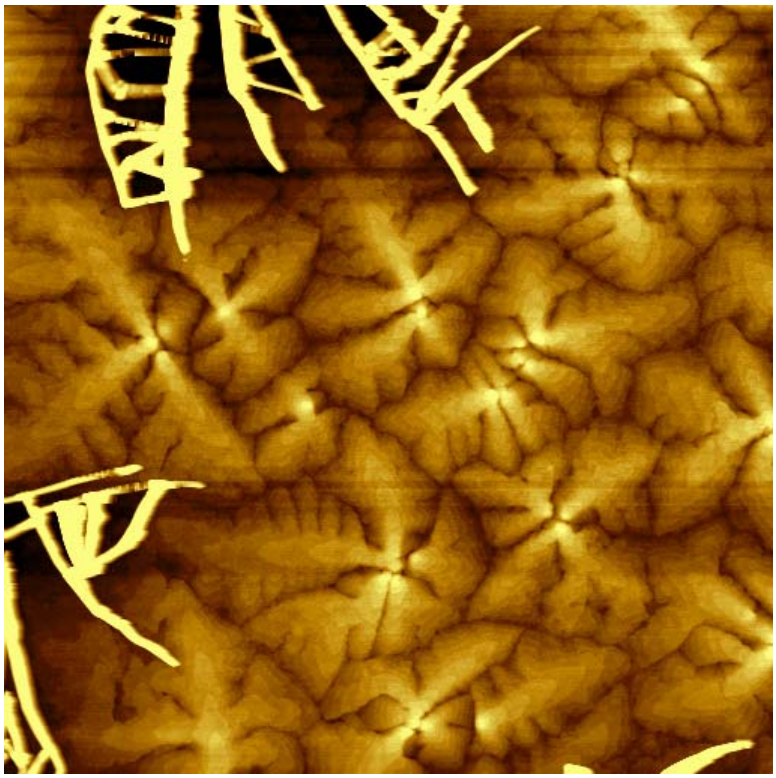

Figure 5-SI-1 AFM image, 10×10 μm^2, of pentacene thin films deposited on PMMA at E_i = 7.0 eV. Bright, needle-like features in the image are up to ~100 nm in height.

6. Nucleation and growth of perfluoropentacene on self-assembled monolayers: significant changes in island density and shape with surface termination[*]

6.1 Overview

We have examined the nucleation and growth of perfluoropentacene (PFP) on SiO_2 and on a variety of surfaces possessing different terminating self assembled-monolayers (SAMs) using *in situ* synchrotron x-ray scattering and *ex situ* atomic force microscopy (AFM). The SAMs ranged from very low surface energy hydrophobic surfaces (perfluorooctyltrichlorosilane, FOTS), to higher surface energy hydrophilic surfaces (3-methacryloxypropyltrichlorosilane, MAOPTS). From real-time x-ray scattering we find that the growth of PFP, while crystalline, becomes very 3D after completion of the first 1-2 monolayers, independent of the substrate surface termination. Concerning growth in the submonolayer regime, we find that nucleation is homogeneous, and that the absolute density of islands depends strongly on the surface termination, while the relative change of the island density with increasing growth rate is essentially independent of the underlying SAM. From the latter, we find that a critical island size of ~ 2-3 molecules can describe all the data. On the other hand, the dependence of the island density on termination implicates a significant change in the diffusivity of PFP with the identity of the SAM. The shape of the islands also depends on the surface termination, but somewhat unexpectedly—the islands are most compact and facetted on surfaces where the diffusivity of isolated

[*] *J. Phys. Chem. C* **2010**, *114*, 20120-20129

PFP molecules is the smallest. This result highlights the difference in transport mechanisms concerning diffusion across the substrate and that around the periphery of an island in molecular systems. Finally, on all surfaces, the films formed in the multilayer regime are similar, and are described by rough, highly anisotropic features, perhaps dominated by a single low-index face.

6.2 Introduction

The study of complex conjugated molecules for applications in organic thin film electronics and photonics has received much attention owing to their ability to form highly ordered thin films with excellent electrical properties.**[1-3]** Studies have shown that the interface between the organic semiconducting layer and the dielectric is critical to charge transport and that the majority of charge carriers are generated in the first few monolayers (MLs) of the organic layer.**[4-7]** Several studies have also shown that the deposition of organic semiconductors on low energy surfaces such as self-assembled monolayers (SAMs) significantly improves the electrical properties of the organic thin film transistor (OTFT).**[8-12]** The exact reasons as to why this improvement is observed are still a matter of debate, however. Clearly, the development of a better understanding of the effects of SAMs on the nucleation and the initial stages of growth of organic semiconductors, particularly in the submonolayer regime, will greatly aid in resolving these issues.

There have been a number of investigations of the nucleation of pentacene on clean, unmodified, silicon dioxide (SiO_2), and the consensus is that the nucleation is

homogeneous with the size of the critical cluster being ~2-6 molecules.**[13-15]** Study of the effects of SAMs on the nucleation of organic semiconductors, pentacene or otherwise, has proven to be more challenging. A major obstacle to be overcome in these systems is that pentacene and other organic thin films undergo significant, and sometimes rapid, post-growth reorganization and dewetting when deposited on low energy surfaces.**[16, 17]** One system, due to its low intrinsic surface energy, that might be expected not to dewet low energy surfaces of SAMs is the *n*-type organic semiconductor perfluoropentacene (PFP). Thus, this property of PFP can be exploited to examine in detail effects occurring in the submonolayer nucleation and growth of organic small molecule thin films on surfaces terminated with self-assembled monolayers.

Here we report on the effects of self-assembled monolayers on the nucleation and growth of PFP using a combination of both *in situ* and *ex situ* surface sensitive probes. Concerning the SAMs, we consider four layers that differ in terms of their size (thickness) and chemical nature: octyltrichlorosilane (OTS), $(Cl)_3Si\text{-}(CH_2)_7\text{-}CH_3$, perfluorooctyltrichlorosilane (FOTS), $(Cl)_3Si\text{-}(CH_2)_2(CF_2)_5\text{-}CF_3$, 3-methacryloxypropyltrichlorosilane (MAOPTS), $(Cl)_3Si\text{-}(CH_2)_3\text{-}O\text{-}(C{=}O)(C(CH_3){=}CH_2)$ and hexamethyldisilazane, (HMDS), $HN(Si(CH_3)_3)_2$. The first three of these hydrolyze to form $–Si(\text{-}O\text{-})_3$ linkages to the SiO_2 surface of the substrates, whereas HMDS decomposes and releases $–Si(CH_3)_3$ fragments, which then bind to the surface. For comparison, we also consider unmodified SiO_2. In terms of surface energies, the SAMs follow the order (high-to-low): unmodified SiO_2, MAOPTS, HMDS, OTS and FOTS. We deposit thin films of PFP in ultrahigh

vacuum (UHV) using a collimated supersonic molecular beam **[13, 18, 19]**, and make use of *ex situ* atomic force microscopy (AFM) to probe the thin film morphology, focusing on the submonolayer regime. We also employ *in situ* real-time synchrotron x-ray scattering measurements at the "anti-Bragg" configuration **[20]** to directly probe the filling of each successive molecular layer of PFP. We will find below that the nature of the SAM affects significantly both the density and the shape of the islands formed at submonolayer coverages.

6.3 Experimental Procedures

Refer to chapter 2 for details. Only a brief summary on experimental procedures is provided in this section. The experiments were carried out in the G3 station of the Cornell High Energy Synchrotron Source in a custom-designed UHV system fitted with Be windows that is described elsewhere **[18, 19]**. Briefly, the system consists of four separately pumped chambers: a main scattering chamber, a source and antechamber, which act to produce the supersonic beam, and a fast entry load-lock. All chambers are pumped by high-throughput turbomolecular pumps. The base pressure of the chamber was typically $\sim 4 \times 10^{-9}$ Torr and samples were loaded via the load-lock chamber, which was evacuated to $\sim 10^{-7}$ Torr prior to sample transfer into the main chamber.

Substrates were Si(100) wafers (Wacker-Siltronic, *p*-type, 100 mm dia., 500-550 μm thick, 38-63 Ω-cm) subject to a SC-1 clean, 15 s HF dip and a SC-2 clean followed by growth of ~ 300-nm-thick SiO_2 films by wet thermal oxidation at 1100°C.

Next, these wafers were cleaned and degreased by sonication for 15 min in anhydrous $CHCl_3$ solution (99 %+), sonicated in deionized (DI) water for 15 min, washed with DI water, dried with N_2 and exposed to UV-ozone for 15 min. These processes provided a clean and reproducible hydrophilic surface. Finally, the SAMs were deposited using established procedures.**[21]** Briefly, the FOTS and MAOPTS layers were deposited from the vapor phase using an MVD-100 system, while the HMDS was deposited from the vapor phase using a YES LP-III Vapor Prime Oven. OTS was deposited from the solution phase in a N_2-purged glove box.

Supersonic molecular beams of PFP were generated by passing He (99.999% Air Gas Inc.) as a carrier gas over an *in situ* temperature controlled evaporator located upstream of the 150 μm dia. nozzle in the source chamber. The flow of He was set by a mass flow controller. The beam passes through a 1.5-mm-diameter skimmer, into the antechamber and through an aperture to produce a well-defined beam spot on the substrate (4×15 mm^2) at normal incidence. The kinetic energy of the beam was measured using time-of-flight mass spectrometric techniques **[18]** and kept constant for all experiments at $E_i = 4.6$ eV. For all experiments described here the substrate temperature during growth was $T_s = 40$ °C, and in all cases the beam was incident normal to the substrate surface, and could be blocked using a shutter in the antechamber. Multiple experiments could be carried out on the same substrate, which is made possible by translating the substrate perpendicular to the supersonic molecular beam, and due to the high beam-to-background flux ratio. Following deposition, AFM was conducted *ex situ* in tapping mode using a Digital Instruments 3100 Dimension microscope.

The SiO_2 substrates modified with FOTS, OTS, HMDS and MAOPTS, were characterized by contact angle and x-ray reflectivity (XRR). First, contact angles were measured in two solvents (water and formamide). Next, using the Young-Dupre equation **[22]**, we calculated the surface energy of FOTS, OTS, HMDS and MAOPTS, and found values of 11.1, 16.7, 32.7 and 40.1 mJ-m^{-2}, respectively. In comparison, the surface energy of clean, unmodified SiO_2 has been reported to lie between 50 and 60 mJ-m^{-2}.**[23, 24]** Fits to the XRR data (not shown) were performed with the Parratt32 software package **[25]** (based on the Parratt formalism **[26]**), from which we obtain the thickness of the organic layers, and the mean electron density. Knowledge of the molecular weight of the SAM molecules permits us to estimate the 2D surface concentration of the SAMs. For all four SAMs we found values in the range of 2-3 × 10^{14} molec-cm^{-2}, similar to values found using XRR and x-ray photoelectron spectroscopy **[27]** for these same SAMs.

6.4 Results and Discussion

We first consider measurements of film growth using *in situ* real time synchrotron x-ray scattering. Here, growth of PFP was monitored using 9.82 keV X-rays incident at an angle of 1.15° (with respect to the substrate surface) with a flux of ~ 10^{13} photons-s^{-1} (unattenuated value, the beam was attenuated for all experiments) incident to the sample through a Be window with energy resolution of 1%, which was dictated by the use of a multilayer monochromator. An avalanche photodiode was used for measuring the scattered x-ray intensity. First we consider x-ray reflectivity measurements at the so-called "anti-Bragg" condition (00½; $q_z = q_{Bragg}/2 = 0.40/2$ Å^{-1}),

which is an effective monitor of the nature of growth, *i.e.*, layer-by-layer (LbL) vs. 3D islanded growth.**[19, 28, 29]**

In Figure 6-1(a) we plot the scattered intensity measured *in situ* and in real-time for the growth of PFP on HMDS at E_i = 4.6 eV. As may be seen, for growth on this surface we observe a single sharp, cusp-like peak, which coincides with completion of the first monolayer, but the anticipated second (small, similar to the zero-coverage intensity), third (large, similar to the first peak) and other subsequent maxima are almost completely obscured. Beyond the deposition of 4 monolayers (MLs) the intensity remains constant. This suggests that growth becomes 3D quickly after completion of the first 1-2 monolayers. The intensity oscillation can be fitted using a modified version **[30]** of the mean-field, rate equation model of growth first proposed by Cohen and co-workers **[31]**. The fit to the intensity is indicated by the solid blue line, and we see that the fit to the experimental data is excellent. In Figure 6-1(a) we also show the coverage (occupancy) of each layer with solid black lines that are predicted by the fit to the intensity oscillations. After a total growth of 2 MLs, the 2^{nd} layer is ~ 81% full, whereas after 4MLs the 4^{th} layer is only ~ 59% full. These results indicate that PFP grows in an LbL mode for approximately 2 MLs before significant roughening begins to occur. Indeed, we observe essentially identical behavior concerning the intensity oscillations at the anti-Bragg condition for growth on all 4 SAMs examined here, on unmodified SiO_2, and for incident kinetic energies over the range of E_i = 4.6-16.4 eV. We note that this behavior has also been observed for growth of PFP from a thermal effusion source on a thin layer of native silicon dioxide.**[32, 33]**

Figure 6-1 (a) X-ray intensity at the anti-Bragg condition as a function of exposure to the molecular beam (E_i = 4.6 eV) for thin films of PFP deposited on a SiO_2 surface terminated with HMDS. Substrate temperature, T_s = 40 °C, and the rate of growth was 0.0103 ML-s^{-1}. Thick solid blue line (left ordinate) indicates a fit of the data to a model and thin solid black curves (right ordinate) represent predicted coverages of the individual layers. Representative (b) line scan and (c) surface height histogram obtained from AFM of a submonolayer PFP thin film (0.36 ML) grown on HMDS.

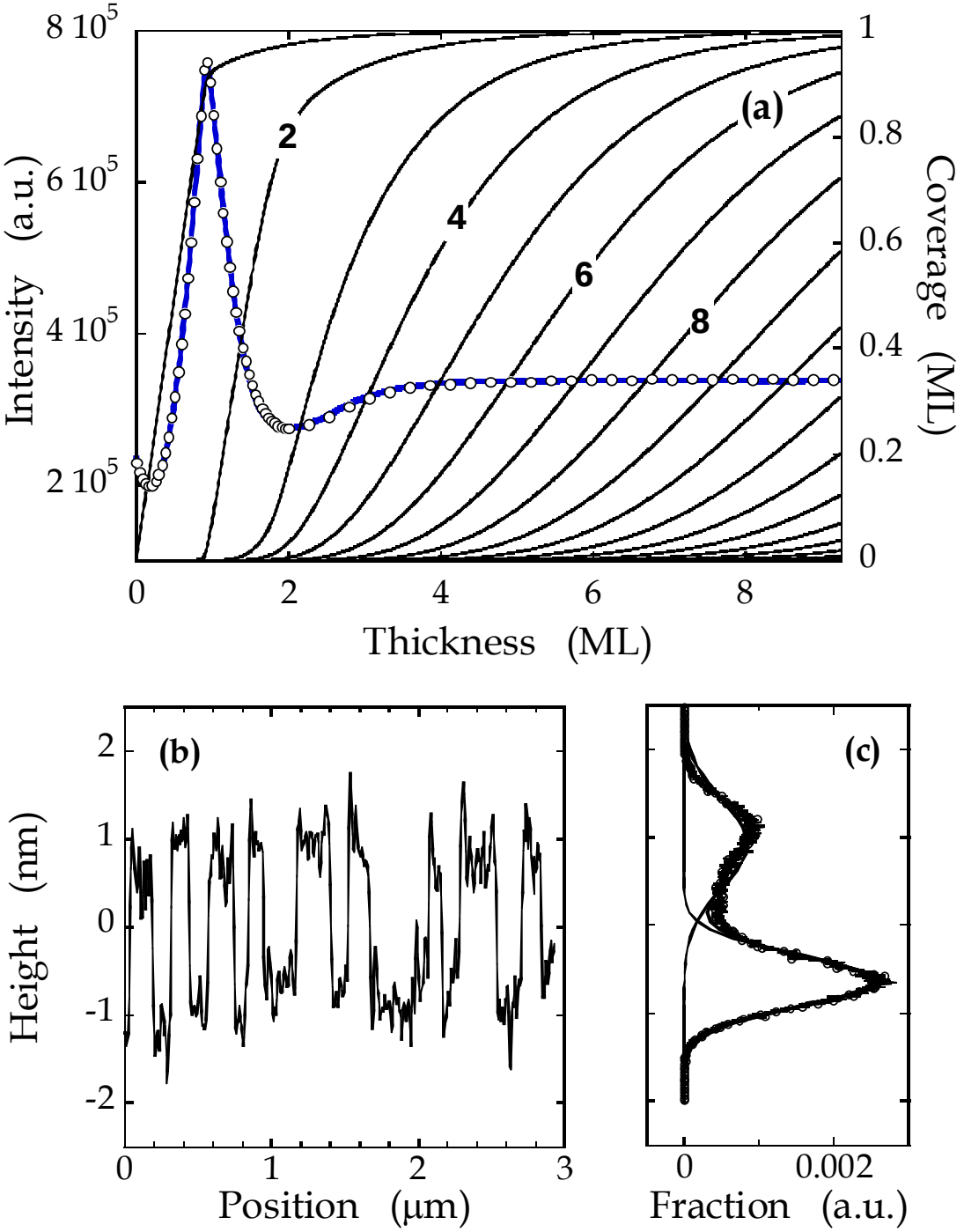
8 10^5
6 10^5
4 10^5
2 10^5
Intensity (a.u.)
1
0.8
0.6
0.4
0.2
0
Coverage (ML)
(a)
2
4
6
8
0
2
4
6
8
Thickness (ML)
(b)
2
1
0
-1
-2
Height (nm)
0
1
2
3
Position (μm)
(c)
0
0.002
Fraction (a.u.)

In Figure 6-1(b), we display a representative line profile obtained from *ex situ* AFM of the islands formed after deposition of ~ 0.36 ML of PFP on a HMDS-terminated surface at a growth rate of 0.0056 ML-s^{-1}. In Figure 6-1(c) we display a histogram of surface heights calculated from the entire AF micrograph. The line profile and histogram indicates that the islands of PFP on HMDS are single monolayer-tall islands with an average height of ~ 1.61 ± 0.04 nm. This height is consistent with *ex situ* specular XRR measurements of ~ 10 ML thick films of PFP deposited on a variety of surfaces (including clean, unmodified SiO_2) where a unit cell height of d_{001} = 1.57 ± 0.02 nm was found.**[32-35]** We note that following deposition, AF micrographs of submonolayer growth of PFP reveal single monolayer tall high islands on all of the surfaces we have investigated. This is also the case where the submonolayer films have experienced extended ageing, post-deposition, for time periods in vacuum for ≥ 2 hours (as opposed to < 2 min. more typically here) and in air for several months. This indicates that PFP does not re-organize or "dewet" on these surfaces unlike other conjugated organic semiconductors such as pentacene **[16]** and diindenoperylene (DIP), where such behavior has been observed on surfaces terminated with both HMDS and FOTS layers. The relative stability of the submonolayer islands of PFP is of course essential to the main objectives of this work.

In Figures 6-2(a-d), we display AF micrographs of PFP deposited on HMDS at a series of growth rates, *GR*, increasing in sequence from 0.0024 to 0.018 ML-s^{-1}, with all other parameters (e.g., E_i, T_s) fixed. The growth rate of PFP has been tuned by varying the temperature of the *in situ* evaporator. On this surface, the shapes of the islands at all growth rates are polygons and anisotropic, with an aspect ratio ~ 2-3. At

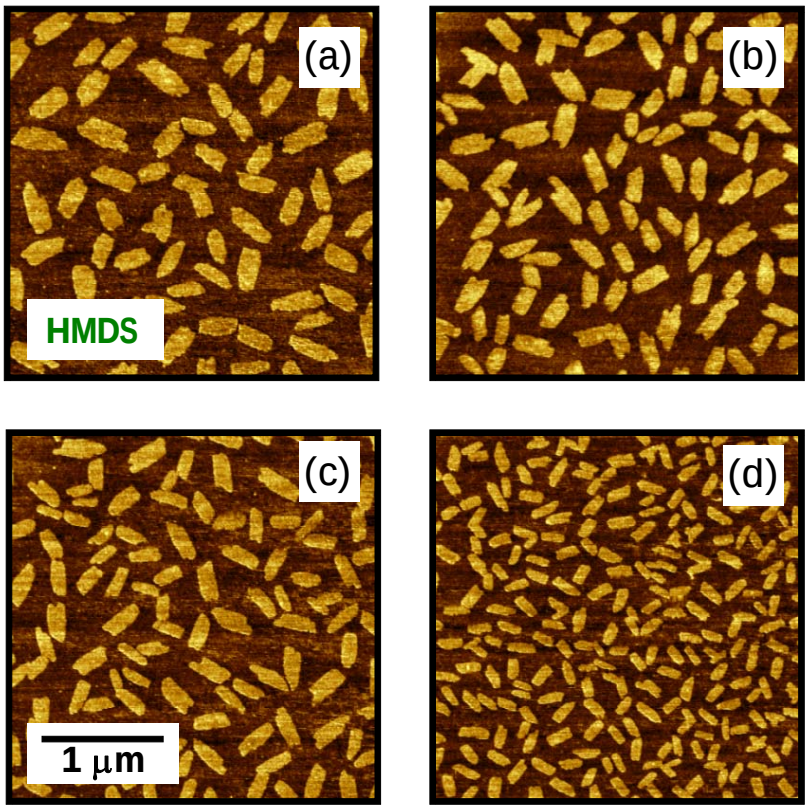

Figure 6-2 Atomic force micrographs, 3 × 3 μm^2, of submonolayer thin films of PFP grown on a SiO_2 surface terminated with HMDS at rates of **(a)** 0.00240, **(b)** 0.00424, **(c)** 0.00561, and **(d)** 0.0180 ML-s^{-1}. In all cases incident kinetic energy was E_i = 4.6 eV, and substrate temperature, T_s = 40 °C.

this stage of growth, the islands are also mostly isolated from each other, such that we can use these images to calculate the maximum island density. As the field of view is the same in all cases (3×3 μm^2) we see by inspection that the island density of PFP increases with increasing *GR*. The scaling of the island density with *GR* in this way is exactly as expected from classical nucleation theory for homogeneous nucleation **[36-38]**, which states that the maximum island density, N_x, for 2D islands and complete condensation (adsorption is irreversible) is given by the following expression:

$$N_x = \eta(\theta, i^*)(GR/D)^{i^*/(i^*+2)} \exp(E_{i^*}/(i^*+2)k_B T_s), \quad (6\text{-}1)$$

where D is the tracer diffusivity of the molecule, i^* is the critical cluster size, E_{i^*} is the binding energy of the critical cluster and k_B is the Boltzmann constant. The critical cluster size is defined as the largest unstable cluster, such that a cluster with $i^* + 1$ molecules is more likely to grow than to decay. The dimensionless prefactor $\eta(\theta, i^*)$ is nearly a constant—only weakly dependent on i^* and coverage, θ.**[37]** Thus, one straightforward measurement of the critical cluster size is to quantify how the maximum island density varies with *GR* **[36-39]** [*cf.* Figures 6-2(a-d)].

In Figure 6-3 we display the maximum island density as a function of *GR* for PFP on the 5 surfaces we consider here. The maximum island densities of PFP were measured at submonolayer coverages ($\theta < 0.43$ ML) before island coalescence took place using 10×10 μm^2 (3×3 μm^2 for PFP on FOTS) AF micrographs. As may be seen in the figure, the maximum island density of PFP increases with increasing *GR* on all surfaces, and the data are described very well by a power law in all cases. This

would seem to argue against any interpretation involving defects in the SAMs playing a significant or dominant role in the nucleation. Thus it seems that regardless of the nature of the underlying interfacial layer, PFP exhibits homogeneous nucleation on all surfaces. The critical cluster size of PFP can be determined from the power law fit to the data and our results are displayed in the inset of Figure 6-3. Here in a fit to the data we have considered explicitly the uncertainty in each value for the density of the islands ($N^{1/2}$, where N is the direct count of the islands in the image). As may be seen, we find similar values for the power law exponents and they span the range of $i^* =$ 2.4-3.7. The results on HMDS, OTS, unmodified SiO_2 and MAOPTS are all very similar, and the mean value for these 4 surfaces is given by $i^* = 2.66 \pm 0.36$. FOTS is somewhat of an outlier from these results, albeit the uncertainty is greater, and we find $i^* = 3.68 \pm 0.61$. Thus, possibly excepting for the case of FOTS, the interactions between the substrate surface and the PFP molecules do not significantly affect the critical cluster size of PFP.

Unlike the slopes of the curves shown in Figure 6-3, at a comparable growth rate the maximum island density of PFP depends strongly on the nature of the substrate. In particular, the maximum island density of PFP is greatest on FOTS, followed by HMDS, OTS, SiO_2 and MAOPTS. Because $N_x \propto (GR/D)^{i^*/(i^*+2)}$, and since we observed essentially the same value for i^* on all 5 surfaces, this suggests that the diffusivity, D, of PFP differs on the 5 surfaces and is mostly responsible for the offsets. An underlying assumption concerning this conclusion is that the prefactor η in Equation (6-1) does not contribute significantly to the observed changes in N_x. For the range of coverages we consider here ($\theta \sim 0.1$-0.4 ML), and the values for the size of

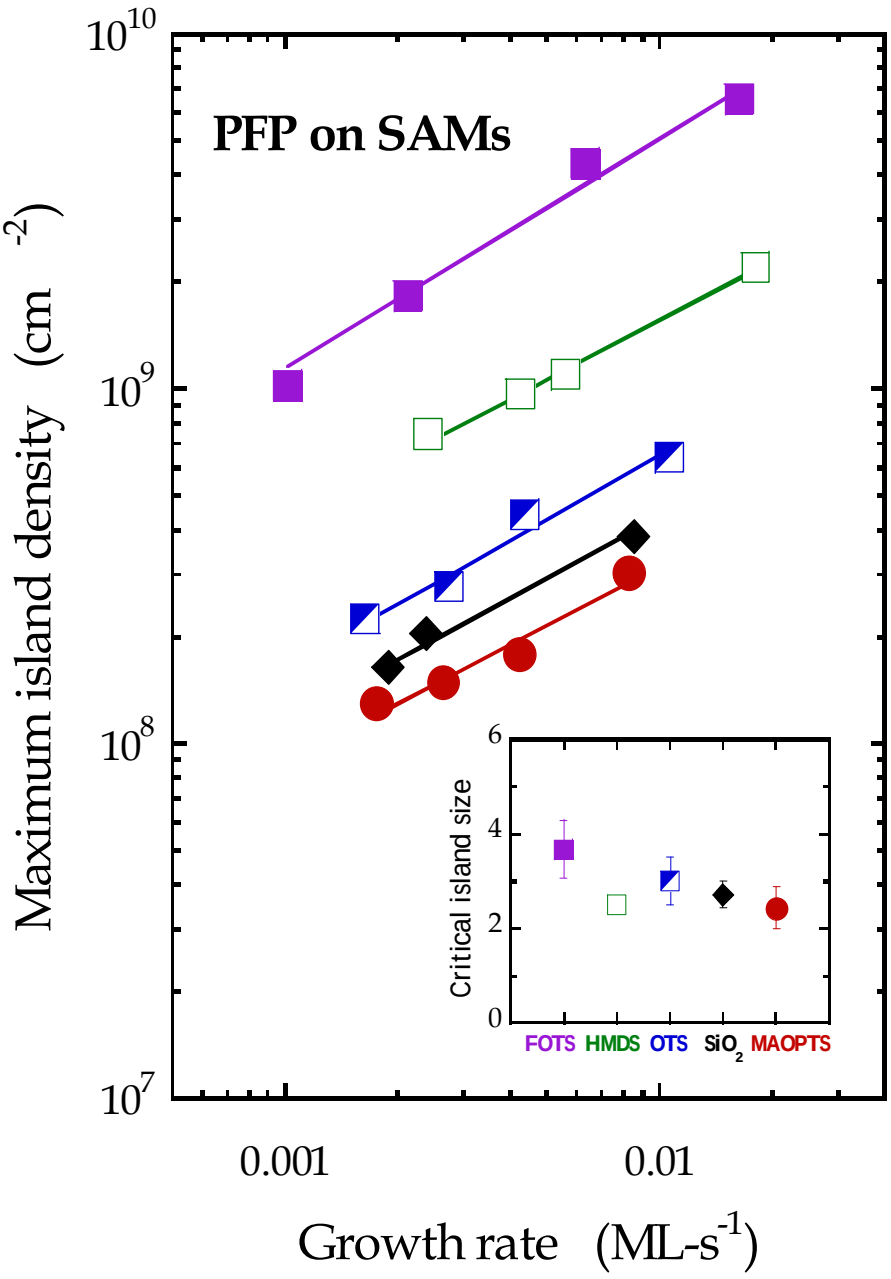

Figure 6-3 Maximum island density as a function of submonolayer growth rate for the deposition of PFP on SiO_2, and SiO_2 terminated with 4 different self-assembled monolayers. In all cases incident kinetic energy was E_i = 4.6 eV, and substrate temperature, T_s = 40 °C. The straight lines represent a fit to a power law. The inset shows the critical island size, *i**, as a function of surface termination.

the critical cluster ($i^* \sim 2$-4) we estimate $\eta(\theta, i^*)$ to lie in range 0.2–0.3 for PFP on all surfaces investigated.**[37]** This difference (less than a factor of 2) clearly does not account for the change in N_x that we observe. Thus, we are left with an explanation that the change in N_x observed has to be the result of a change in the diffusivity, D, of PFP on each surface.

The relative diffusivity of PFP can be estimated by taking the ratio of N_x on any two surfaces at a constant GR (0.005 ML-s^{-1}) and using the relationship, $D_2 = D_1/[(N_{x,1}/N_{x,2})^{((i^*+2)/i^*)}]$. If we let $D_1 = D_{FOTS} = 1$ and assume $i^* = 2.66$ (*vide supra*), then by implication, $D_{HMDS} = 7.1$, $D_{OTS} = 35$, $D_{SiO_2} = 67$ and $D_{MAOPTS} = 115$. *This analysis suggests that the diffusivity of PFP is a strong function of the chemical and structural nature of the underlying substrate*. Other work has found differences in island densities with surface termination—in particular, concerning growth of pentacene on SiO_2 vs. Si(100) surfaces terminated with H **[40]**, or cyclohexene **[15]**. In these studies, the island densities were highest on a chemically oxidized SiO_2 surface **[40]**, and a plasma-cleaned and annealed thin SiO_2 gate oxide **[15]**.

The thin films of PFP have also been characterized using grazing incidence diffraction (GID) at the CHESS G2 station to verify the in-plane crystalline structure, and to examine the possibility if the structure was sensitive to the underlying layer. *Ex situ* analysis using GID on ~ 4 ML thick PFP films on all surfaces showed essentially no differences in the positions of the in-plane reflection planes, and the positions of the peaks were consistent with earlier reports.**[33, 35]** *Ex situ* analysis using GID on thinner ~ 1.5 ML PFP films showed only minor differences in the positions of the (120) and (130) reflection planes (the most intense observed here) on all surfaces. For

example, from previous work $q_{(120)}$ = 1.771 **[33]** and 1.772 Å^{-1} **[35]**, whereas we found values ranging from 1.762 to 1.773 Å^{-1}. Likewise in previous work $q_{(130)}$ = 2.158 **[33]** and 2.153 Å^{-1} **[35]**, whereas we found values ranging from 2.149 to 2.168 Å^{-1}. These values represent a difference of at most 0.6-0.7%. We do not believe such small changes in the crystal structure in the monolayer regime are significant enough to explain other observations that we make here concerning phenomena that show a dependence on surface termination.

The nature of the SAM not only affects the island density of PFP but also the submonolayer island shapes. In Figure 6-4, we display representative AF micrographs of PFP in the submonolayer regime for growth on all the surfaces examined here. The corresponding coverages and *GR*s for these films are all within a factor of ~ 2, and are given in the figure. On FOTS, HMDS and OTS, the PFP islands are anisotropic with a compact polygonal shape. The aspect ratio of these islands is approximately ~ 2-4, and it is greater on FOTS compared to HMDS and OTS. In contrast, the islands on MAOPTS and SiO_2 are clearly not compact polygons, and are much more irregular. The shapes of these islands are similar to those reported for growth of pentacene on SiO_2 **[13, 15, 40]**, but are not nearly as fractal as those reported for pentacene on H- and cyclohexene-terminated Si(100) **[15, 40]**.

We note that the changes we observe in island shape with surface termination do not depend on the growth rate for each surface examined. To examine this explicitly we consider again the results we presented in Figure 6-2 concerning the growth of PFP on HMDS. In Figure 6-5 we present micrographs representing the lowest and highest growth rate examined, where we have scaled the images such that

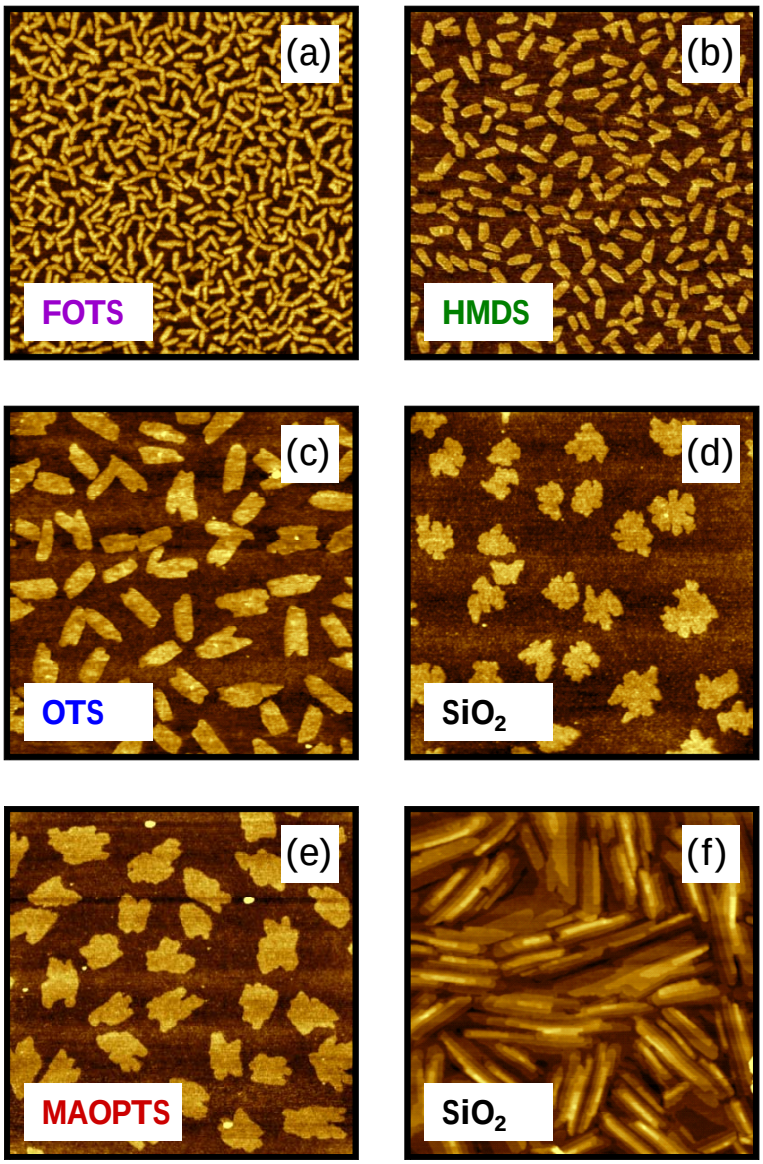

Figure 6-4 Atomic force micrographs, 3 × 3 μm^2, of submonolayer thin films of PFP grown on 5 different surfaces: **(d)** SiO_2 (0.24 ML of PFP), and SiO_2 terminated with **(a)** FOTS (0.56 ML), **(b)** HMDS (0.42 ML); **(c)** OTS (0.39 ML) and **(e)** MAOPTS (0.33 ML). The micrographs are in order of decreasing island density: (a) to (e). In **(f)** we present an AF micrograph of a PFP film deposited on a SiO_2 surface, representing a thickness of 3.61 ML. In all cases incident kinetic energy was E_i = 4.6 eV, and substrate temperature, T_s = 40 °C.

the apparent island density (number of islands in the image) is constant, even while the growth rate changes from 2.4×10^{-3} to 18.0×10^{-3} ML-s^{-1}, or a factor of 7.5. As may be seen, the shapes and aspect ratios of the islands for the two extremes of growth rates examined are essentially indistinguishable from each other. Thus, it is clear that the change in the rate of growth cannot explain the change in the island shape, and that the differences observed in submonolayer island shapes are most strongly influenced by the substrate-PFP interactions.

Unlike the features formed in the submonolayer regime, once the substrate is covered, the morphologies of the PFP thin films in the multilayer regime are all remarkably similar. A representative micrograph is shown in Figure 6-4(f) for the case of a ~ 4ML thick film on SiO_2. As may be seen the features in this coverage regime are very anisotropic, and are narrow and rod-like, similar to what has been reported previously.**[32,33]** As expected for growth on substrates lacking crystallographic order, we see that different grains are evidently randomly oriented with respect to each other and to the substrate. However, there is some short range order as small "bundles" of these rod-like features are observed. It is interesting to note that the submonolayer islands that most resemble these features observed in the multilayer regime are those formed on FOTS.

The shape of islands in the submonolayer regime can be the consequence of both energetic (thermodynamic) and kinetic factors. Not unlike the situation concerning the 3D evolution of surface morphology and roughness, similar molecular scale events contribute to the structures that are formed in 2D. There are important differences, however, between these essentially 2D and 3D phenomena. Our results

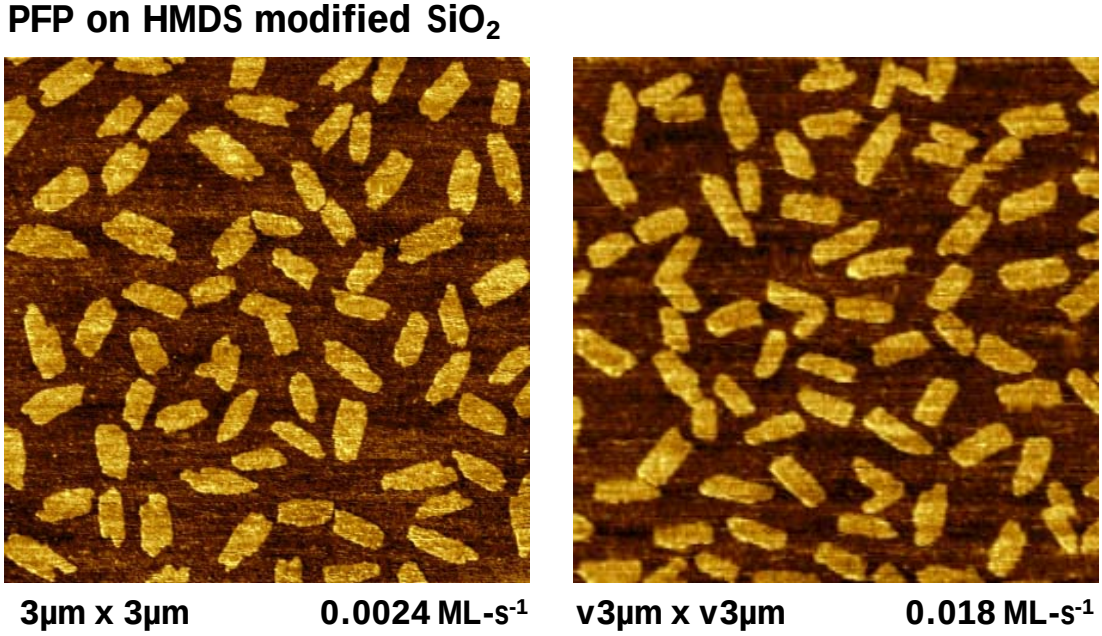

Figure 6-5 Atomic force micrographs of submonolayer thin films of PFP grown on a SiO_2 surface terminated with HMDS at rates of **(a)** 0.00240 and **(b)** 0.0180 ML-s^{-1}. As presented, the scale in **(a)** is 3 × 3 μm^2, while that in **(b)** is $\sqrt{3} \times \sqrt{3}$ μm^2. The axes have been scaled to produce what appear to be equivalent island densities to highlight the similarities in island shapes. In all cases incident kinetic energy was E_i = 4.6 eV, and substrate temperature, T_s = 40 °C.

indicate that the diffusivity of PFP varies greatly on the five surfaces examined here, by as much as 2 orders of magnitude. We expect that diffusion of PFP on these starting substrates involves the molecule laying flat (to maximize van der Waals interactions), assuming the underlying SAM is sufficiently dense such that PFP is unlikely to penetrate the organic monolayer. In contrast, the molecules that are part of both the growing islands and multilayer thin film are standing up, with their long molecular axis nearly perpendicular to the surface. Thus, the interaction with the underlying substrate is expected to be fundamentally different concerning diffusing admolecules vs. molecules incorporated into the crystals. Thus, fast diffusion on a substrate need not translate into fast diffusion around the periphery of an island, or *vice versa*.

In terms of molecular scale events that occur as islands grow and begin to adopt a shape, the first event has to involve attachment of a molecule to the island edge. At low coverages, and assuming adsorption is irreversible on the substrate surface, prior to attachment these molecules will adsorb first on the bare substrate, and then diffuse to the island edge (as compared to adsorbing on top of the island and diffusing to the island edge). Given the shape of these molecules, and the nature of the molecule-substrate and molecule-molecule interactions (essentially van der Waals) there could be a *barrier* to the attachment process, as the molecule must reorient itself with respect to binding flat on the substrate surface to binding nominally upright at the island edge (*vide infra*). Some sort of sliding or flipping motion would seem to be necessary, which may be facilitated by nearby molecules either in the island or representing the underlying SAM. We note that such motions involving reorientation

do not occur in atomic (epitaxial) systems such as Pt on Pt(111), where island shapes have been the focus of several investigations **[41]**, as they are properly modeled as particles with spherical symmetry. The final state—a molecule bound to an island edge—is expected to depend on the local structure, e.g., which crystal face is exposed at the island edge. In extreme cases one might imagine that molecules diffusing on a particular substrate and impacting a particular crystal face of an island edge may be reflected, whereas some other combination could lead to very efficient incorporation/attachment. Such "anisotropic sticking," or "anisotropic accommodation" as suggested in work on atomic epitaxial systems **[41, 42],** could explain the formation of anisotropic islands, which has been suggested to occur in other small molecule organic systems **[43]**.

Island shape can also be determined by energetic/thermodynamic factors. Given differences in the surface energy of different crystallographic orientations, an island may seek to minimize high energy edges vs. low energy ones. Such a process would depend on the fast diffusion of molecules around the edges of islands, including corners where added barriers to diffusion may exist. In 3D, diffusion of atoms from one terrace to another is hampered by the well-known step-edge, or Ehrlich-Schwoebel, barrier. **[44, 45]** Such a barrier also exists in molecular systems **[46-48]**, which we examine here. In 2D, an analogous "island corner crossing" barrier has been identified concerning atomistic epitaxial growth.**[49]** Undoubtedly a similar barrier exists for molecular systems. If energetic factors are determining island shapes, and we are below a temperature where entropy-driven island edge roughening is important, then one would expect compact islands, with possibly relatively straight

edges. Such seems to be the case for the islands on FOTS, HMDS and OTS, not so for the islands formed on MAOPTS and SiO_2.

Reviewing our results as a whole concerning island shape we consider some potential scenarios. First, can the islands formed here re-structure/reorganize during growth, and hence influence the shapes that are formed? One test of the extent of post-deposition island shape evolution is to examine what occurs under extended ageing. For example, concerning near-monolayer coverages of *pentacene* on FOTS and HMDS we have found that these films undergo significant post-deposition reorganization if left under vacuum for a period of time ranging from a few min. (on FOTS) to ~ 120 min. (on HMDS).**[16]** To test this possibility here, we compared AF micrographs for samples of PFP on SiO_2 and FOTS where, in each case, samples were removed almost immediately after growth (~2min.) or were left under vacuum for *ca*. 150 min. The images for these sub-monolayer films (not shown here) were essentially indistinguishable in terms of both island shape and density. Additional ageing in air for ~ 2 months also did not produce any changes in island shape and density. Thus, either the films formed here either do not reorganize, or they do on a time scale that is short with respect to the time it takes to remove a sample from vacuum (< 2 min.). We note this latter time period is not so different from the time of growth [~ 0.4-0.7 min. for Figures 6-4(a)-(e)]. Indeed, reviewing the results from Figure 6-5, where the total time of growth varied from 0.4 to 2.5 min., we do not observe any noticeable changes in island shape, even while the density is changing by a factor of ~ 3.

Based on the previous discussion we are left with a picture where either reorganization does not occur, or it is very fast compared to the time scale of the

experiments (« min.). We can argue against the latter interpretation using the following argument. If reorganization is fast, then it is on both SiO_2 and FOTS for the conditions examined here, as both terminations showed no effects during post-deposition ageing. In this case, we would be left with the unusual situation where reorganization leads to different island shapes depending on the underlying substrate, also while the densities of these islands are changing. We believe this to be unlikely, thus we are left with the conclusion that other factors are contributing to the island shapes.

Island shape can be influenced by the kinetics of admolecule attachment. As described above, the molecular motions associated with attachment of a molecule at an island edge can be quite complex, and may involve contributions of molecules present in the underlying layer. We note that this is quite unlike atomistic epitaxial growth, as indicated above, and a simple comparison is displayed in schematic form in the upper panel of Figure 6-6. Indeed, as discussed above, it is actually likely that a barrier exists to admolecule attachment as the molecule reorients from lying down to standing up. Once attached, the molecule may diffuse around the periphery of an island before finding a preferred binding site, exhibiting a form of transient mobility. We would distinguish such a process from large-scale reorganization if the final step of binding to a preferred site is effectively irreversible.

How might the bonding of PFP vary from site to site on an island edge? If we use pentacene as a guide, calculations using DFT-LDA indicate that the binding of pentacene varies significantly concerning the likely low-index crystalline facets present on the edges of the islands.**[50]** For example, pentacene is bound by ~ 0.9 eV

Figure 6-6 Upper panel: Schematic representation of the motions associated with adatom attachment to a submonolayer island, and admolecule attachment to a submonolayer island, where these molecules are "standing upright." Lower panel: A simple model for the shape of an island of PFP formed in the submonolayer regime, based on the known crystal structure, where the surface exposed is the (001) plane. We assume here that the herringbone angle is exactly 90°, where a PFP molecule can be represented in-plane by a rectangle. The two in-plane lattice vectors are shown, a = 11.4 Å, b = 4.5 Å.

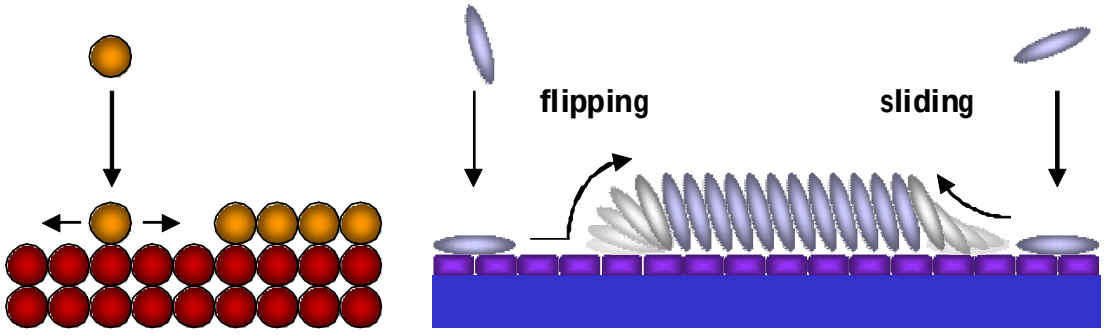

atomistic epitaxial growth

organic small molecule crystal growth

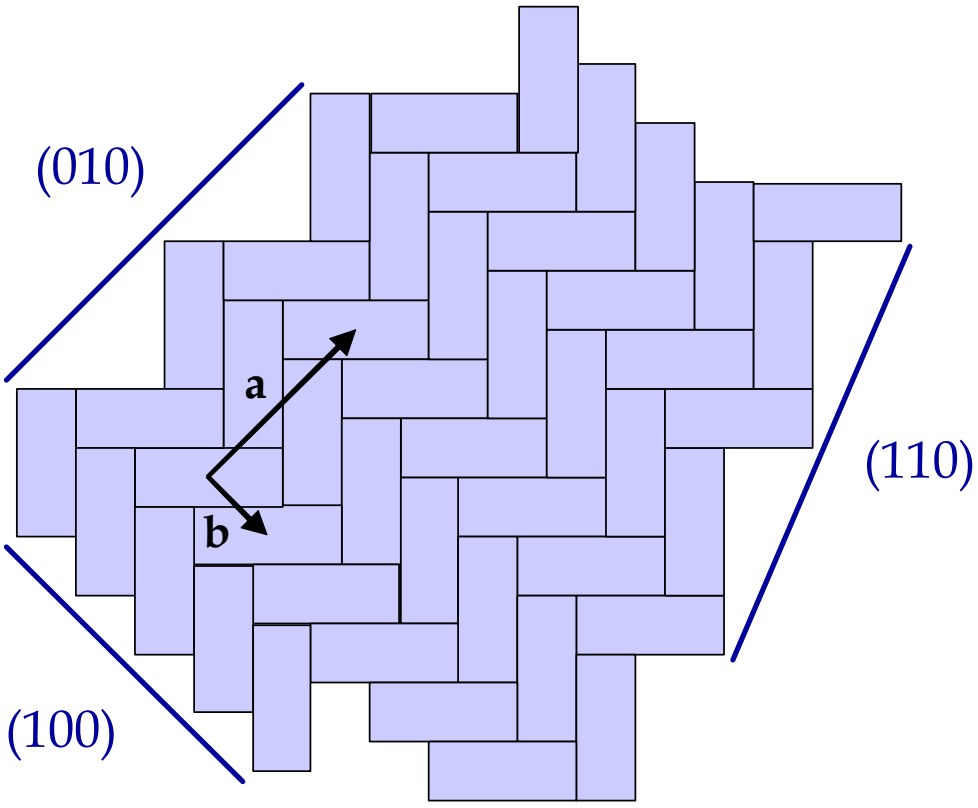

on the relatively smooth (100) face, ~ 0.75 eV on the (110) and (1-10) faces, and ~ 1.2 eV on the (010) face. More recent calculations of this same system using a density functional that better describes van der Waals interactions suggests that these energies may be underestimated by 25-50%.**[51]** Using these results, the binding of pentacene to the (100), (110) and (010) faces may be closer to 1.25, 1.13 and 1.52 eV. At room temperature, using these binding energies the difference in residence time between the (100) and (010) faces could be on the order of 4×10^4-1×10^5. In this scenario the (010) faces could act effectively as sinks, and growth could preferentially proceed in this direction.

In terms of equilibrium shapes, we are aware of no studies of PFP concerning this issue. There are examinations of pentacene, however. Concerning pentacene, calculations indicate that islands should be approximately hexagonal in shape, consisting of (100), (110), and (1-10) edges, and either devoid of (010) edges **[50]** or possessing small facets presenting this face **[51]**. No study predicts the presence of square corners in the equilibrium crystal shape produced by the intersection of (100) and (010) faces. Examining the images given in Figures 6-2, 6-4 and 6-5 we observe a variety of acute, obtuse and, without question, *some right angles*, especially on HMDS and OTS. How might these images be related to PFP equilibrium crystal shapes? To answer this question, we now consider what is known about the crystal structure of PFP.

The structure of PFP is similar to that of pentacene, but there are important differences. For example the angle between neighboring molecules in the herringbone rows is nearly 90° (91.2°) for PFP vs. 51.9° for pentacene.**[34]** Using what is known

about the size and shape of the unit cell of PFP **[34]** we can construct a simple model for the shape of the PFP islands in the submonolayer regime. In particular, the in-plane lattice constants are given by a = 11.40-11.48 Å, b = 4.49-4.53 Å, and γ = 90°.**[33-35]** In the lower panel of Figure 6-6 we consider a simple model for the packing of PFP molecules in the unit cell, where we assume that the herringbone angle is exactly 90°. In this case the in-plane space occupied by each PFP molecule can be approximated by a rectangle, where the aspect ratio is determined by the ratio of lattice constants $b/a \sim 0.39$ **[34]**. Based on this simple construction, similar to what has been applied to the case of pentacene **[50]**, the (100) face can be expected to be a low surface energy face. The other low index face, the (010), although exhibiting more molecular scale roughness as shown in Figure 6-6, might also be expected to be a low surface energy face. Perhaps of most interest here, the (110) face would appear to be almost degenerate in surface energy with the (010) face.

If we assume that the islands formed possess a number of edges that represent the low-index (100), (110) and (010) faces then a quantitative analysis of the island shapes would seem to be in order. Unlike the analysis of 3D topology, analysis of 2D shapes formed in the submonolayer regime is not widely reported, and there or no standard or well established methods that are commonly employed (outside of fields such as cartography). We make use of two methods here, which are by no means unique. We will also only report the results for the analyses on FOTS, HMDS and SiO_2. The results for OTS are quite similar to those on HMDS, while the same is true for MAOPTS and SiO_2. First, we used MATLAB to produce a topological map of the submonolayer structures. By selecting the appropriate "height", the islands become a

series of closed curves. Islands not making closed curves, e.g., those at the edge of the micrographs, were not included in the analyses. Next, given these curves we then applied the Douglas–Peucker algorithm **[52, 53]** to find "best fit" polygons for each island. Here the analysis was somewhat subjective, as depending on the size of the tolerance parameter used in the fit, the algorithm can fit a shape to a very large number of vertices giving an uninformative, and perhaps, unphysical representation of the island shape. For example, for the relatively compact islands observed on FOTS, HMDS and OTS, one expects to limit the number of vertices to fewer than those for the islands on MAOPTS and SiO_2.

In Figures 6-7 and 6-8 we present the results of our analysis of the island shapes. To clearly illustrate our method in Figure 6-7 we consider only the analysis of single islands formed on HMDS and SiO_2. The first row includes the shapes found by applying the Douglas–Peucker algorithm, and the longest edge is highlighted by a dotted line in each case. In the second row we plot the (unweighted) histograms for the vertex angles, and as may be seen the island on SiO_2 gives both convex and concave vertices. In the third row we consider another representation of the island shapes. Here we consider the angles that the faces make with each other, regardless if the facets meet to make a corner. In this analysis, the longest side of each polygon defines 0°, and the edges are treated as vectors such that the possible angles range from 0° to 360°. In this construction we also weight the distribution by the length of the edge. For HMDS, the long, nearly parallel faces produce a peak in the distribution, whereas on SiO_2 the distribution is much broader.

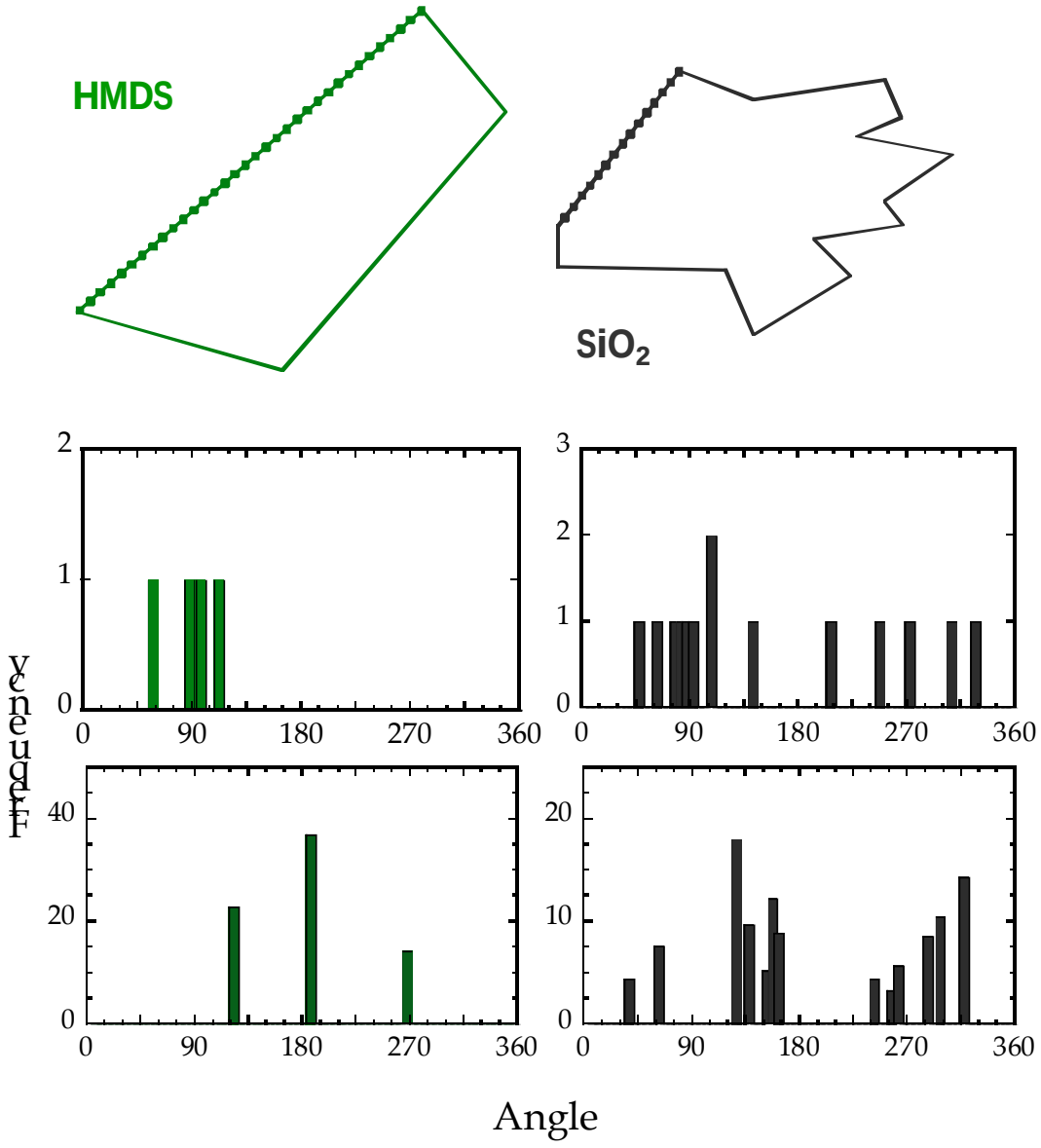

Figure 6-7 Illustrative figure demonstrating the method we use to analyze island shapes. First row: shapes of single islands found from an analysis of the atomic force micrographs of PFP on HMDS and SiO_2. Second row: histograms of the vertex angles represented by the polygons. Third row: histograms of the angles of relative orientation between the sides of the polygons, with respect to the longest edge, and weighted to the length of the edge.

In Figure 6-8 we present a full analysis of the islands formed on FOTS, HMDS and SiO_2, where in the top row we present micrographs for films deposited at rates of 0.0021, 0.0056 and 0.0019 ML-s^{-1}, representing coverages of 0.119, 0.361 and 0.388 MLs, respectively. In the second row we present the shapes that were fit to each of the islands analyzed. The number of islands analyzed were 135, 74 and 131 for PFP on FOTS, HMDS, and SiO_2, respectively. Here for the number of vertices our analysis gave these values (mean and standard deviation): 4.70 ± 1.17, 5.70 ± 2.28 and 14.61 ± 6.58 for PFP on FOTS, HDMS, and SiO_2, respectively. As may be appreciated, the shapes have been well captured by this analysis. In the third row we plot histograms of the unweighted population of vertex angles in the fitted polygons. Here we see an obvious difference for the results on FOTS and HMDS, vs. that on SiO_2. As the former two surfaces are populated mostly by compact islands, these histograms are described by a single Gaussian distribution. For FOTS we find that the mean is ~ 99°, with a standard deviation of 33°, while for HMDS we find 104° and 37°, respectively. On SiO_2 we see that the distribution is bimodal, owing from the non-compact shapes, and that two Gaussians fit the data: 103° ± 27°, and 264° ± 38°. If the low index faces dominate the populations, we would expect peaks in the distribution (for angles < 180°) at angles of 43°, 69°, 90°, 111°, and 137° (*cf*. Figure 6-6). These values are certainly represented in all cases examined here, but we hesitate to make a stronger conclusion at this point in the analysis.

In the fourth row of Figure 6-8 we plot the histograms of the relative angles between edges of the fitted polygons and the longest edge, applying a weighting factor given by the length of the edge, as we described in connection with Figure 6-7. Again,

Figure 6-8 First row: Atomic force micrographs of submonolayer thin films of PFP grown on (left-to-right) FOTS, HMDS and SiO_2. The first two of these images are 3×3 μm^2, the latter is 10×10 μm^2. Second row: Analysis of island shapes as simple polygons using the approach described in the text. Third row: Histograms of the vertices represented by the polygons. Fourth row: Histograms of the angles of relative orientation between the sides of the polygons, with respect to the longest edge, and weighted to the length of the edge.

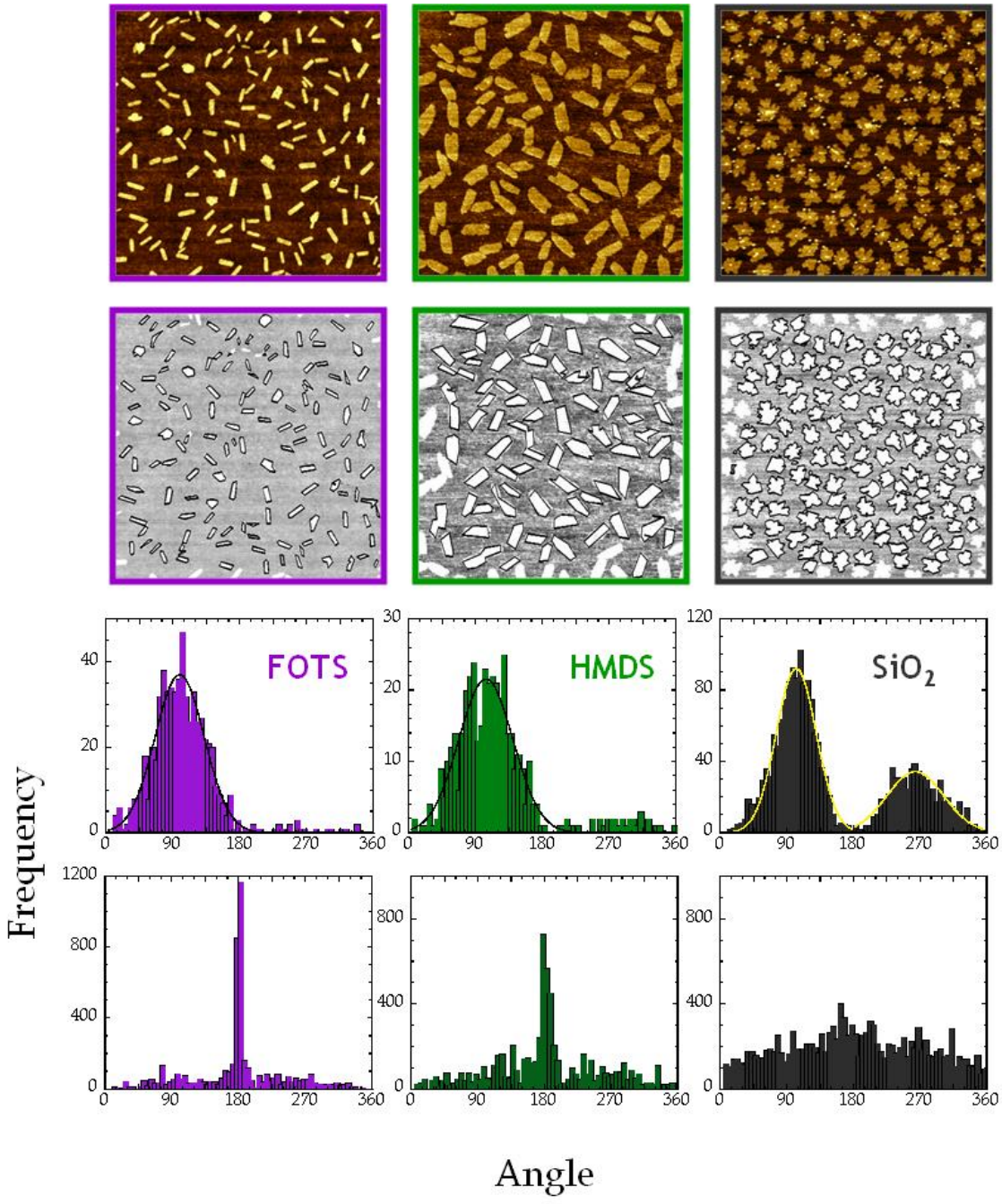
FOTS
HMDS
SiO2
Frequency
Angle

we take note of important differences concerning the results for FOTS, HMDS and SiO_2. First, the distribution on FOTS is highly peaked at an angle of ~ 180°. Indeed, the two bins representing angles from 175-185° represent 39% of this length-weighted histogram, while a fit to a Gaussian gives a mean and standard deviation of 180.7° ± 3.5°. This means that on FOTS there is a strong tendency for the formation of islands possessing parallel facets or edges. Given the structure discussed above in connection with Figure 6-6, it seems likely that these would be the (100) and $(\bar{1}00)$ faces. There is also a hint of higher frequencies for angles of ~ 80°-100°, but a peak in this range is much less obvious. On HMDS, the histogram is similar to that on FOTS, but not as peaked at an angle of ~ 180°. Here the four bins representing angles from 170-190° represent 29% of this length-weighted histogram, while a fit to a Gaussian gives a mean and standard deviation of 181.0° ± 7.9°. Thus, this surface also tends to form islands that possess parallel edges, but the larger contribution of edges not close to 180°, as compared to FOTS, indicates that the aspect ratios of the islands are smaller on this surface. Finally, on SiO_2 the edge-length weighted distribution is very broad, and does not exhibit an obvious peak. A fit of these data to a Gaussian gives a mean and standard deviation of 180° ± 137°. These results are consistent with the non-compact nature of the islands that are formed on SiO_2.

Summing up the results of our analysis displayed in Figure 6-8 concerning the shapes of the islands, we find that the largely objective analysis described above mostly verifies what is seen by the naked eye. First, the islands on FOTS and HMDS (and OTS, *cf*. Figure 6-4) are compact, and ~ 70% of the vertex angles lie within a

range of 65°-140°, with the distribution peaking near 100°. These results are consistent with the existence of corners produced by the intersection of (100) edges with both (110) and (010) edges. The large predominance of parallel edges, particularly on FOTS, but less dominant on HMDS (and OTS), strongly suggests that many islands possess long (100) and $(\bar{1}00)$ faces as edges. These parallel edges are also quite noticeable for multilayer films of PFP on all surfaces, *cf*. Figure 6-4(f). On SiO_2 (and MAOPTS) the islands are not compact and a number of vertex angles lie in the range of 180°-360°. Also, on these surfaces, there is only a very weak tendency to form islands with parallel edges.

In concluding our discussion of island shape variation with surface termination we make the following observation. Although it is likely that equilibrium shapes are not achieved on any surface, there is a connection between equilibrium concepts and those based on molecular events such as admolecule attachment, diffusion along edges and across corners, and preferential binding. Low energy edges, such as the (100), will bind admolecules weakly, and tend to "donate" these molecules to bind at higher energy edges such as the (010) and the (110). Thus, if corner crossing is facile, then one can imagine the formation of islands with straight parallel (100) edges. Large barriers to island corner crossing, however, will tend to lead to instabilities in the evolution of island shape, and islands that are not compact will tend to form.[49] If barriers to island corner crossing are playing a role in the islands that are formed on SiO_2 and MAOPTS, then these barriers are apparently much different for PFP on FOTS, HMDS and OTS. As the short edge of PFP interacts most directly with the underlying substrate, this sensitivity is unexpected. This is particularly curious as the

mobility of flat lying, isolated PFP molecules is highest on the MAOPTS and SiO_2 surfaces.

6.5 Conclusions

In conclusion, we have examined the nucleation and growth of perfluoropentacene (PFP) on a series of surfaces represented by differing chemical terminations and surface energies. PFP was chosen because of its low intrinsic surface energy—we do not expect it to dewet or reorganize on low energy surfaces. This enabled us to study the effect of SAMs on the nucleation and growth of a crystalline organic thin film, which is otherwise very problematic to examine. On all surfaces examined, PFP forms single molecule-high islands in the submonolayer regime, which are stable in density, shape and size with extended ageing. Furthermore, PFP exhibits the characteristics of homogeneous nucleation on all surfaces. We found that the chemical structure of the SAM significantly affects the nucleation density of PFP under otherwise identical conditions of growth. In particular, the density of islands on FOTS (the lowest surface energy SAM examined) exceeded that on MAOPTS (the highest surface energy SAM examined) by over an order of magnitude. At the same time, the size of the critical nucleus indicated by the change in island density with growth rate showed no dependence on surface termination, and a value of $i^* \sim 2\text{-}3$ could describe all data. We are left to conclude that the change in island density is due to a change in the diffusivity of PFP admolecules on these surfaces by as much as 2 orders of magnitude. The chemical structure of the SAM also significantly affects the

shapes of the islands of PFP formed in the submonolayer regime. Interestingly, the islands are most compact and facetted on those surfaces where diffusion of isolated PFP admolecules is indicated to be the slowest. The shapes of the islands formed on all surfaces were analyzed in terms of simple polygonal shapes. These shapes were consistent with the islands possessing a number of the low-index edges, i.e., the (100), (010) and (110), including parallel (100) edges on surfaces terminated by FOTS, HMDS and OTS. Our observations suggest that the molecular motions and intermolecular interactions describing the diffusion of isolated admolecules are quite different from those concerning molecules moving on the periphery of a growing island. Finally, once the substrate surface is covered, the growth becomes very 3-dimensional on all surfaces, and a rough multilayer morphology is observed. For these thick films, very anisotropic features are formed, which may suggest the predominance of a single face at these coverages, such as the (100) orientation.

6.6 References

1. Hamers, R. J.; *Nature* **2001**, *412*, 489-490.
2. Dimitrakopoulos, C. D. ; Malenfant, P. R. L. *Adv. Mater.* **2002**, *14*, 99-117.
3. Lin, Y. Y.; Gundlach, D. J.; Nelson, S. F.; Jackson, T. N. *IEEE Electron Device Letters* **1997**, *18*, 606-608.
4. Ruiz, R.; Papadimitratos, A.; Mayer, A. C.; Malliaras, G. G. *Adv. Mater.* **2005**, *17*, 1795-1798.

5. Dinelli, F.; Murgia, M.; Levy, P.; Cavallini, M.; Biscarini, F.; de Leeuw Dago M. *Phys. Rev. Lett.* **2004**, *92*, 116802-116804.

6. Muck, T.; Wagner, V.; Bass, U.; Leufgen, M.; Geurts, J.; Molenkamp, L. W. *Synthetic Metals* **2004**, *146*, 317-320.

7. Dodabalapur, A.; Torsi, L.; Katz, H. E. *Science* **1995**, *268*, 270-271.

8. Kelley, T. W.; Boardman, L. D.; Dunbar, T. D.; Muyres, D. V.; Pellerite, M. J.; Smith, T. P. *J. Phys. Chem. B* **2003**, *107*, 5877-5881.

9. Yang, H.; Shin, T. J.; Ling, M. M.; Cho, K.; Ryu, C. Y.; Bao, Z. *J. Am. Chem. Soc.* **2005**, *127*, 11542-11543.

10. Virkar, A.; Mannsfield, S.; Oh, J. H.; Toney, M. F.; Tan, Y. H.; Liu, G.; Scott, J. C.; Miller, R.; Bao, Z. *Adv. Funct. Mater.* **2009**, *19*, 1962-1970.

11. Shtein, M.; Mapel, J.; Benziger, J. B.; Forrest, S. R. *Appl. Phys. Lett.* **2002**, *81*, 268-270.

12. Klauk, H.; Halik, M.; Zschieschang, U.; Schmid, G.; Radlik, W.; Weber, W. *J. Appl. Phys.* **2002**, *92*, 5259-5263.

13. Killampalli, A. S.; Schroeder, T. W.; Engstrom, J. R. *Appl. Phys. Lett.* **2005**, *87*, 033110/1-033110/3.

14. Ruiz, R.; Nickel, B.; Koch, N.; Feldman, L. C.; Haglund, R. F., Jr.; Kahn, A.; Family, F.; Scoles, G. *Phys. Rev. Lett.* **2003**, *91*, 136102/1-136102/4.

15. Meyer zu Heringdorf, F.-J.; Reuter, M. C.; Tromp, R. M. *Appl. Phys. A: Mater. Sci. Process.* **2004**, *78*, 787-791.

16. Amassian, A.; Pozdin, V.; Desai, T. V.; Hong, S.; Woll, A. R.; Ferguson, J. D.; Brock, J. D.; Malliaras, G. G.; Engstrom, J. R. *J. Mater. Chem.* **2009**, *19*, 5580-5592.

17. Burke, S. A.; Topple, J. M.; Grütter, P. *J. Phys: Cond. Mater.* **2009**, *21*, 423101/1-423101/16.

18. Schroeder, T. W. *Cornell University: Ph.D. Thesis* **2004**.

19. Hong, S.; Amassian, A.; Woll, A. R.; Bhargava, S.; Ferguson, J. D.; Malliaras, G. G.; Brock, J. D.; Engstrom, J. R. *Appl. Phys. Lett.* **2008**, *92*, 253304/1-253304/3.

20. Krause, B.; Schreiber, F.; Dosch, H.; Pimpinelli, A.; Seeck, O. H. *Europhys. Lett.* **2004**, *65*, 372-378.

21. Schreiber, F. *Prog. Surf. Sci.* **2000**, *65***,** 151-256.

22. Kaelble, D. H. *J. Appl. Polym. Sci.* **1974**, *18*, 1869-1889.

23. Knieling, T.; Lang, W.; Bencke, W. *Sensors and Actuators B: Chemical* **2007**, *126*, 13-17.

24. Kawai, A.; Kawakami, J. *J. Photopolym. Sci. Technol.* **2003**, *16*, 665-668.

25. Braun, C. *Parratt32 program*; Berlin Neutron Scattering Center (BENSC): Hahn-Meitner Institut, 1997.

26. Tolan, M. *X-ray scattering from Soft-Matter Thin Films*; Springer: Berlin, 1999.

27. Killampalli, A. S.; Engstrom, J. R. *Appl. Phys. Lett.* **2006**, *88*, 143125/1-143125/3.

28. Amassian, A.; Desai, T. V.; Kowarik, S.; Hong, S.; Woll, A. R.; Malliaras, G. G.; Schreiber, F.; Engstrom, J. R. *J. Chem. Phys.* **2009**, *130*, 124701/1-124701/9.

29. Kowarik, S.; Gerlach, A.; Skoda, M.; Sellner, S.; Schreiber, F. *Eur. Phys. J. Special Topics* **2009**, *168*, 11-18.

30. Woll, A. R.; Desai, T. V.; Engstrom, J. R. *under review at the J. Phys. Rev. B.*

31. Cohen, P. I.; Petrich, G. S.; Pukite, P. R.; Whaley, G. J.; Arrott, A. S. *Surface Sci.* **1989**, *216*, 222-248.

32. Hinderhofer, A.; Heinemeyer, U.; Gerlach, A.; Kowarik, S.; Jacobs, R. M. J.; Sakamoto, Y.; Suzuki, T.; Schreiber, F. *J. Chem. Phys.* **2007**, *127*, 194705/1-194705/6.

33. Kowarik, S.; Gerlach, A.; Hinderhofer, A.; Milita, S.; Borgatti, F.; Zontone, F.; Suzuki, T.; Biscarini, F.; Schreiber, F. *Phys. Stat. Sol.* **2008**, *2*, 120-122.

34. Sakamoto, Y.; Suzuki, T.; Kobayashi, M.; Gao, Y.; Fukai, Y.; Inoue, Y.; Sato, F.; Tokito, S. *J. Amer. Chem. Soc.* **2004**, *126*, 8138-8140.

35. Salzmann, I.; Duhm, S.; Heimel, G.; Rabe, J. P.; Koch, N.; Oehzelt, M.; Sakamoto, Y.; Suzuki T. *Langmuir* **2008**, *24*, 7294-7298.

36. Venables, J. A. *Phys. Rev. B* **1987**, *36*, 4153-4162.

37. Venables, J. A.; Spiller, G. D. T.; Hanbücken, M. *Rep. Prog. Phys.* **1984**, *47*, 399-459.

38. Zhang, Z.; Lagally, M. G. *Science* **1997**, *276*, 377-383.

39. Brune, H. *Surf. Sci. Rep.* **1998**, *31*, 121-229.

40. Ruiz, R.; Nickel, B.; Koch, N.; Feldman, L.C.; Haglund, R. F.; Kahn, A.; Scoles, G. *Phys. Rev. B* **2003**, *67*, 125406/1-125406/7.

41. Michely, T.; Hohage, M.; Bott, M.; Comsa, G. *Phys. Rev. Lett.* **1993**, *70*, 3943-3946.

42. Mo, Y.-W.; Swartzentruber, B. S.; Kariotis, R.; Webb, M. B.; Lagally, M. G. *Phys. Rev. Lett.* **1989**, *63*, 2393-2396.

43. de Oteyza, D. G.; Barrena, E.; Sellner, S.; Ossó, J. O.; Dosch, H. *J. Phys. Chem. B* **2006**, *110*, 16618-16623.

44. Ehrlich, G.; Hudda, F. G. *J. Chem. Phys.* **1966**, *44*, 1039-1049.

45. Schwoebel, R. L.; Shipsey, E. J. *J. Appl. Phys.* **1966**, *37*, 3682-3686.

46. Fendrich, M.; Krug *J. Phys. Rev. B* **2007**, *76*, 121302/1-121302/3.

47. Hlawacek, G.; Puschnig P.; Frank, P.; Winkler, A.; Ambrosch-Draxl, C.; Teichert, C. *Science* **2008**, *321*, 108-111.

48. Goose, J. E.; First, E. L.; Clancy, P. *Phys. Rev. B* **2010**, *81*, 205310/1-205310/20.

49. Zhong, J.; Zhang, T.; Zhang, Z.; Lagally, M. G.; Phys. Rev. B **2001**, *63*, 113403/1-113403/4.

50. Northrup, J. E.; Tiago, M. L.; Louie, S. G. *Phys Rev. B* **2002**, *66*, 121404/1-121404/4.

51. Nabok, D.; Puschnig, P.; Ambrosch-Draxl, C. *Phys. Rev. B* **2008**, *77*, 245316/1-245316/4.

52. Ramer, U. *Comput. Graphics Image Process.* **1972**, *1*, 244-256.

53. Douglas, D. H.; Peucker, T. K. *The Canadian Cartographer* **1973**, *10*, 112-122.

7. Hyperthermal growth of *N,N'*-ditridecylperlyene-3,4,9,10-tetracarboxylic diimide on self-assembled monolayers: adsorption dynamics, sub- and multilayer thin film growth

7. 1 Overview

We have examined the nucleation, growth, and dynamics of adsorption of *N,N'*-ditridecylperlyene-3,4,9,10-tetracarboxylic diimide (PTCDI-C_{13}) on SiO_2 surfaces modified by self-assembled monolayers (SAMs) and on a pre-deposited monolayer of pentacene using *in situ* synchrotron x-ray scattering and *ex situ* atomic force microscopy. From real-time x-ray scattering we find that PTCDI-C_{13} exhibits prolonged layer-by-layer growth for approximately the first 10 monolayers (MLs) of deposition on all three SAMs examined. Concerning adsorption on the pristine SAM-terminated surfaces, in all cases we observe a smooth decrease in the probability of adsorption of PTCDI-C_{13} with increasing incident kinetic energy, indicative of trapping-mediated adsorption. Once these surfaces are covered by PTCDI-C_{13}, the probability of adsorption no longer depends on the identity of the SAM, but still exhibits a significant decrease with increasing incident kinetic energy. The adsorption probability of PTCDI-C_{13} on itself is similar to that observed on two SAMs that possess aromatic endgroups, but it differs significantly to that observed on a relatively short, methyl-terminated SAM. These differences could reflect mechanisms such as direct molecular insertion of PTCDI-C_{13} into either the existing PTCDI-C_{13} film, or the longer chain SAMs with aromatic endgroups. Concerning growth in the submonolayer regime, we find that nucleation is homogeneous, and that the absolute

density of islands depends on the nature of the surface, while the relative change of the island density with increasing growth rate is essentially independent of the underlying SAM. From the latter we find that a critical island size of a single molecule of PTCDI-C_{13} can describe all the data.

7.2 Introduction

The study of complex conjugated molecules for applications in organic thin film electronics and photonics has received much attention due to their ability to form highly ordered thin films with excellent electrical properties at relatively low temperatures **[1-3]**. An important challenge recently has been to develop and improve methods to integrate both *p*-type (e.g., pentacene) and *n*-type small molecule organic semiconductors into the same device microstructure. This is imperative to develop devices with superior properties such as small organic molecule based photovoltaics, field effect transistors, ambipolar devices and complementary invertors. Previous studies have shown that the deposition of organic semiconductors on low energy surfaces such as self-assembled monolayers (SAMs) significantly improves the electrical properties of organic thin films **[4-8]**. Despite these observations, there is still a significant lack of understanding of the basic mechanisms of organic crystal growth, especially concerning the molecular-scale events that occur between these molecules and surfaces terminated with SAMs, and how these interactions affect small molecule organic thin film growth.

One *n*-type organic semiconductor that is attracting significant interest is *N,N'*-ditridecylperlyene-3,4,9,10-tetracarboxylic diimide (PTCDI-C_{13}). Previous studies

have reported that the electrical properties of PTCDI-C_{13} thin films can be improved by increasing the substrate temperature during deposition **[9,10]**, and with post-growth annealing treatments **[11,12]**, resulting in electron mobilities as high as 2.1 $cm^2V^{-1}s^{-1}$ **[11]**. In other work, the effects of polymeric dielectrics on the electrical properties of PTCDI-C_{13} have been investigated **[10,12-15],** in addition to investigating the effects of other deposition parameters such as the growth rate **[10,15]**. Thin films of PTCDI-C_{13} have also been studied in conjunction with pentacene for applications in organic based ambipolar transistors **[16]** and complementary inverters **[12,17-19]**. Finally, the combined use of PTCDI-C_{13} and pentacene in organic photovoltaics **[20,21]** has also been investigated, where power conversion efficiencies as high as 2% have been reported **[21]**.

Here we report on the effects of self-assembled monolayers on the thin film growth of PTCDI-C_{13}, concentrating on the dynamics of adsorption, and nucleation and growth in the submonolayer regime using a combination of both *in situ* and *ex situ* surface sensitive techniques. The focus is to develop a better understanding of the interactions that take place between PTCDI-C_{13} and surfaces terminated with SAMs and their effects on PTCDI-C_{13} thin film growth. Concerning the SAMs, we consider three layers that differ in terms of their thickness and chemical nature, namely: 1-napthylmethyltrichlorosilane, (NMTS), 6-phenylhexyltrichlorosilane, (PHTS) and hexamethyldisilazane, (HMDS). The former two SAMs were chosen for their aromatic endgroups, so as to mimic a "pentacene-like" surface. We deposit thin films of PTCDI-C_{13} in ultrahigh vacuum (UHV) using a collimated supersonic molecular beam **[22-24]** and, as with our previous studies **[24-26]**, we use *in situ* real-time

synchrotron x-ray scattering to monitor the dynamics of adsorption and growth from the submonolayer to the multilayer regime. To probe the effects of the SAMs on the submonolayer nucleation of PTCDI-C_{13} we use *ex situ* atomic force microscopy (AFM) to quantify island densities. In addition to examining nucleation on SAMs, we have also examined nucleation of PTCDI-C_{13} on a pre-deposited monolayer (ML) of pentacene. We show that PTCDI-C_{13} exhibits prolonged layer-by-layer growth on all SAMs examined here, and the nature of the SAM affects both the dynamics of adsorption and the submonolayer island density at otherwise identical conditions of growth.

7.3 Experimental Procedures

Refer to chapter 2 for details. Only a brief summary on experimental procedures is provided in this section. The experiments conducted *in situ* and in real time were carried out in the G3 station of the Cornell High Energy Synchrotron Source (CHESS) in a custom-designed UHV system fitted with Be windows that is described elsewhere **[23]**. Briefly, the system consists of four separately pumped chambers: a main scattering chamber, a source and antechamber, which act to produce the supersonic beam, and a fast entry load-lock. All chambers are pumped by high-throughput turbomolecular pumps. The base pressure of the chamber was typically ~ 4×10^{-9} Torr and samples were loaded via the load-lock chamber, which was evacuated to ~10^{-7} Torr prior to sample transfer into the main chamber. X-ray reflectivity (XRR) experiments, conducted *ex situ*, were carried out in the G2 station at CHESS.

Substrates were Si(100) wafers (Wacker-Siltronic, *p*-type, 100 mm dia., 500-550 μm thick, 38-63 Ω-cm) subject to a SC-1 clean, 15 s HF dip and a SC-2 clean followed by growth of ~ 300-nm-thick SiO_2 films by wet thermal oxidation at 1100°C. Next, these wafers were cleaned and degreased by sonication for 15 min in anhydrous $CHCl_3$ solution (99 %+), sonicated in deionized (DI) water for 15 min, washed with DI water, dried with N_2 and exposed to UV-ozone for 15 min. These processes provided a clean and reproducible hydrophilic surface. Finally the SAMs were deposited using established procedures **[26,27]**. HMDS was deposited from the vapor phase using a YES LP-III Vapor Prime Oven while NMTS and PHTS (both Gelest Inc., Morrisville, PA) were deposited from the solution phase in a N_2-purged glove box.

The SiO_2 substrates modified with NMTS, PHTS and HMDS, were characterized by contact angle and XRR. Contact angles were measured in two solvents (water and formamide) and using the Young-Dupre equation **[28]** we calculated the energy of surfaces terminated with NMTS, PHTS and HMDS, and found values of 32.5, 33.4, and 32.7 mJ-m^{-2}, respectively. In comparison, the surface energy of the (001) crystal plane of pentacene is reported to be 50-82 mJ-m^{-2} **[29,30]**. Fits to the XRR data were performed, as described in detail elsewhere **[25]**, with the Parratt32 software package **[31]** (based on the Parratt formalism **[32]**), from which we obtain the thickness of the organic layers, and the mean electron density. Knowledge of the molecular weight of the SAM molecules permits us to estimate the 2D surface concentration of the SAMs. Details concerning the properties of the SAMs are given in Table 7-1.

Supersonic molecular beams of PTCDI-C_{13} were generated by using He as a carrier gas and is described in detail elsewhere **[25]**. By varying the He flow rate, the beam energy could be varied from 6.3 to 14.3 eV as determined from time of flight measurements **[23]**, while the PTCDI-C_{13} beam flux was varied by adjusting the temperature of the *in situ* temperature controlled evaporator. Multiple experiments could be carried out on the same substrate, by translating the substrate perpendicular to the supersonic molecular beam, and due to the high beam-to-background flux ratio. During deposition the substrate temperature was kept at T_s = 40 °C, and in all cases the beam was incident along the surface normal. The growth rate of PTCDI-C_{13} (*vide infra*) ranged between 0.004 and 0.011 monolayers (ML)-s^{-1} for the sub-monolayer regime, and 0.0089 and 0.011 ML-s^{-1} for the multilayer regime.

Time-resolved and *in situ* measurements of the scattered x-ray synchrotron intensity were made using a silicon avalanche photodiode detector (APD, Oxford Danfysik, Oxford, UK). During PTCDI-C_{13} thin film growth the intensity was monitored at the anti-Bragg position (00½; $q_z = q_{Bragg}/2 = 0.23/2$ $Å^{-1}$), which is an effective monitor of the nature of growth, i.e., layer-by-layer (LbL) vs. 3D islanded growth **[33]**. Following deposition and x-ray analysis, the samples were removed for *ex situ* analysis using atomic force microscopy (AFM), conducted in tapping mode using a DI 3100 Dimension microscope.

The x-ray data at the anti-Bragg position was fitted using a modified version **[25,34]** of the mean-field rate equation model of growth first proposed by Cohen and co-workers **[35].** Briefly, the equations for the coverage of individual layers (θ_n) are given by:

$$\frac{d\theta_n}{dt} = S_{n-1}F\left[\left(\theta_{n-1} - \theta_n\right) - \alpha_{n-1}\left(\theta_{n-1} - \theta_n\right)\right] + S_nF\alpha_n\left(\theta_n - \theta_{n+1}\right) \tag{7-1}$$

where n = 0 represents the substrate, n = 1 the first molecular layer, etc., S_n is the probability of adsorption for molecules incident on the n^{th} layer, F is the incident molecular flux (ML-s^{-1}), and α_n is the fraction of molecules that initially impact and land on top of the n^{th} layer, but rather than staying on the top of that layer, drop down and become part of that layer via some mechanism. In this model we also assume that there are two values for the probability of adsorption: one for adsorption on the substrate (S_0), and one for that on previously existing molecular layers, independent of their thickness ($S_1 = S_2 = S_3\ldots$).

Once layer coverages have been calculated by integrating Equation (7-1), these can then be used to calculate the scattered x-ray intensity as a function of time **[25,33-35]**. The intensity of the scattered beam (I) depends upon the layer population, θ_n(t), according to the following relationship:

$$I(t) = \left| r_{subs}e^{-i\phi} + r_{film}\sum_{n}^{\infty}\theta_n(t)e^{-iq_z dn}\right|^2 \tag{7-2}$$

where r_{subs} and r_{film} are the scattering amplitudes of the substrate and the film, ϕ is the phase change upon reflection, q_z is the out-of-plane scattering vector and d is the out-of-plane interplanar spacing. At the anti-Bragg position, $q_z d = \pi$, which results in a

change in the sign of the thin film terms in the summation. If each layer fills sequentially, such as in perfect LbL growth, an oscillation in the intensity results.

7.4 Results and Discussion

A. Characterization of the self-assembled monolayers

The SAMs were characterized using the methods described above in section 7-3, namely: contact angle measurements and synchrotron x-ray reflectivity measurements. Based on prior work on simple noble gases **[36-42]**, the density, the degrees of freedom associated with the terminal group, the strength of the molecule-(SAM)surface interaction, and the rigidity and thickness of the SAMs may be expected to play an important role in energy dissipation and, hence, the dynamics of adsorption. Reflecting upon the molecular models displayed in Figure 7-1, we see that two of the SAMs (NMTS and PHTS) present aromatic groups at their surface, while representing organic layers possessing different thicknesses, whereas the shortest interfacial organic layer (IOL) examined here, HMDS, possesses a terminal $-Si(CH_3)_3$ group. Thus, with these SAMs, we can investigate the effects of the thickness and chemical termination of the SAMs on the dynamics of PTCDI-C_{13} adsorption and submonolayer nucleation and growth.

First, we consider the results from x-ray reflectivity (XRR) of the SAMs themselves.. In Figure 7-2 we plot the reflected intensity as a function of the out-of-plane scattering vector, q_z, for a monolayer of PHTS. In this figure, we plot only 50%

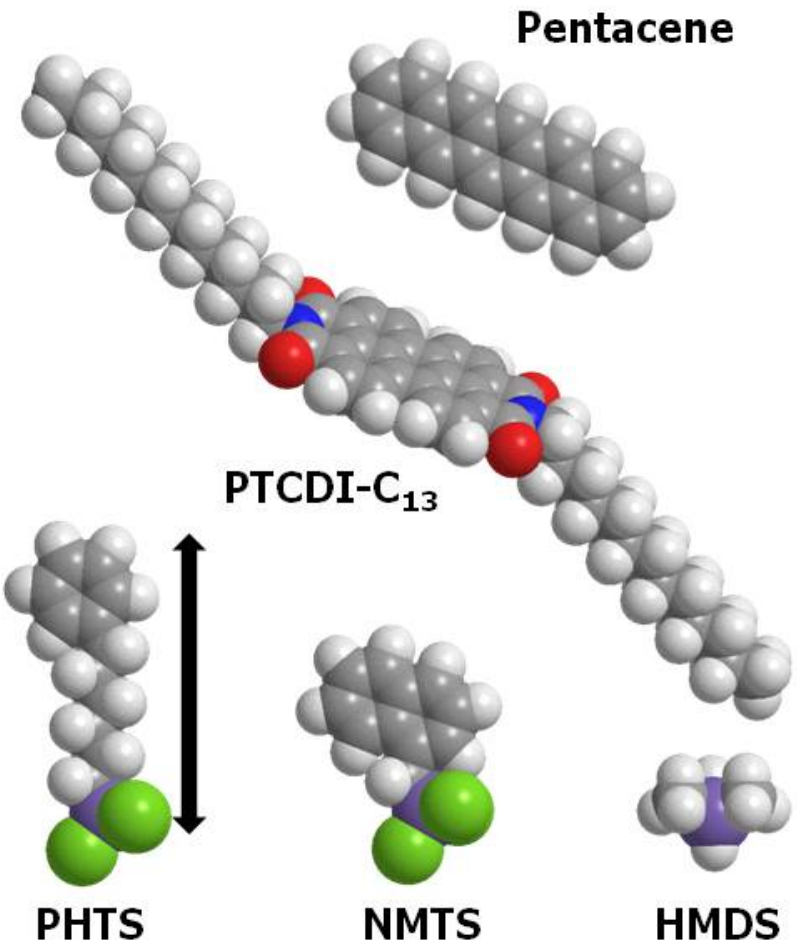

Figure 7-1 Space filling models for the molecule of interest here, *N,N'*-ditridecylperlyene-3,4,9,10-tetracarboxylic diimide (PTCDI-C_{13}), pentacene and the three molecules that form the SAMs examined here: 1-napthylmethyltrichlorosilane, (NMTS), 6-phenylhexyltrichlorosilane, (PHTS), and the chemisorbing species formed upon exposure of SiO_2 to hexamethyldisilazane (HMDS), $HSi(CH_3)_3$, where H represents the SiO_2 surface.

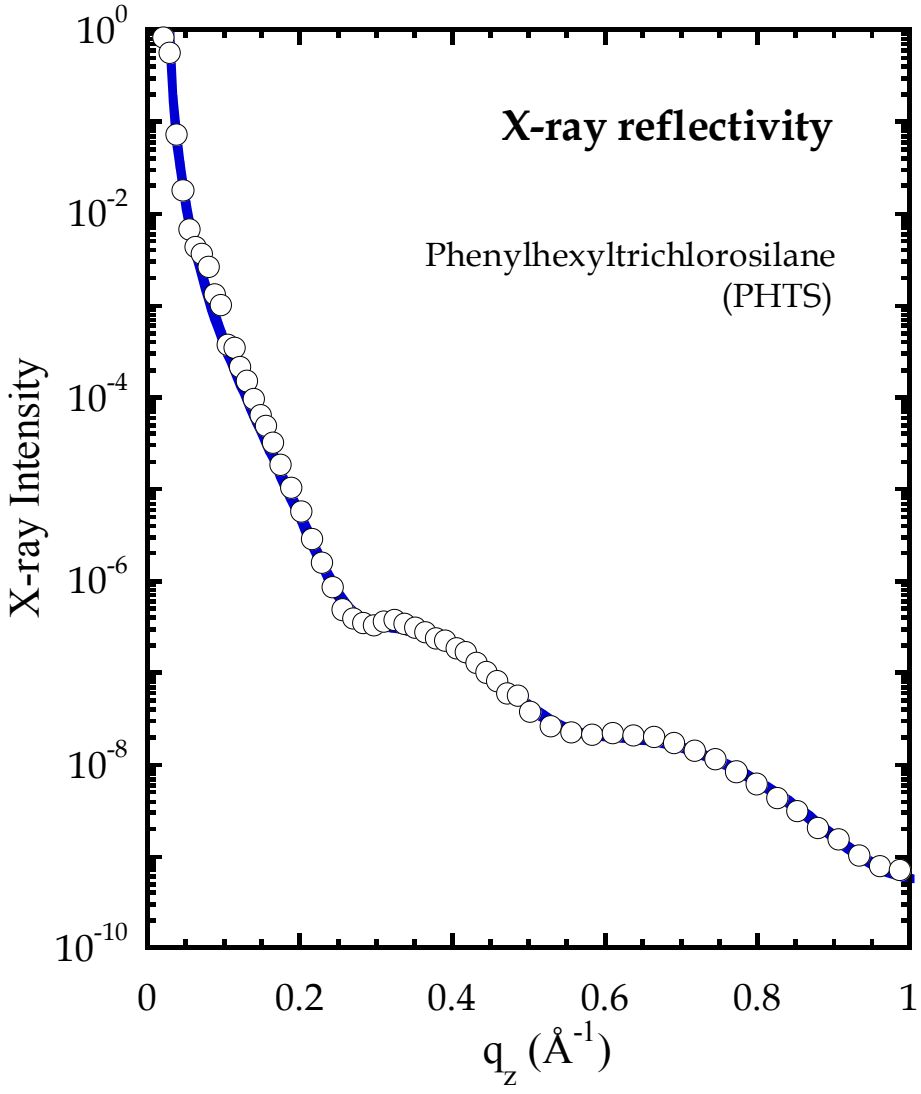

Figure 7-2 Scattered x-ray intensity as a function of the out-of-plane scattering vector, q_z, for a monolayer of 6-phenylhexyltrichlorosilane on SiO_2. For clarity, only 1 of every 2 data points is plotted. The solid curve represents a fit of the data to a model based on the Parratt formalism (reference **[32]**).

of the data (1 of every 2 points) to show the quality of the fit, which is shown by the smooth curve. The fit to the data is excellent, and from the fit we extract a thickness $d_{SAM} = 11.5 \pm 0.1$ Å, and electron density of $p_{el,SAM} = 0.33 \pm 0.02$ Å^{-3}. Making use of the number of electrons in the PHTS backbone, we find the density of the PHTS molecules is $n_{SAM} = 4.18 \pm 0.19 \times 10^{14}$ molec-cm^{-2} **[43]**. In a separately made batch of the PHTS SAM (XRR data not shown), we found a similar thickness of 11.0 ± 0.1 Å and a density of $n_{SAM} = 4.05 \pm 0.09 \times 10^{14}$ molec-cm^{-2}. For the other SAM deposited here from the solution phase (XRR data not shown), NMTS, we find similar molecular densities, namely, $n_{SAM} = 4.22 \times 10^{14}$ molec-cm^{-2}, and a thickness of ~ 8.13 Å. These and other properties of the organic layers considered in this study are given in Table 7-1.

The surface energy **[44]** and static contact angles (water) **[45-47]** measured for NMTS and PHTS agree well with values reported for other similar phenyl-terminated SAMs deposited on a silicon thermal oxide or native oxide. The thicknesses estimated for NMTS and PHTS from the fits to the XRR are similar to the length of the molecule as determined using ChemDraw (CambridgeSoft) after energy minimization (*cf.* Table 7-1, and Figure 7-1). This suggests that the PHTS and NMTS films are tightly packed, single molecule high layers, with their long molecular axis approximately perpendicular to the substrate. This result is consistent with other reports, where good agreement has been found between experimentally measured and theoretically predicted thicknesses for other similar aromatic-terminated SAMs **[45-47]**. Finally, we also characterized the layer formed upon exposure to HMDS. The thickness of the

Table 7-1 Properties of the self-assembled monolayers*

Monolayer	Contact angle (H_2O/ formamide)	Surface energy (mJ-m^{-2})	Thickness, XRR (Å)	Molecular length (Å)	Electron density (Å^{-3})	Density of SAM (nm^{-2})
HMDS	79°/60°	32.7				2.3 ± 0.5 **[46]**
NMTS	81°/61°	32.5	8.13 ± 0.01	7.11	0.39 ± 0.02	4.22 ± 0.05
PHTS** (a)			11.45 ± 0.12	11.68	0.32 ± 0.01	4.18 ± 0.19
(b)	83°/69°	33.4	10.98 ± 0.05	11.68	0.33 ± 0.01	4.05 ± 0.09

*this work, unless noted otherwise
**XRR results from two batches of PHTS (a, b) are reported.

HMDS layer is expected to be on the order of 2-5 Å, comparable to the expected roughness of the SiO_2 surface. Because of this, and the fact that our XRR measurements were performed only up to $q_z = 1$ Å^{-1} (where a minimum in the intensity would correspond to a layer of 3.1 Å in thickness), XRR on the HMDS-treated substrates was virtually indistinguishable from that on bare SiO_2. The HMDS layer was characterized using contact angle measurements and we found static angles (water) of 79°. In previous work we have estimated the coverage of the HMDS fragment, -Si$(CH_3)_3$, to be ~ $2.3 \pm 0.5 \times 10^{14}$ molec-cm^{-2}.

B. Morphology and X-ray reflectivity of a multilayer of PTCDI-C_{13}

In Figure 7-3(a), we display an AF micrograph of a multilayer thin film of PTCDI-C_{13} deposited on NMTS at a growth rate of 0.011 ML-s^{-1} (E_i = 6.3 eV and T_s = 40 °C). Exposure to the molecular beam was 871 s, and the film thickness determined from XRR was ~ 30 nm (*vide infra*). We describe below the results that are utilized to calculate the thin film growth rate. As can be seen from the image, the morphology of the thin film is represented by relatively smooth areas, where single molecule high steps are observed, interspersed with tall protrusions that are up to ~30 nm in height. These protrusions account for < 8% of the total area. Excluding the areas represented by the protrusions we calculate a RMS surface roughness of ~ 2.1 nm (~ 0.8 ML, *vide infra*). Including the protrusions gives a roughness of ~ 3.71 nm. Similar morphologies were observed for PTCDI-C_{13} deposited on HMDS and PHTS for the same conditions of growth (E_i and T_s). Indeed, similar morphologies have also been

reported for the growth of thin films of PTCDI-C_{13} on other substrates such as SiO_2, and a number of polymer thin films, at similar growth rates and substrate temperatures, T_s **[10, 12]**.

In Figure 7-3(b) we display the corresponding specular x-ray reflectivity for PTCDI-C_{13} deposited on NMTS. The scattered intensity exhibits Bragg reflections (up to the 4th order) with well defined Laue oscillations that are characteristic of a highly ordered lamellar structure. From the reflectivity data, the coherent thickness, D ($D = 2\pi/\Delta q$, where Δq is the period of the Laue oscillations about the 00l Bragg peaks) of the film was determined to be 30 nm. X-ray reflectivity profiles exhibiting similarly highly ordered lamellar films were observed for the growth of PTCDI-C_{13} on HDMS and PHTS at the same conditions of deposition. The average d_{001} spacing for the PTCDI-C_{13} thin films on all surfaces was determined to be 26.8 ± 0.1 Å, similar to other reported studies **[10,11]**. Well-defined Laue oscillations, such as those in Figure 7-3(b), arise from interference between smooth surfaces, in apparent contradiction with the presence of large protrusions and roughness in Figure 7-3(a). However, these protrusions are highly localized, accounting for only ~8% of the surface, and as a result have only a small effect on the fringes. More specifically, it is incorrect to conclude, on the basis of Figures 7-3(a,b), that the protrusions are noncrystalline, amorphous, or have different crystalline orientation that the remainder of the film. We shall return to the issue of the evolution of the surface morphology and roughness of these thin films of PTCDI-C_{13} below. We will now turn our attention to the dynamics of adsorption of PTCDI-C_{13} on HMDS, NMTS and PHTS.

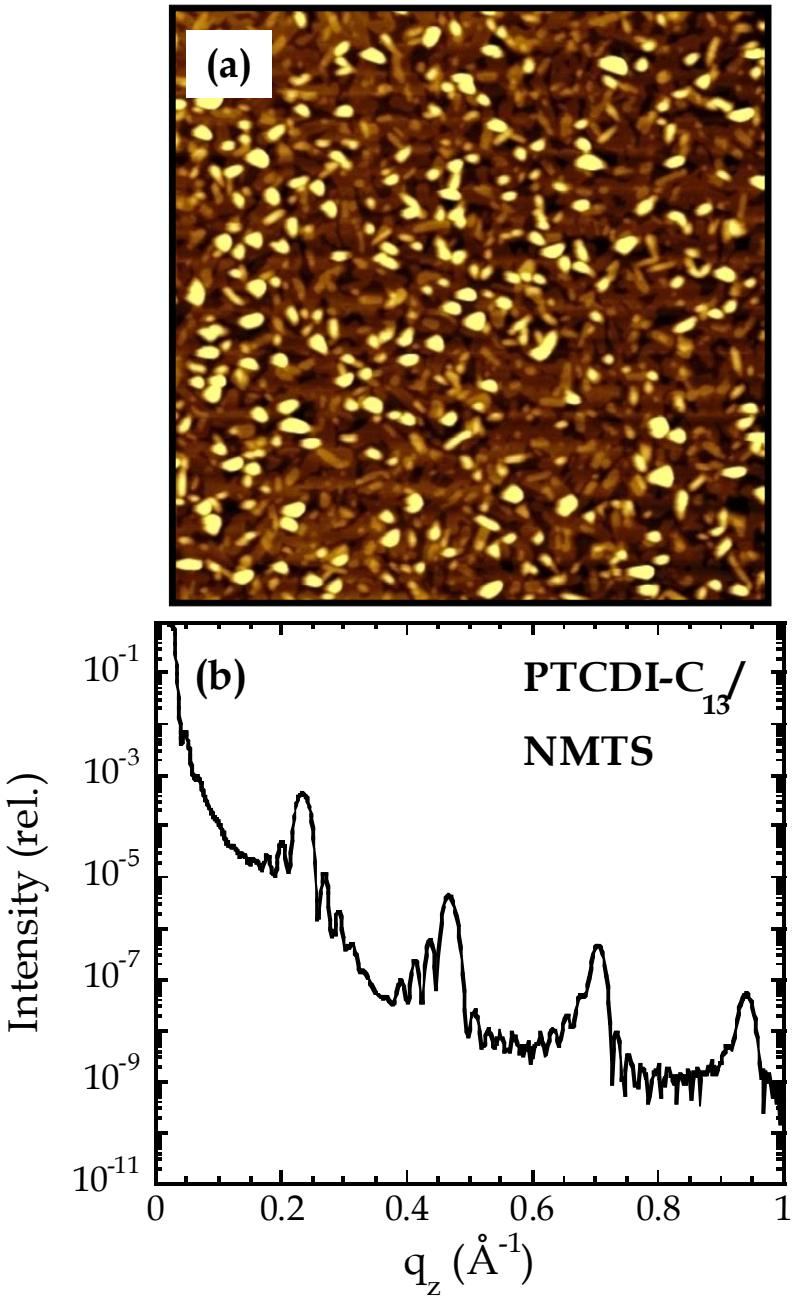

Figure 7-3 (a) A 3 × 3 μm^2 AF micrograph of 30 nm PTCDI-C_{13} film deposited on SiO_2 modified with NMTS at GR = 0.011 ML-s^{-1} (b) Specular x-ray reflectivity (XRR) of film shown in Figure 7-3(a).

C. Adsorption and growth of PTCDI-C_{13} on self-assembled monolayers

In Figures 7-4 to 7-6, we present a subset of experiments we have conducted concerning the growth of PTCDI-C_{13} on HMDS, NMTS, and PHTS. The data shown represent the lowest (6.3 eV) and highest (14.3 eV) kinetic energies examined here using the supersonic molecular beam source. All experiments were conducted at T_s = 40 ºC. Growth was conducted at this substrate temperature to minimize any possible effects associated with the potential degradation of the SAMs, or substrate temperature-induced increases in the surface roughness. As explained in greater detail in our previous work **[24-26]**, the intensity oscillations at the anti-Bragg condition, observed on all 3 surfaces, are expected for layer-by-layer growth due to the alternating contributions of the odd and even layers to the magnitude of the scattered intensity [*cf*. Equation (7-2)]. As may be seen in Figures 7-4 to 7-6, the shape of the anti-Bragg oscillations vary slightly depending on the nature of the starting surface. For example, comparing the different starting surfaces we see that there are differences in the relative intensities at t = 0, at the peak of the first oscillation (~ 1 ML coverage) and for the "saturation" intensity, $t \rightarrow \infty$. These are readily understood as manifestations of the differences in the phase (ϕ) and reflection amplitudes (r_{subs} and r_{film}) that appear in Equation (7-2), which are functions of the thickness and electron density of the SAM/IOL **[25-26, 33-34]**.

In order to examine the features in detail on each SAM, we begin with the growth of PTCDI-C_{13} on HMDS as shown in Figure 4. In Figure 7-4(a) we present the scattered x-ray intensity acquired in real time at the anti-Bragg condition (q_z =

00½) for the growth of PTCDI-C_{13} on HMDS at E_i = 6.3 eV. In a typical case (i.e., the values for ϕ, r_{subs} and r_{film}) when roughness builds slowly, one expects the oscillations to repeat every 2 MLs, with a sharp cusp-like feature appearing after each monolayer is completed, with these features separated by smooth, nearly parabolic minima. In some cases the amplitudes associated with the completion of odd and even layers can vary greatly, and one of the cusp-like maxima may be significantly obscured. Such is the case for most of the oscillations observed here for PTCDI-C_{13}. For growth on HMDS we observe the strong cusp-like maximum after the deposition of 2 MLs, followed by smaller maxima representing approximately the completion of the deposition of 4, 6 and 8 MLs. The expected smaller maxima representing the completion of the odd layers are mostly obscured, appearing mostly to make the intensity near 1 ML appear asymmetrical and non-parabolic. The observation of intensity oscillations at coverages as high as 8 MLs is nevertheless very significant, and it indicates that PTCDI-C_{13} grows in a layer-by-layer (LbL) mode up to several (approaching 10) monolayers.

The kinetics of growth can be modeled more precisely by making use of Eqs. [1] and [2] and these results are also shown in Figures 7-4(a) and 7-4(b). In (a) we show the coverage of each layer (solid black curves) predicted by the fit to the intensity oscillations (solid blue line). We find that, to fit the data, we need to assume that $S_0F \sim 0.00960$ ML-s^{-1}, whereas $S_{n\geq 1}F \sim 0.0114$ ML-s^{-1}. These data imply that the rate of growth has accelerated modestly with increasing PTCDI-C_{13} coverage. Since desorption can be assumed negligible at T_s = 40 ºC, these data indicate that the

Figure 7-4 (a) X-ray intensity at the anti-Bragg condition as a function of exposure to the molecular beam (E_i = 6.3 eV) for thin films of PTCDI-C_{13} deposited on SiO_2 modified with HMDS. T_s = 40 °C. Thick solid lines (right ordinate) indicate a fit of the data to a model and thin solid curves (left ordinate) represent predicted coverages (θ_n) of the individual layers. (b) Total coverage (θ_{tot}, left ordinate) and growth rate (right ordinate) predicted by a fit of the data displayed in (a). These figures are repeated in (c) and (d), for PTCDI-C_{13} incident at the higher incident kinetic energy (E_i = 14.3 eV) for this same surface.

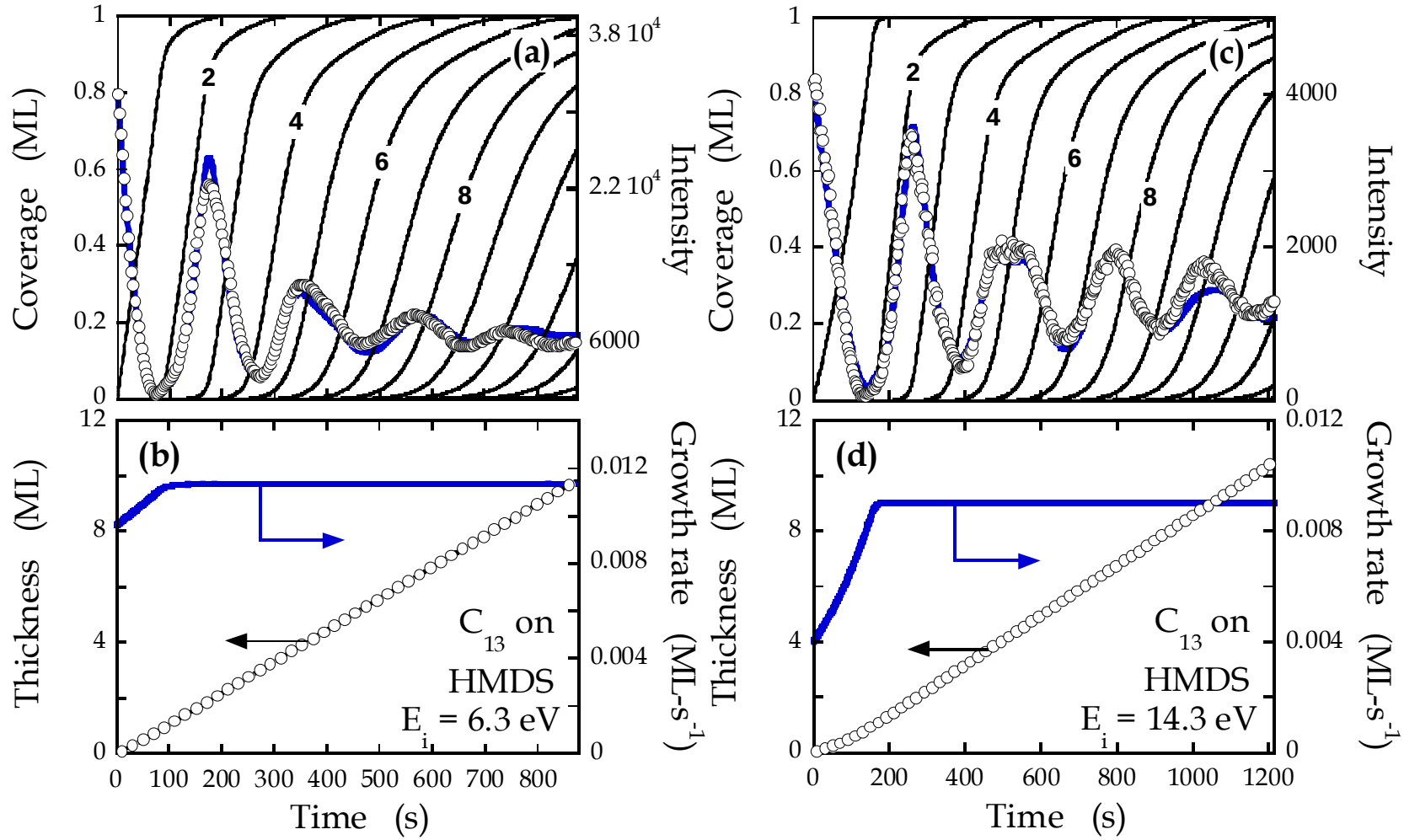
(a)
(b)
(c)
(d)
Coverage (ML)
Intensity
Thickness (ML)
Growth rate (ML-s^{-1})
Time (s)
2
4
6
8
C_{13} on
HMDS
E_i = 6.3 eV
E_i = 14.3 eV
3.8 10^4
2.2 10^4
6000
4000
2000
0.012
0.008
0.004

acceleration in the rate is due to an increase in the probability of adsorption S with increasing coverage. In this case the adsorption probability has increased by about 18%. The highly LbL nature of the growth of PTCDI-C_{13} on HMDS as observed at the anti-Bragg condition apparently occurs nearly simultaneously with the formation of the tall protrusions as shown in Fig 3(a). These protrusions become evident at a coverage of about 4 ML. Comparing these results to what has been reported for the *in-situ* real-time growth of other small molecule organic systems, e.g., pentacene **[24, 48]** diindenoperylene (DIP) **[25-26]** and perfluoropentacene (PFP) **[49-50]**, we take note of the fact that PTCDI-C_{13} grows in a significantly more sustained LbL mode at similar conditions of growth.

In Figures 7-4(c) and 7-4(d), we consider growth of PTCDI-C_{13} incident on HMDS at E_i = 14.3 eV. In comparison to growth of PTCDI-C_{13} on HMDS at 6.3 eV, we see that the anti-Bragg oscillations are slightly more pronounced indicating that LbL growth is extended to even higher coverages for these conditions. To fit these data, we must assume that $S_0F \sim 0.00401$ ML-s^{-1}, whereas $S_{n\geq 1}F \sim 0.00902$ ML-s^{-1}, an increase of ~125%. If we consider intermediate kinetic energies, not shown here, we find that the acceleration in the rate of growth follows a consistent trend with E_i, namely a ~29% increase at E_i = 8.8 eV, and 93% at E_i = 12.8 eV. We also see similar significant increases in the rate of growth, and hence the probability of adsorption, with increasing coverage for the case of another molecule, DIP, deposited on HMDS **[25, 26]**.

In Figure 7-5(a) we present the scattered x-ray intensity acquired in real time at the anti-Bragg condition for growth of PTCDI-C_{13} on NMTS at E_i = 6.3 eV. In this

Figure 7-5 X-ray intensities, predicted layer occupancies, total coverages and growth rates for PTCDI-C_{13} incident on NMTS|SiO_2 at (a,b) E_i = 6.3 eV and (c,d) 14.3 eV. Details concerning the layout are otherwise identical to Figure 7-4.

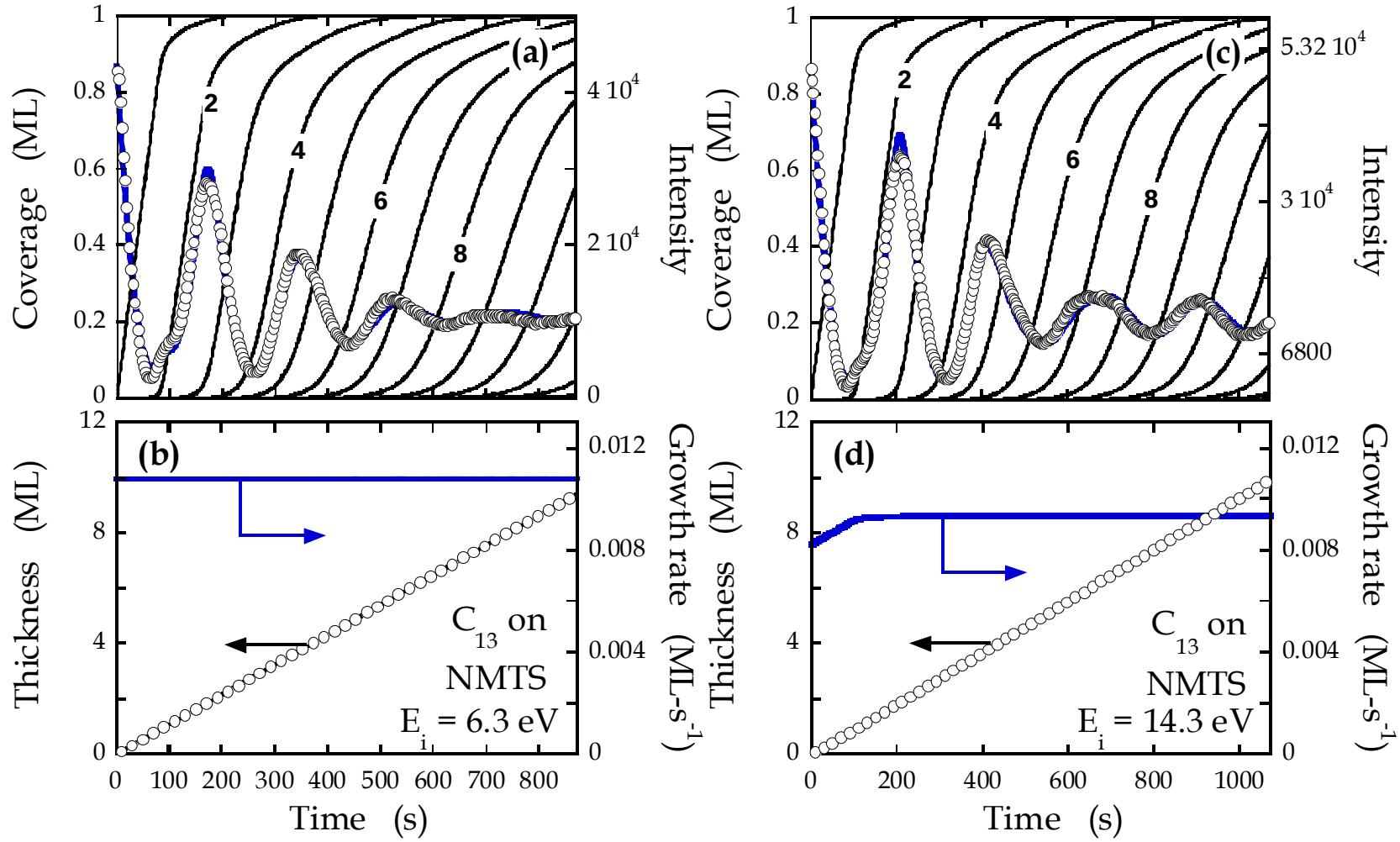
(a)
(b)
(c)
(d)
Coverage (ML)
Intensity
Thickness (ML)
Growth rate (ML-s^{-1})
Time (s)
2
4
6
8
C_{13} on
NMTS
E_i = 6.3 eV
E_i = 14.3 eV
4 10^4
2 10^4
5.32 10^4
3 10^4
6800

case a small maximum at ~ 1 ML coverage is barely visible as a kink in the intensity rise following the first minimum. Concerning other features, the intensity oscillations are comparable to those observed on HMDS: clear maxima as 2, 4, 6 and 8 MLs are completed. Concerning the kinetics of growth, as shown in Figure 7-5(b), we find that the data can be described by a model where there is no acceleration in the rate of growth. In Figures 7-5(c) and 7-5(d), we consider growth of PTCDI-C_{13} incident on NMTS at E_i = 14.3 eV. In comparison to growth of PTCDI-C_{13} on NMTS at 6.3 eV, we see that the anti-Bragg oscillations are slightly more pronounced at the higher coverages, indicating more sustained LbL growth for these conditions. We find the data is best modeled by assuming an acceleration in the rate of growth of ~14%. If we consider intermediate kinetic energies, not shown here, we find that the acceleration in the rate of growth follows a consistent trend with E_i, namely a ~ 0% increase at E_i = 8.8 eV, and 4% at E_i = 12.8 eV. In comparison to HMDS as discussed above, the magnitude of the rate of change in growth on NMTS is much smaller at all incident energies, implying that the adsorption probability of PTCDI-C_{13} on NMTS is close to that on PTCDI-C_{13} itself. We have observed similar trends for DIP, where we observed greater adsorption probabilities of DIP on thicker, alkyl backbone and –CH_3 terminated SAMs, as opposed to the relatively thin layers produced by HMDS **[26]**.

In Figure 7-6 we display the results for the growth of PTCDI-C_{13} on PHTS. At the lowest incident kinetic energy (6.3 eV) from Figure 7-6(a) we see strong intensity oscillations for the first ~ 10 MLs, similar to what we observe on NMTS and HMDS. From Figure 7-6(b) we see that a change in the rate of growth is also observed on PHTS, and for this energy the amount of increase is ~ 17%. At the highest incident

Figure 7-6 X-ray intensities, predicted layer occupancies, total coverages and growth rates for PTCDI-C_{13} incident on PHTS|SiO_2 at (a,b) E_i = 6.3 eV and (c,d) 14.3 eV. Details concerning the layout are otherwise identical to Figure 7-4.

(a)
(b)
(c)
(d)
Coverage (ML)
Intensity
Thickness (ML)
Growth rate (ML-s^{-1})
Time (s)
2
4
6
8
1.64 10^4
9600
2800
1.08 10^4
6000
1200
0.012
0.008
0.004
0
C$_{13}$ on
PHTS
E$_i$ = 6.3 eV
E$_i$ = 14.3 eV

kinetic energy (14.3 eV) for PTCDI-C_{13} on PHTS, in Figure 7-6(c) we also observe sustained LbL growth, up to coverages of ~ 10 MLs. The acceleration in the rate of growth on the PHTS-modified surface at the highest energy is about 13%. If we consider intermediate kinetic energies, not shown here, we find that the acceleration in the rate of growth is 12% at E_i = 8.8 eV, and 9% at E_i = 12.8 eV. Thus, on this surface, the rate of acceleration is nearly independent of the incident kinetic energy and the magnitude of the rate of change in growth is much smaller at all incident energies, as compared to HMDS, implying that similar to NMTS, the adsorption probability of PTCDI-C_{13} on PHTS is close to that on PTCDI-C_{13} itself.

In order to examine the effects of the incident kinetic energy on the probability of adsorption (and hence the growth rate) we need to account for changes in the incident molecular flux as we varied the kinetic energy. In order to do this we have measured the direct intensity of the molecular beam using quadrupole mass spectrometry, which measures the molecular density in the ionization region, and subsequently corrected for the effect of molecular velocity to calculate a relative incident flux. Making use of this relative molecular flux we can then calculate relative probabilities of adsorption. From the discussion of the systems investigated above, it is clear that on SiO_2 modified with HMDS, the adsorption probability of PTCDI-C_{13} differs significantly in the sub-monolayer and multilayer regimes and this effect is more pronounced with increasing incident energy. On the other hand, for SiO_2 modified with NMTS and PHTS, the difference in adsorption probability for PTCDI-C_{13} in the sub-monolayer and multilayer regimes is less drastic.

In Figure 7-7 we plot the relative probabilities of adsorption for all surfaces examined here for (a) PTCDI-C_{13} on the growing PTCDI-C_{13} thin film; and (b) PTCDI-C_{13} on the starting substrates as a function of incident kinetic energy, after making an appropriate adjustment for the change in the incident flux with kinetic energy. In passing we note that we estimate that the uncertainty in the reproducibility of the flux between experiments to be about ± 5 %, not exceeding ± 10 %, whereas the change in incident flux during the experiment, which would impact any change in the growth rate, to be much less, ± 1 %. In Figure 7-7 the probabilities of adsorption have been normalized to the highest flux corrected growth rate we observe here among these three surfaces, namely, (multilayer) growth on HMDS at E_i = 6.3 eV.

Concerning adsorption on the starting surfaces, the data exhibits the behavior expected for trapping-mediated adsorption—a smooth decrease of the probability with increasing incident kinetic energy. We have observed this behavior previously concerning the adsorption of both pentacene **[22, 51, 52]** and DIP **[25, 26]** on clean SiO_2 and SiO_2 modified with HMDS and a number of SAMs. In Figure 7-7(a) for PTCDI-C_{13} on PTCDI-C_{13} we see that there is little "memory" of the starting substrate at each specific energy, and that all of the values lie within a band of about ± 5% (approximately the experimental uncertainty for these values). Concerning multilayer growth, it is clear from Figure 7-7(a) that for these 3 systems, the probability of adsorption of PTCDI-C_{13} on PTCDI-C_{13} also exhibits trapping-mediated adsorption, and there is a significant decrease in the probability of adsorption (about a factor of 2) as E_i increases from 6.3 to 14.3 eV. This behavior is similar to what we have reported previously for pentacene on a growing pentacene thin film on SiO_2 **[52]**, where the

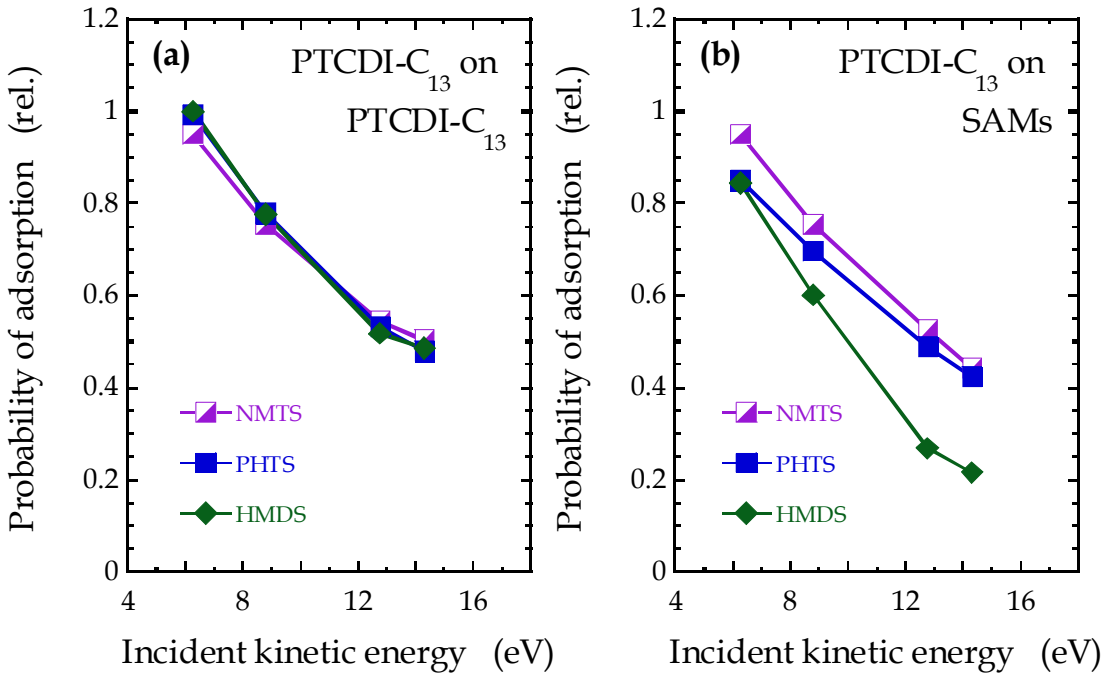

Figure 7-7 Relative probabilities of adsorption vs. the incident kinetic energy for PTCDI-C_{13} incident on (a) the PTCDI-C_{13} -covered substrates and (b) the 3 starting substrates. The probabilities have been normalized to the highest flux-corrected growth rate, which was for multilayer growth of PTCDI-C_{13} on HMDS-modified surface at E_i = 6.4 eV.

adsorption probability decreased by a factor of ~ 2 as the incident kinetic energy increased from ~ 1.5 to 4.5-6.7 eV. These results for pentacene were in good agreement with results from molecular simulation using the MM3 potential **[51]**, and compare well to PTCDI-C_{13} if we factor in the likely differences in the intermolecular potentials due to molecular size (*cf.* Figure 7-1) and normalize the incident kinetic energy appropriately. Comparing these results to the adsorption of DIP on SiO_2 and SiO_2 modified with HMDS **[25]** and other thicker –CH_3–terminated and fluorinated SAMs **[26]**, we have found somewhat more modest changes in the adsorption probability of DIP on DIP, with the probability decreasing ~ 20% as the incident kinetic energy is increased from ~ 6 to 12 eV.

Moving on to the results for the adsorption of PTCDI-C_{13} on the starting surfaces, we observe in Figure 7-7(b) that the adsorption of PTCDI-C_{13} is equally efficient on NMTS and PHTS as it is on itself but significantly more efficient on itself as compared to on bare HMDS. As we have discussed elsewhere **[25,26,51]** there are two mechanisms that can be associated with more efficient trapping of a small molecule organic on itself vs. on a bare substrate such as SiO_2, or on a relatively thin organic modifier such as HMDS. First, there is more efficient momentum transfer as a result of better mass-matching for a molecule impinging on itself. This effect, however, loses strict applicability as the size, complexity and number of internal degrees of freedom of the molecule increases. Second, mechanisms such as direct molecular insertion become operative at sufficiently high incident kinetic energy, and can contribute significantly to adsorption **[25,26,51]**.

In Figure 7-8 we plot the ratio of the trapping probability in the monolayer regime to that in the multilayer regime (or equivalently the growth rates, as the incident flux is the same for each set of conditions). We see that in this representation, there is little to no change in the in the ratio for the adsorption of PTCDI-C13 on NMTS and PHTS (ratio ~ 1) as expected as the trapping probability of PTCDI-C_{13} on NMTS and PHTS is equally efficient as on itself. On the other hand, on HMDS, we see a sharp decrease in the ratio of the monolayer to multilayer growth rate, indicative of the fact the trapping probability of PTCDI-C_{13} is significantly greater on itself as compared to on HMDS, and this difference increases with incident energy.

Why is trapping different on HMDS vs. NMTS and PHTS? First, the SAMs/IOLs examined here are all relatively low energy surfaces with contact angles (water) of ~ 80°. Thus, contact angle measurements, often linked to the density and presence of organic functional groups, are of little help here. Thickness of the organic layer seems to play some role, as trapping seems to be the most efficient on the thicker organic layers (NMTS and PHTS), and least efficient on the thinnest (HMDS). Returning to the arguments associated with the trapping of PTCDI-C_{13} on itself, we referred to the effect of particle mass from the point of view of two-body elastic scattering (obviously over-simplified), and the effect of molecular insertion. Concerning the latter mechanism, direct molecular insertion of PTCDI-C_{13} into a HMDS layer is clearly not possible on HMDS to any significant extent, due to the thickness of the layer (< 5 Å). For PTCDI-C_{13} incident on NMTS and PHTS, however, insertion may play a role, particularly for side-on interactions between PTCDI-C_{13} and these layers. As indicated above, in previous work we have measured

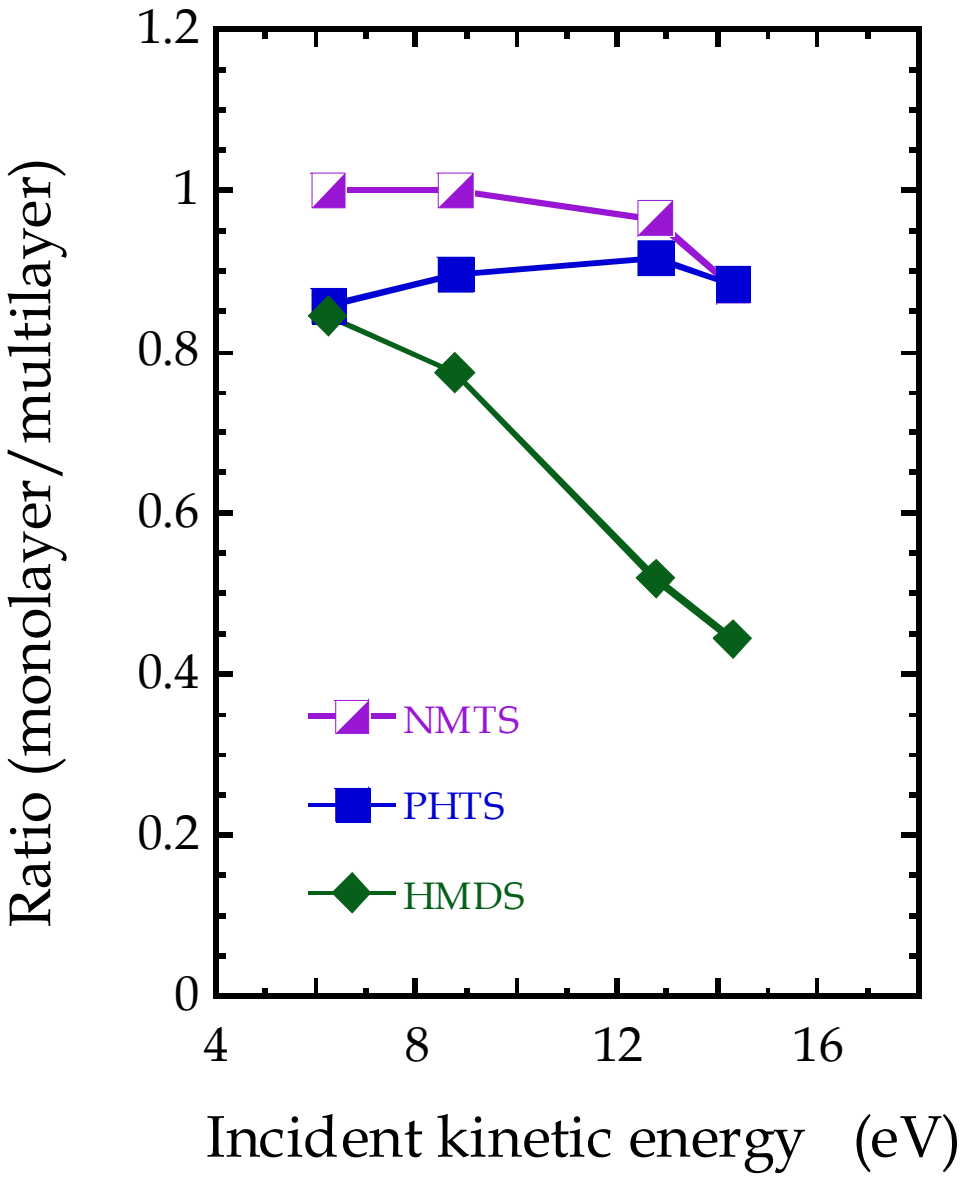

Figure 7-8 Ratio of the probabilities of adsorption (initial monolayer/multilayer) vs. the incident kinetic energy for PTCDI-C_{13} on the 3 substrates considered here.

the probability of adsorption of pentacene on pentacene and compared these results to molecular dynamics (MD) simulations **[51]**. In related work we also examined the adsorption of DIP on three alkyl backbone (two C_8, one C_{18}) SAMs and also made comparisons to MD simulations **[26]**. In both studies a significant role for molecular insertion either into a pre-existing layer, or into to the SAMs themselves was implicated. In other work, it has been observed that molecules such as Ar **[41]** and Xe **[53]** that are sufficiently energetic are capable of penetrating into SAMs. Thus, it seems that molecular insertion may be relatively commonplace concerning molecule-SAM interactions.

Concerning the adsorption of PTCDI-C_{13} on NMTS and PHTS based on previous examples we have just cited we would argue that insertion events are likely, and possibly frequent. For example, for DIP incident on a layer of octyltrichlorosilane ($\equiv$Si-$(CH_2)_7$-CH_3), which possesses a physical length of ~ 11.6 Å and a thin film thickness of 6.3 Å as measured from XRR, we found that of the molecules that eventually adsorb, ~ 60-90% of those do so by inserting first into the SAM layer **[26]**. In comparison, the PHTS and NMTS layers examined here possess physical lengths of 11.7 and 7.1 Å, and thin film thicknesses of 11.5 and 8.3 Å as measured from XRR, respectively. Thus, if the thickness of the SAM plays a role in determining the relative importance of molecular insertion, then PTCID-C_{13} may be also expected to insert into these layers. Molecules that do penetrate the organic layer will experience many collisions with the constituents that comprise the organic layer (head group, back bone groups), and these events will act as a drag or frictional force as the molecule penetrates the layer, possibly encounters the underlying substrate, and then rebounds.

This kind of trajectory would effectively dissipate the molecule's incident kinetic energy. Such trajectories will be short-lived, if they exist at all, on HMDS, while they may occur much more frequently on the two thicker PHTS and NMTS layers examined here.

D. Thin film morphology and the evolution of surface roughness

We next consider the thin film morphology and the evolution of surface roughness for PTCDI-C_{13} grown on the three SAMs examined here, as determined from *ex situ* AFM and from the fits to the *in situ* real-time x-ray scattering data (*cf*. Figures 7-4 to 7-6). Concerning the latter, as the fits produce layer occupancies, calculation of the interface width (RMS) is straightforward. In Figure 7-9 we display results from AFM for a thin film of PTCDI-C_{13} deposited on HMDS at a coverage of 1.13 ML. The film was deposited at an incident energy of E_i = 6.3eV, T_s = 40 °C and at a growth rate of ~ 0.017 ML-s^{-1}. Here, we make use of independent knowledge of the thickness of the film from *in situ* x-ray diffraction to make assignments of the layers represented in the AFM image, which for this coverage is relatively easy. For this 1.13 ML film [Figure 7-9(a)], we see that the first layer appears to be entirely completed, with the presence of only a second monolayer of mostly unconnected islands, consistent with LbL growth. In Figure 7-9(b), we display a representative line scan corresponding to the arrow in Figure 7-9(a). Essentially only two layers are represented in this line scan. This is further exemplified in Figure 7-9(c) where we plot the histogram of surface heights calculated from the entire AF micrograph of the

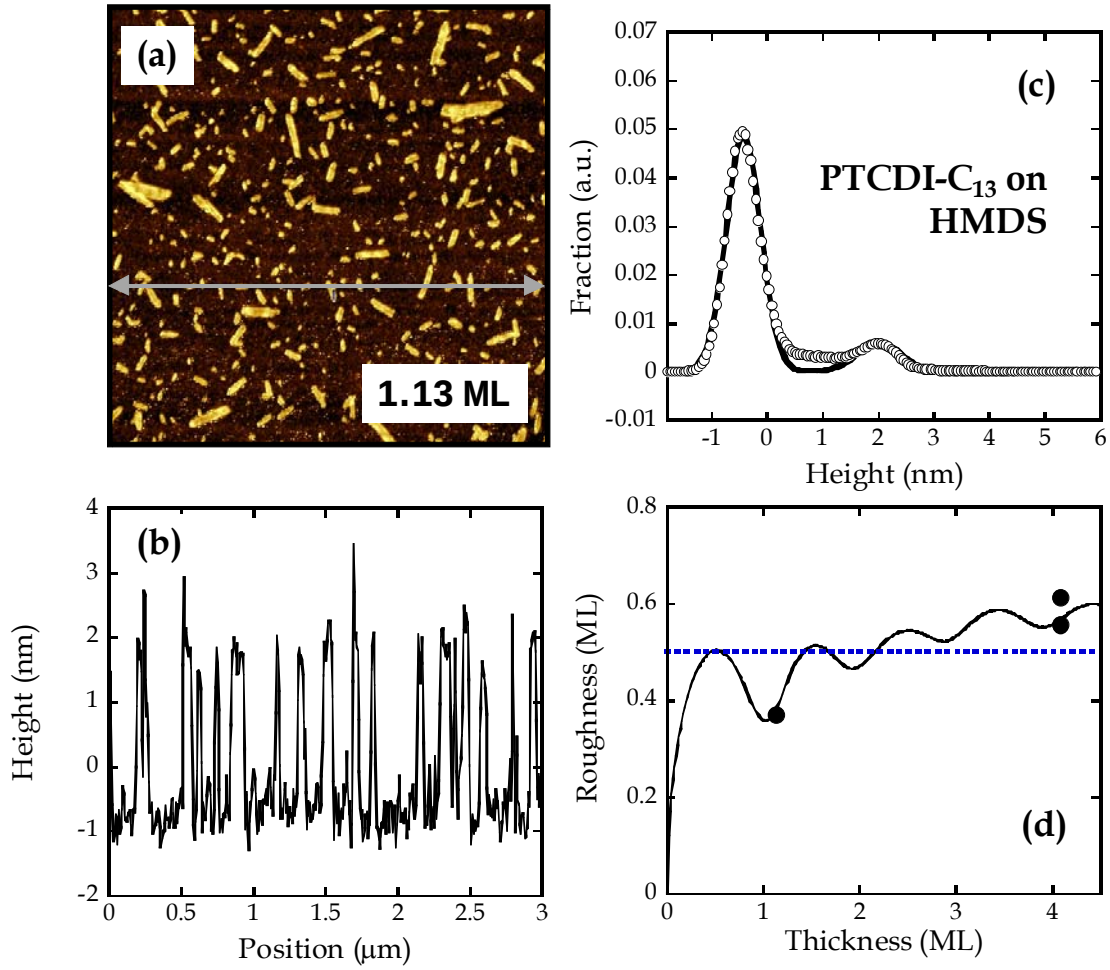

Figure 7-9 (a) A 3 × 3 μm^2 AF micrograph of PTCDI-C_{13} film deposited on HMDS-terminated SiO_2 at *GR* = 0.017 ML-s^{-1} (for multilayer) and coverage of 1.13ML. (b) Line profile of AF micrograph shown in Figure 7-9(a) as indicated by horizontal arrow. (c) Height histogram of AF micrograph shown in Figure 7-9(a). (d) Thin film roughness of PTCDI-C_{13} on HMDS-terminated SiO_2 as a function of PTCDI-C_{13} thickness as predicted by the fit to the x-ray data. Solid circles represent roughness obtained directly from AF micrographs shown in Figure 7-9(a) and 7-10(a).

1.13 ML film shown in Figure 7-9(a). As may be seen, we can fit this histogram to two peaks, separated by ~ 2.43 ± 0.01 nm, a value that is within 10% of the d_{001} lattice spacing.

In Figure 7-10 we display results from AFM for a thin film of PTCDI-C_{13} deposited on HMDS at a coverage of 4.1 ML, for conditions identical to those considered in Figure 7-9. Here the assignment of the absolute layer coverages is less straightforward. First, about at this coverage, we begin to observe the tall protrusions discussed above in connection with Figure 7-3(a). As examples we display in Figure 7-10 line scans that (b) contain one of these protrusions (red arrow), and (d) that do not (gray arrow). We count about 12 of these protrusions in Figure 7-10(a), which account for < 0.5% of the total area, and < 0.03 MLs in terms of volume. Based on these observations, we can safely ignore the contributions of the protrusions and assign the layer most represented in Figure 7-10(a) to the fourth layer, i.e., that identified as "0" in the line scan in Figures 7-10(b,d). As may be seen from the image, at this coverage we also observe the third layer (darker regions), and simultaneously a fifth layer (brighter regions), and some of the tall protrusions (brightest) we have just discussed. In Figure 7-10(c), we display a histogram of surface heights calculated from the entire AF micrograph of the 4.1 ML film shown in Figure 7-10(a). The histogram at this coverage, which is quite symmetrical, is described by three peaks, shifted by 2.46 ± 0.04 nm. This value is again in good agreement with the d_{001} lattice spacing identified above. Excluding the areas represented by the protrusions we calculate a RMS surface roughness of ~ 1.37 nm (~ 0.56 ML). Including the protrusions gives a roughness of ~ 1.51 nm (~ 0.61 ML).

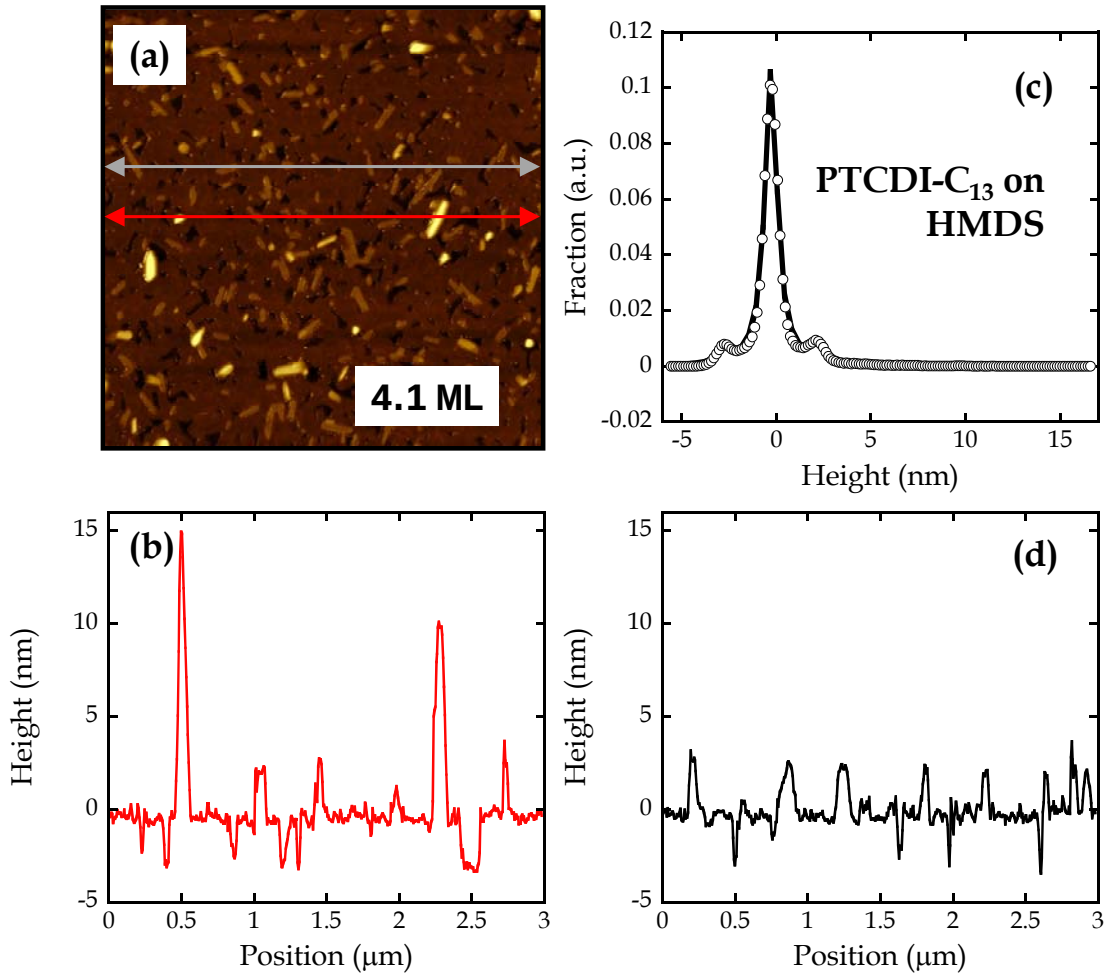

Figure 7-10 (a) A 3 × 3 μm^2 AF micrograph of PTCDI-C_{13} film deposited on HMDS-terminated SiO_2 at *GR* = 0.017 ML-s^{-1} (for multilayer) and coverage of 4.1ML. (b) Line profile of AF micrograph shown in Figure 7-10(a) as indicated by red horizontal arrow. (c) Height histogram of AF micrograph shown in Figure 7-10(a). (d) Line profile of AF micrograph shown in Figure 7-10(a) as indicated by gray horizontal arrow.

Next, we consider the evolution of surface roughness. Again, from a fit to the *in situ* real-time x-ray scattering data, we obtain the layer occupancies directly, and the roughness can be calculated rather easily. To compare directly to the data from AFM, we convert the AFM roughness from nm into ML using the height of the ML as determined from the histogram of heights (*cf.* Figures 7-9(c) and 7-10(c)). We note that both techniques are susceptible to inaccuracies: the roughness from *in situ* x-ray scattering depends on the accuracy of the model, but nevertheless does represent a real time result; whereas the results from *ex situ* AFM may be compromised by post-deposition reorganization of the thin film **[54]**. In Figure 7-9(d) we plot the RMS surface roughness of thin films of PTCDI-C_{13} deposited on HMDS as a function of total coverage as predicted by the fit to the x-ray data (smooth line) for the conditions used to deposit the films displayed in Figures 7-9(a) and 7-10(a). For comparison we also plot the values obtained from the *ex situ* AFM. For the 4.1 ML coverage film, we include the AFM roughness for both with and without the protrusions. Also shown by the (blue) dashed line is the maximum roughness expected for the case of perfect LbL growth, which would occur at coverages of n + ½ MLs. Although we present only two points from the AFM results, the agreement between the two methods is nevertheless excellent, reinforcing the result from x-ray scattering that strongly suggests sustained LbL growth for PTCDI-C_{13} for these conditions for at least the first 4 MLs, before significant roughening commences. In contrast, for this coverage regime (~ 4 ML), thin films of pentacene, DIP and PFP deposited on HMDS-terminated SiO_2 at comparable conditions (T_s = 40 °C and E_i ~ 3-5 eV) are

significantly rougher, where RMS values of ~ 1.3, 1.1 and 1.3 ML are observed, respectively (*cf.* ~ 0.6 ML for PTCDI-C_{13}).

In Figure 7-11, we consider results for growth on all three of the SAMs examined here. In all cases the incident kinetic energy and substrate temperature were the same during growth (E_i = 6.3 eV and T_s = 40 °C). The growth rates in each case were within 15% of each other, namely: 0.017, 0.017 and 0.015 ML-s^{-1} for the deposition of PTCDI-C_{13} on HMDS, NMTS and PHTS, respectively. We see from these data that the growth of the roughness on all three surfaces is relatively slow over the range of coverages considered in Figure 7-11. In comparing the three surfaces we see that growth on HMDS and NMTS is similar, whereas the buildup of roughness on PHTS is clearly larger than the other two surfaces. The reasons for this greater increase in roughness are not totally clear at this point. First, from the dynamics of adsorption we found that PTCDI-C_{13} interacts differently on HMDS vs. NMTS and PHTS. This grouping, of course, differs from the grouping based on the results shown in Figure 7-11, where NMTS is paired with HMDS, and not PHTS. In terms of conformational flexibility, the PHTS layer may possess the most, due to its C_6 alkyl backbone, which is absent in the other two layers, HMDS and NMTS. If true, this explanation would suggest a connection between underlying layer flexibility and roughening.

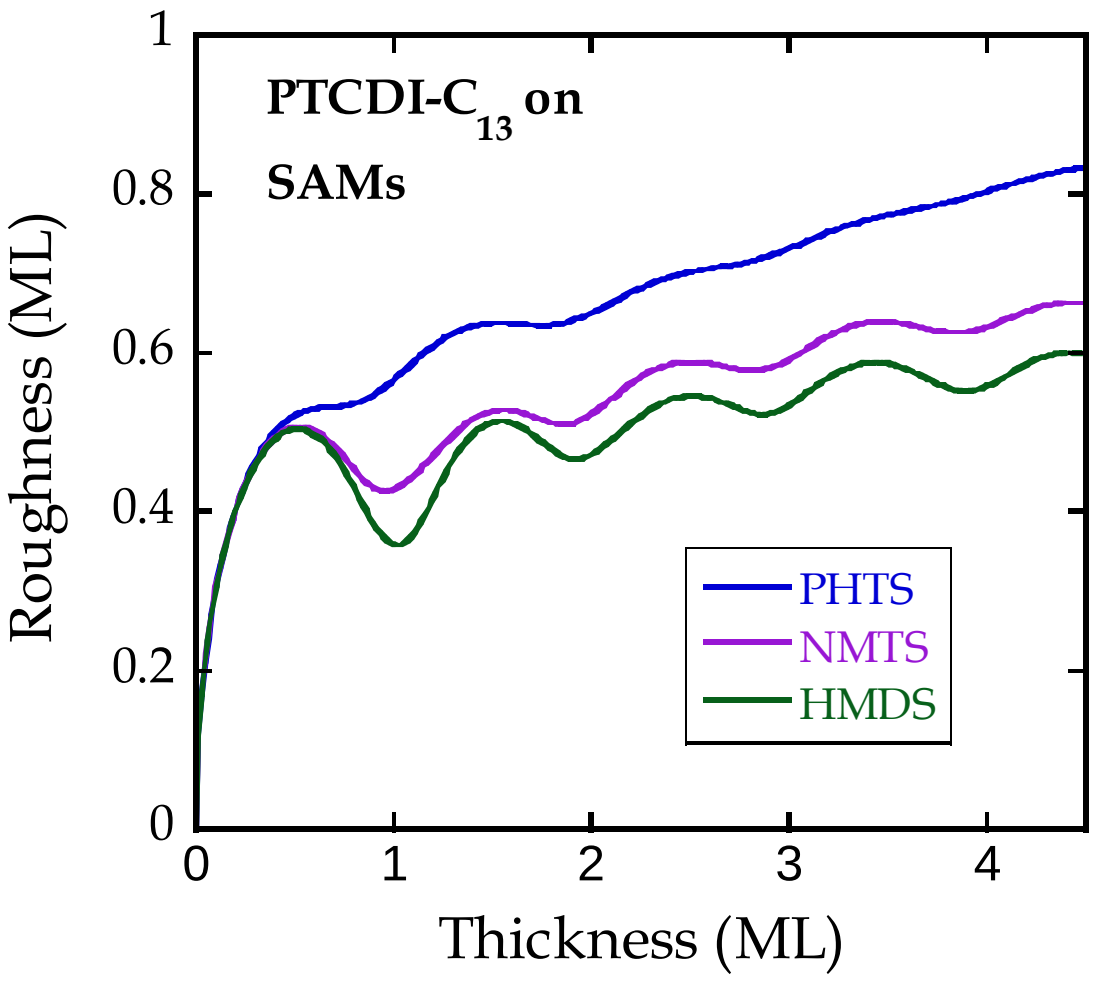

Figure 7-11 Thin film roughness of PTCDI-C_{13} as a function of PTCDI-C_{13} thickness as predicted by the fit to the x-ray data and comparing HMDS, NMTS and PHTS.

E. Submonolayer nucleation dynamics

We have also examined the effects of the growth rate (*GR*) and the nature of the substrate on the submonolayer nucleation dynamics of PTCDI-C_{13}. In Figures 7-12(a-d), we show AF micrographs of submonolayer thin films of PTCDI-C_{13} deposited on NMTS at varying *GR*, keeping all other parameters (E_i = 6.3 eV, T_s = 40 °C) fixed. All four images are 1 × 1 μm^2. The growth rate of PTCDI-C_{13} has been tuned by varying the temperature of the *in situ* evaporator, which affects directly the incident molecular flux. Here the growth rate varied from **(a)** 0.00362 to **(d)** 0.0256 ML-s^{-1}, or a factor of ~ 7. First, we observed single ML-tall high islands for these coverages, and we found no evidence for the dewetting of the PTCDI-C_{13} thin films on NMTS, or on any other surface we examined. Second, the shapes of the islands at all growth rates are similar—compact islands exhibiting no obvious tendency (at this resolution) for facet formation. Third, at this stage of growth, the islands are mostly isolated from each other, such that we can use these images to calculate the maximum island density. By inspection we see that the island density of PTCDI-C_{13} increases from **(a)** to **(d)** as the growth rate also increases.

The scaling of the island density with *GR* can be described by classical nucleation theory in the context of homogeneous nucleation **[55, 56]**. In our case, namely for 2D islands and complete condensation (adsorption is irreversible), the maximum island density, N_{max}, is given by the following expression:

$$N_{max} = \eta(\theta, i^*)(GR/D)^{i^*/(i^*+2)} \exp[E_{i^*}/(i^*+2)k_B T_s], \quad (7\text{-}3)$$

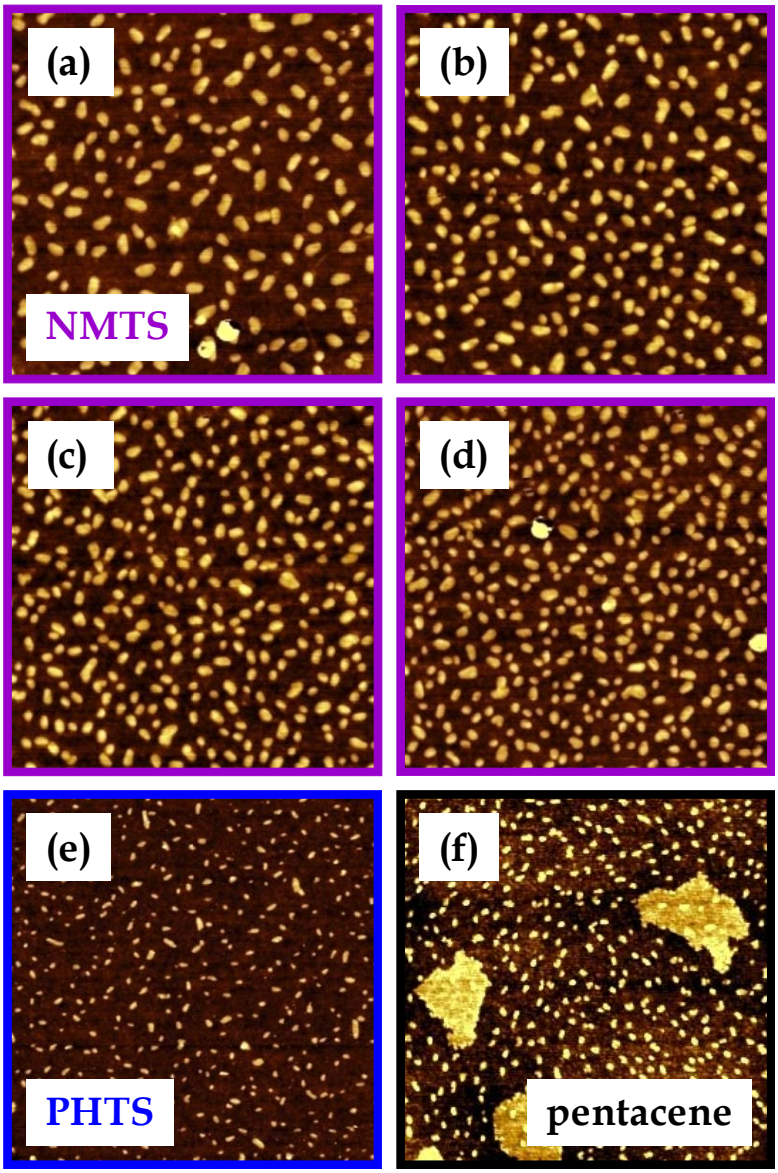

Figure 7-12 Atomic force micrographs, 1 × 1 μm^2, of submonolayer thin films of PTCDI-C_{13} grown on NMTS at rates of (a) 0.00362, (b) 0.00750, (c) 0.0146, and (d) 0.0256 ML-s^{-1}. Atomic force micrographs, 2 × 2 μm^2, of submonolayer thin films of PTCDI-C_{13} grown on (e) PHTS, 0.0190 ML-s^{-1} and (f) near-ML of pentacene, 0.00378 ML-s^{-1}. In all cases incident kinetic energy was E_i = 6.3 eV, and substrate temperature, T_s = 40 °C.

where D is the tracer diffusivity of the molecule, i^* is the critical cluster size, E_{i^*} is the binding energy of the critical cluster and k_B is the Boltzmann constant. The critical cluster size is defined as the largest unstable cluster, such that a cluster with $i^* + 1$ molecules is more likely to grow than to decay. The dimensionless prefactor $\eta(\theta, i^*)$ is nearly a constant—only weakly dependent on i^* and coverage, θ. **[56]** Thus, one straightforward measurement of the critical cluster size is to quantify how the maximum island density varies with GR **[55-57]**, determining the power law relationship using data such as those provided by Figures 7-12(a-d).

In Figure 7-13 we plot the maximum island density vs. the growth rate for PTCDI-C_{13} on NMTS (and other surfaces, *vide infra*). From this log-log representation we see that the data are described well by a power law. We have fit these data to a power law, considering explicitly the uncertainty in each value for the density of the islands ($N^{1/2}$, where N is the direct count of the islands in the image), and we find that $i^* = 1.09 \pm 0.06$. Thus, the meeting of two PTCDI-C_{13} molecules on this surface represents the formation of a stable island.

We have also examined the submonolayer nucleation of PTCDI-C_{13} on two other surfaces: PHTS, and a pre-deposited monolayer of pentacene. Concerning the latter, many device architectures require both *n*- and *p*-type semiconductors, and PTCDI-C_{13} and pentacene would provide such a pair. First, we consider growth on PHTS. In Figure 7-12(e) we display an AF micrograph for PTCDI-C_{13} grown on PHTS for a GR = 0.0190 ML-s^{-1} and conditions (E_i = 6.3 eV, T_s = 40 °C) otherwise identical to those for growth on NMTS. The image here is 2 × 2 μm^2. This growth rate is about midway between that used for growth on NMTS shown in Figures 7-

12(c) and 7-12(d). Again, we observe single monolayer high islands, that are compact and well separated such that their density can be calculated. In Figure 7-13 we plot the island density as a function of growth rate for PTCDI-C_{13} on PHTS. For growth on PHTS we conducted two sets of experiments, using two separate batches of SAMs, and we report both sets of results. The properties of these two SAM layers as deduced by XRR are also given in Table 7-1. From Figure 7-13 we see that there is a difference between the two sets of results, where the island densities are offset by ~ 40% from each other. At a fixed growth rate, the batch that produced a denser SAM resulted in a higher density of PTCDI-C_{13} islands. A fit to each data set to a power law gives values of $i^* = 1.21 \pm 0.28$ and 1.64 ± 0.44. One of these values is easily within the uncertainties of $i^* = 1$, which was implicated for growth on NMTS.

For a third example of submonolayer nucleation we examined the growth of PTCDI-C_{13} on a pre-deposited monolayer of pentacene. A representative image is shown in Figure 7-12(f). The image here is 2×2 μm^2. In this case the growth rate of PTCDI-C_{13} was 0.00378 ML-s^{-1}, and the conditions (E_i = 6.3 eV, T_s = 40 °C) were otherwise identical to those used for growth on NMTS and PHTS. The pentacene thin film was deposited *in situ* employing a separate thermal effusive source (mounted to the deposition chamber) immediately prior to the deposition of the PTCDI-C_{13}. The growth rate of the pentacene film was ~ 0.0057-0.0084 ML-s^{-1} as judged by the intensity oscillations observed in real-time with synchrotron x-rays (e.g., similar to those shown in Figures 7-4 to 7-6). As indicated by the large 2nd layer islands, the coverage of pentacene was slightly above 1 ML. We see that PTCDI-C_{13} also forms single monolayer high islands on this surface, which are compact and well separated

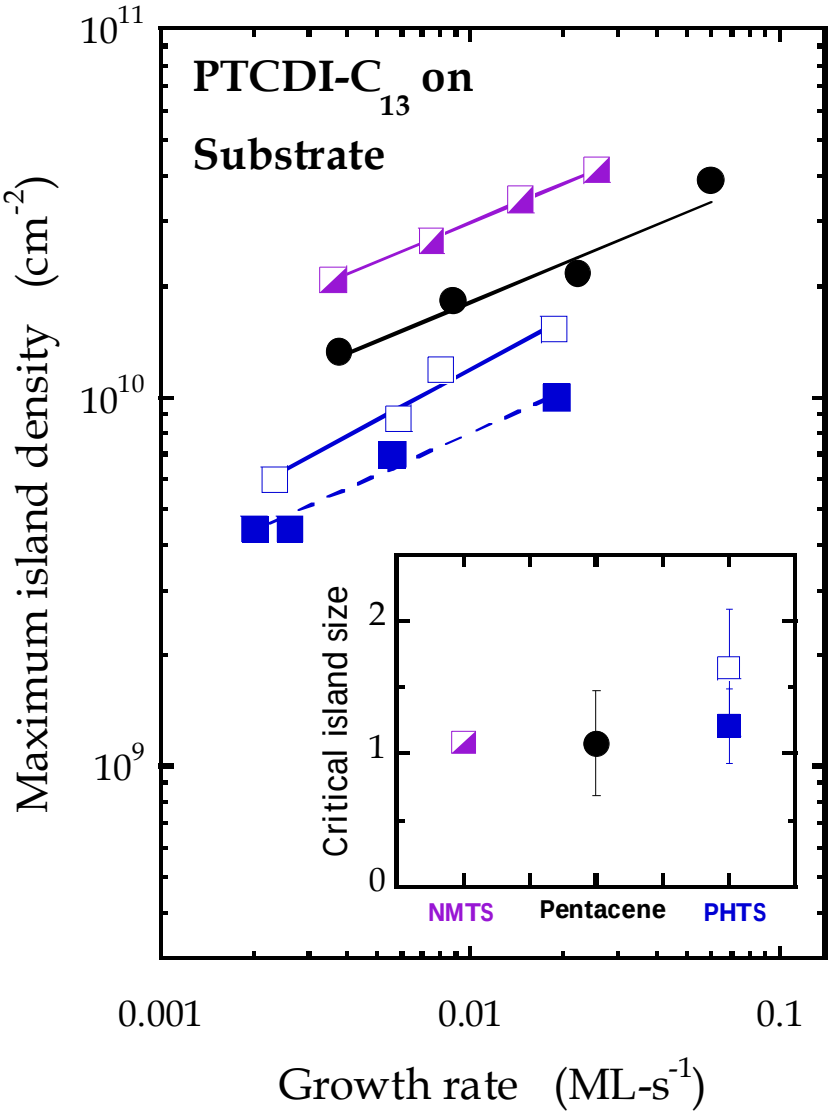

Figure 7-13 Maximum island density as a function of submonolayer growth rate for the deposition of PTCDI-C_{13} on NMTS, PHTS and a near-ML of pentacene. In all cases incident kinetic energy was E_i = 6.3 eV, and substrate temperature, T_s = 40 °C. The straight lines represent a fit to a power law. The inset shows the critical island size, i^*, as a function of surface termination. The data for PHTS represent two batches of this SAM, identified in Table 7-1, where batch (a) is the open symbols; batch (b) is the closed symbols.

such that their density can be calculated. We note that islands form on both the 1st and 2nd layers of pentacene, and their density is not significantly different in those two areas. In Figure 7-13 we plot the PTCDI-C_{13} island density vs. growth rate for deposition on the pentacene monolayer. As may be seen, the data in this case are also described well by a power law, and a fit to the data gives $i^* = 1.08 \pm 0.39$.

Summarizing all of the results for the submonolayer nucleation of PTCDI-C_{13} on the 3 surfaces investigated here, we find that the maximum island density increases with increasing *GR* on all 3 surfaces, and the data are described very well by a power law in all cases. This would seem to argue against any interpretation involving defects in the SAMs playing a significant or dominant role in the nucleation. Thus it seems that regardless of the nature of the underlying surface layer (SAM or organic thin film), PTCDI-C_{13} exhibits homogeneous nucleation on all surfaces. Furthermore the critical nucleus is similar, if not identical, in all cases. A simple average of the values for the critical nucleus gives a value of $i^* = 1.26 \pm 0.16$ (excluding the one result for PHTS gives $i^* = 1.13 \pm 0.12$). We are tempted to conclude that all of the data represent the same critical nucleus, i.e., $i^* = 1$. In any event, the size of the critical nucleus in these cases is not significantly perturbed by the nature of the underlying substrate.

Unlike the slopes of the curves shown in Figure 7-13, at a comparable growth rate the maximum island density of PTCDI-C_{13} varies moderately depending on the nature of the substrate. In particular, the maximum island density of PTCDI-C_{13} is greatest on NMTS, followed by pentacene and PHTS. Because $N_{max} \propto (GR/D)^{i^*/(i^*+2)}$, and since we observed essentially the same value for i^* on all surfaces, this suggests

that the diffusivity, D, of PTCDI-C_{13} differs on the surfaces, and therefore is mostly responsible for the offsets **[50]**. The relative diffusivity of PTCDI-C_{13} can be estimated by taking the ratio of N_{max} on any two surfaces at a constant GR (0.005 ML-s^{-1}) and using the relationship, $D_2 = D_1\{(N_{x,1}/N_{x,2})^{[(i^*+2)/i^*]}\}$. If we let $D_1 = D_{NMTS} = 1$ and assume $i^* = 1.26$ (*vide supra*), then by implication, $D_{Pent} = 3.6$ and $D_{PHTS} = 13\text{-}32$. This analysis suggests that the diffusivity of PTCDI-C_{13} varies moderately depending on chemical and structural nature of the underlying substrate.

Is there precedent for such behavior, namely, no apparent change in the size of the critical nucleus, while simultaneously there is implicated a large change in the diffusivity? The answer is, yes. For example, in early work differences were found in island densities depending on surface termination—in particular, concerning growth of pentacene on SiO_2 vs. Si(100) surfaces terminated with H **[58]**, or cyclohexene **[59]**. Similar observations have also been made for the submonolayer growth of pentacene on polymeric substrates. Here it was found that the critical cluster size for pentacene was independent of the underlying polymeric dielectric, but the absolute island density varied considerably with the nature of the underlying polymeric surface **[60, 61]**. Another example is provided by our recent work examining the submonolayer growth of perfluoropentacene (PFP) on a variety of SAMs, similar to the kind of system we examine here **[50]**. For PFP we found a single value of $i^* \sim 2.7$ could describe all the data, whereas at a fixed growth rate the island density varied by as much as a factor of 15, and the implicated diffusivities by a factor of ~ 120. In comparison, here the densities for PTCDI-C_{13} vary by as much as a factor of 4, whereas the diffusivities vary by as much as a factor of ~ 30.

Viewed as a whole both sets of studies point to this being a behavior that can be expected to be common in these systems—small molecule organics on self-assembled monolayers (or other organics). Why might this be? First, many of the small molecule organics that have been examined tend to crystallize in a way such that they "stand up" on the substrate on which they are grown. A reason for this is that the molecule-molecule interaction is often stronger that the molecule-SAM interaction. Since the molecule-molecule interaction obviously has the greatest impact on the size of the critical nucleus, one can understand how the value of i^* has little or no dependence on the identity of the underlying substrate in these systems. The tracer diffusivity, on the other hand, is in effect determined entirely by the molecule-SAM interaction. Thus, the change in island density with surface termination is easily understood as reflecting changes in this molecule-SAM interaction.

7.5 Conclusions

We have examined the effects of self-assembled monolayers on the adsorption dynamics and the thin film growth, both multilayer and submonolayer, of *N,N'*-ditridecylperlyene-3,4,9,10-tetracarboxylic diimide, or PTCDI-C_{13}, a *n*-type organic semiconductor. Regarding the mode of growth , PTCDI-C_{13} exhibits prolonged layer-by-layer (LbL) growth on all three SAMs examined here, namely NMTS, PHTS and HMDS, up to coverages of at least ~ 10 MLs, with well-ordered lamellar thin films. This picture of smooth, ideal LbL growth is somewhat distorted by the appearance of a small density of tall protrusions at a total coverage of ~ 4 ML. Thin film growth is the smoothest on the surfaces terminated with NMTS and HMDS. Regarding the

dynamics of adsorption, here we have examined the kinetics of the first few monolayers of growth as a function of the incident kinetic energy, as reflected by the probability of adsorption on the starting surfaces, and on the growing thin film. For growth on HMDS, NMTS and PHTS the probability of adsorption on the starting surface decreases significantly with increasing incident kinetic energy, with the decrease being the strongest on the HMDS surface. This is consistent with conventional trapping-mediated adsorption, where a sufficient fraction of the incident kinetic energy must be transferred to the substrate surface. Once these surfaces are covered by the growing PTCDI-C_{13} film, we also observe trapping mediated adsorption, with the probability decreasing with increasing incident energy. In this regime, however, there is no "memory" of the starting substrate, and the trapping probability is independent of the starting surface. Comparing the probabilities of adsorption for the submonolayer and the multilayer regime we observe that the adsorption of PTCDI-C_{13} is equally efficient on NMTS and PHTS as it is on itself, but significantly more efficient on itself as compared to on HMDS. Efficient trapping of PTCDI-C_{13} on NMTS, PHTS and on itself is probably due to efficient momentum transfer due to better mass-matching and direct molecular insertion events. Binding energy effects, and certainly the thinness of the layer that precludes insertion events, contribute to the relative inefficiency of the HMDS layer to trap PTCDI-C_{13}. Regarding nucleation in the submonolayer regime, on all three surfaces examined, namely NMTS, PHTS, and a pre-deposited monolayer of pentacene, we observed homogenous nucleation where the island density scaled with the growth rate via a power law. Analysis of this data revealed that nucleation on all surfaces can be

explained by a critical cluster size of $i^* \sim 1$, where two PTCDI-C_{13} molecules constitute a stable island. While the critical nucleus was independent of the starting surface, the density of islands at a fixed growth rate, and by implication the diffusivity, did depend on surface termination. We have observed this behavior in the submonolayer regime for other small molecule organic thin films grown on SAMs, which suggests that this may be a general phenomenon.

7.6 References

1. Hamers, R. J.; *Nature* **2001**, *412*, 489-490.
2. Dimitrakopoulos, C. D.; Malenfant, P. R. L. *Adv. Mater.* **2002**, *14*, 99-117.
3. Lin, Y. Y.; Gundlach, D. J.; Nelson, S. F.; Jackson, T. N. *IEEE Electron Device Letters* **1997**, *18*, 606-608.
4. Kelley, T. W.; Boardman, L. D.; Dunbar, T. D.; Muyres, D. V.; Pellerite, M. J.; Smith, T. P. *J. Phys. Chem. B* **2003**, *107*, 5877-5881.
5. Yang, H.; Shin, T. J.; Ling, M. M.; Cho, K.; Ryu, C. Y.; Bao, Z. *J. Am. Chem. Soc.* **2005**, *127*, 11542-11543.
6. Virkar, A.; Mannsfield, S.; Oh, J. H.; Toney, M. F.; Tan, Y. H.; Liu, G.; Scott, J. C.; Miller, R.; Bao, Z. *Adv. Funct. Mater.* **2009**, *19*, 1962-1970.
7. Shtein, M.; Mapel, J.; Benziger, J. B.; Forrest, S. R. *Appl. Phys. Lett.* **2002**, *81*, 268-270.
8. Klauk, H.; Halik, M.; Zschieschang, U.; Schmid, G.; Radlik, W.; Weber, W. *J. Appl. Phys.* **2002**, *92*, 5259-5263.
9. Puigdollers, J.; Pirriera, M. D.; Marsal, A.; Orpella, A.; Cheylan, S.; Voz, C.; Alcubilla, R. *Thin Solid Films* **2009**, *517*, 6271-6274.
10. Vasseur, K.; Cedric, R.; Stijn, V.; Temst, K.; Froyen, L.; Heremans, P. *J. Phys. Chem. C.* **2010**, *114*, 2730-2737.
11. Tatemichi, S.; Ichikawa, M.; Koyama, T.; Taniguchi, Y. *Appl. Phys. Lett.* **2006**, *89*, 112108/1-112108/3.
12. Jang, J.; Nam, S.; Chung, D. S.; Kim, S. H.; Yun, W. M.; Park, C. E. *Adv. Func. Mat.* **2010**, *20*, 2611-2618.

13. Narayanan Unni, K. N.; Pandey, A. K.; Nunzi, J-M. *Chem. Phys. Lett.* **2005**, *407*, 95-99.

14. Hong, K.; Kim, S. H.; Yang, C.; Jang, J.; Cha, H.; Park, C. E. *Appl. Phys. Lett.* **2010**, *97*, 103304/1-103304/3.

15. Rolin, C.; Vasseur, K.; Schols, S.; Jouk, M.; Duhoux, G.; Muller, J.; Genoe, J.; Heremans, P. *Appl. Phys. Lett.* **2008**, *93*, 033305/1-033305/3.

16. Narayanan Unni, K. N.; Pandey, A. K.; Alem, S.; Nunzi, J-M. *Chem. Phys. Lett.* **2006**, *421*, 554-557.

17. Walser, M. P.; Kalb, W. L.; Mathis, T.; Batlogg, B. *Appl. Phys. Lett.* **2009**, *95*, 233301/1-233301/3.

18. Tatemichi, S.; Ichikawa, M.; Kato, S.; Koyama, T.; Taniguchi, Y. *Phys. Stat. Sol.* **2008**, *2*, 47-49.

19. Briseno, A. L.; Mannsfeld, S. C. B.; Reese, C., Hancock, J. M.; Xiong, Y.; Jenekhe, S. A.; Bao, Z.; Xia, Y. *Nano Lett.* **2007**, *7*, 2847-2853.

20. Pandey, A. K.; Unni, K. N. N.; Nunzi, J-M. *Thin Solid Films* **2006**, *511/512*, 529-532.

21. Pandey, A. K.; Dabos-Seignon, S.; Nunzi, J-M. *Appl. Phys. Lett.* **2006**, *89*, 113506/1-113506/3.

22. Killampalli, A. S.; Schroeder, T. W.; Engstrom, J. R. *Appl. Phys. Lett.* **2005**, *87*, 033110/1-033110/3.

23. Schroeder, T. W. *Cornell University: Ph.D. Thesis* **2004**.

24. Hong, S.; Amassian, A.; Woll, A. R.; Bhargava, S.; Ferguson, J. D.; Malliaras, G. G.; Brock, J. D.; Engstrom, J. R. *Appl. Phys. Lett.* **2008**, *92*, 253304.

25. Amassian, A.; Desai, T. V.; Kowarik, S.; Hong, S.; Woll, A. R.; Malliaras, G. G.; Schreiber, F.; Engstrom, J. R. *J. Chem. Phys.* **2009**, *130*, 124701/1-124701/9.

26. Desai, T.; Hong, S.; Woll, A. R.; Hughes, K. J.; Ananth, P.; Clancy, P.; Engstrom, J. R. *Journal of Chemical Physics* **2011**, *134*, 224702.

27. Chen, R.; Kim, H.; McIntyre, P. C.; Bent, S. F. *Chem. Mater.* **2005**, *17*, 536.

28. Kaelble, D. H. *J. Appl. Polym. Sci.* **1974**, *18*, 1869-1889.

29. Northrup, J. E.; Tiago, M. L.; Louie, S. G. *Phys Rev. B* **2002**, *66*, 121404/1-121404/4.

30. Nabok, D.; Puschnig, P.; Ambrosch-Draxl, C. *Phys. Rev. B* **2008**, *77*, 245316/1-245316/4.

31. Braun, C. *Parratt32 program*; Berlin Neutron Scattering Center (BENSC): Hahn-Meitner Institut, 1997.

32. Parratt, L. G. *Phys. Rev. B.* **1954**, *95*, 359.

33. Kowarik, S.; Gerlach, A.; Skoda, M.; Sellner, S.; Schreiber, F. *Eur. Phys. J. Special Topics* **2009**, *168*, 11.

34. Woll, A. R.; Desai, T. V.; Engstrom J. R. *under review at J. Phys. Rev. B*.

35. Cohen, P. I.; Petrich, G. S.; Pukite, P. R.; Whaley, G. J.; Arrott, A. S. *Surface Sci.* **1989**, *216*, 222-248.

36. Cohen, S. R.; Naaman, R.; Sagiv, J. *Phys. Rev. Lett.* **1987**, *58*, 1208

37. Day, B. S.; Shuler, S. F.; Dcure, A.; Morris, J. R. *J. Chem. Phys.* **2003**, *119*, 8084

38. Bennett, M. E.; Alexander, W. A.; Lu, J. W.; Troya, D.; Morris, J. R. *J. Phys. Chem. C* **2008**, *112*, 17272

39. Ferguson, M. K.; Lohr, J. R.; Day B. S.; Morris, J. R. *Phys. Rev. Lett.* **2004**, *92*, 073201

40. Shuler, S. F.; Davis, G. W.; Morris, J. R. *J. Phys. Chem.* **2002**, *116*, 9147

41. Day, B. S.; Morris, J. R. *J. Chem. Phys.* **2005**, *122*, 234714.

42. Day, B. S.; Morris, J. R. *J. Phys. Chem. B* **2003**, *107*, 7120.

43. S. R. Wasserman, G. M. Whitesides, I. M. Tidswell, B. M. Ocko, P. S. Pershan, and J. D. Axe, J. Amer. Chem. Soc. **111**, 5852 (1989).

44. Janssen, D.; De Palma, R.; Verlaak, S.; Heremans, **P.; D**ehaen, W. *Thin Solid Films* **2006**, *515*, 1433-1438.

45. Liu, Z.; Bol, A. A.; Haensch, W. *Nano Lett.* **2011***, 11*, 523-528

46. Yam, C. M.; Samuel, S. Y.; Kakkar, A. K.; *Langmuir* **1998**, *14*, 6941-6947.

47. Patrone, L.; Gadenne, V.; Desbief, S. *Langmuir* 2010, *26*, 17111-17118.

48. Mayer, A. C.; Ruiz, R.; Headrick, R. L.; Kazimirov, A.; Malliaras, G. G. *Organic Electronics* **2004**, *5*, 257.

49. Kowarik, S.; Gerlach, A.; Hinderhofer, A.; Milita, S.; Borgatti, F.; Zontone, F.; Suzuki, T.; Biscarini, F.; Schreiber, F. *Phys. Stat. Sol.* **2008**, *2*, 120-122.

50. Desai, T. V.; Woll, A. R.; Schreiber, F.; Engstrom, J. R. *J. Phys. Chem. C.* **2010**, *114*, 20120.

51. Goose, J. E.; Killampalli, A. S.; Clancy, P.; Engstrom, J. R. *J. Phys. Chem C.* **2009**, *113*, 6068-6073.

52. Killampalli, A. S.; Engstrom, J. R. *Appl. Phys. Lett.* **2006**, *88*, 143125.

53. Isa, N.; Gibson, K. D.; Yan, T.; Hase, W.; Sibener, S. J. *J. Chem. Phys.* **2004**, *120*, 2417.

54. Amassian, A.; Pozdin, V.; Desai, T. V.; Hong, S.; Woll, A. R.; Ferguson, J. D.; Brock, J. D.; Malliaras, G. G.; Engstrom, J. R. *J. Mater. Chem.* **2009**, *19*, 5580-5592.

55. Venables, J. A. *Phys. Rev. B* **1987**, *36*, 4153-4162.

56. Venables, J. A.; Spiller, G. D. T.; Hanbücken, M. *Rep. Prog. Phys.* **1984**, *47*, 399-459.

57. Brune, H. *Surf. Sci. Rep.* **1998**, *31*, 121-229.

58. Ruiz, R.; Nickel, B.; Koch, N.; Feldman, L.C.; Haglund, R. F.; Kahn, A.; Scoles, G. *Phys. Rev. B* **2003**, *67*, 125406/1-125406/7.

59. Meyer zu Heringdorf, F.-J.; Reuter, M. C.; Tromp, R. M. *Appl. Phys. A: Mater. Sci. Process.* **2004**, *78*, 787-791.

60. Stadlober, B.; Haas, U.; Maresch, H.; Haase, A. *Phys. Rev. B* **2006**, *74*, 165302/1-165302/9.

61. Ribic, P. R.; Kalihari, V.; Frisbie, C. D.; Bratina, G. *Phys. Rev. B* **2009**, *80*, 115307/1-115307/8.

8. Summary

This thesis discussed the thin film deposition of small molecule organic semiconductors. Small molecule organics are attracting significant interest primarily due to their ability to form well ordered thin films at low temperatures with reasonable electronic properties. Potential applications of organic based electronics include thin film transistors, display technologies, flexible integrated circuits and photovoltaics. The growth and morphology of these organic thin films is very sensitive to the nature (chemical and physical) of the underlying dielectric. A significant challenge in fabricating organic thin film devices with superior electrical characteristics is that of controlling, and more importantly, understanding the properties at the interface between the organic semiconducting layer and the underlying substrate. In this thesis, the use of supersonic molecular beams as a means to deposit organic thin films is discussed in conjunction with *in situ* real-time synchrotron scattering and *ex situ* atomic force microscopy as thin film characterization techniques. This thesis discussed the effects of the incident kinetic energy of the small molecule organic and the nature of dielectric (clean silicon dioxide, SiO_2; or SiO_2 modified with SAMs of varying thickness and chemical functionality; or SiO_2 modified with polymers of varying surface energy) on the fundamental thin film processes occurring at the organic semiconductor/substrate interface. The results indicate that the incident kinetic energy and the nature of the dielectric have significant effects on these fundamental thin film processes including adsorption, nucleation and diffusion, and the filling up of individual monolayers during thin film growth. The following will briefly summarize the observations made.

Chapter three examined the initial stages of growth of DIP on surfaces terminated with SAMs where the effects of the thickness of the SAM, and less so, the chemical composition of the terminating layer were considered explicitly. For growth on bare SiO_2, and SiO_2 modified by both HMDS and FOTS, the probability of adsorption of DIP on the starting surface decreases significantly with increasing incident kinetic energy. This is consistent with conventional trapping-mediated adsorption, where a sufficient fraction of the incident kinetic energy must be transferred to the substrate surface. On these same surfaces, once the substrate is covered by the growing DIP thin film, the adsorption probability increases significantly. This increase in the adsorption probability reflects more efficient energy exchange between the incident DIP, and the DIP present in the growing thin film, due to better mass-matching, and the possible contributions of direct molecular insertion into the DIP layer. Concerning adsorption on OTS and ODTS, we find efficient trapping both on the starting surfaces, and on the DIP thin film in these two cases. These results suggest that there are energy dissipation channels that contribute significantly on the OTS- and ODTS- terminated surfaces, either not present on the surfaces terminated by the shorter SAM produced by HMDS, or that contribute less on the fluorinated SAM, FOTS. Experimental data suggest that molecular insertion can play a role in more efficient energy transfer on the OTS- and ODTS- terminated surfaces, while it clearly will have a much reduced role on the much thinner HMDS-terminated layer on SiO_2. Results from molecular simulation bear out these interpretations in the case of OTS and ODTS, and back the conclusion that molecular insertion is significant on these surfaces.

Chapter four investigated the effect of substrate temperature (T_s), incident energy (E_i), and chemical nature of a SAM on the growth and morphology of DIP thin films. Concerning substrate temperature, T_s, the results indicated that increasing T_s leads to smoother films with larger in-plane features/grains on both clean SiO_2 and HMDS modified SiO_2. Smoother films are probably a result of enhanced interlayer transport at higher T_s, and larger in-plane feature/grain sizes are probably due to enhanced surface diffusivity of DIP at higher T_s. Varying the incident energy, E_i, does not have a significant impact on DIP morphology on both clean SiO_2 and HMDS at all T_s investigated. Concerning growth on SAMs (at constant T_s = 40 °C), the results showed that DIP grows similarly on all surfaces except on ODTS-terminated SiO_2, where it grows the roughest, especially at the early stages of film growth. Rougher films on ODTS are probably due to enhanced "upward" interlayer transport, perhaps facilitated by the flexibility of the ODTS layer. The chemical nature of the surface also significantly affects the in-plane feature/grain size. At identical deposition conditions, the largest features are formed on FOTS, intermediate sized features on HMDS and OTS and smallest sized features on ODTS and SiO_2. Incident energy, E_i, does not affect the in-plane feature/grain size on any of the surfaces investigated. Viewing the results as a whole, chapter four investigated the effect of three process parameters, namely T_s, E_i and chemical nature of SAM, on the DIP thin film growth and morphology. Of these process parameters, our results indicate that E_i has the least effect on DIP thin film growth and morphology whereas T_s and chemical nature of SAM have the greatest.

Chapter five examined the effects of polymeric dielectrics on the thin film growth of pentacene. Chapter five also compared the results to pentacene growth on clean SiO_2. From *in situ* real-time x-ray scattering, the results indicate that pentacene exhibits layer-by-layer (LbL) growth on all surfaces (polymers and clean SiO_2) investigated, but the extent of LbL growth is a strong function of the underlying substrate. In particular, LbL growth is significantly more prolonged on PEI, (up to ~6 MLs), followed by SiO_2 and PMMA (up to ~4 MLs) and finally PS (up to ~ 3 MLs). The extent of LbL growth and therefore the final thin film roughness follows a trend with the surface energy of the underlying substrate – pentacene thin film growth is more LbL-like and smoother as the surface energy of the underlying substrate increases.

Chapter six examined the nucleation and growth of PFP on a series of surfaces represented by differing chemical terminations and surface energies. PFP was chosen because of its low intrinsic surface energy and PFP is not expected to dewet or reorganize on low energy surfaces – this enabled the study of the effect of SAMs on the nucleation and growth of a crystalline organic thin film, which is otherwise very problematic to examine. On all surfaces examined, PFP forms single molecule-high islands in the submonolayer regime, which are stable in density, shape and size with extended aging. Furthermore, PFP exhibits the characteristics of homogeneous nucleation on all the surfaces examined. The results indicate that the chemical structure of the SAM significantly affects the nucleation density of PFP under otherwise identical conditions of growth. In particular, the density of islands on FOTS (the lowest surface energy SAM examined) exceeded that on MAOPTS (the highest

surface energy SAM examined) by over an order of magnitude. At the same time, the size of the critical nucleus indicated by the change in island density with growth rate showed no dependence on surface termination, and a value of $i^* \sim 2$-3 could describe all data. The results indicate that the change in island density is due to a change in the diffusivity of PFP admolecules on these surfaces by as much as 2 orders of magnitude. The chemical structure of the SAM also significantly affects the shapes of the islands of PFP formed in the submonolayer regime. Interestingly, the islands are most compact and facetted on those surfaces where diffusion of isolated PFP admolecules is indicated to be the slowest. The experimental observations suggest that the molecular motions and intermolecular interactions describing the diffusion of isolated admolecules are quite different from those concerning molecules moving on the periphery of a growing island. Finally, once the substrate surface is covered, the growth becomes 3-dimensional on all surfaces, and a rough multilayer morphology is observed.

Finally, chapter seven examined the effects of SAMs on the adsorption dynamics and the thin film growth, both multilayer and submonolayer, of PTCDI-C_{13}. Regarding the mode of growth, PTCDI-C_{13} exhibits prolonged layer-by-layer (LbL) growth on all three SAMs examined namely NMTS, PHTS and HMDS, up to coverages of at least ~ 10 MLs, with well-ordered lamellar thin films. Regarding the dynamics of adsorption, chapter seven examined the kinetics of the first few monolayers of growth as a function of the incident kinetic energy, as reflected by the probability of adsorption on the starting surfaces, and on the growing thin film. For growth on HMDS, NMTS and PHTS the probability of adsorption on the starting

surface decreases significantly with increasing incident kinetic energy, with the decrease being the strongest on the HMDS surface. This is consistent with conventional trapping-mediated adsorption, where a sufficient fraction of the incident kinetic energy must be transferred to the substrate surface. Once these surfaces are covered by the growing PTCDI-C_{13} film, trapping-mediated adsorption is also observed, with the adsorption probability decreasing with increasing incident energy. In this regime, however, there is no "memory" of the starting substrate, and the trapping probability is independent of the starting surface. Comparing the probabilities of adsorption for the submonolayer and the multilayer regime, we observe that the adsorption of PTCDI-C_{13} is equally efficient on NMTS and PHTS as it is on itself, but significantly more efficient on itself as compared to on HMDS. Efficient trapping of PTCDI-C_{13} on NMTS, PHTS and on itself is probably due to efficient momentum transfer due to better mass-matching and direct molecular insertion events. Binding energy effects, and certainly the thinness of the layer that precludes insertion events, contribute to the relative inefficiency of the HMDS layer to trap PTCDI-C_{13}. Regarding nucleation in the submonolayer regime on NMTS, PHTS, and a pre-deposited monolayer of pentacene, we observed homogenous nucleation where the island density scaled with the growth rate via a power law. Analysis of this data revealed that nucleation on all surfaces can be explained by a critical cluster size of $i^* \sim 1$, where two PTCDI-C_{13} molecules constitute a stable island. While the critical nucleus was independent of the starting surface, the density of islands at a fixed growth rate, and by implication the diffusivity, did depend moderately on surface termination.

9. Appendices

9.1 Temperature calibration

The substrates in the G-Line deposition chamber were heated using a Thermionics power supply (model 7ds-800-1) with an in-built Eurotherm (model 2204e). Shown in Figure 9-1 are temperature calibration curves relating the temperature at the surface of the sample with respect to the temperature registered by a thermocouple mounted at the back of the PBN sample heater (T_{ref}). The Si sample size used for temperature calibration was ~ 1.5 cm × 2 cm. The surface temperature was measured using two different ways: *(1)* the sample was mounted on the Mo solid back platen substrate holder provided with a transferable thermocouple which was used to measure the temperature at the surface of the sample (T_s). This transferable thermocouple was sandwiched between the sample and a mounting clip – this is the temperature indicator (T_s) that the Eurotherm uses to heat up the sample; *(2)* a separate thermocouple (T_{arm}) attached onto the load-lock transfer arm was brought into to the main chamber and forcibly made contact at the middle of the Si substrate. Pictures of method *(2)* are shown Figure 9-2.

As observed from Figure 9-1, the temperature as measured by T_s is greater than the temperature as measured by T_{arm} – this discrepancy is most likely due to inaccuracies resulting from sandwich between the sample and a mounting clip. The temperature as measured by T_{arm} is the more accurate measurement. The calibration curves shown in Figure 9-1 were employed in controlling sample temperature during experiments involving the deposition of DIP on SiO_2 and HMDS at elevated substrate

temperatures (see section 4). Note that LN2 cooling of the substrate was not employed during experiments at elevated substrate temperatures and during substrate temperature calibration experiments. Also note that, if the transferable thermocouple on the substrate holder is altered in any way, then a recalibration of the surface temperature using the above methods should be repeated.

Thermocouple T_{arm} in Figure 9-1 is fit (solid black line) to a polynomial function:

$$T_{arm} = A + BT_s + CT_s^2 \tag{9-1}$$

where T_{arm} is the temperature of the surface using method *(2)* and T_s is the temperature of the surface using method *(1)*. The best fit to the data for sample temperature yielded the following parameters: A = 8.4678, B = 0.5982 and C = 0.001217.

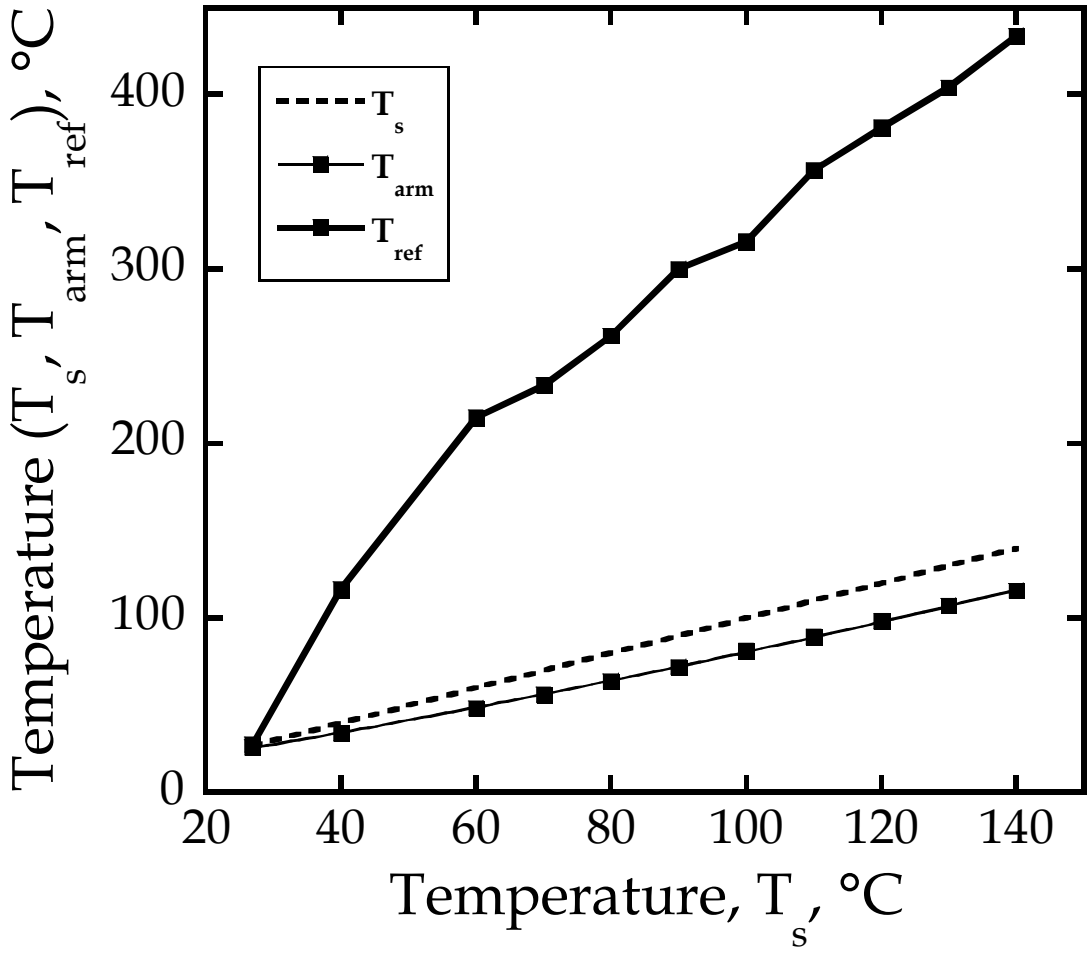

Figure 9-1 Thermocouple temperature of T_s, T_{arm} and T_{ref} versus T_s.

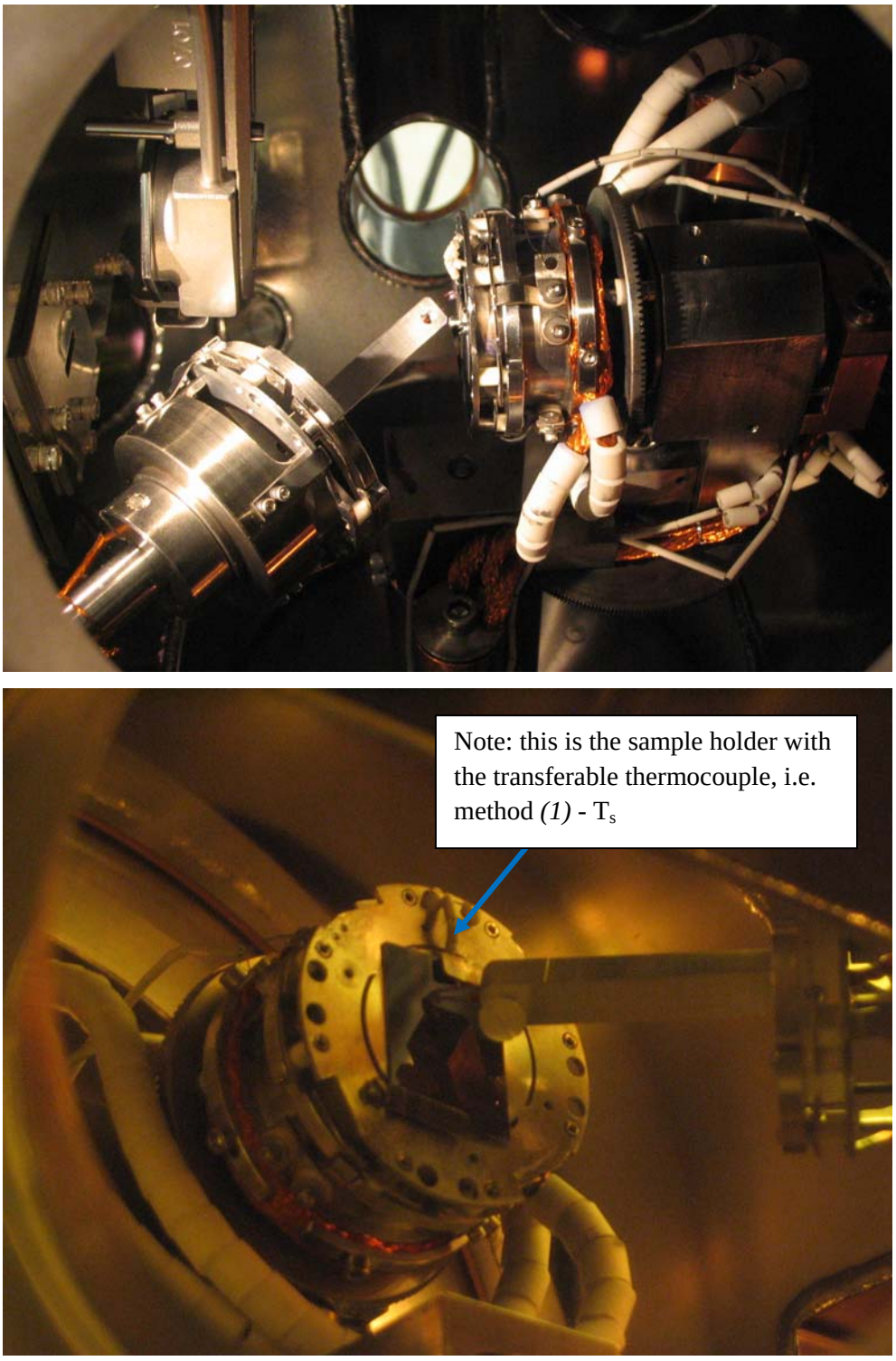

Figure 9-2 Pictures showing method *(2)* to measure surface temperature (T_{arm}).

9.2 Time-of-flight pictures

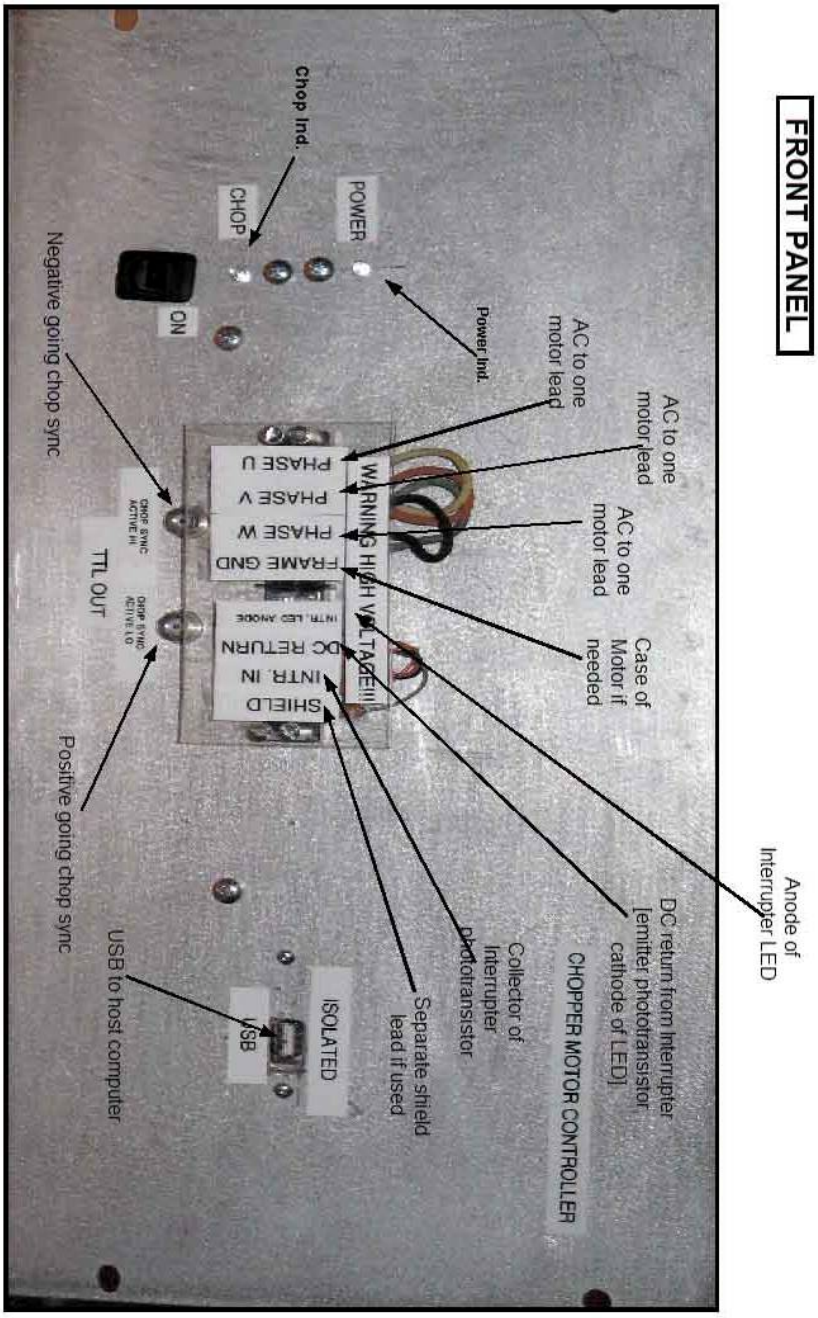

Figure 9-3 Picture showing front panel of chopper-controller.

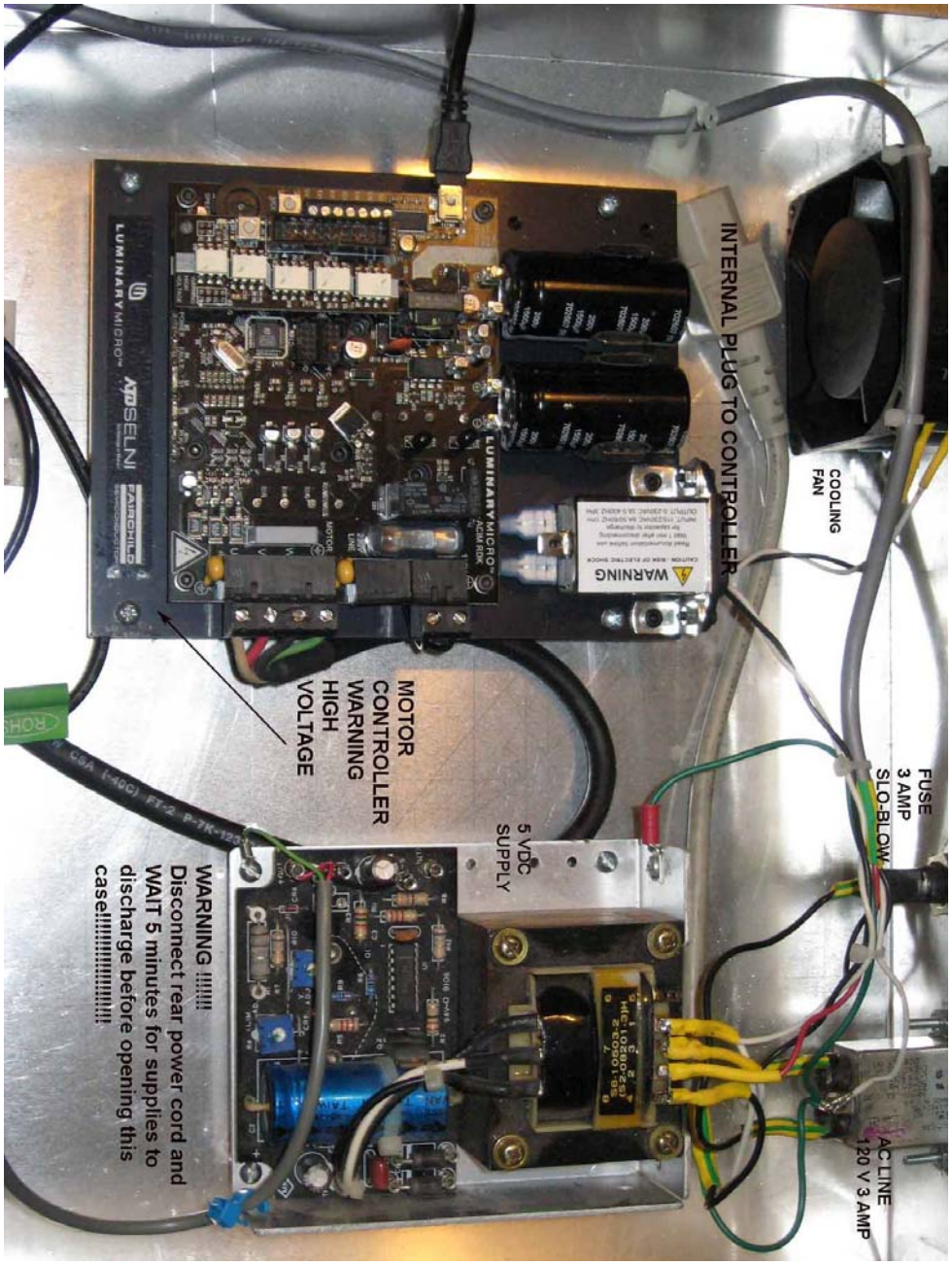
INTERNAL PLUG TO CONTROLLER
COOLING FAN
FUSE 3 AMP SLO-BLOW
AC LINE 120 V 3 AMP
5 VDC SUPPLY
MOTOR CONTROLLER WARNING HIGH VOLTAGE
WARNING !!!!!!!
Disconnect rear power cord and WAIT 5 minutes for supplies to discharge before opening this case!!!!!!

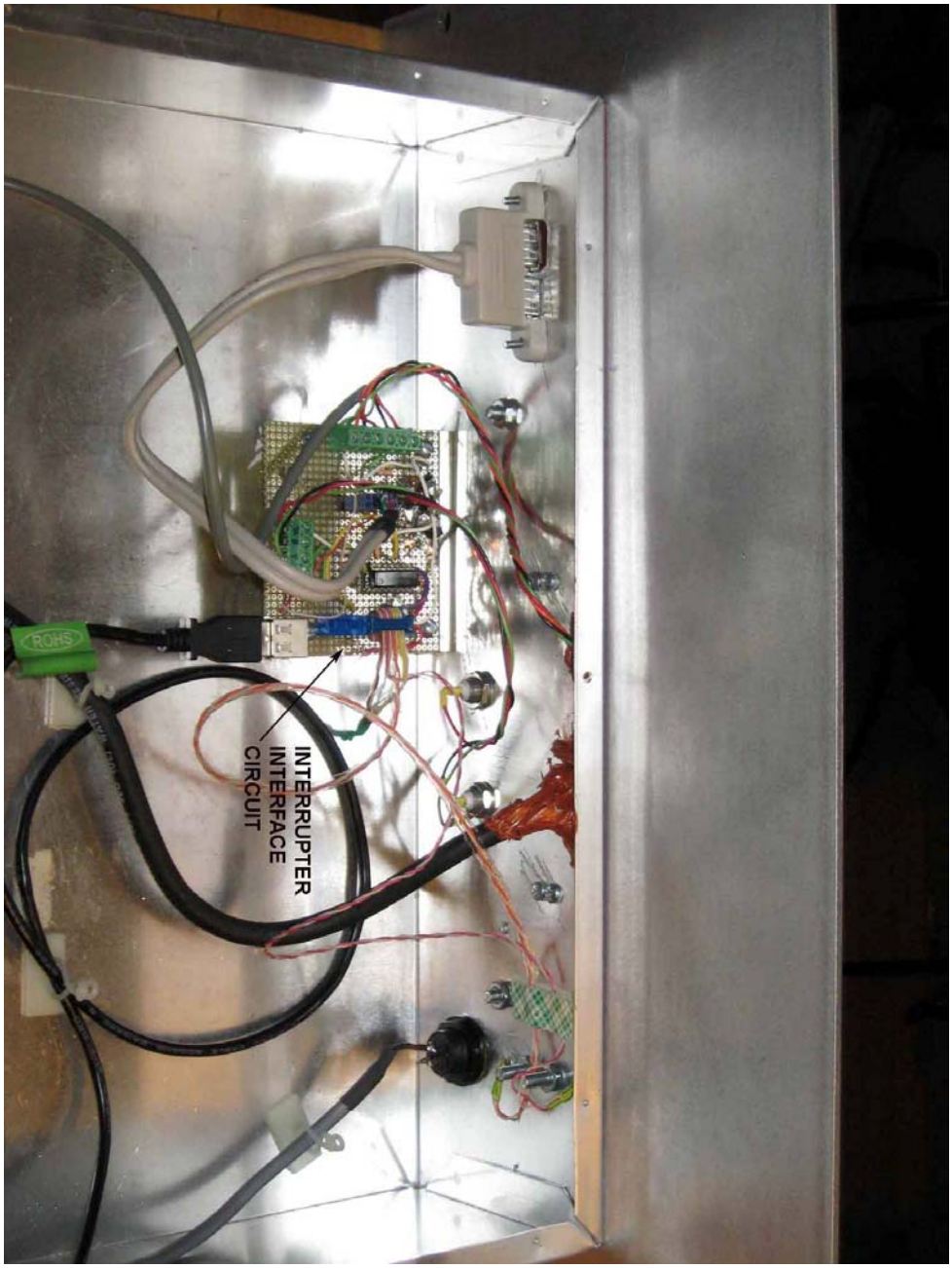

Figure 9-5 Picture showing inside of chopper-controller, in particular the photo-interruptor interface circuitry.

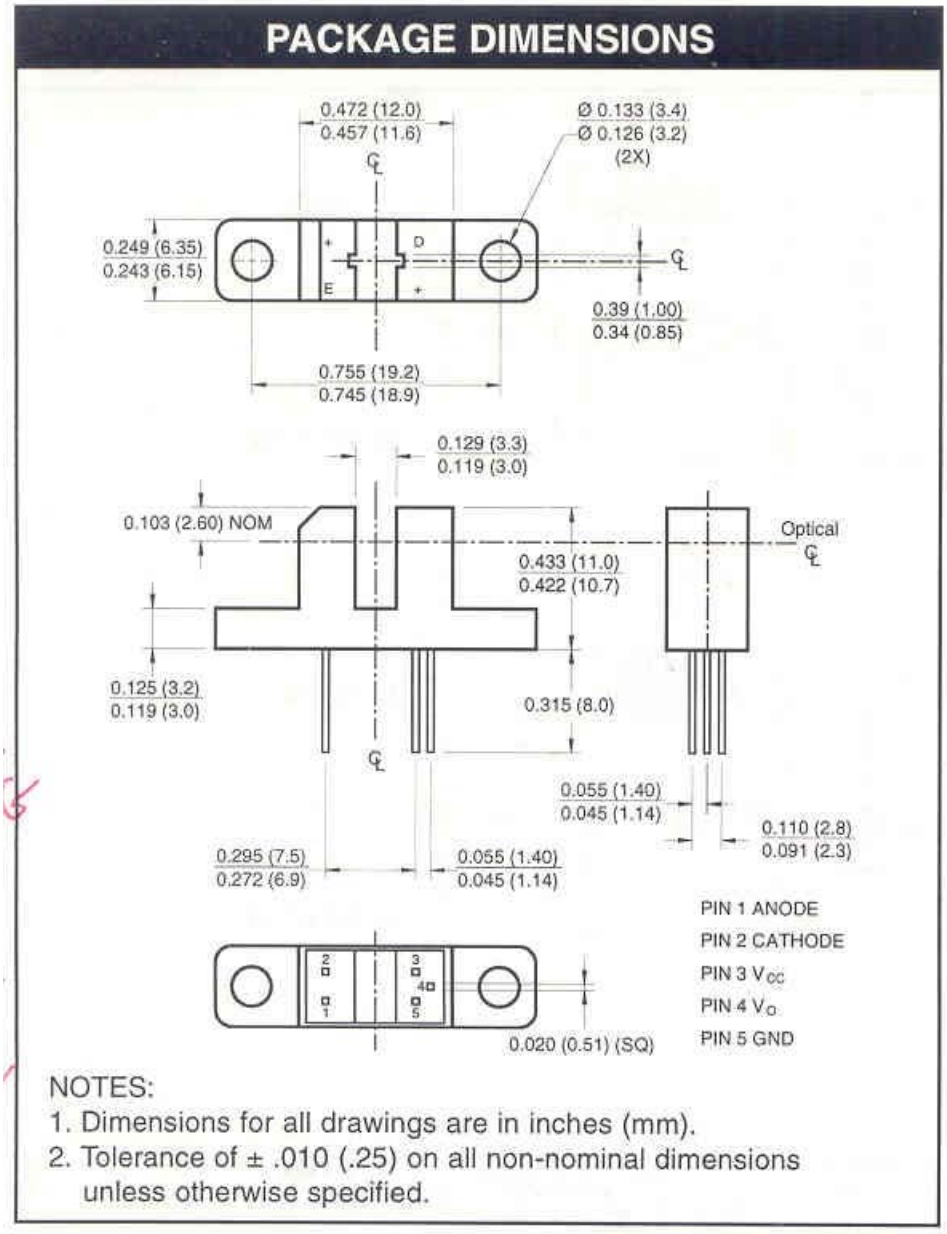

Figure 9-6 Picture showing the specifications and pin assignments of the photo-interruptor. See Figure 9-7 for how the various pins of the photo-interruptor (anode, cathode, V_{cc}, V_0 and GND are connected to the front panel of the chopper-controller).

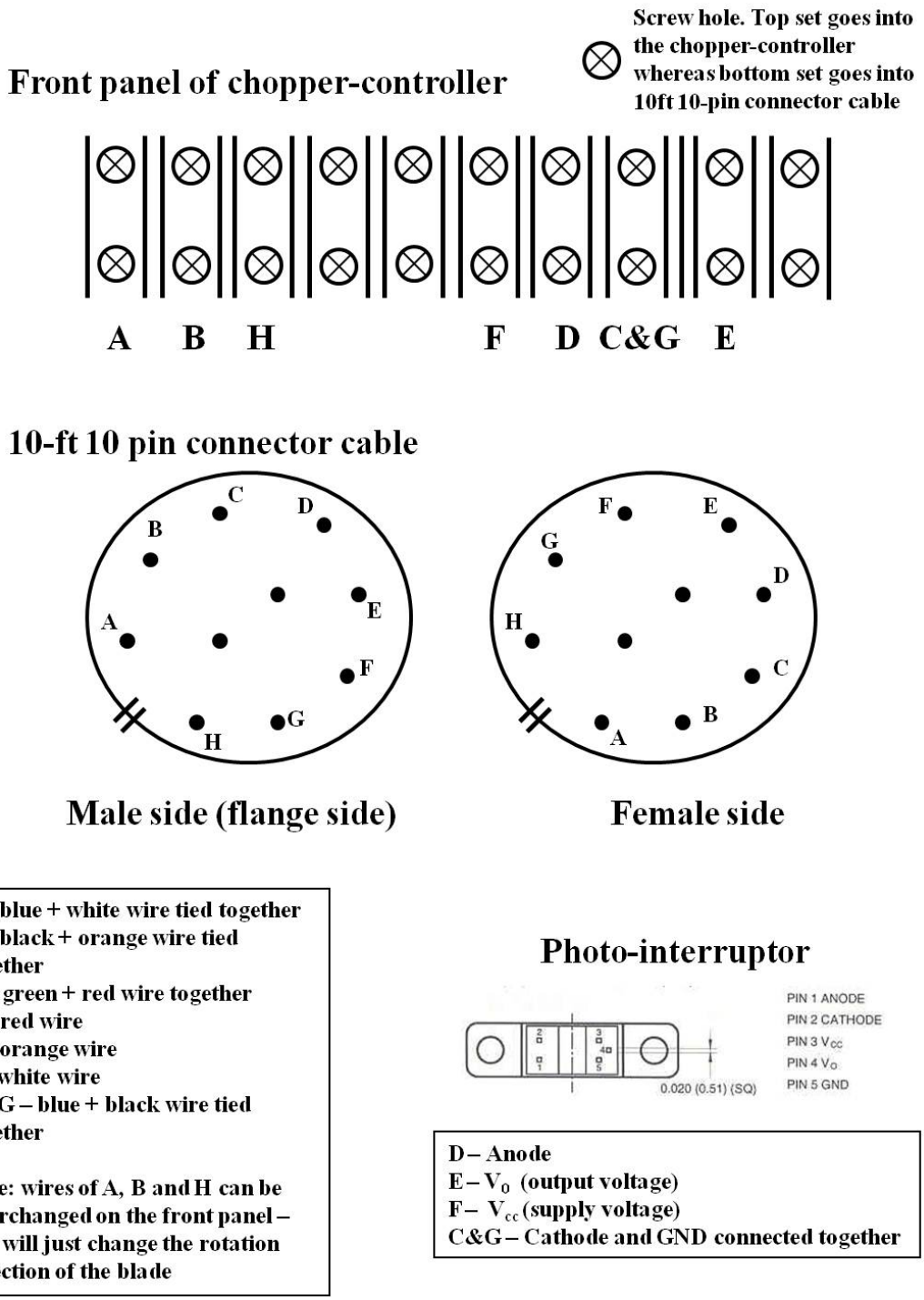

Figure 9-7 Pin assignments that the 10 ft 10-pin connector cable makes between the chopper flange and the chopper-controller.

9.3 SAM and polymer contact angle measurements

Table 9-1 Contact angle and surface energy measurements of SiO_2, SAMs and polymers studied in this thesis.

Surface	**Static contact angle (H_2O/formamide)**	**Advancing angle (H_2O)**	**Receding angle (H_2O)**	**Hysteresis**	**Surface energy (mJm^{-2})**
ODTS	94.3±1.9	103±1.6	88±2.2	15	
OTS	102.5±0.9 103.4±0.8/87.9±2.5	104±1.9	89±2.0	15	16.7
FOTS	104±4.3 106.4±1.0/97.4±1.2	107±2.1	89±1.2	18	11.1
MAOPTS	66.9±1.7/48.7±0.9				40.2
HMDS	77.3±1.1 79.1±0.6/60.5±1.0	88±1	69±2	19	32.7
NMTS	80.8±2.9/61.2±1.9				32.5
PHTS	83.2±2.7/68.6±1.8				33.4
PS	91.6±1.4/73.6 ±1.0				25.0
PMMA	70.5±1.1/56.0±2.3				35.6
PEI	~0/0				≥73.4
SiO_2	~0				

Appendix 9-4 SAM and polymer thin film properties

Table 9-2 shown below summarizes the properties of the SAMs and polymers studied in this thesis. These properties include electron density (ρ, $Å^{-3}$), interface width (σ, Å), and film thickness (d, Å). With the knowledge of the number of electrons (N_{el}) in the SAM backbone, one can then estimate the 2D surface coverage through $\rho d/N_{el}$. The properties displayed in Table 9-2 were determined from fitting specular XRR data of the SAMs and polymers using the Parratt32 software. In all cases the electron density of the bulk SiO_2 layer was fixed to 0.671 $Å^{-3}$. In two cases (OTS and FOTS), the imaginary component of the refractive index, β (see section 2.5), was also fit which resulted in a better fit. As observed though, fitting the β parameter only seemed to affect the interface widths significantly. Note that Parratt32 software scales the β parameter slightly differently in its fitting algorithm. To get the 'true' β parameter from Parratt32 software, one has to take the imaginary fit parameter from Parratt32 software and multiply it by $\lambda^2/2\pi$ where λ is the x-ray wavelength.

In some cases (ODTS and PHTS), including an interfacial-layer (ψ) in between the bulk SiO_2 layer and the SAM layer was required in order to get a good fit **[1]**. Physically, the interfacial layer could represent the head group of the SAM **[1]**. Under the interface width column in Table 9-2: $\sigma_{1,\psi}$ = interface width of the bulk SiO_2/interfacial-layer interface, $\sigma_{\psi,2}$ = interface width of the interfacial-layer/SAM or polymer interface and $\sigma_{2,3}$ = interface width of the SAM or polymer/vacuum interface.

If no interfacial-layer is present then $\sigma_{1,2}$ = interface width of the bulk SiO_2/ SAM or polymer interface.

For the case of ODTS and PHTS, we observe from Table 9-2, that the electron density of the interfacial-layer is estimated to be greater than the bulk SiO_2 layer (0.671 $Å^{-3}$): $1.17\rho_{SiO2}$ - $1.32\rho_{SiO2}$. In addition, from Table 9-2, we see that the estimated thickness of the interfacial layer ranges between 0.72 – 3.38 Å. Other studies, which also investigated the modeling of synchrotron XRR data of SAMs reported similar observations regarding the larger (relative to bulk SiO_2) interfacial-layer electron density **[1]** and interfacial-layer thickness ranges **[1, 2]**.

In Table 9-2, we observe that the interface width of the polymer/vacuum interface for the case of polystyrene (PS) and polymethylmethacrylate (PMMA) is significantly larger than observed for other SAM or polymer/vacuum interfaces. The XRR of PS and PMMA were done on films which had been sitting in air for several months – it was confirmed from *ex situ* AFM that the surfaces of these films were covered with tall features, most likely composed of contaminants from air. Dewetting of the polymer was not observed. A more accurate estimate of the surface roughness of PS and PMMA (using *ex situ* AFM) is shown in section 5 where a smooth flat surface was observed without tall features – these measurements were done immediately after polymer spin-coating.

Table 9-2 Properties of SAMs and polymers

Note: ψ = SAM interfacial-layer (head group)

Surface	**Electron density, ρ, ($Å^{-3}$)**	**Interface width, σ, (Å)**	**Thickness, *d*, (Å)**	**2D Surface coverage (nm^{-2})**
Bulk SiO_2 (fixed)	0.671			
ODTS	0.24±0.02 $\psi = 1.32\rho_{SiO2}$	$\sigma_{1,\psi}$=5.5±0.8 $\sigma_{\psi,2}$=4.8±1.0 $\sigma_{2,3}$=2.5±0.6	17.3±1.8 ψ =3.38±0.67	2.83±0.29
OTS	0.22±0.03	$\sigma_{1,2}$=5.0±0.2 $\sigma_{2,3}$=2.9±0.1	8.02±0.13	2.70±0.36
OTS (fitted β) $\beta = 8.3\times10^{-7}$	0.29±0.03	$\sigma_{1,2}$=4.3±0.4 $\sigma_{2,3}$=3.1±0.2	6.27±0.65	2.74±0.28
FOTS (fitted β) $\beta = 9.0\times10^{-7}$	0.53±0.04	$\sigma_{1,2}$=4.4±0.2 $\sigma_{2,3}$=3.2±0.1	6.32±0.50	1.97±0.12
FOTS	0.51±0.01	$\sigma_{1,2}$=2.9±0.01 $\sigma_{2,3}$=5.7±0.03	7.21±0.03	2.18±0.01
MAOPTS	0.24±0.03	$\sigma_{1,2}$=2.5±0.07 $\sigma_{2,3}$=2.7±0.15	5.87±0.15	2.00±0.17
NMTS	0.39±0.02	$\sigma_{1,2}$=2.4±0.04 $\sigma_{2,3}$=2.4±0.03	8.13±0.01	4.22±0.05
PHTS	0.32±0.01 $\psi = 1.25\rho_{SiO2}$	$\sigma_{1,\psi}$=1.8±0.4 $\sigma_{\psi,2}$=4.0±0.3 $\sigma_{2,3}$=2.0±0.1	11.45±0.12 ψ =0.72±0.13	4.18±0.19
PHTS (separate batch)	0.33±0.01 $\psi = 1.17\rho_{SiO2}$	$\sigma_{1,\psi}$=1.4±0.1 $\sigma_{\psi,2}$=3.2±0.1 $\sigma_{2,3}$=2.1±0.1	10.98±0.05 ψ =0.72±0.13	4.05±0.09
PS	0.44±0.00	$\sigma_{1,2}$=2.9±0.00 $\sigma_{2,3}$=6.0±0.01	23.9 nm	
PMMA	0.49±0.00	$\sigma_{1,2}$=2.4±0.01 $\sigma_{2,3}$=7.8±0.00	50.2 nm	
PEI	0.35±0.04	$\sigma_{1,2}$=2.9±0.4 $\sigma_{2,3}$=3.6±0.4	8.58±0.33	

9.5 Parratt Formalism code

```
%  code calculates reflected intensity using Parratt formalism - proof of concept that
%  Parratt32 software does what it supposed to do this code is for a 3-layer system:
%  vacuum - SAM or polymer -  substrate. It can be easily modified for extra layers
clc
close all
clear all

lam = 1.300241368;  % x-ray wavelength
k = 2*pi/lam;   %modulus of wavevector
psam = 0.38928318; %electron density sam 1/A^3
psio2 = 0.671; %electron density sio2 1/A^3

pim_sam = 0; %imaginary part of sam electron density. Note that Parratt32 scales the
imaginary part slightly differently. In order to use this code with this parameter, take
the fit parameter from Parrtt32 and multiply it by lam^2/(2*pi).

pim_sio2 = 0; %imaginary part of sio2 electron density. Note that Parratt32 scales the
imaginary part slightly differently. In order to use this code with this parameter, take
the fit parameter from Parrtt32 and multiply it by lam^2/(2*pi).

dsam = 8.13; %thickness of sam or polymer
```

```
rsv =  2.356; %roughness of sam/vac interface

rbs =  2.37; %roughness of bulk sio2/sam interface

r0 = 2.8180E-05;    %Thompson scattering length

del_sam = (lam^2/(2*pi))*psam*r0;   %calculate delta of n_sam. Alternatively,

psam*r0 is also the scattering length that is the fit parameter in Parratt32


del_b = (lam^2/(2*pi))*psio2*r0; %calculate delat of n_sio2. Alternatively, psio2*r0

is also the scattering length that is the fit parameter in Parratt32


n_air = 1;      % n of vacuum

n_sam = 1-del_sam+1i*pim_sam; % n of sam or polymer

n_bulk = 1-del_b+1i*pim_sio2; %n of bulk sio2

Q = 0.01:0.1:15;    % degree range

Y = ((4*pi)/lam)*sin(Q*pi/360); % change degree to q_z A^-1

Q = Q*pi/360; % change 2theta degree into radian incident angle


[a b] = size(Q);


for j=1:b

   kz1(j) = k*(n_air^2 - cos(Q(j))^2)^0.5; %wavevector transfer through vacuum

   kz2(j) = k*(n_sam^2 - cos(Q(j))^2)^0.5; %wavevector transfer through sam

   kz3(j) = k*(n_bulk^2 - cos(Q(j))^2)^0.5; %wavevector transfer through bulk sio2

end
```

```
 % fresnel coefficient at vacuum/sam interface
r12 = ((kz1-kz2)./(kz1+kz2)).*exp(-2*kz1.*kz2*rsv^2);

% fresnel coefficient at sam/sio2 interface
r23 = ((kz2-kz3)./(kz2+kz3)).*exp(-2*kz2.*kz3*rbs^2);

% intensity reflected from air/sam interface
R = (r12+r23.*exp(2*1i.*kz2*dsam))./(1+r12.*r23.*exp(2*1i.*kz2*dsam));

RR = (abs(R).^2)'; %square of intensity R

%addition of any background - this will vary based on the raw XRR data
RR = RR+5.06e-10;
```

9.6 References

1. Tidswell, I. M.; Ocko, B. M.; Pershan, P. S.; Wasserman, S. R.; Whitesides, G. M.; Axe, J. D. *Phys. Rev. B* **1990**, *41*, 1111-1128.

2. Richter, A. G.; Durbin, M. K.; Yu, C.-J; Dutta, P. *Langmuir* **1998**, *14*, 5980-5983.